

Imperial College London  
Department of Aeronautics

# **Feedback Control of Three-Dimensional Bluff Body Wakes for Efficient Drag Reduction**

Rowan D. Brackston

June 2017

Submitted in part fulfilment of the requirements for the degree of  
Doctor of Philosophy in Aeronautics of Imperial College London  
and the Diploma of Imperial College London

# Declaration

I herewith certify that all material in this dissertation which is not my own work has been properly acknowledged.

Rowan D. Brackston

The copyright of this thesis rests with the author and is made available under a Creative Commons Attribution Non-Commercial No Derivatives licence. Researchers are free to copy, distribute or transmit the thesis on the condition that they attribute it, that they do not use it for commercial purposes and that they do not alter, transform or build upon it. For any reuse or redistribution, researchers must make clear to others the licence terms of this work.



# Abstract

The wakes of bluff bodies, such as automotive vehicles, exhibit complex behaviour due to three-dimensionality and high Reynolds numbers, and are furthermore responsible for significant aerodynamic drag. There are significant environmental and economic incentives for reducing drag, however practicalities limit the extent to which this can be achieved through changes to the vehicle shape. This motivates the use of active feedback control methods that modify the flow directly, without significant geometric changes.

In this thesis we develop feedback control strategies for two generic three-dimensional bluff bodies, a bullet-shaped body and the widely used Ahmed body. After first applying an extremum-seeking controller to a pre-existing open-loop strategy, we then examine the control of specific coherent structures within the wakes. Two such structures understood to be related to the drag are the static symmetry breaking (SB) mode and the quasi-oscillatory vortex shedding. The former of these is observed as a large-scale asymmetry within the recirculating region. We find, through simultaneous surface pressure and wake velocity measurements, that both the SB mode and vortex shedding may be observed in real-time using practical pressure sensors. Through the use of forcing flaps, we further demonstrate that we are able to strongly interact with both these coherent structures. Statically deflected flaps also prove effective at drag reduction under cross-wind conditions. In order to guide feedback controller design, we develop stochastic models for each of the coherent structures, describing their dynamics and response to forcing. Controllers are then implemented, achieving an efficient drag reduction of 2% when suppressing the asymmetry of the SB mode. Vortex shedding control proved ineffective at drag reduction, despite the suppression of measured fluctuations around the frequency at which oscillations are observed.

# Preface

Journal publications produced during the course of this work:

- i R. D. Brackston, A. Wynn & J. F. Morrison. Extremum seeking to control the amplitude and frequency of a pulsed jet for bluff body drag reduction. *Exp. Fluids*, **57(10)**, 2016.
- ii R. D. Brackston, J. M. García de la Cruz, A. Wynn, G. Rigas & J. F. Morrison. Stochastic modelling and feedback control of bistability in a turbulent bluff body wake. *J. Fluid Mech.*, **802**, 2016.
- iii G. Rigas, A. S. Morgans, R. D. Brackston, & J. F. Morrison. Diffusive dynamics and stochastic models of turbulent axisymmetric wakes. *J. Fluid Mech.*, **778 R2**, 2015.

This work was presented at the following conferences:

- i R. D. Brackston, A. Wynn, J. M. García de la Cruz & J. F. Morrison. Modelling and Feedback control of the Ahmed body wake for Efficient Drag reduction, 52<sup>nd</sup> *3AF International Conference AERO2017, Lyon*, 2017.
- ii J. M. García de la Cruz, R. D. Brackston & J. F. Morrison. Adaptive base-flap under variable cross-wind, 52<sup>nd</sup> *3AF International Conference AERO2017, Lyon*, 2017.
- iii R. D. Brackston, A. Wynn, J. M. García de la Cruz, G. Rigas & J. F. Morrison. Modelling and Feedback Control of Bistability in a Turbulent Bluff Body Wake, 69<sup>th</sup> *Annual Meeting of the APS Division of Fluid Dynamics, Portland*, 2016.
- iv R. D. Brackston, J. M. García de la Cruz, A. Wynn, G. Rigas & J. F. Morrison. Drag Reduction of the Flat-Backed Ahmed Body by Active Suppression of Wake Asymmetry. *Aerovehicles 2, Göteborg*, 2016.

- v R. D. Brackston, A. Wynn, J. M. García de la Cruz, G. Rigas & J. F. Morrison. Feedback control of bistability in the turbulent wake of an Ahmed body. *68<sup>th</sup> Annual Meeting of the APS Division of Fluid Dynamics, Boston*, 2015.
- vi R. D. Brackston, A. Wynn & J. F. Morrison. Observability of the turbulent wake behind an axisymmetric bluff body, *67<sup>th</sup> Annual Meeting of the APS Division of Fluid Dynamics, San Francisco*, 2014.

# Acknowledgements

I would firstly like to thank my supervisors Dr Andrew Wynn and Professor Jonathan Morrison for their help and guidance over the past three years. Andy's sharp eye for detail and checking of this thesis has no doubt improved it immensely. I am also appreciative to Jonathan for giving me the freedom to explore as I saw fit, and for providing the practical and financial resources to make this possible.

Within the research group I would like to thank Antony Oxlade for much initial guidance with experiments and for the excellent axisymmetric model that I inherited at the beginning; Georgios Rigas for the initial idea behind forcing flaps and for considerable encouragement and enthusiasm over many discussions; Marcos García de la Cruz Lopez for his excellent work in the construction and intricate design of the Ahmed Model as well as for countless entertaining and thought provoking conversations. Hopefully our efforts will not have been in vain and Active flap still has a future.

I would finally like to thank my parents for all their support and my wife Jane for her patience and understanding over many years.

Financial support from the Imperial College President's Scholarship is also gratefully acknowledged.

# Nomenclature

## Acronyms

CoP	Center of pressure	m
ES	Extremum seeking	
FPE	Fokker-Planck equation	
LSE	Linear stochastic estimation	
PDF	Probability density function	
PIV	Particle image velocimetry	
POD	Proper orthogonal decomposition	
PSD	Power spectral density	
RHP	Right-half-plane	
rms	Root mean square	
SB	Symmetry breaking	
SDE	Stochastic differential equation	
SISO	Single input single output	
SNR	Signal to noise ratio	
ZNMF	Zero net mass flux	

## Greek symbols

$\alpha$	Growth rate	$\text{s}^{-1}$
$\beta$	Body yaw angle	degrees
$\delta$	Instability timescale	s
$\theta$	Flap angle	degrees

$\zeta$	Damping ratio	
$\lambda$	Saturation parameter	$\text{m}^{-2} \text{s}^{-1}$
$\xi$	Random variable	
$\rho$	Air density; CoP radius	$\text{kg m}^{-3}$ ; m
$\sigma$	Noise intensity	$\text{m s}^{-1}$
$\tau$	Time delay	s
$\phi$	CoP angle	rad
$\phi$	Normalised pressure mode shape	
$\varphi$	Instantaneous phase; Phase shift	rad
$\psi$	Vortex shedding phase	rad
$\omega$	Angular frequency	$\text{rad s}^{-1}$

**Roman symbols**

$a$	Dither signal amplitude; Vortex shedding amplitude	
$A$	Actuator transfer function; Base area	degrees $\text{V}^{-1}$ ; $\text{m}^2$
$A, B, C, D$	State-space matrices	
$b$	Flap gain	
$C_D$	Drag coefficient	
$C_p$	Local pressure coefficient	
$d$	Dither signal; Transfer function denominator	
$D$	Bullet shaped body diameter	m
$e$	Feedback error	
$E$	Expectation operator	
$f$	Frequency	Hz
$F$	Mapping function	
$g$	Plant transfer function DC gain	
$G$	Plant transfer function	
$H$	Ahmed body height	m

---

$K$	Controller transfer function	
$m$	Pressure mode coefficient	
$n$	Transfer function numerator	
$p$	Local static pressure	Pa
$P$	Probability	
$r$	ES reference parameter; Dimensionless RSB mode amplitude	
$\mathbb{R}$	Real part	
$Re$	Reynolds number	
$s$	Laplace transform variable	
$S$	Power spectral density; Sensitivity function	
$St$	Strouhal number	
$T$	Mean flipping period	s
$u, x, y$	State-space variables: inputs, states, outputs	
$U_\infty$	Free stream velocity	$\text{m s}^{-1}$
$v$	Flap motor driving voltage	V
$V$	Energy potential	$\text{m}^2 \text{s}^{-1}$
$w$	Frequency weighting function	
$W$	Ahmed body width	m
$x, y, z$	Cartesian coordinates	m
$\boldsymbol{x}$	Global mode amplitude	
$Y, Z$	Dimensionless CoP coordinates	

# Contents

<b>Abstract</b>	<b>2</b>
<b>Preface</b>	<b>3</b>
<b>Acknowledgements</b>	<b>5</b>
<b>1 Introduction and literature review</b>	<b>10</b>
1.1 The aerodynamic drag of bluff body wakes . . . . .	11
1.2 Key characteristics of three-dimensional bluff body wakes . . . . .	14
1.2.1 Low Reynolds numbers and bifurcations . . . . .	14
1.2.2 Multistability and the axisymmetric wake . . . . .	16
1.2.3 Bistability and the Ahmed body wake . . . . .	18
1.2.4 Implications for drag reduction . . . . .	20
1.3 Feedback control of fluid flows . . . . .	22
1.3.1 Extremum seeking control . . . . .	22
1.3.2 Low-dimensional modelling for feedback control . . . . .	24
1.3.3 Flow measurement . . . . .	26
1.4 Conclusions and thesis plan . . . . .	27
<b>2 Experimental and analytical methods</b>	<b>29</b>
2.1 The axisymmetric bluff body . . . . .	29
2.1.1 Extremum-seeking control experiments . . . . .	30
2.1.2 Synchronised PIV experiments . . . . .	31
2.2 The Ahmed body . . . . .	32
2.2.1 Actuator characteristics . . . . .	33
2.2.2 Base pressure metrics . . . . .	34
2.3 Experimental procedures . . . . .	39



---

2.3.1	Open-loop forcing with flaps . . . . .	39
2.3.2	Closed-loop control with flaps . . . . .	39
2.4	Other analyses . . . . .	40
2.4.1	Frequency response . . . . .	40
2.4.2	The proper orthogonal decomposition . . . . .	41
<b>3</b>	<b>Extremum seeking control of the axisymmetric wake</b>	<b>43</b>
3.1	Analysis . . . . .	43
3.1.1	Principle of operation . . . . .	44
3.1.2	Frequency optimisation . . . . .	46
3.1.3	Stability . . . . .	49
3.1.4	Performance . . . . .	50
3.2	Experimental implementation . . . . .	52
3.2.1	System properties . . . . .	52
3.2.2	Extremum seeking algorithm . . . . .	54
3.2.3	Parametric investigation . . . . .	55
3.2.4	Single variable implementations . . . . .	57
3.2.5	Dual variable implementation . . . . .	59
3.2.6	Adaptation to changing conditions . . . . .	60
3.3	Concluding remarks . . . . .	61
<b>4</b>	<b>Observability of coherent structures</b>	<b>63</b>
4.1	Background to the observability problem . . . . .	63
4.2	Acquisition configuration . . . . .	65
4.3	Choice of velocity-field features . . . . .	67
4.4	Decompositions of base pressure data . . . . .	69
4.5	Correlations . . . . .	72
4.6	Discussion and conclusions . . . . .	74

<b>5</b>	<b>Open-loop control with flaps</b>	<b>77</b>
5.1	Harmonic forcing . . . . .	78
5.1.1	Frequency response . . . . .	78
5.1.2	The forced flow . . . . .	82
5.1.3	Discussion and concluding remarks . . . . .	84
5.2	Static forcing . . . . .	85
5.2.1	Optimal flap positioning . . . . .	86
5.2.2	Bistability at yaw . . . . .	89
5.2.3	Concluding remarks . . . . .	92
<b>6</b>	<b>Stochastic modelling of coherent structures</b>	<b>95</b>
6.1	A general model . . . . .	95
6.2	Symmetry breaking in the axisymmetric bluff body wake . . . . .	97
6.2.1	Stochastic model . . . . .	97
6.2.2	Experimental data . . . . .	98
6.3	Symmetry breaking in the Ahmed body wake . . . . .	100
6.3.1	Stochastic model . . . . .	100
6.3.2	Parameter normalisation . . . . .	102
6.3.3	Unforced flow . . . . .	104
6.3.4	Response to harmonic forcing . . . . .	105
6.3.5	Offset response . . . . .	108
6.3.6	Parameter extraction . . . . .	108
6.4	A model for the vortex shedding . . . . .	110
6.4.1	The stochastic model . . . . .	111
6.4.2	Simulations . . . . .	112
6.5	Summary . . . . .	114
<b>7</b>	<b>Closed-loop control with flaps</b>	<b>117</b>
7.1	System interpretation . . . . .	117
7.1.1	Implications for feedback control . . . . .	119
7.1.2	Control approaches . . . . .	120
7.2	Control of bistability . . . . .	121
7.2.1	System formation . . . . .	122

7.2.2	Preliminary control design . . . . .	124
7.2.3	Detailed control design and performance . . . . .	125
7.2.4	The controlled flow . . . . .	130
7.3	Control of vortex shedding . . . . .	132
7.3.1	System formation . . . . .	133
7.3.2	Control design . . . . .	133
7.3.3	Controller performance . . . . .	137
7.3.4	Analysis of the controlled flow . . . . .	138
7.4	Summary . . . . .	141
<b>8</b>	<b>Conclusions</b>	<b>145</b>
8.1	Possible future work . . . . .	146
	<b>Bibliography</b>	<b>151</b>
<b>A</b>	<b>Open-loop forcing with four flaps</b>	<b>165</b>
A.0.1	Summary . . . . .	168
<b>B</b>	<b>Stochastic differential equations</b>	<b>169</b>
B.1	Fokker-Planck equation . . . . .	170
<b>C</b>	<b>Miscellaneous proofs</b>	<b>171</b>
C.1	Extremum seeking with a square dither signal . . . . .	171
C.2	Statistics of bistable processes . . . . .	173
C.2.1	Switching statistics . . . . .	173
C.2.2	Power spectral density . . . . .	174
<b>D</b>	<b>Analyses</b>	<b>177</b>
D.1	Bubble length estimation . . . . .	177
D.2	Time delay estimation . . . . .	178
D.3	Least squares fitting . . . . .	178
<b>E</b>	<b>Parameter influence in the stochastic models</b>	<b>181</b>

# List of Tables

2.1	Parameters for the PIV experiments. . . . .	31
3.1	Parameters of the ES algorithm and their effect on system performance.	47
3.2	Variation of the system performance with the choice of parameters when seeking in amplitude. . . . .	56
6.1	Dimensionless parameters for the low dimensional model (6.6). The parameters are determined from the experimental data. . . . .	103
6.2	Dimensionless parameters for the low dimensional model (6.4). Values are non-dimensionalised from those given in Rigas <i>et al.</i> (2015). . . .	103
6.3	Dimensionless parameters for the low dimensional model (6.17). The growth rate is determined by $\alpha_r$ while the natural frequency ( $\omega_0$ ) is determined by $\alpha_i$ . By definition $\lambda_r a_e^2 / \alpha_r = 1$ , and by choice $\lambda_i = 0$ . .	112
7.1	The controllers and their performance including the controller gain, drag reduction, base pressure change, actuation power as a percent- age of the power saving and the most amplified frequency. For com- parison, the results for the open-loop forcing giving approximately maximal drag reduction are also shown. . . . .	125

# List of Figures

1.1	Schematic of the control volume used by Balachandar <i>et al.</i> (1997). The solid lines indicate the boundary of the body and the time averaged streamlines bounding the separation bubble. Image reproduced with permission of the rights holder, Cambridge University Press. . . .	12
1.2	The low $Re$ SB mode in three-dimensional wakes: (a) the axisymmetric bullet-shaped body from Bury & Jardin (2012) and (b) the rectilinear Ahmed body from Grandemange <i>et al.</i> (2012a). Images reproduced with permission of the rights holders, Elsevier (a) and the American Physical Society (b). . . . .	15
1.3	Plan view of the Ahmed body showing a conditional average of one of the symmetry breaking states of the wake, obtained from PIV. The streamlines demonstrate the asymmetry, showing the stationary vortex adjacent to the base. . . . .	19
1.4	Variation of drag over a range of low Reynolds numbers: (a) data for the sphere from Pier (2008), for which the static mode bifurcation occurs at $Re_1$ , followed by the vortex shedding at $Re_2$ ; (b) base suction data for circular cylinders from Roshko (1993). Images reproduced with permission of the rights holders, Cambridge University Press (a) and Elsevier (b). . . . .	21
2.1	Experimental setup: side view of the model (left) and detailed view of the base including instrumentation (right). The body diameter is $D = 0.1965$ m. . . . .	30
2.2	View of the Ahmed body showing the overall assembly (left) and detailed view of the base (right). The model is here shown fitted with lateral flaps and has a width $W$ of 0.216 m. . . . .	32
2.3	Detailed view of the flap actuators including the static and dynamic motors. Pivot locations are shown by the green dots, while the springs (obscured from view) are shown by the dashed red lines. . . . .	35

2.4	Typical frequency response of the actuator between voltage input $v$ and angle output $\theta$ . The blue/red dots are for flaps mounted on each of the left/right sides respectively. Also shown by the black dashed line is a linear 2nd-order fit. . . . .	35
2.5	The normalised pressure modes $\phi_L$ and $\phi_V$ , plotted on the base of the Ahmed body. . . . .	37
2.6	Ratio of the Fourier transform of the average measurement from the 64 ESPappings on the base to the 8 pressure transducers. . . . .	38
3.1	(a) Examples of common nonlinear mappings and (b) the standard extremum seeking control algorithm applied to a SISO system. . . . .	44
3.2	Frequency optimisation: (a) an illustrative mapping between forcing frequency and output and (b) the single sided spectrum of the input $u$ in the case of a standard dither (red) or a square wave dither signal (blue). . . . .	47
3.3	Frequency response of the moving average filter of period $T = 2\pi/\omega_d$ . . . . .	51
3.4	The two dimensional steady-state mapping for the open-loop system of Oxlade <i>et al.</i> (2015). Spatially averaged base pressure is given as a function of forcing amplitude and frequency, where the forcing amplitude is defined in terms of the rms of the pressure ( $p_c$ ) inside the cavity. Negative contours are shown by the dashed lines. . . . .	53
3.5	The modified ES algorithm implemented experimentally. The output $y$ is the pressure instantaneously averaged over the base, while the reference $r$ is either the forcing amplitude or frequency. . . . .	54
3.6	Amplitude only optimisation at a frequency of 650 Hz: (a) the spatially averaged base pressure evolution and (b) the controller variables $r(t)$ and $e(t)$ . Inset is the trajectory over the mapping shown in figure 3.4. . . . .	57
3.7	Frequency only optimisation at an amplitude of 250 Pa: (a) the spatially averaged base pressure evolution and (b) controller variables $r(t)$ and $e(t)$ . Inset is the trajectory over the mapping shown in figure 3.4. . . . .	58
3.8	Extremum seeking in two variables: (a) time series and (b) trajectory across the mapping of figure 3.4. . . . .	60
3.9	The response of the controller to a slow variation in the tunnel speed. . . . .	61
4.1	The time-averaged (a) pressure and (b) velocity fields over a given acquisition period. . . . .	66

4.2	The most energetic velocity field POD mode $\phi_{u1}$ , (a) displayed in terms of the velocity magnitude $\mathbf{u}$ and (b) the pre-multiplied PSD of the modal coefficient. The modal coefficient $a_1$ is chosen as the first velocity-field state $x_1$ . . . . .	68
4.3	Illustration of the region defining the recirculation metric $\Gamma$ , chosen as the velocity-field state $x_2$ . . . . .	69
4.4	Illustration of velocity field metric $x_s$ used for velocity-field state $x_3$ , showing the selected location for a particular velocity field snapshot. .	70
4.5	The base pressure POD modes in a rotating frame of reference. . . .	71
4.6	Simultaneous time-series and normalised cross-correlation between first velocity POD mode coefficient $a_{u1}$ and CoP radius $\rho$ . . . . .	73
4.7	Simultaneous time-series and normalised cross-correlation between the near base circulation $\Gamma$ and the second pressure POD mode coefficient $a_{p2}$ . . . . .	73
4.8	Simultaneous time-series and normalised cross-correlation between stagnation point location $x_s$ and spatially averaged base pressure $\langle p \rangle$ . .	74
4.9	Premultiplied PSD for the CoP radius $\rho$ . The black dashed lines approximately demarcate the frequency range of the vortex shedding. .	76
5.1	Effect of lateral anti-symmetric forcing. Plots show the frequency response (upper, middle) and average drag change (lower), as a function of forcing frequency $St_W$ and for varying forcing amplitudes. . . . .	79
5.2	Phase-averaged response of the lateral pressure metric to lateral forcing, for a number of key forcing frequencies. Data are displayed for a speed of $15 \text{ ms}^{-1}$ and forcing amplitude of $7.5^\circ$ . . . . .	80
5.3	Effect of vertical anti-symmetric forcing. Plots show the frequency response (upper, middle) and average drag change (lower), as a function of forcing frequency $St_H$ and for varying forcing amplitudes. . . . .	81
5.4	Phase-averaged response of the vertical pressure metric to vertical forcing, for a number of key forcing frequencies. Data are displayed for a speed of $15 \text{ ms}^{-1}$ and forcing amplitude of $7.5^\circ$ . . . . .	82
5.5	Effect of lateral anti-symmetric forcing on the distributions of vertical and lateral pressure metrics, compared with the unforced case given by the black dashed line. Data are displayed for a speed of $15 \text{ ms}^{-1}$ and forcing amplitude of $7.5^\circ$ . . . . .	83

5.6	Effect of vertical anti-symmetric forcing on the distributions of lateral and vertical pressure metrics, compared with the unforced case given by the black dashed line. Data are displayed for a speed of $15 \text{ ms}^{-1}$ and forcing amplitude of $7.5^\circ$ . . . . .	84
5.7	Plan view of the Ahmed body detailing the sign convention for the angles $\beta$ , $\theta_1$ , $\theta_2$ used for static forcing. Yaw angles $\beta$ are positive as a clockwise rotation about the $z$ axis while flap angles $\theta$ are positive towards the base of the body. . . . .	86
5.8	Maps of $C_D$ against the flap angles $\theta_1$ and $\theta_2$ . Data is shown here for yaw angles $\beta = 0^\circ, 3^\circ, 6^\circ, 9^\circ$ and for flap lengths $\delta = 9\%$ (upper row), and $\delta = 13\%$ (lower row). White crosses mark the configuration giving minimum drag. . . . .	87
5.9	Base suction coefficient $-\langle C_p \rangle$ , drag coefficient $C_D$ and lateral force coefficient $ C_y $ as a function of each of $\theta_1$ and $\theta_2$ with the other held constant. For these data $\beta = 6^\circ$ and $\delta = 13\%$ . . . . .	88
5.10	Base suction coefficient $-\langle C_p \rangle$ , drag coefficient $C_D$ and lateral force coefficient $ C_y $ as a function of each of $\theta_R$ and $\theta_B$ with the other held constant. For these data $\beta = 6^\circ$ and $\delta = 13\%$ . . . . .	89
5.11	Contour maps of $-\langle C_p \rangle$ (upper row) and the variance of the pressure metric ( $\text{var}(m_l)$ ) (lower row) as a function of $\theta_1$ , $\theta_2$ . Dark colours correspond to low pressure drag in the upper row which coincides with high $\text{var}(m_l)$ (light colours) in the lower row. The flap length is $\delta = 13\%$ . . . . .	90
5.12	Effect of flap positioning on the distribution of the lateral pressure metric $m_l$ . Cases for which $\theta_1 = \theta_2 = 0$ are displayed in (a) while those giving a bistable wake are displayed in (b). . . . .	91
5.13	Schematic of the effect of ruddering and yaw angles in the flow. Under aligned conditions small $\theta_R$ preferentially selects one of the two asymmetric states of the wake. Under non-zero $\beta$ one of the states is also selected, however ruddering of the flaps is able to restore the flow to a situation in which the other state can exist. . . . .	92
5.14	Frequency response between anti-symmetric flap forcing and pressure metric $m_l$ under aligned and yawed conditions. For the case $\beta = 1.5^\circ$ the mean ruddering angle of the flaps is $\theta_R = 7.8^\circ$ . . . . .	93
6.1	Time series of the centre of pressure coordinates $(\rho, \phi)$ . Large changes in $\phi$ are seen to correspond to times when $\rho$ is small. . . . .	98



6.2	Statistics for the CoP angle $\phi$ showing (a) the power spectral density, and (b) the escape time statistics. The solid black line shows the dimensionless exponential distribution: $p(\tau_q) = \exp(-\tau_q/\langle\tau_q\rangle)$ . Inset is the mean escape time $\langle\tau_q\rangle$ as a function of the number of bins $q$ . . . . .	99
6.3	(a) The potential well $V(r)$ for $\theta = 0$ , and (b) an example time series demonstrating the time-scales $T$ and $\delta$ . . . . .	101
6.4	Properties of the mode $r$ at the three tested $Re$ : (a) probability density function and (b) power spectral density. . . . .	104
6.5	Analytical solutions to the frequency response according to (6.14) for varying forcing amplitudes and (6.12) for the case $r_K = \alpha$ . . . . .	107
6.6	Frequency response between the antisymmetric flap oscillation and the mode $r$ at the three $Re$ . The flap oscillation amplitude is $10^\circ$ . . . . .	107
6.7	Response of the wake to static forcing: (a) Steady state PDF $P(r)$ under a range of steady flap angles $\theta$ and (b) skewness as a function of $\theta$ . The dashed line in (b) shows the linear fit used to establish the parameter $b$ , fitted for $-2^\circ < \theta < 2^\circ$ . . . . .	109
6.8	Unforced time series (left) and power spectral density (right) for the variable $y = a \sin(\psi)$ of (6.17). . . . .	113
6.9	Frequency response of the model (6.17) between real input $u_r = U \sin(\omega t)$ and output $y = a \sin(\psi)$ . Also shown is a linear 2nd-order fit to the data. . . . .	114
7.1	A schematic of the feedback control loop comprising the wake $G_{1,2}$ , actuator $A$ and feedback controller $K$ . $G_1$ captures the low-frequency dynamics of the bistability (lateral) or near-wake deflection (vertical), while $G_2$ captures the vortex shedding and shear layer dynamics at higher frequencies. . . . .	121
7.2	Linear fits to the actuator dynamics (left) and higher frequency wake dynamics (right). A second-order fit is found for the actuator, between an input in volts and output in degrees. The red and blue dots are for each of the two lateral actuators. A fifth-order linear fit to the wake dynamics is found using the MATLAB command <code>fitfrd</code> , applied only to the part of the frequency response to the right of the shaded region. . . . .	123
7.3	PDF for $r$ (a) and premultiplied PSD (b) under the three controllers. The solid black line shows the uncontrolled case for comparison. . . . .	126
7.4	Bode plot for the controllers (left) and the expected sensitivity function $S$ (right). . . . .	127

7.5	The Nyquist diagram for the three controllers. For stabilisation of the SB mode we require one encirclement of the $-1$ location, as marked by the red cross. . . . .	128
7.6	Time series of the pressure metric ( $r$ ), drag coefficient ( $C_D$ ) and lateral force coefficient ( $C_y$ ). The controller is turned on at $t = 0$ . Red lines show the low pass filtered $r$ and mean forces over the uncontrolled and controlled periods. . . . .	131
7.7	The dynamics of the actuator showing (a) a short time series of the mode $r$ and flap angles $\theta$ , and (b) their power spectrum. . . . .	131
7.8	Comparison of the experimental frequency response and the composite model evaluated as the sum $G_1(s) + G_2(s)$ . . . . .	133
7.9	Drag change with open-loop forcing frequency (a) and PSD of the vertical pressure metric $m_v$ for the unforced flow (b). . . . .	134
7.10	A schematic of the feedback control loop of figure 7.1, reformatted for the $\mathcal{H}_\infty$ synthesis problem. The additional blocks $w_1$ and $w_2$ are weighting functions that are chosen in order to specify the desired properties of the closed-loop system. . . . .	135
7.11	Illustration of a particular control design showing the weighting functions $w_1$ , $w_2$ and the corresponding closed-loop transfer functions $S$ , $KS$ . . . . .	136
7.12	Scatter plot of the drag and base pressure changes achieved by all of the tested controllers. Positive $\Delta C_D$ corresponds to a drag increase. . . . .	137
7.13	PSD of the vertical pressure metric $m_v$ for a particular controller. Suppression is achieved around $St_H \approx 0.2$ , however the drag is not reduced. . . . .	138
7.14	(a) A comparison of the best-fit weighting function $\hat{F}$ with the uncontrolled spectrum, and (b) a comparison of the actual and predicted drag changes from the least-squares fit. . . . .	140
7.15	The frequency weighting function $w(z, \omega)$ , displayed as a function of $St_H$ . . . . .	141
A.1	Effect of symmetric harmonic forcing with all four flaps operating either synchronously or asynchronously. Drag coefficient $C_D$ and base suction coefficient $-\langle C_p \rangle$ are shown by the solid and dashed lines respectively. . . . .	166
A.2	Waterfall plots illustrating the effect of harmonic forcing on the spectra of the pressure modes $m_l$ , $m_v$ , under synchronous forcing (a), (b) and asynchronous forcing (c), (d). . . . .	167

---

D.1	The response of the wake shown in figure 6.6 along with the linear fit used to estimate the time delay $\tau$ . . . . .	178
E.1	Unforced power spectral density for the parameter $y = a \sin(\psi)$ for varying noise intensity. . . . .	182
E.2	Unforced power spectral density for the parameter $y = a \sin(\psi)$ for varying ratios $\alpha_i/\alpha_r$ . . . . .	182

# Chapter 1

## Introduction and literature review

Fluid flows over bluff bodies are ubiquitous throughout areas of engineering interest, a key example being the flow over automotive vehicles such as cars and lorries. These flows are highly turbulent and three-dimensional, consisting of flow features over a range of length and time-scales, yet the efficient drag reduction of such bluff body flows has significant environmental and economic incentives. While the aerodynamic drag may be reduced significantly by adjusting the shape of road vehicles, practical and aesthetic constraints make this undesirable. In this thesis we therefore investigate the application of active feedback control techniques, to achieve this drag reduction efficiently and with minimal geometric change.

The work in this thesis has formed part of a continued effort within the Flow Control Group to design efficient drag reduction strategies for three-dimensional bluff bodies. The work initially involved the use of zero-net-mass-flux (ZNMF) jets to increase the base pressure of an axisymmetric bluff body (Qubain, 2009; Oxlade, 2013; Oxlade *et al.*, 2015) and a rectilinear truck model (Cabitza, 2014). These drag reduction strategies were “open-loop” in nature, consisting of parametric studies aimed at determining the optimal forcing parameters for drag reduction. These studies found novel and effective forcing strategies for drag reduction but suffered from low efficiency. Further efforts have been concentrated on the modelling and physical characteristics of bluff body wakes (Rigas *et al.*, 2014; Rigas, 2014), with the aim of developing low order models that give physical understanding and would enable the development of feedback control. It is from here that the work in this thesis continues, with the aim of further developing low-order models and implementing efficient drag reduction strategies.

The key objective of this work is a practical one: to develop efficient drag reduction strategies for bluff bodies with three-dimensional turbulent wakes. While this objective does not directly entail specific research questions, there are also many key fundamental issues that are advantageous to address; related both to the nature of bluff body wakes and to the limitations of feedback control. These will be discussed alongside each issue of practical importance.

## 1.1 The aerodynamic drag of bluff body wakes

Before looking to control bluff body flows for drag reduction it is important to understand the nature of these flows and the underlying causes of drag. If the principle mechanisms behind the aerodynamic drag are understood then these mechanisms can be targeted by an active control system. We will therefore firstly give an overview of bluff body wakes in general before moving onto the specific geometries examined in this work.

Although bluff bodies can come in a range of different shapes, bluff body flows usually share a number of common features including a large region of separated flow, high pressure drag and significant wake unsteadiness (Roshko, 1993). Although these qualitative wake features are clear, quantifying how they relate to drag remains a challenge. One way to try and understand the cause of drag is to look at methods of calculating it. This is a problem that started with D'Alembert's paradox in 1752. The first attempt to resolve the issue was made by Kirchhoff (1869) who modelled an infinite separated wake at constant pressure, which, although providing a finite drag estimate, provides an underestimate. More recent models (Roshko, 1993; Balachandar *et al.*, 1997) have improved upon that of Kirchhoff and are based on a control volume analysis of the time-averaged separation bubble (see figure 1.1). The principle here is to balance the time-averaged forces over the mean separation bubble in order to calculate the mean pressure force over the base. If  $\bar{p}_b$  is the base pressure,  $T_{ij}$  the component of the stress tensor acting in the  $i$  direction on a surface with normal  $j$ , and  $\partial\Omega$  the boundary of the time averaged circulation bubble

$$\begin{aligned}
 \int \bar{p}_b \, dy &= \int_{\partial\Omega} \bar{T}_{11} \, dn_1 + \int_{\partial\Omega} \bar{T}_{12} \, dn_2 \\
 &= \int_{\partial\Omega} \left( -\bar{p} + 2\mu \frac{\partial \bar{u}_1}{\partial x_1} - \overline{\rho u'_1 u'_1} \right) \, dn_1 + \int_{\partial\Omega} \left( \mu \left( \frac{\partial \bar{u}_1}{\partial x_2} + \frac{\partial \bar{u}_2}{\partial x_1} \right) - \overline{\rho u'_1 u'_2} \right) \, dn_2 \\
 &\approx \int_{\partial\Omega} (-\bar{p} - \overline{\rho u'_1 u'_1}) \, dn_1 + \int_{\partial\Omega} (-\overline{\rho u'_1 u'_2}) \, dn_2.
 \end{aligned} \tag{1.1}$$

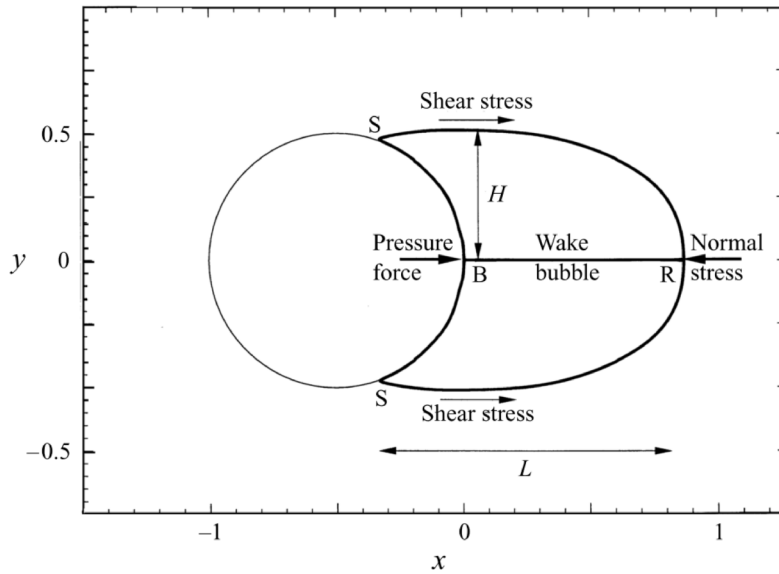


Figure 1.1: Schematic of the control volume used by Balachandar *et al.* (1997). The solid lines indicate the boundary of the body and the time averaged streamlines bounding the separation bubble. Image reproduced with permission of the rights holder, Cambridge University Press.

On average the pressure at the base is therefore balanced by the pressure, Reynolds normal and Reynolds shear stresses acting over the separating streamlines. For example Roshko (1993) considered the balance of pressure and Reynolds shear stresses acting over the surface of the separation bubble in order to estimate the base pressure behind a circular cylinder. A similar analysis was later followed by Balachandar *et al.* (1997) and applied to both experimental and numerical data behind cylinders and 2D flat plates. In this study an attempt was made to isolate the contribution of the vortex shedding to the terms in (1.1), although this proves increasingly difficult with increasing  $Re$ .

The value of these control volume analyses is in providing some insight into features of the wake responsible for the drag. For example if the Reynolds normal stresses could be controlled and reduced, the base pressure could be increased and the drag reduced. Under certain conditions<sup>1</sup>, an alternative way to look at the drag  $F_D$  is to equate the power required by a body moving at velocity  $U$  to the total resulting dissipation  $\epsilon$  within the fluid,

$$UF_D = \iiint_{\Omega} \epsilon \, d\Omega. \quad (1.2)$$

<sup>1</sup>Note that for e.g. a vehicle travelling under cross-wind conditions this does not hold, as some dissipation will occur regardless of the vehicle speed.

Although a very simple relation, this highlights the point that for a bluff body, the drag is inextricably linked to the dissipative phenomena occurring within the flow. Such dissipation may be related, for example, to the turbulent kinetic energy generated in the wake, or to the vorticity generated by the body. Such flow characteristics often have physical interpretation and are related to particular unsteady flow features or to the cross-stream forces.

A third related viewpoint that links the drag to the wake features, is that of entrainment and its underlying mechanisms. The control volume analysis detailed above clearly relates the pressure drag to the mean properties of the separation bubble. For example one implication is that if the separation bubble is very short, the drag will be high as the streamline curvature associated with the rapid closure implies very low pressure over the boundary of the bubble. The closure of the separation bubble is generally understood to be controlled by the entrainment of flow from the free-stream into the low-velocity wake region. For turbulent flows, entrainment is governed by the turbulent/non-turbulent interface (da Silva *et al.*, 2014), therefore mechanisms for the regulation of this interface have direct implications for the aerodynamic drag.

Both the control volume and dissipation based analyses ultimately yield a similar question: what are the contributions of particular coherent structures to the Reynolds stresses / dissipation / entrainment? This remains a matter of some debate, largely because it is very difficult to decouple the effects of any particular flow feature. Furthermore, all of the above analyses must remain consistent given any change to the wake. For example, if a hypothetical control device were used that gave drag reduction, most likely the wake would be less energetic, the entrainment would be lower and any control volume analysis would demonstrate that the balance of forces was consistent with an increase in base pressure. Nevertheless we may still draw some broad conclusions:

- Significant unsteadiness has an associated drag penalty. This may be inferred from the additional dissipation involved in the dampening out of fluctuations, the possible additional Reynolds stresses over the separation bubble or the increased entrainment. Attempts have been made to give this argument a firm theoretical basis (Dalla Longa *et al.*, 2017), although heuristic arguments may be sufficient.
- Cross-stream forces have an associated drag penalty. Reminiscent of the notion of induced drag in aeronautics, numerous studies have shown that there is a

strong relation between the cross-stream and drag forces on three-dimensional bluff bodies. Just as for the lift on a finite span wing, any cross-stream force leads to additional trailing vorticity in the wake. Since vorticity is diffused through viscous effects, there must be a drag penalty through the associated dissipation.

## 1.2 Key characteristics of three-dimensional bluff body wakes

As first proposed by Ruelle & Takens (1971), bluff bodies undergo the bifurcation route to turbulence such that the flow undergoes a number successive bifurcations that lead to particular features within the transitional flow. This is in contrast to e.g. a pipe flow for which the flow remains theoretically stable to infinitesimal disturbances up to infinite Reynolds number (Eckhardt *et al.*, 2007). For the two-dimensional cylinder wake the first bifurcation is of Hopf type (Jackson, 1987; Sreenivasan *et al.*, 1987), and leads to the oscillatory vortex shedding. For such wakes the vortex shedding remains in the flow as a coherent structure up to extremely large Reynolds numbers and is known to have a strong influence on the aerodynamic drag (Roshko, 1993). Similarly, three-dimensional bluff body wakes also undergo a sequence of bifurcations that ultimately affect the turbulent wake.

In this section we will provide a review of the wake features specific to three-dimensional wakes and the implications for efficient drag reduction. This will be with particular attention to the so-called Ahmed body used in this study. First used by Ahmed *et al.* (1984), this geometry provides a generic representation of a road vehicle, including the essential features of a real vehicle flow field such as three-dimensional separation and ground effect. While we will also include details of the axisymmetric body on which the experiments of chapters 3 and 4 are performed, the reader is also referred to the recent review in the thesis of Oxlade (2013) for a more detailed account.

### 1.2.1 Low Reynolds numbers and bifurcations

The low Reynolds number flows over axisymmetric bodies has been relatively extensively studied and is illustrative of a range of three-dimensional wake flows. With



increasing  $Re$  the flow can be seen to undergo essentially three persistent bifurcations whilst remaining laminar. These bifurcations are common to the sphere, disk and bullet shaped body reported by each of Tomboulides & Orszag (2000), Fabre *et al.* (2008) and Bohorquez *et al.* (2011); Bury & Jardin (2012) respectively.

1. Symmetry breaking (SB) steady bifurcation - After an initially axisymmetric flow at low Reynolds numbers the flow is seen to exchange axisymmetry for planar symmetry whilst remaining steady (see figure 1.2(a)). The azimuthal orientation of the symmetry plane is arbitrary and depends upon some small disturbance. This steady bifurcation is in contrast to 2D bodies that first undergo the unsteady bifurcation to vortex shedding.
2. Unsteady bifurcation - Beyond a second critical Reynolds number the flow becomes unsteady, shedding vortex loops with a specific frequency. The planar symmetry is maintained with the same orientation.
3. Laminar chaos - Beyond a third critical Reynolds number the azimuthal angle of the instantaneous symmetry plane begins to vary with time. This manifests as random reorientations that recover the axisymmetry of the flow in the long time average.

The flow behind the Ahmed body appears to undergo an analogous series of bifurcations. Initially at low Reynolds numbers of order 100, the flow behind the Ahmed body is steady and is characterised by reflectional symmetry with respect to the vertical symmetry plane of the body (Grandemange *et al.*, 2012a). Due to the presence of the ground, a top-bottom asymmetry exists with respect to the horizontal symmetry plane. Increasing the Reynolds number, the flow undergoes a steady supercritical bifurcation and the resulting steady flow loses the remaining spatial symmetry. The flow breaks the left-right reflectional symmetry and, depending on the initial conditions, relaxes in one of two possible stable asymmetric states, as shown in figure 1.2(b). For even higher Reynolds numbers, the flow becomes unsteady and periodic shedding starts to occur. These two regimes have been observed experimentally for  $Re > 340$  and  $Re > 410$ , respectively by Grandemange *et al.* (2012a) and numerically by Evstafyeva *et al.* (2017). For higher Reynolds number still, the sense of the initial asymmetry begins to switch randomly leading to a bistable behaviour that is the equivalent of the reorientations in axisymmetric wakes.

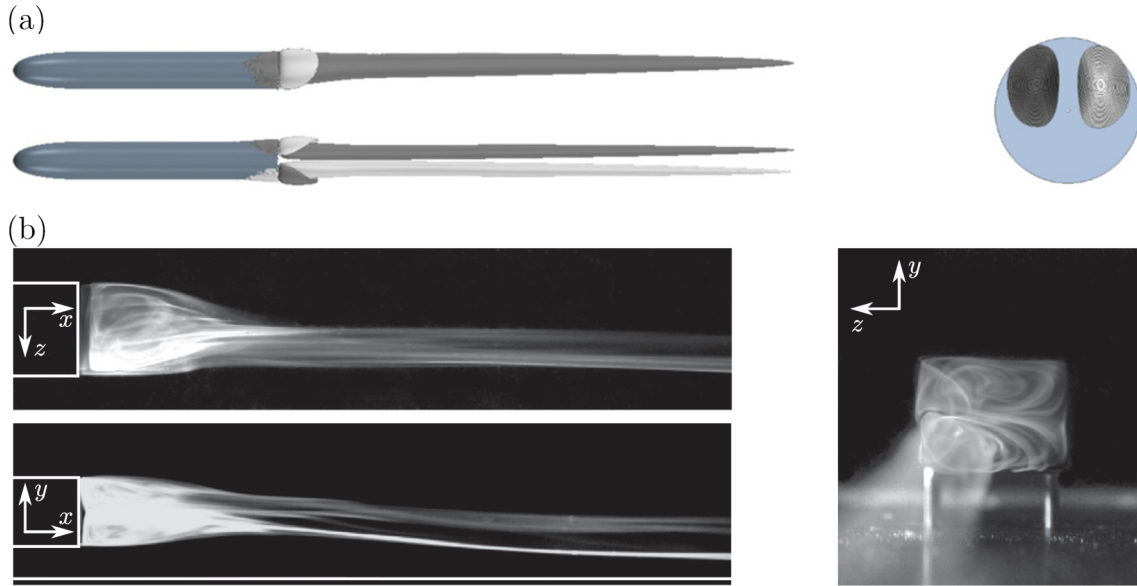


Figure 1.2: The low  $Re$  SB mode in three-dimensional wakes: (a) the axisymmetric bullet-shaped body from Bury & Jardin (2012) and (b) the rectilinear Ahmed body from Grandemange *et al.* (2012a). Images reproduced with permission of the rights holders, Elsevier (a) and the American Physical Society (b).

An important point here is that the flows over both axisymmetric bodies and the rectilinear Ahmed body undergo essentially the same sequence of bifurcations, suggesting that this is a general feature of three-dimensional bluff body wakes. In both cases the wake starts out steady and with symmetry imposed by the boundary conditions. There is then first a steady bifurcation breaking spatial symmetry, hereafter referred to as the SB mode of the flow, before a subsequent bifurcation leads to periodically unsteady behaviour superimposed on the asymmetric mean flow. With further increases in  $Re$  chaotic dynamics are observed and the flow explores the full range of possible asymmetric configurations. The order of these flow bifurcations is different to that for two-dimensional bluff bodies such as the cylinder, for which the first bifurcation leads to the unsteady shedding, and a subsequent bifurcation breaks spatial symmetry along the span of the cylinder (Williamson, 1996).

### 1.2.2 Multistability and the axisymmetric wake

In addition to the investigations into the low  $Re$  transitional behaviour of axisymmetric wakes, there have been many experimental investigations into the behaviour at high (turbulent) Reynolds numbers. For these studies the axisymmetry of the

flow permits decomposition into azimuthal modes, referred to by their wavenumber  $m$ . We will provide here a brief overview of the key features as they are relevant to the results of chapter 4.

1. Vortex shedding - Consistent between multiple studies is the existence of vortex shedding with a specific Strouhal number ( $St$ ). This is believed to be the saturated result of an absolute instability in the wake with azimuthal wavenumber  $m = \pm 1$  (Monkewitz, 1988), and can be linked back to the unsteady bifurcation of the laminar wake. This shedding was initially believed to have a helical structure by Monkewitz (1988) as well as by Berger *et al.* (1990), inspired by their observation of a helical mode under forced nutation of a disk<sup>2</sup>. However the following investigation of Lee & Bearman (1992) found through the use of conditional averaging in the wake of a disk that shedding instead had reflectional symmetry; the phase angle of velocity fluctuations changes rapidly through  $180^\circ$  for angular separations of  $90^\circ$ . This is largely supported by the observations of the sphere wake by Vilaplana *et al.* (2013) who found single sided vortex shedding rather than helical structures. These observations are consistent with the result of the second, unsteady bifurcation of the laminar wake that results in shedding with the preservation of a symmetry plane.
2. Bubble pumping - In addition to the  $m = \pm 1$  vortex shedding, a component of unsteadiness is also observed with azimuthal wavenumber  $m = 0$ , and at a lower frequency than the vortex shedding. Berger *et al.* (1990) observed this feature in the wake of a disk but found that unlike the  $m = \pm 1$  mode it was not possible to lock-in using motion of the disk. This suggests that it is not a global mode in the same sense: i.e. that it is not a self excited oscillation resulting from a global instability. This feature has also been observed for the bullet shaped body of this study by Oxlade (2013); Rigas *et al.* (2014) and has been suggested by Rigas (2014) to be caused by fluctuations in the magnitude of the large-scale asymmetric structure.
3. Asymmetry and reorientations - In many of the observations of vortex shedding it has been noted that shedding is one sided but that axisymmetry is recovered in the long time average. However the true nature of this asymmetry was probably first detailed by Grandemange *et al.* (2012b). They investigated the flow behind a bullet shaped body supported by two aerofoils imposing an  $m = 2$

---

<sup>2</sup>This involves inclining the axis of symmetry away from the free stream and rotating the direction of this inclination.

perturbation. They found that the wake always had instantaneously one of two asymmetric configurations and that switches between these two occurred randomly in time. While in this configuration ( $m = \pm 2$  rotational symmetry) the wake is seen to be bistable, the result is consistent with the observations of asymmetry and random reorientations observed in truly axisymmetric flows. For example Berger *et al.* (1990) observed their helical mode to be “an anti-symmetric structure, ... random in time”, and Vilaplana *et al.* (2013) observed the one sided shedding from a sphere to have a random orientation with time. Furthermore, consistent with the observation of Grandemange *et al.* (2012b) that disturbances to axisymmetry strongly bias the orientation of the asymmetry, Vilaplana *et al.* (2013) found that the  $m = 1$  disturbance of a small sphere in the wake could also force shedding to occur only on the opposite side, suggesting high sensitivity. This is also consistent with the recent observations of Mariotti & Buresti (2013) who investigated the bullet shaped body with a single support. They found a high degree of asymmetry in the flow, from either the support or misalignment, and noted that wake unsteadiness was also asymmetric in the same sense, thereby suggesting one sided vortex shedding. The same asymmetry and sensitivity to yaw angles has also been recently observed by Gentile *et al.* (2016, 2017). All these observations of asymmetry and reorientations are illustrative of the behaviour of the SB mode, and are consistent with the first and third bifurcations of the laminar wake.

### 1.2.3 Bistability and the Ahmed body wake

Although it has only more recently been properly understood, the large-scale asymmetry has been observed in axisymmetric wakes for some time. By contrast for rectilinear wakes such as that behind the Ahmed body, such behaviour has only fairly recently been noted. In turbulent rectilinear wakes the large-scale asymmetry results in bistability, consisting of an instantaneous asymmetry of the wake, even under nominally symmetric flow conditions, and a random switching between two such asymmetric states. This bistability was first recognised by Herry *et al.* (2011) who observed mean flow asymmetry and high sensitivity to side slip angle for the flow over a three-dimensional double backward facing step. Since then, a large number of recent studies have examined this same feature on the Ahmed body used in this study.

The first key publication detailing the bistable wake behaviour in the turbulent

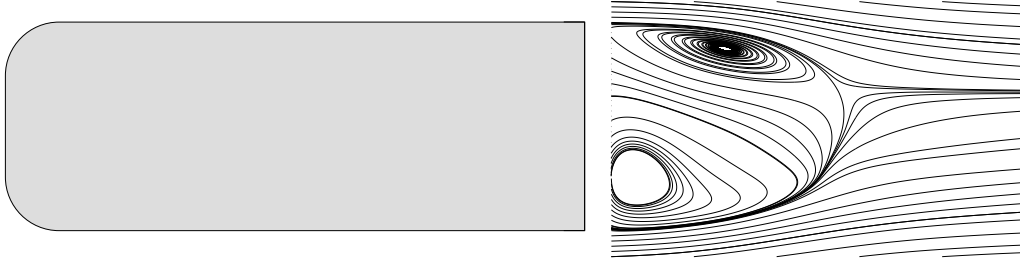


Figure 1.3: Plan view of the Ahmed body showing a conditional average of one of the symmetry breaking states of the wake, obtained from PIV. The streamlines demonstrate the asymmetry, showing the stationary vortex adjacent to the base.

regime were from Grandemange *et al.* (2013c). For a body aligned with the flow, the asymmetric structure is demonstrated to flip randomly between two asymmetric states, each the mirror image of the other. In the long time average this “flipping” leads to a statistically symmetric wake, while instantaneously the wake is typically asymmetric with an associated lateral force on the body. The structure of this asymmetric flow is displayed in figure 1.3, and consists of a static vortex adjacent to the base towards one side, leading to a low pressure region. The flipping process has two time scales associated with it, the flipping period ( $T$ ) defining the average time between flips, and the instability time scale ( $\delta$ ) defining the duration of a flipping event. The former is generally many orders of magnitude greater than the latter. Grandemange *et al.* (2013c) demonstrated that the time between flipping events was exponentially distributed, indicating that the events themselves are independent in time. Further to this it was found that the mean flipping rate scales approximately linearly with flow speed, such that in a dimensionless sense the rate is likely to be constant.

Just as for the axisymmetric wake (Gentile *et al.*, 2017), the bistability is known to be highly sensitive to yaw angle. For example Volpe *et al.* (2015) demonstrated that for yaw angles  $\beta \gtrsim 1^\circ$ , one of the two bistable states is permanently selected. The same behaviour was confirmed by Cadot *et al.* (2015) and Grandemange *et al.* (2015) who found a tighter bound of  $\beta \gtrsim 0.5^\circ$ .

While the extreme sensitivity to yaw angle may be seen to suggest that the bistable behaviour is only applicable under very precise conditions, other work has indicated that the feature remains fairly general. For example Meile *et al.* (2016) examined the flow behind an Ahmed body with a slanted rear at large yaw angles  $10^\circ < \beta < 15^\circ$ , finding the lift and pitching moments to exhibit bistable behaviour. In addition to the yaw angle, the feature is also known to be sensitive to the body geometry and the ground clearance. In a systematic study Grandemange *et al.* (2013b) examined

the influence of these two factors together, finding that the bistability could exist in either a top/down or lateral sense. This generality of the feature has recently been extended by the results of Bonnavion *et al.* (2017) who find a much richer set of asymmetric configurations in the wakes of real car geometries. Other studies have also confirmed that the feature is present up to industrial scale Reynolds numbers (Grandemange *et al.*, 2015).

While there have been a number of studies in which the bistable behaviour has been observed, fewer studies have sought to model it. Some work has gone in this direction, for example Cadot *et al.* (2015) found that the bistability resulted from an (imperfect) supercritical pitchfork bifurcation, finding the ground clearance to act as a bifurcation parameter. This was further supported by the work of Evrard *et al.* (2015) who discussed the bistability in terms of bifurcation theory and considered its modelling by a Langevin equation, similar to the work of Rigas *et al.* (2015). Similarly, the recent work of Varon *et al.* (2017) demonstrated that the dynamics of the large-scale asymmetry exhibited chaotic behaviour. While interesting, such work gives limited physical insight, and a thorough understanding of the underlying instability mechanism is still lacking.

One way in which to further investigate the instability mechanisms is to examine methods for control. A number of studies have looked at passive methods to control the SB mode. For example Grandemange *et al.* (2014a); Cadot *et al.* (2015) both applied a vertical control cylinder in the wake of the Ahmed body, finding that if correctly located, the bistable behaviour could be suppressed achieving a small concomitant drag decrease. More recently, Evrard *et al.* (2015) found that a base cavity was also able to achieve bistability suppression with even larger drag reductions. Active feedback control methods have also recently been employed by Li *et al.* (2016) and Evstafyeva *et al.* (2017), although in the latter of these studies the SB mode was not the target of control. While these varying control methods have proven effective, the requirements for suppression of the SB mode remain unclear. Moreover, it remains to be seen whether the mode can be suppressed without significant geometric modification or large energy input. This motivates the use of other active feedback control techniques.

## A note on similar flows

It is worth noting at this point that the static instability observed in three-dimensional wakes is not unique or entirely unusual, in fact similar static symmetry breaking in-

stabilities are observed in many other fluid flows. This ranges from the flow of a shear-thinning fluid through a circular pipe (Wen *et al.*, 2017), to the von Kármán “washing machine” flow (Ravelet *et al.*, 2004), to turbulent convection within a closed container (Sreenivasan *et al.*, 2002). The latter two of these examples may be particularly pertinent, as they both consist of internal recirculating flows. The recirculation within the separation bubble of a bluff body wake certainly has some qualitative similarity in this sense, so it may be that some insight into the instability mechanism of three-dimensional wakes may be obtained from these other flows.

### 1.2.4 Implications for drag reduction

For three-dimensional wakes the literature highlights two key features: the static SB mode and the unsteady vortex shedding. It is important for our purposes to understand the influence of these features on the aerodynamic drag. Heuristically, and based on the discussion above in § 1.1 we may expect that the SB mode would increase the drag due to the associated cross-stream force, while the vortex shedding would increase the drag due to the increased unsteadiness and dissipation.

A first direct comparison of the effect of particular bifurcations may be made by examining the variation of drag over a range of low  $Re$ , compared with a case in which the bifurcation is suppressed. Data from two previous studies are displayed in figure 1.4. Figure 1.4(a) displays results from the sphere from Pier (2008), demonstrating that both the steady and unsteady bifurcation increase the drag relative to a case in which a steady axisymmetric flow is imposed. Figure 1.4(b) displays a similar result for the two-dimensional cylinder wake from Roshko (1993). In this case the unsteady bifurcation again increases the drag relative to the steady case, although the difference is much more marked. The implication of these results is that suppression of either the symmetry breaking or vortex shedding may be expected to reduce the drag in three-dimensional wakes, although the effect may not be so pronounced as for the suppression of vortex shedding in two-dimensional cases.

In addition to the data over low Reynolds numbers some work has sought to understand the influence of these features in the turbulent regime. One way in which the link between particular features and the drag may be established is through the use of passive control devices. For example García de la Cruz *et al.* (2014) applied splitter plates to a bullet shaped body, finding drag reductions of up to 30% once suppression of both the SB mode and shedding was achieved. Grandemange *et al.* (2014a) looked to establish the influence of the SB mode alone, estimating a



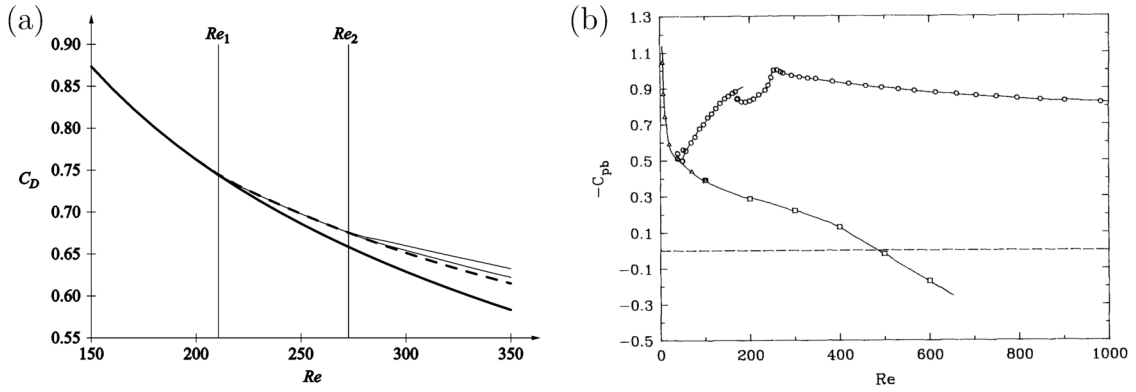


Figure 1.4: Variation of drag over a range of low Reynolds numbers: (a) data for the sphere from Pier (2008), for which the static mode bifurcation occurs at  $Re_1$ , followed by the vortex shedding at  $Re_2$ ; (b) base suction data for circular cylinders from Roshko (1993). Images reproduced with permission of the rights holders, Cambridge University Press (a) and Elsevier (b).

drag contribution of between 4% and 9%. The contribution of the unsteady vortex shedding is often speculated to be less in three-dimensional wakes, but remains undetermined.

### 1.3 Feedback control of fluid flows

The field of flow control is often split into passive and active, the latter being either closed- or open-loop (Choi *et al.*, 2008). While some passive and active open-loop methods show promise in terms of drag reduction, closed loop methods would be expected to offer many advantages. As for any closed loop control system these include robustness to uncertainty, adaptation to disturbances and changing conditions as well as the adjustment of system properties with the potential for optimisation. However, closed-loop control of fluid flows has historically proven to be challenging because of infinite degrees of freedom of the fluid continuum and strongly nonlinear dynamics. Numerous approaches have been used to address this challenge in the past, we will give here an overview of some methods and considerations relevant to the control of bluff body wakes.

The control strategies we apply in this work must necessarily be practically implementable based only on surface pressure measurements and body mounted actuators. We firstly apply a model-free extremum seeking control approach in chapter 3, and therefore give details of this class of methods in § 1.3.1 below. The second set of



strategies we apply are based on reduced-order models of the flow that focus only on some of the particular coherent structures discussed above in § 1.2. We therefore provide a review of suitable modelling strategies in § 1.3.2, followed by a review of methods to observe the flow based upon surface pressure measurements in § 1.3.3.

### 1.3.1 Extremum seeking control

Many feedback control methods aim to force a system to track a reference trajectory or to maintain a demanded input in the presence of disturbances. Further to this, many such methods are based on a linear systems approach. However in the context of fluid flows not only are the underlying dynamics nonlinear, but often the desired reference is not known *a priori*. Furthermore both the model and “best” reference may change with time due to changing conditions. In such situations it is often desirable to simply seek to maximise or minimise some parameter such as drag, mixing or heat transfer, adapting to a new optimum as conditions change. In such cases an extremum or slope seeking controller may be appropriate.

ES control is a form of adaptive closed-loop control that acts as a real-time optimisation method. This is appropriate for systems with a nonlinear equilibrium map, valid in a time-averaged sense, on which an unknown target location may be identified by its gradient. In this case no model is required for the flow, only the assumption of a peak or location of known gradient in the equilibrium mapping between a reference parameter and the output. For example such a mapping could be that between the angle of attack and the lift of an aerofoil, which exhibits a peak at a certain attack angle. ES control was first suggested in 1922 (see Tan *et al.*, 2010, for a review), but has in the last decade or so seen a resurgence of interest following proofs of stability by Krstić & Wang (2000); Krstić (2000). Included in this recent interest has been the application to a number of fluid flow systems. For example ES control has been used to directly control the parameters involved in open-loop control systems: Becker *et al.* (2007) and Pastoor *et al.* (2008) controlled the amplitude of pulsed jets used on an aerofoil and bluff body respectively. Alternatively ES control can be used to adapt some parameter within a closed-loop system. For example Kim *et al.* (2009) used an ES controller to adapt the phase shift of the feedback gain used in the control of a cavity flow.

While a standard algorithm exists for ES, many previous authors have suggested modifications, including in the context of flow control. For example Beaudoin *et al.* (2006) used a variant on the traditional gradient estimation, computing a real-time

fast Fourier transform as an alternative to the often used demodulation (see § 3.1.1). Alternative gradient estimation methods have also been suggested by Henning *et al.* (2008) who used an extended Kalman filter, finding it to be much faster than the estimation of the standard algorithm. This algorithm was also tested by Wu *et al.* (2015) who confirmed this result. Authors have alternatively looked at methods to adapt the control gains. For example Chabert *et al.* (2014, 2016) used a fuzzy-logic method to adapt the gains according to the current conditions. In general, many different modifications may be advantageous, however their suitability depends upon the particular system to be controlled.

While the application of ES to fluid flows has been demonstrated to be effective, there are considerations pertinent to flow control which have not previously been addressed. Principle among these is the challenge involved in optimising the frequency of a harmonic signal. In open-loop flow control this is a particularly common scenario. For example in the use of synthetic jets (Kotapati *et al.*, 2010; Kourta & Leclerc, 2013), pulsed blowing (Seifert *et al.*, 2008; Chabert *et al.*, 2016), oscillating tabs (Bigger *et al.*, 2009) or in a number of other situations (Greenblatt & Wygnanski, 2000), the control consists of a periodic forcing. In many such cases, performance of the open-loop system is dependent on the frequency of the periodic signal, the optimal frequency depending upon the particular control mechanism and the particular operating conditions. There are therefore advantages to be gained through the application of ES controllers, both to find an optimal frequency and to adapt as conditions change. We will show that frequency optimisation of a harmonic signal cannot be done with a standard algorithm and propose a modified algorithm suitable for this purpose.

### 1.3.2 Low-dimensional modelling for feedback control

While some flow control methods such as extremum seeking and machine learning control (Gautier *et al.*, 2015) are model free, many more rely on having a mathematical model of the fluid system. As summarised in the review of Brunton & Noack (2015), modelling approaches for flow control may be categorised as either black-box, gray-box or white-box, depending upon the level of physical detail that is captured. If the end goal is feedback control of a particular flow feature, the purpose of a model is to facilitate the control design process, or to give sufficient insight into the type of control to be implemented. Within this context, the required properties of a model may therefore be quite different to those that would be required for an

accurate open-loop simulation (Jones *et al.*, 2015).

A first set of models are those based on high-dimensional discretisations and/or linearisations of the underlying Navier-Stokes equations (Kim & Bewley, 2007). Such methods generally require knowledge of the full flow-field which consists of a very high-dimensional system. Various approaches may then be applied to reduce the dimension of this system, including Galerkin projection onto global modes (Barbagallo *et al.*, 2009) or POD modes (Tadmor *et al.*, 2011; Barbagallo *et al.*, 2012). Following such projections standard linear control methods may be applied, although accurate nonlinear Galerkin models such as that of Noack *et al.* (2003) may also allow the use of effective nonlinear control algorithms to be designed (Aleksić-Roeßner *et al.*, 2014). However, many of these methods would be completely impractical to implement experimentally, given that full knowledge of the flow-field can never be obtained.

An alternative to approaches based directly on the governing equations is system identification, which may again be performed using knowledge of the full flow-field, or based purely on input-output measures. A good example of the latter of these approaches is the ERA of Juang & Pappa (1985), described in a fluids context by Ma *et al.* (2010), and applied by numerous authors including e.g. Illingworth (2016); Flinois & Morgans (2016). The ERA forms a linear state-space model of the flow, based upon discrete-time snapshots of the impulse response. This is in principle applicable experimentally, but effectively generating impulse response data may prove challenging. Other forcing strategies for system identification may consist of a set of pure frequencies, from which a frequency response transfer function may be obtained. This has been successfully applied to the backward-facing step by Dahan *et al.* (2012) as well as to two- and three-dimensional wake flows by Dalla Longa *et al.* (2017); Evstafyeva *et al.* (2017). Another approach applied to the convectively unstable backward-facing step is the ARMAX algorithm (Hervé *et al.*, 2012; Gautier & Aider, 2014). This provides a statistical mapping between upstream inputs and disturbances and the downstream output and is particularly suitable for so-called “noise amplifier” flows (Schmid & Sipp, 2016), in which convective instabilities dominate the measured response. For the flow features considered in this work such an approach would be unlikely to work as the flow is dominated by global instabilities. In these cases it is instead useful to have a good model for these “intrinsic” dynamics.

While many of the modelling approaches discussed above seek to model the complete flow or input-output behaviour, in this work we will target specific flow features that

we believe to be of importance with respect to the aerodynamic drag. We therefore may be able to look for models that principally describe the dynamics of these features alone. For the vortex shedding behind two-dimensional bluff bodies there have been considerable efforts towards developing low-dimensional models, some of which have been used for feedback control. A first “toy” model that describes qualitatively the oscillatory nature and underlying mechanisms of the vortex shedding is the Ginzburg-Landau equation (Roussopoulos & Monkewitz, 1996; Lauga & Bewley, 2003, 2004; Chen & Rowley, 2011). The model consists of partial differential equations defined over space and time, the purpose being to give insight into the challenges and considerations required for successful feedback-control design. While the Ginzburg-Landau model consists of PDEs, an alternative (arguably simpler) model for the vortex shedding may consist of (nonlinear) ODEs, a particular example being the Stuart-Landau equation. This has been applied by Monkewitz (1996) although others have found such a model to compare poorly with experimental data (Le Gal *et al.*, 2001). Alternatively, others have applied purely phenomenological models such as the van der Pol oscillator (Facchinetti *et al.*, 2004), since this describes a system exhibiting saturated self-excited oscillations.

It is finally worth noting that for most feedback control strategies, the model is simply a means to an end. With the exception of some specific methods such as nonlinear model predictive control, once the controller is designed the model of the flow no longer features in the implementation; therefore in principle the controller could simply be chosen through intuition and good luck. There are in fact several examples of flow control for e.g. a cylinder flow (Ffowcs Williams & Zhao, 1989; Son *et al.*, 2011), combustion instabilities (Morgans & Dowling, 2007), or cavity oscillations (Illingworth *et al.*, 2012), in which successful control laws may be chosen by inspection or trial and error. Nevertheless, for high Reynolds number flows such as those investigated in this study this would likely prove very challenging. In general we would expect to provide better control through the use of models that capture the key flow physics than we would through the use of generic or *ad hoc* methods (Ho & Pepyne, 2002).

### 1.3.3 Flow measurement

One of the particular challenges associated with practical flow control implementation is the accurate measurement of the flow from surface mounted sensors alone. In the context of feedback control this may be considered as an observability problem,

as will be discussed further in chapter 4. Here we will give an overview of some of the available methods used by other authors to make suitable flow measurements.

The simplest approach to deducing velocities from pressure involves finding a static mapping between measurements, and may be based on linear stochastic estimation (LSE) (Adrian, 1994). LSE is widely used in turbulence to find conditional coherent structures by looking at the two-point correlations between velocity measurements in different parts of the flow-field, although it may equally be used to investigate the relationship between pressure and velocity measurements. LSE may either be used to link measurements directly, or may be used to deduce the coefficient of POD modes, in which case it is generally referred to as modified LSE (mLSE) (Taylor & Glauser, 2004). This is closely related to the extended POD of Borée (2003). mLSE has been applied to flows such as the backward facing step (Hudy *et al.*, 2007; Ukeiley *et al.*, 2008) and the D-shaped bluff body (Durgesh & Naughton, 2010). LSE is also commonly used with, possibly multiple, time delays in order to take delayed relationships into account, such an approach has been performed for the flow over a cavity (Lasagna *et al.*, 2013), and wall-mounted pyramid (Hosseini *et al.*, 2015). These approaches often prove effective provided sufficient training data is available, consisting of simultaneous and often time-resolved measurements.

One of the arguments for including time delays in LSE is that it allows some degree of dynamics to be taken into account. This process can be taken further by using fully dynamic estimation. For example Pearson (2012) looked at the estimation of the flow over a forward-facing step. From PIV data and the application of the OMD algorithm of Wynn *et al.* (2013), he developed a linear state space model for the flow then applied a Kalman filter to estimate the velocity field from pressure measurements. A combined static and dynamic approach was also employed by Tu *et al.* (2013) who used LSE and an oscillatory model together in a Kalman filter to estimate the POD modes in a bluff body wake based upon a single velocity sensor.

The majority of the previous examples have either looked at convectively unstable flows such as the backward-facing step or largely two-dimensional flows exhibiting an absolute instability that dominates the flow. The challenge for three-dimensional wakes such as those in this work, is that instabilities such as the vortex shedding are much less coherent and of a different spatial structure. The real-time observation of vortex shedding for the purposes of control is therefore something that requires further investigation. As with the previous works outlined above, this will require simultaneous measurements of the surface pressure and velocity field.

## 1.4 Conclusions and thesis plan

In this project we wish to experimentally implement closed-loop flow control strategies that will efficiently reduce the drag. In order to do this we have the following requirements:

1. Physically motivated features that we wish to target. The choice of these features may need to rely on assumed relationships with the mean drag. Given the consensus of the literature, two such suitable features may be the static asymmetry (SB mode) and unsteady vortex shedding observed in three-dimensional wakes.
2. Methods of observing these features in real time, using only surface mounted measurements. In order to assess suitable methods for achieving this we will require simultaneous measurements of the velocity field and base pressure of a bluff body.
3. Method of controlling these wake features using dynamic actuators. We will require body-mounted actuators capable of efficiently regulating the flow features that we choose to control.
4. Reduced order models of the wake features that facilitate control design. Such models will be required to provide sufficient insight to inform the type of controller as well as the details of its implementation.

In chapter 3, we shall discuss the implementation of a model-free extremum seeking controller, applied to the open-loop control system of Oxlade (2013). This work having been previously published in Brackston *et al.* (2016b). Following on from this we shall explore the implementation of model-based controllers. Firstly exploring the observability problem in chapter 4, followed by an investigation into open-loop forcing with dynamic flaps in chapter 5. Based on some of this understanding we will then develop stochastic models in chapter 6 followed finally by the implementation of closed-loop controllers in chapter 7, elements of this work having been previously published in Brackston *et al.* (2016a).

## Chapter 2

# Experimental and analytical methods

For the work in this thesis, experiments were performed on two different bluff bodies: firstly the axisymmetric bluff body previously used by Oxlade (2013) and Rigas (2014) and secondly the commonly used Ahmed body of Ahmed *et al.* (1984), newly built during this work. The axisymmetric body was used for the ES control work described in chapter 3 and the observability work of chapter 4, while the Ahmed body was used for the remainder of the work.

Both experiments were performed in the closed-circuit Donald Campbell wind tunnel, the test section of which measures  $1.37 \text{ m} \times 1.22 \text{ m} \times 3.00 \text{ m}$ . The turbulence intensity of this tunnel is generally found to be less than 0.1%, while the free-stream velocity is measured via a Pitot-static tube and PID controlled to an accuracy of 0.25%. The specific experimental procedures and analytical methods relating to each of the bluff bodies are detailed below.

### 2.1 The axisymmetric bluff body

The principal features of the axisymmetric body experiments are the same as those described in Oxlade (2013); Oxlade *et al.* (2015), consisting of an axisymmetric, bullet shaped bluff body fitted with a pulsed jet actuator. A schematic of the experiment is shown in figure 2.1. The model is instrumented with 8 Endevco 8501C-1 pressure transducers, and 64 static taps, distributed on a polar grid. The pulsed jet actuation is applied by means of a speaker located within a cavity inside



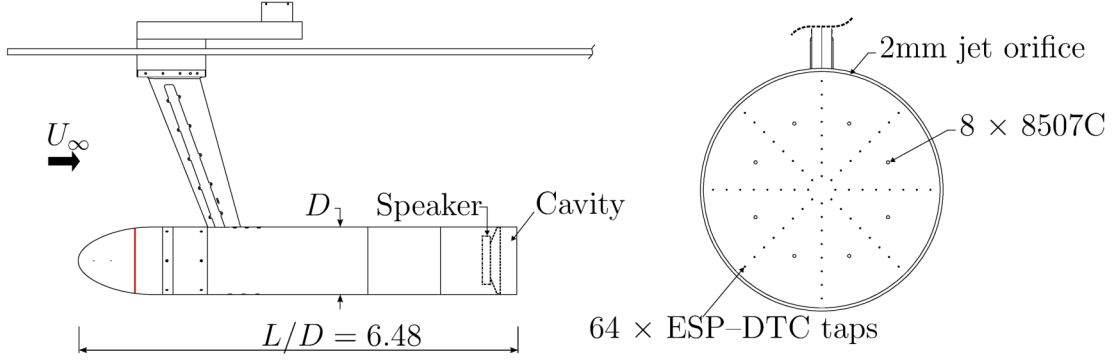


Figure 2.1: Experimental setup: side view of the model (left) and detailed view of the base including instrumentation (right). The body diameter is  $D = 0.1965$  m.

the rear of the model. Oscillation of the speaker diaphragm forces air through an annular slit on the back face of the body, the resulting zero-net-mass-flux (ZNMF) jet emanating in a stream-wise direction. The model was tested at a free-stream velocity of  $15 \text{ ms}^{-1}$ , giving a Reynolds number based on body diameter of  $Re_D = 1.88 \times 10^5$ , and a fully turbulent wake.

### 2.1.1 Extremum-seeking control experiments

As will be detailed in chapter 3, the ES control experiments involved implementation of an algorithm to modify the frequency and amplitude of the ZNMF jet in real-time. Data acquisition and implementation of the controller were both performed on a National Instruments PXIe-1078 chassis with a PXIe-6358 data acquisition card, and running the real-time operating system. The control loop and data acquisition were performed at 2 kHz, and the output to the speaker was sent to the digital to analogue converter of the acquisition card at 90 kHz. While the frequency of the jet forcing could be controlled directly from the actuation signal, forcing amplitude was quantified in terms of the root mean square (rms) pressure ( $\sqrt{p_c^2}$ ) within the cavity, measured via an additional pressure transducer ( $p_c$ ). We use the rms cavity pressure as this scales with the peak jet velocity (Oxlade, 2013) and provides the most practical measurement for use in real-time applications. A calibration between  $\sqrt{p_c^2}$  and the jet velocity was not performed here as this is specific to the free-stream velocity and, moreover, is not required for the control algorithm. Control of the rms pressure was implemented via a PID loop in order to cater for the frequency response of the pulsed-jet system and for any changes in operating conditions.



PIV sampling frequency	720 Hz
PIV sampling duration	3.79 s
Vector field resolution	1.84 mm
Time between laser pulses	140 $\mu$ s
Combined field of view	338 $\times$ 294 mm
Camera lens focal length	50 mm
Camera lens aperture	f/1.4
Mean pixel displacement	10 px

Table 2.1: Parameters for the PIV experiments.

### 2.1.2 Synchronised PIV experiments

Synchronised PIV and pressure measurements for the axisymmetric body form the basis of chapter 4. In these experiments the ZNMF actuator is not used and data is simply recorded for the unforced flow using the same acquisition set-up detailed above. Synchronisation is achieved by recording the trigger signal sent to the PIV camera along with the remainder of the measurements. Time series from the PIV and pressure measurements could therefore be aligned in post-processing.

PIV experiments were performed using a time-resolved LaVision FlowMaster PIV system composed of a Litron LDY300 laser and two 4 Mpx Phantom v641 cameras. The two cameras captured adjacent and overlapping fields of view within the flow in order to achieve a finer spatial resolution. Post-processing was performed using LaVision's DaVis software with which vector fields were first evaluated for each field of view separately, before being stitched together. Further parameters detailing the PIV acquisition are given in table 2.1.

The experimental procedure for the PIV experiment was as follows:

1. Set the tunnel to a low speed ( $U_\infty \approx 2 \text{ ms}^{-1}$ ), turn on the seeding generator. Periodically check the seeding density through the quality of a sample PIV acquisition.
2. Once seeding density is adequate, set the tunnel to full speed ( $U_\infty = 15 \text{ ms}^{-1}$ ).
3. Start acquisition of the pressure measurements and PIV trigger signal, then initiate acquisition of a PIV buffer.
4. Stop the pressure acquisition and check the alignment of the SB mode over the duration of the PIV acquisition. If there was excessive rotation during the PIV acquisition, return to step 3.

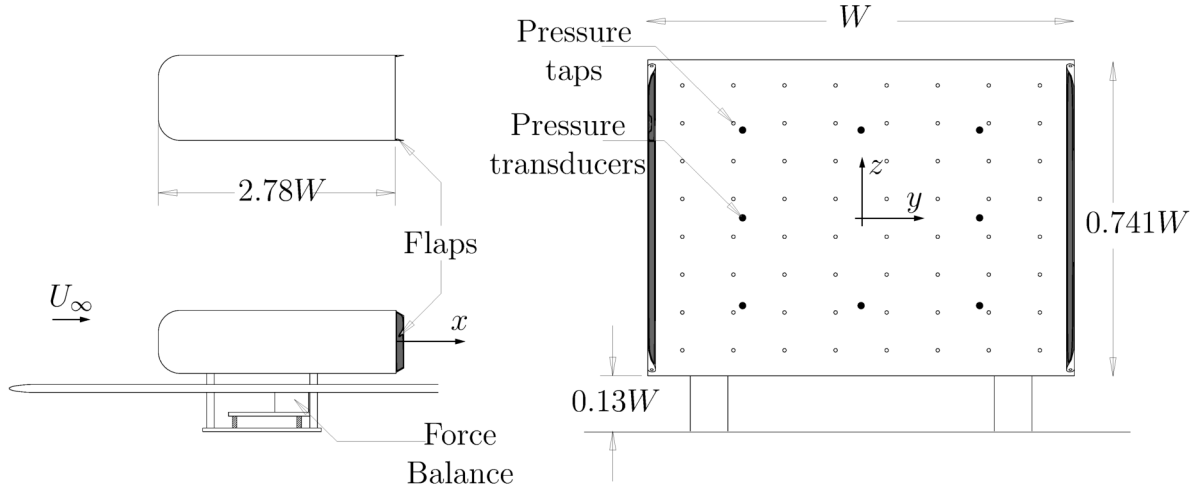


Figure 2.2: View of the Ahmed body showing the overall assembly (left) and detailed view of the base (right). The model is here shown fitted with lateral flaps and has a width  $W$  of 0.216 m.

5. Stop the tunnel, turn off the seeding generator and download the images from the PIV cameras.

## 2.2 The Ahmed body

The experimental setup for the Ahmed body is shown in figure 2.2. The model consists of a scaled down, flat-back Ahmed body of the proportions specified by Ahmed *et al.* (1984). The base of the model measures  $0.216 \text{ m} \times 0.160 \text{ m}$  giving  $Re$  of  $\mathcal{O}(10^5)$ . The model sits  $0.028 \text{ m}$  above a raised floor, ensuring minimal boundary layer thickness over the tunnel floor while maintaining the correct ground effect. A force balance, situated out of the air flow, provides the connection between the model and tunnel, enabling accurate measurement of the total force and moment acting on the body.

In addition to the force balance, the model is instrumented with 8 Endevco 8507C pressure transducers for fluctuating pressure measurements, and an ESP-DTC pressure scanner supplying 64 static pressure measurements distributed over the model base. The static pressure measurements are used to calculate the time-averaged statistics, while the pressure transducers are used for time-resolved pressure measurements and feedback control.

Forcing of the wake is achieved using two flaps located at the trailing edges of

the body, each 0.019 m in stream-wise length and running the length of the edge on which they are mounted. These edges may either be on the left/right or the top/bottom depending on the experiment, the two configurations referred to as lateral or vertical respectively. The flaps are mounted on hinges driven by internal motors powered through an amplifier. The flaps are given a natural equilibrium and oscillatory dynamics through the action of internal springs. The angle of each flap is measured using a 12-bit magnetic encoder, while the power supplied to the flaps is monitored through measurement of the supply voltage and current. The instantaneous electrical power supplied to each flap is simply the product of the voltage and current, which may be integrated over time to find an average. Further details regarding the flaps are given in § 2.2.1 below.

All channels are sampled simultaneously at 25 kHz with the exception of the pressure scanners that are sampled at 250 Hz, and synchronised with every hundredth analogue sample. For open-loop forcing of the wake, the mean angles, fluctuation amplitudes and phases of the flaps are PID controlled to ensure uniform forcing at all frequencies. Feedback control was achieved using a National Instruments Real-Time PXI running a discrete time controller at 5 kHz. The controller obtains pressure measurements from 6 of the Endevco transducers and outputs 2 voltages that are sent to the motors.

### 2.2.1 Actuator characteristics

An important and novel feature of the Ahmed body used in this project is the forcing flaps located at the rear of the model. These were chosen as an alternative to the ZNMF and pulsed jets used in other studies (e.g. Pastoor *et al.*, 2008; Oxlade *et al.*, 2015; Barros *et al.*, 2016b), a key motivation for this choice being the relatively low energy efficiency of jet-type actuators. For the control of large-scale wake features, it is necessary to provide some cross-stream momentum flux to act as a strong forcing. A jet actuator generates this momentum flux directly, by blowing in the cross-stream direction. In contrast a flap may generate this momentum flux through flow deflection, thereby lowering the associated energy cost. An additional benefit of forcing with flaps is that we may expect the forcing to be effective over a wide frequency range, including at DC (zero-frequency). This is important if we wish to cater for static asymmetries, e.g. due to cross-wind. While ZNMF jets may also achieve a quasi-DC forcing through a nonlinear interaction, such jets have a relatively high energy cost, compared with a statically deflected flap which may

consume no power.

In order to achieve efficient forcing in both a static and oscillatory sense, two different motors are required. For static forcing we need a system that can slowly move the flap to a desired angle but consume no power when not in use, irrespective of the position. This can be achieved through the use of a stepper motor, since these motors typically require no power to hold a static position, even under load. For the oscillatory forcing the power consumption will always be non-zero, therefore the efficiency of the motor itself is important. A suitable motor should ideally be both brush-less and gear-less to minimise frictional losses, but need not necessarily be capable of a large range of angles. We therefore chose to use the motor that drives the scanning head of a standard computer hard-disk drive. These motors are capable of generating a fairly high torque that scales approximately linearly with the supply current, and furthermore are both efficient and reliable. Through the use of a suitable power amplifier, the generated torque is proportional to the input voltage, making for straightforward use in feedback-control.

A detailed view of the actuators is given in figure 2.3. As displayed, the dynamic motor drives a linkage rod that moves the flap, the geometry of the mechanism being such that the angular displacement of the flap is equal to that of the motor. The angle of the flap may therefore be obtained by direct measurement of the motor angle using the magnetic angular encoder. The mechanism is given an equilibrium position and oscillatory dynamics through the action of two springs, shown by the dashed red lines. The end location of one of these springs may be adjusted by operating the static motor, and in turn determines the equilibrium angle of the flap.

An important characteristic for a dynamic actuator is the frequency response, as this determines the bandwidth available for control purposes and gives the variation of the forcing with frequency under open-loop conditions. This frequency response is displayed in figure 2.4. The system can be seen to behave like a second-order linear oscillator, the characteristics of which could be tuned by choice of the springs and the addition of masses. The particular characteristics of the response also vary slightly between the lateral and vertical flaps but in each case may be taken into account in the control design by appropriate choice of parameters in the linear transfer function  $A$ . This will be discussed further in chapter 7.

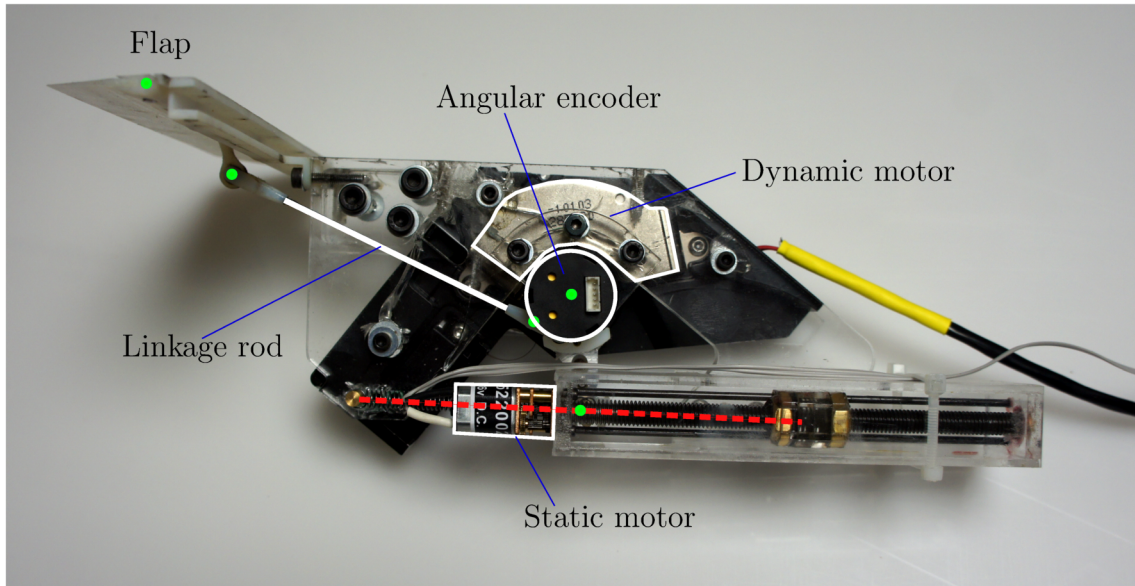


Figure 2.3: Detailed view of the flap actuators including the static and dynamic motors. Pivot locations are shown by the green dots, while the springs (obscured from view) are shown by the dashed red lines.

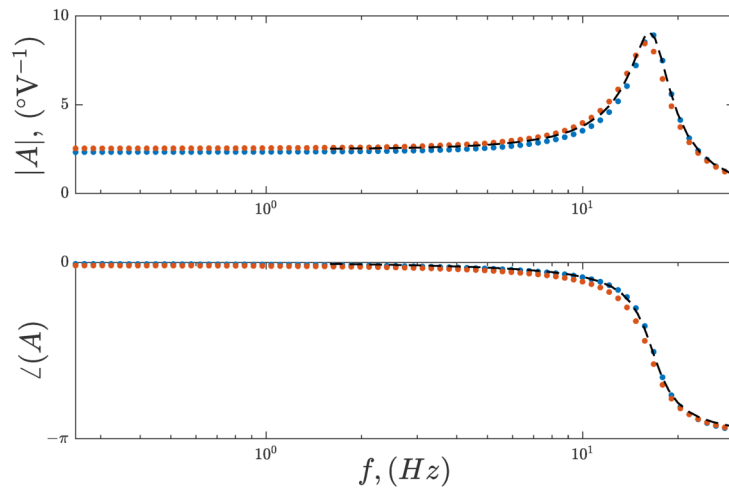


Figure 2.4: Typical frequency response of the actuator between voltage input  $v$  and angle output  $\theta$ . The blue/red dots are for flaps mounted on each of the left/right sides respectively. Also shown by the black dashed line is a linear 2nd-order fit.

## 2.2.2 Base pressure metrics

Given the distribution of pressure measurements displayed in figure 2.2, we may define a number of different pressure metrics. These metrics draw more pertinent information from the 64 base pressure tappings and 8 transducers.

### Centre of pressure

The centre of pressure gives the position at which the pressure force on the base can be considered to act and is evaluated via the first moment of the spatial pressure distribution. For measurements  $p(y, z, t)$  at locations  $\mathbf{X}' = (y, z)$ , the CoP coordinate vector  $\mathbf{X}$  may be evaluated as

$$\mathbf{X}(t) = \frac{1}{\iint_A p(y, z, t) dA} \iint_A p(y, z, t) \mathbf{X}' dA. \quad (2.1)$$

### Normalised pressure modes

While the CoP can be straightforwardly approximated using the 64 base pressure tappings, it is challenging to define an analogous measurement using only the 8 pressure transducers. Furthermore because the CoP involves calculation of the mean pressure, it is influenced by both symmetric and asymmetric perturbations. An alternative approach is to use normalised spatial pressure modes, onto which any number of pressure measurements may be projected. While many options exist for the choice of spatial structure, here we choose the following sinusoidal functions, continuously defined over  $y$  and  $z$ :

$$\Phi_L(y, z) = \sin\left(\frac{\pi y}{W}\right) \quad (2.2a)$$

$$\Phi_V(y, z) = \sin\left(\frac{\pi z}{H}\right). \quad (2.2b)$$

For any given set of  $n$  pressure measurements  $\mathbf{p} = [p_1, \dots, p_n]$  at locations  $\mathbf{y} = [y_1, \dots, y_n]$ ,  $\mathbf{z} = [z_1, \dots, z_n]$ , the normalised modes are defined as:

$$\phi_L(\mathbf{y}) = \sin\left(\frac{\pi \mathbf{y}}{W}\right) / \left| \sin\left(\frac{\pi \mathbf{y}}{W}\right) \right| \quad (2.3a)$$

$$\phi_V(\mathbf{z}) = \sin\left(\frac{\pi \mathbf{z}}{H}\right) / \left| \sin\left(\frac{\pi \mathbf{z}}{H}\right) \right|, \quad (2.3b)$$

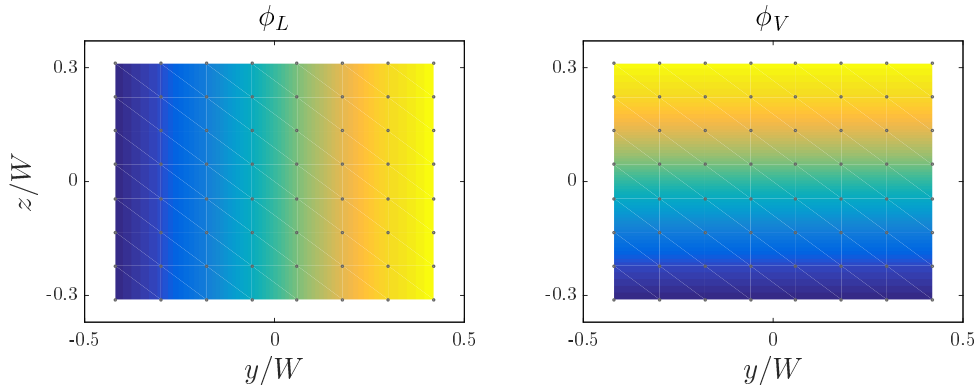


Figure 2.5: The normalised pressure modes  $\phi_L$  and  $\phi_V$ , plotted on the base of the Ahmed body.

where  $|\cdot|$  denotes the 1-norm of the vector. These pressure modes are displayed in figure 2.5. A pressure mode coefficient  $m(t)$  may then be evaluated by the dot-product as e.g.

$$m_V(t) = \phi_V \cdot \mathbf{p}(t). \quad (2.4)$$

Note that the pressure measurements may be normalised by the dynamic head to allow comparison between different free-stream velocities, or left as raw pressure for feedback control purposes.

### A comparison of the pressure measurements

Given that the model is equipped with two different pressure measurement sources, it is important to understand the advantages and limitations of each. The Endevco pressure transducers are mounted flush with the base of the model and thereby measure the pressure directly at the location of interest. In contrast the ESP pressure scanner has a short length of tubing between the surface of the body and the bank of transducers. Such tubing is known to have a frequency dependant attenuation affect that is generally related to the frequency of the first acoustic mode of the tube. More specifically, for a tube of length  $L$  the attenuation will be expected to be relevant for frequencies  $f \gtrsim f_c$  given by,

$$f_c = \frac{c}{4L}, \quad (2.5)$$

where  $c$  is the speed of sound. While we expect the ESP measurements to be limited at higher frequencies, the Endevco transducers have limitations at low frequencies.



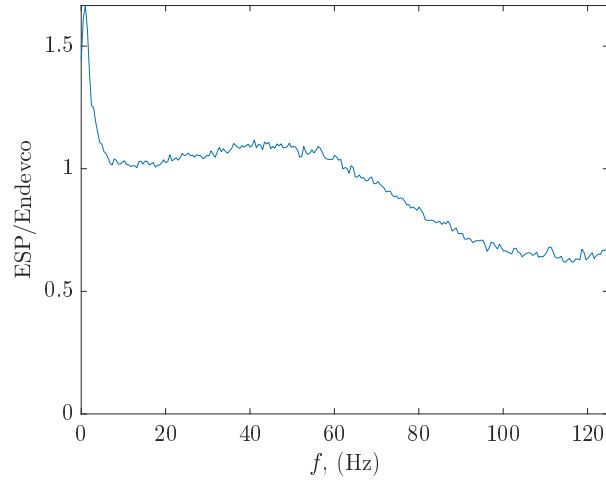


Figure 2.6: Ratio of the Fourier transform of the average measurement from the 64 ESPappings on the base to the 8 pressure transducers.

In particular, at DC and very low frequencies the transducers suffer from drift, partly temperature induced. By contrast the ESP scanners are temperature compensated and are designed to drift to a much smaller extent.

In order to provide a direct comparison and understand the extent of the limitations of the two pressure measurements, we test the systems under the influence of a white noise source. A speaker is positioned adjacent to the base of the model with a cowling around the edges to provide an almost closed cavity containing all of the pressure measurement locations. The volume of the cavity is chosen to be small and the speaker is placed close to the base in order to generate almost uniform pressure fluctuations. The average ESP and Endevco measurements can then be compared in the frequency domain to assess performance.

Figure 2.6 shows the ratio of the measurements from the ESP relative to the Endevcos, plotted as a function of frequency. The data demonstrates that at very low frequencies  $f \lesssim 5$  Hz, the ESP generally gives a large response relative to the Endevco transducers, up to a maximum factor of around 1.7. There is then a wide range of good agreement up to  $f \approx 60$  Hz at which point the ESP measurements begin to decay with frequency. The low-frequency discrepancy is likely a limitation of the Endevco transducers which are not designed for low-frequency or DC measurements while the higher frequency differences are indicative of the attenuation of the tubing. We may conclude that for all cases in which frequencies less than 60 Hz are required, the ESP will provide an accurate measurement system offering much higher spatial resolution, without the need for a calibration.



A final point is that while the ESP scanner provides accurate time-resolved data, it is not data that can easily be accessed in real-time by a control system. For feedback-control purposes the Endevco transducers will therefore be used.

## 2.3 Experimental procedures

Three different sets of experiments were performed on the Ahmed body fitted with forcing flaps: open-loop harmonic forcing, open-loop static forcing and closed-loop control. In each case care needed to be taken to accurately record the drag and base pressure, the procedures for which are detailed below.

### 2.3.1 Open-loop forcing with flaps

For the open-loop forcing the flaps were either oscillated at a range of frequencies or held at a range of static positions, at which the forces and pressure were measured. Generally a sweep of forcing parameters may take around 12 hours, therefore particular care was taken to account for drift in the measurements that would usually occur over this time. Possibly due to changes in temperature it was found necessary to not only record a zero-reading of the instrumentation, but also to regularly record a baseline (unforced) reading. In this way we could accurately measure changes with respect to the baseline configuration. The procedure is detailed below:

1. Generate the sequence of forcing parameters.
2. Check that  $U_\infty \approx 0$ , then record all data for 10 s.
3. Start the tunnel and set the flaps to stationary positions of  $\theta_1 = \theta_2 = 0^\circ$ . Once both  $U_\infty$  and  $\theta_{1,2}$  are set, record all data for 30 s.
4. Stop the tunnel, check that  $U_\infty \approx 0$ , then record all data for 10 s.
5. Start the tunnel and operate the flaps according to the  $i$ 'th set of forcing parameters. Once both  $U_\infty$  and the flap motion are set, record all data for 300 s.
6. Stop the tunnel, check that  $U_\infty \approx 0$ , then record all data for 10 s.
7. Return to step 3.

### 2.3.2 Closed-loop control with flaps

For closed-loop control, the measurement of absolute drag and pressure values was unimportant, however the accurate measurement of changes to these values was. The procedure to achieve this is as follows:

1. Start the tunnel and set the flaps to stationary positions of  $\theta_1 = \theta_2 = 0^\circ$ . Once both  $U_\infty$  and  $\theta_{1,2}$  are set, start recording all data.
2. After 100 s, start operating the feedback control, running for a further 300 s.

## 2.4 Other analyses

### 2.4.1 Frequency response

The frequency response is a common method of analysis for linear systems for which a sinusoidal input always gives a sinusoidal output. The frequency response quantifies how the relative magnitude and phase of the output sinusoid varies with the frequency of the input. For nonlinear systems a frequency response may still give useful information about the response of the system to periodic forcing.

For a periodic input  $u = U \sin(2\pi ft)$  we expect a component of the output to be periodic with the form  $y = Y \sin(2\pi ft - \varphi)$ , where the amplitude and phase of the output are frequency dependent. For experimentally generated data neither the input or output will be purely harmonic and we therefore need to extract a single frequency component from the signals. For a signal  $s(t)$  measured over a time period  $T$ , and forcing frequency  $f$  we firstly evaluate the coefficients,

$$a_s = \frac{2}{T} \int_0^T s \cos(2\pi ft) dt \quad (2.6a)$$

$$b_s = \frac{2}{T} \int_0^T s \sin(2\pi ft) dt. \quad (2.6b)$$

The amplitude and phase of this signal are then given by

$$S = |a_s + ib_s| \quad (2.7a)$$

$$\varphi_s = \angle(a_s + ib_s). \quad (2.7b)$$

The complex frequency response between two signals  $u$  and  $y$  is then defined as,

$$G(f) = \frac{Y}{U} e^{i(\varphi_y - \varphi_u)}. \quad (2.8)$$

Generally, the complex gain  $G$  will be evaluated for a range of forcing frequencies and displayed by plotting the magnitude and phase.

## 2.4.2 The proper orthogonal decomposition

The proper orthogonal decomposition (POD) is widely used both within and beyond fluid mechanics, and is variously known as principle component analysis, singular value decomposition or Karhunen-Loève analysis. In this work we use it to empirically identify coherent features in both the velocity and pressure fields. The calculation method used is subtly different in each case and, while this is widely documented elsewhere (e.g. Holmes *et al.*, 1998), we will give here a brief description of the calculations employed.

In fluid mechanics the POD is usually applied to velocity field data from e.g. PIV, for which the number of samples is much greater in space than in time. Performing the decomposition then requires the method of snapshots given by Sirovich (1987), and distinguishes the POD applied to fluid flows from similar methods such as principle component analysis widely applied elsewhere. Given velocity field data  $\mathbf{V}(x, y, t) \in \mathbb{R}^{N_x \times N_y \times N_t}$ , we first rearrange the data into a “snapshots” matrix  $S \in \mathbb{R}^{N_s \times N_t}$ , where  $N_s = N_x N_y$  is the total number of spatial samples. We then form the correlation matrix  $R$  as

$$R = S^\top S. \quad (2.9)$$

Given that  $N_s > N_t$ , this has the effect of reducing the dimension of the problem since  $R \in \mathbb{R}^{N_t \times N_t}$ . We then perform an eigenvalue decomposition on  $R$  to form a matrix  $W$  of ranked eigenvectors. The matrix of ranked POD modes may then be evaluated by the multiplication,

$$\Phi = SW, \quad (2.10)$$

thereby projecting the eigenvectors back up to the full spatial dimension  $N_s$ . Finally, a matrix of temporal coefficients may be evaluated through the multiplication,

$$A = \Phi^\top S. \quad (2.11)$$

For some of the work in chapter 4, POD is applied to the data from the 64 static pressure tappings on the rear of the axisymmetric body. In this case the method is broadly the same but with two key differences. Firstly, there are fewer points in space than in time, i.e.  $N_s < N_t$ , and secondly the measurement locations are not uniformly distributed. The evaluation of  $R$  therefore follows a modified version of (2.9) as,

$$R_p = SS^\top M, \quad (2.12)$$

where  $M \in \mathbb{R}^{N_s \times N_s}$  is a diagonal matrix of weightings that reflects the varying areas that each pressure tapping may be allocated. Following the evaluation of  $R_p$  and its eigen-decomposition, the POD modes are obtained directly as the eigenvectors.

# Chapter 3

## Extremum seeking control of the axisymmetric wake

As a first application of feedback control, this chapter examines the application of an extremum seeking (ES) controller to the open-loop control system of Oxlade *et al.* (2015). The purpose of the work in this chapter is both to demonstrate an application of effective closed-loop flow control to a high Reynolds number three-dimensional wake, and to provide a bench-mark against which further flow control schemes may be assessed.

In this chapter we first present a heuristic analysis and overview of the extremum seeking method, with particular attention to modifications which we find to be advantageous to the algorithm, and to the considerations involved in frequency optimisation. We then present the successful application of the controller to the open-loop system of Oxlade *et al.* (2015): a highly turbulent bluff body wake forced by a periodically-pulsed jet, variable in both amplitude and frequency. We demonstrate that in the presence of broadband noise we are able to optimise both the forcing amplitude and frequency of the open-loop system, either individually or simultaneously in a step-wise manner. We finally demonstrate the ability of the system to adapt in real time to changing conditions, in this case varying free-stream velocity.

### 3.1 Analysis

Before presenting our experimental results we first give a brief overview of the standard ES algorithm followed by particular issues and suggested modifications.

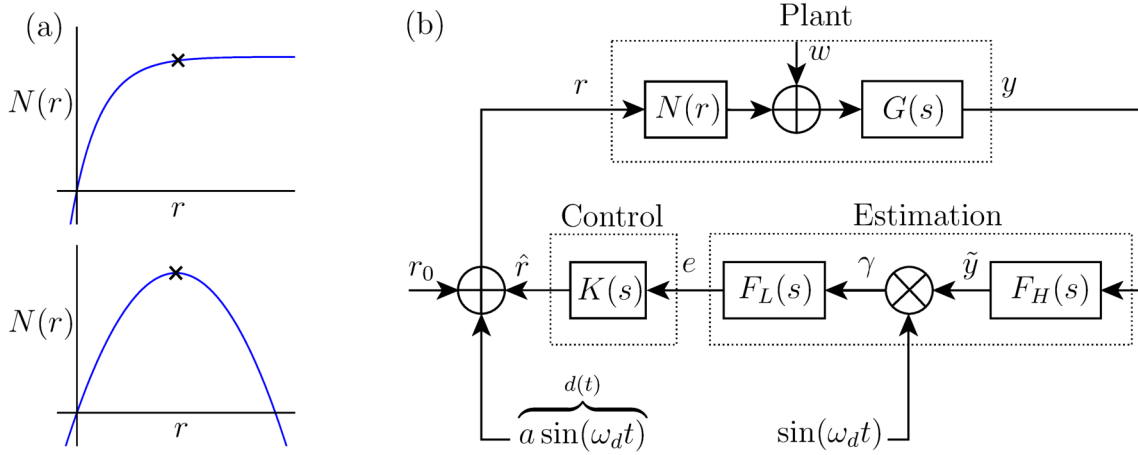


Figure 3.1: (a) Examples of common nonlinear mappings and (b) the standard extremum seeking control algorithm applied to a SISO system.

### 3.1.1 Principle of operation

Figure 3.1(a) shows schematically two scenarios for the steady-state mapping between a reference parameter  $r$  and an output  $N(r)$ : the upper displaying a desired location with finite gradient and the lower a desired location with zero gradient. Here we look predominantly at the extremum seeking method (for zero gradient) although the same principles and stability guarantees can be applied to both (Ariyur & Krstić, 2003). While many variants of extremum seeking controllers exist (Calli *et al.*, 2012), the perturbation method is the most commonly applied and is straightforward to analyse and understand. A block diagram for the method is given in figure 3.1 (b).

The perturbation method involves adding a perturbation or “dither” signal  $d(t)$  to the plant input, the form of which may vary (Tan *et al.*, 2008; Nešić, 2009), but the most commonly used being a sinusoid. The ES system involves an estimation phase, the purpose of which is to produce a signal  $e$ , proportional to the local gradient of the mapping, while attenuating the disturbances arising from both the unmodelled dynamics of the plant and the dither signal. The control must act on this estimation signal to produce a change to the reference with the goal of driving the gradient to zero. We will consider first the case of a single input single output (SISO) plant with a nonlinear mapping  $N(r)$  ( $N : \mathbb{R} \rightarrow \mathbb{R}$ ); internally generated noise  $w$ , and frequency response defined by  $G(s)$ , where  $s$  is the Laplace transform variable. It is important to note here that neither  $N(r)$  or  $G(s)$  need to be known in order to implement the controller, and that  $G(s)$  may in general be nonlinear, i.e. amplitude or time dependent. The only assumption is that an operating point can be decided

based upon the gradient  $N'(r) = \left. \frac{dN}{dr} \right|_r$ .

The equations governing an ES controller applied to this system are given below, while the influence of each of the parameters are summarised in table 3.1. Each of the terms featured below may be referred to on the block diagram of figure 3.1 (b).

The reference  $r$  is composed as the sum of some initial value  $r_0$ , the dynamically varying control correction  $\hat{r}$  and the dither signal:

$$r = r_0 + \hat{r} + \underbrace{a \sin(\omega_d t)}_{d(t)}. \quad (3.1)$$

As given in (3.2) below, the output  $y$  from the plant then consists of: a slowly varying part,  $\bar{y}$ ; a sinusoidal term proportional to the local gradient of the mapping  $N'(r_0 + \hat{r})$ ; and noise  $w_G$  arising from the unmodelled dynamics within the plant. This comes from taking a Taylor expansion about the current location on the mapping  $N$ , under the assumption that  $\hat{r}$  varies slowly relative to the dither signal. For input to output dynamics governed by a linear or weakly nonlinear  $G(i\omega)$ , the signal at output will be sinusoidal with a phase lag  $\varphi_{G(i\omega)}$  with respect to the dither signal and will be attenuated (or amplified) according to a gain  $|G(i\omega)|$ . Such an effect may arise due to the finite response time of the system or due to effects such as hysteresis (Benard *et al.*, 2009).

$$y \approx \bar{y} + aN'(r_0 + \hat{r}) |G(i\omega)| \sin(\omega_d t - \varphi_{G(i\omega)}) + w_G. \quad (3.2)$$

The high pass filter  $F_H(i\omega)$  then removes the slowly varying term, induces an additional phase lag  $\varphi_{F_H}$  and slightly modifies the noise,

$$\tilde{y} \approx aN'(r_0 + \hat{r}) |G(i\omega)| \sin(\omega_d t - \varphi_{G(i\omega)} - \varphi_{F_H(i\omega)}) + \tilde{w}_G. \quad (3.3)$$

This output is then multiplied by a unity magnitude dither signal in order to achieve a demodulated signal  $\gamma$ . This operation results in three components: a DC term proportional to the local gradient; a harmonic of the dither signal, and modulated noise.

$$\begin{aligned} \gamma \approx \frac{1}{2} aN'(r_0 + \hat{r}) |G(i\omega)| \cdot \left( \cos(\varphi_{G(i\omega)} + \varphi_{F_H(i\omega)}) - \cos(2\omega_d t - \varphi_{G(i\omega)} - \varphi_{F_H(i\omega)}) \right) \\ + \tilde{w}_G \sin(\omega_d t). \end{aligned} \quad (3.4)$$

A low pass filter is then applied to remove the harmonic terms and leave a value

proportional to the gradient of the mapping. This will be referred to as the error signal,  $e$ , where

$$e \approx \left( \frac{1}{2} a N' (r_0 + \hat{r}) |G(i\omega)| \cos(\varphi_{G(i\omega)} + \varphi_{F_H(i\omega)}) \right) + w_e. \quad (3.5)$$

As will be discussed below, for the case of frequency optimisation it may be advantageous to choose the dither signal to be a square wave. In this case the above analysis shows (see appendix C.1) that  $e$  may instead be written as the Fourier series:

$$e \approx \frac{1}{2} a N' (r_0 + \hat{r}) \sum_{m=1}^{\infty} \left[ \frac{|G(i(2m-1)\omega_d)|}{(2m-1)^2} \times \cos(\varphi_{G(i(2m-1)\omega_d)} + \varphi_{F_H(i(2m-1)\omega_d)}) \right] + w_e. \quad (3.6)$$

Finally the controller evaluates the correction based upon the value of  $e$  with the objective of moving the reference in the direction of the gradient of the mapping. Specifically,  $K$  will increase  $\hat{r}$  if  $e$  is positive and vice versa:

$$\hat{r} = K(s)e. \quad (3.7)$$

Typically  $K$  is chosen to be an integral controller ( $k/s$ ) in order to drive the system to the desired reference gradient.

### 3.1.2 Frequency optimisation

As discussed in § 1.3.1, for many open-loop flow control systems the input to the plant may be a harmonic signal,  $u = c \sin(2\pi f t)$ . For example the input may be a sinusoidally pulsed jet, the effect of which may vary with frequency, as illustrated schematically in figure 3.2 (a). In many such cases we may therefore wish to adapt the frequency of the harmonic signal with the ES controller, i.e.  $f$  will be the reference parameter  $r$ .

Following the standard method described in § 3.1.1 and applying a sinusoidal dither signal to perturb the frequency, the input to the plant would be,

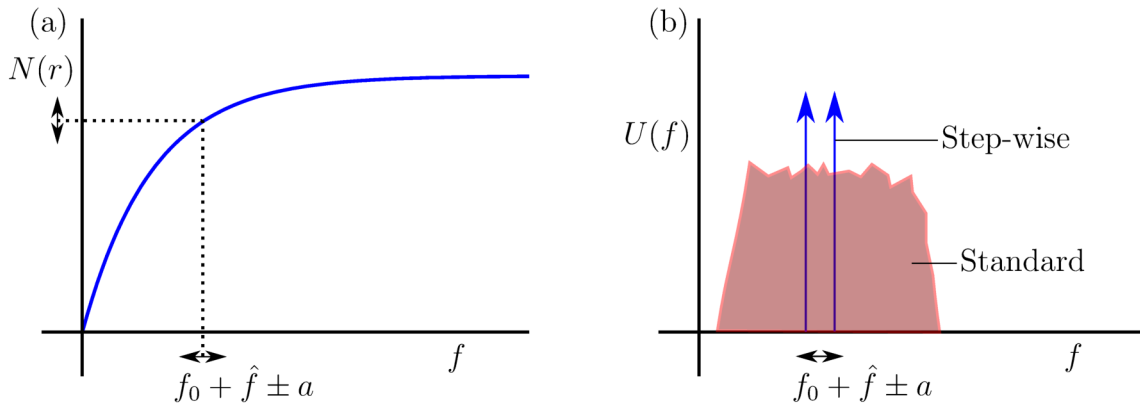
$$u = c \sin \left( 2\pi \left( f_0 + \hat{f} + a \sin(\omega_d t) \right) t \right). \quad (3.8)$$

To analyse the effectiveness of this perturbation strategy, we wish to determine the instantaneous frequency content of this signal, since, to determine the gradient of



Parameter	Purpose and benefits	Limitations
$a$	Increasing $a$ improves adaptation speed and improves the SNR of $e$ .	Larger $a$ leads to larger perturbations once a steady state is reached.
$\omega_d$	Increased $\omega$ allows increased adaptation speed while maintaining separation of time-scales.	At high $\omega_d$ instability may arise due to large phase lags and the SNR may be reduced by filtering through the plant.
$F_H(s)$	Removes the DC and slowly varying component before demodulation.	Induces an additional phase lag between the plant and demodulation.
$F_L(s)$	Removes both the sinusoidal perturbations and reduces the noise in the error signal.	Slows down the system by imposing a finite bandwidth.
$K(s)$	Directly controls the speed of adaptation.	If too large, may amplify disturbances or cause instability by violating the separation of timescales.

Table 3.1: Parameters of the ES algorithm and their effect on system performance.

Figure 3.2: Frequency optimisation: (a) an illustrative mapping between forcing frequency and output and (b) the single sided spectrum of the input  $u$  in the case of a standard dither (red) or a square wave dither signal (blue).

the mapping in figure 3.2 (a), we must vary the frequency in the range  $f_0 + \hat{f} \pm a$ . For a signal written in terms of a sin function the instantaneous frequency is the derivative of the argument of the sin. That is, for  $u = c \sin(\varphi(t))$ , we need to find  $f(t) = \frac{1}{2\pi} \dot{\varphi}(t)$ . For the system in (3.8) this gives,

$$f(t) = f_0 + \hat{f} + a \sin(\omega_d t) + \omega_d a \cos(\omega_d t) t. \quad (3.9)$$

Hence, the instantaneous frequency is given by the slowly varying base frequency ( $f_0 + \hat{f}$ ), a sinusoidal perturbation and an additional time increasing term,  $\omega_d a \cos(\omega_d t) t$ . This final term will cause the input to have a far more broadband spectrum, as indicated schematically in figure 3.2 (b), rather than one that probes the system within the required range. Alternatively, this final term may be thought of as an additional noise component of the reference parameter  $r$ . This noise grows with time and is unbounded as  $t \rightarrow \infty$ . This unbounded frequency input will cause erratic behaviour of the system and acts to make the system unstable, in the sense that the reference parameter grows without limit as time increases. Two methods to deal with this problem are now suggested.

**Sinusoidal phase deviation** The first method can be found by explicitly calculating the phase argument  $\varphi(t)$  that gives the required variation in frequency,  $f(t)$ . For a sinusoidal perturbation of the frequency of  $u = c \sin(\varphi(t))$  we require

$$\frac{1}{2\pi} \frac{d}{dt} [\varphi(t)] = f_0 + \hat{f} + a \sin(\omega_d t). \quad (3.10)$$

Hence,

$$\begin{aligned} \varphi(t) &= 2\pi \int \left( f_0 + \hat{f} + a \sin(\omega_d t) \right) dt \\ &\approx 2\pi \left( f_0 + \hat{f} \right) t - \frac{2\pi a}{\omega_d} \cos(\omega_d t). \end{aligned} \quad (3.11)$$

Here the approximation results from the assumption that compared with the sinusoid,  $\hat{f}$  changes only very slowly so can be considered constant within the integral. Hence for a sufficiently slow adaptation of  $\hat{f}$ , a sinusoidal dither can be implemented when the reference parameter is a frequency.

**Step-wise changes in  $r$**  A limitation of the above method comes from the fact that changes in  $\hat{f}$  must be sufficiently slow to avoid introducing undesired frequencies into the input. An alternative solution to the problem is to instead change the forcing

frequency in a step-wise manner, akin to the square wave dither signal applied by Tan *et al.* (2008). In this case we can choose the value of  $\hat{f}$  to be updated only when step changes in the dither signal occur, thus avoiding the above problem. The input is now given by

$$u = c \sin \left( 2\pi \left( f_0 + \hat{f}_{T_{2k}} \pm a \right) t \right). \quad (3.12)$$

Here we use the subscript  $T_{2k}$  to denote the value at the beginning of each half cycle of the square wave. We can now evaluate the instantaneous frequency at all times other than when the step changes occur as

$$f(t) = f_0 + \hat{f}_{T_{2k}} \pm a. \quad (3.13)$$

The instantaneous frequency now simply follows step-wise changes with time and will, over the dither period, have the frequency content shown in figure 3.2 (b). Furthermore it can be shown (see appendix C.1) that this step-wise dither signal will operate in the same way as the sinusoidal dither, giving the result shown in (3.6). Therefore a frequency optimisation scheme can be set up in this way and may then be expected to be subject to the same considerations as the standard ES scheme.

### 3.1.3 Stability

While proofs of stability for a sinusoidal dither are given in Krstić & Wang (2000); Krstić (2000) among others, we aim to give a brief heuristic overview here. Instability of the extremum seeking system can at first be separated into instabilities of the plant itself and instabilities of the controller. The first situation, instability of the plant, is the most obvious but need not be considered. The purpose of an extremum seeking controller is not to stabilise unstable dynamics but to change the average, long term output of the plant. Hence it should only be used in situations in which the plant itself is open-loop stable.

Stability of the controller can now be considered on the basis of the analysis above. The key instance in which the controller can induce instability is if the error signal,  $e$ , is of the wrong sign. In general this will be due to phase lags between the dither input and the multiplicative stage. This is clear from the expression for  $e$  in (3.5). If the total phase lag  $\varphi_G + \varphi_{F_H}$  is greater than  $\pi/2$ , the cosine term will change sign, resulting in the control action being in the wrong sense. That is,  $r$  will be adapted in the direction away from the peak. Neglecting  $\varphi_{F_H}$  this could, for example, happen

for a second order plant perturbed above its resonant frequency. An instability of this kind will result in a diverging output from the plant in the opposite direction of the extremum.

Instability may also arise under conditions for which the above analysis is invalid. In particular it is assumed that the time-scales of the dither signal and the adaptation are sufficiently separate. This scale separation is dependent, other things being equal, on the relative values of the control gains  $K(s)$  and  $\omega_d$ . A similar observation is noted in the analysis of Krstić (2000); Tan *et al.* (2010). The implication of this limitation will be discussed in § 3.1.4.

### 3.1.4 Performance

The performance of the extremum seeking system may be considered in terms of three key features, the gradient estimation, disturbance attenuation and control. The performance of estimation and control may be considered separately, as shown schematically in figure 3.1(b), although disturbance attenuation is affected by both parts of the system. A summary of the implications of the analysis below is given in table 3.1.

**Estimation** As shown in (3.5),  $e$  is composed of the true estimation value, proportional to  $N'(r)$ , and additive noise. For brevity we will therefore decompose the error signal as  $e = e_t + w_e$ . Estimation quality can now be considered in terms of a signal-to-noise ratio (SNR) for  $e$ , defined as,

$$\text{SNR} = \left( \frac{e_t}{w_e} \right)^2. \quad (3.14)$$

It is shown from (3.5) that  $e_t$  depends upon the amplitude of the dither signal, the local gradient of the mapping and the frequency response of the plant at the perturbation frequency. Of these, only the dither amplitude  $a$  can be directly chosen. The local gradient is a property of the plant, is generally unknown, and will vary during operation of the ES system. The plant frequency response may also be uncertain, but its influence may be changed by the choice of  $\omega_d$ . In general we wish to maximise SNR, hence we wish to maximise the combined term  $|G| \cos(\varphi_G + \varphi_{F_H})$ . It is important to note that all the constituents of this term are frequency dependent, since in general the magnitude of the frequency response of a physical system decays

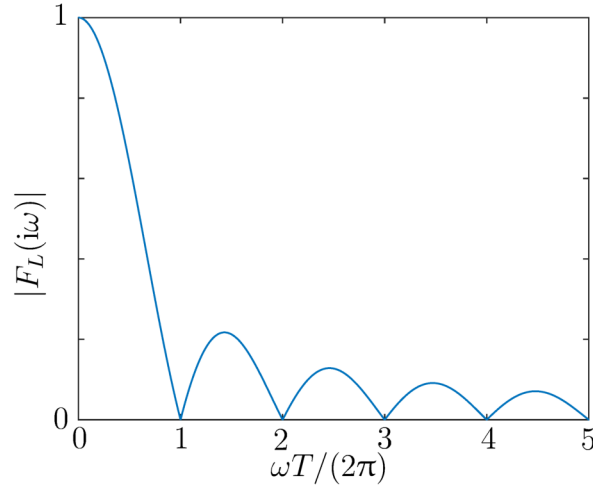


Figure 3.3: Frequency response of the moving average filter of period  $T = 2\pi/\omega_d$ .

at higher frequencies while the phase angle decreases. This consideration therefore provides a limit on the perturbation frequency. The effect of the phase lag may be improved upon by applying a similar phase lag to the demodulating signal, that is, to multiply by  $\sin(\omega_d t - \varphi)$  (Krstić, 2000). If  $\varphi$  can be chosen to be very similar to  $\varphi_G$  then the SNR may be improved, however in general  $\varphi_G$  may be unknown and limitations on  $\omega_d$  will still remain.

**Disturbance attenuation** The other approach to maximising the SNR is to minimise the noise,  $w_e$ . A significant part of this noise comes from the dither signal and its harmonics: demodulation leads to the sinusoidal term in (3.4), while nonlinearities within the plant may lead to higher harmonics (e.g.  $2\omega_d, 3\omega_d, \dots$ ) of the dither signal in the output  $y$ . These harmonic terms can be especially damaging to the control performance because, being at relatively low frequencies of  $\mathcal{O}(\omega_d)$ , they are attenuated very little by an integral controller. Successful elimination of these terms therefore depends upon the properties of  $F_L(i\omega)$ . A particularly good choice for this filter is a moving average filter with period  $T = 2\pi/\omega_d$ , since the frequency response of such a filter has zero gain at multiples of  $\omega$ . This is shown in figure 3.3.

In general the majority of the remainder of the noise will originate from the internal dynamics of the plant, and will have spectral characteristics that depend on the plant properties. For example these spectral properties may be similar to those of the plant transfer function  $G(i\omega)$ . In general these noise components will be attenuated by the moving average filter as well as by the integral controller.

While the low-pass filter is intended to remove noise after the demodulation, the

purpose of the high-pass filter is to remove the DC component  $\bar{y}$  from  $y$ , thereby isolating the harmonic perturbation. Exclusion of the high-pass filter simply leads to an additional harmonic term in  $\gamma$  (see (3.4)) of frequency  $\omega_d$ . However as discussed, such a harmonic may be effectively removed by the low-pass filter. The high-pass filter may therefore be redundant. In summary, we may expect to be able to remove the high-pass filter, thereby avoiding the associated phase lag. Although this lag may be catered for by including an additional lag in the demodulating signal, it may still impose speed restrictions on the adaptation of the whole algorithm.

**Control** Historically, ES controllers have often used a pure integral controller (Ariyur & Krstić, 2003),  $K(s) = k/s$ . This guarantees zero steady-state error and has the added benefit of acting as a low pass filter to the many disturbances passing around the loop. However, if the gradient estimation is of sufficient quality then  $K(s)$  can be designed to be more aggressive, using a PID or more general frequency domain controller. For example Krstić (2000) proposes that  $K(s)$  include a dynamic compensator, the properties of which are decided based upon  $G(s)$  and the properties of the expected changes in the operating point.

## 3.2 Experimental implementation

Based upon the analysis above we apply an ES controller to the open-loop control system of Oxlade *et al.* (2015). The open-loop system here has a steady-state mapping between the parameters of sinusoidal pulsed jet forcing and the base pressure (corresponding to the drag) of an axisymmetric bluff body. For this system the mapping is two dimensional: mean base pressure is a function of both forcing amplitude and forcing frequency. The experimental setup is as described in § 2.1, while the system properties will now be described in more detail.

### 3.2.1 System properties

For an extremum seeking controller, the most important feature of the plant is the steady-state mapping  $N(r)$ . For the system in this study, the mapping is two-dimensional ( $N : \mathbb{R}^2 \rightarrow \mathbb{R}$ ), giving spatially averaged base pressure as a function of forcing amplitude and frequency as shown in figure 3.4. Here the temporally and

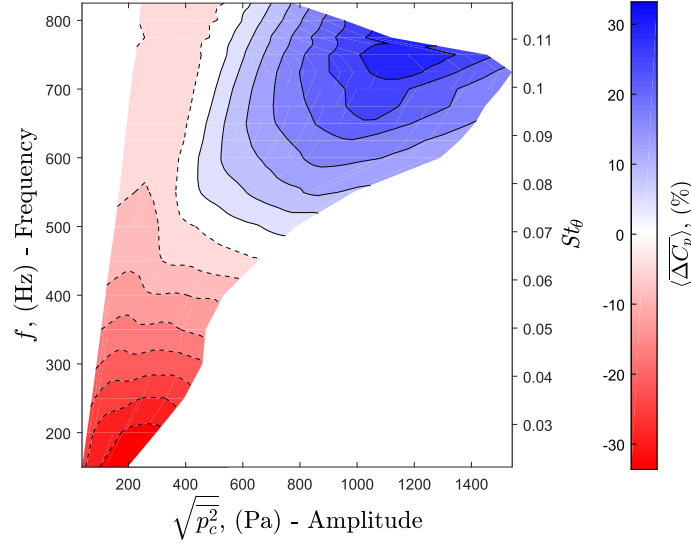


Figure 3.4: The two dimensional steady-state mapping for the open-loop system of Oxlade *et al.* (2015). Spatially averaged base pressure is given as a function of forcing amplitude and frequency, where the forcing amplitude is defined in terms of the rms of the pressure ( $p_c$ ) inside the cavity. Negative contours are shown by the dashed lines.

spatially averaged base pressure change is defined as

$$\langle \Delta C_p \rangle = \lim_{T \rightarrow \infty} \frac{1}{T} \iint_A \int_0^T \frac{C_p - \hat{C}_p}{\hat{C}_p} dt dA, \quad (3.15)$$

where  $A$  is the area over the base,  $\hat{C}_p$  is the pressure coefficient without forcing and  $C_p$  is the pressure coefficient under forced conditions. The mapping is smooth with a single global maximum located at values of amplitude and frequency of 1200 Pa rms and 750 Hz respectively. Areas for which data are not shown are outside the range of the actuator, and therefore cannot be explored in open-loop or reached during operation of the ES controller.

For a bluff body such as that tested here, much of the drag is form drag. A positive  $\langle \Delta C_p \rangle$  therefore corresponds to a drag reduction. The mapping displays a drag reduction for large amplitudes and for frequencies  $f \gtrsim 500$  Hz, corresponding to a situation in which the forcing frequency is sufficiently decoupled from those of the shear layer and coherent structures of the wake. The forcing jet has zero net mass flux, but is not referred to here as a synthetic jet as the mechanism of operation does not rely on self induced streaming. Instead the forcing generates a discrete train of vortices bounded by strong shear layers that provide a sheltering effect on the wake, reducing entrainment. We refer the reader to Oxlade *et al.* (2015) for further details

on the drag reduction mechanism and actuator details.

While the data shown here is for a fixed free stream velocity  $U_\infty = 15 \text{ ms}^{-1}$ , one might expect the mapping to evolve in a predictable way as conditions change. Dimensional analysis and knowledge of the drag reduction mechanism tells us that  $\langle \Delta C_p \rangle$  is a function of jet momentum coefficient  $C_\mu = \frac{u_j^2 A_j}{U_\infty^2 A}$ , Strouhal number  $St_\theta = \frac{f\theta}{U_\infty}$  and Reynolds number  $Re_\theta = \frac{\rho U_\infty \theta}{\mu}$ . Here  $u_j$  and  $A_j$  are respectively the jet velocity and area,  $f$  is the forcing frequency and  $\theta$  is the boundary layer momentum thickness at separation. Provided that the Reynolds dependence of the dimensionless mapping is small, it may be expected that the optimal jet velocity and frequency will scale linearly with  $U_\infty$ .

### 3.2.2 Extremum seeking algorithm

The implemented ES controller was operated to adjust the amplitude and frequency of the harmonically forced jet described above, either of these parameters thereby acting as the reference  $r$  described in § 3.1.1. The output of the system ( $y$ ) is taken to be  $\langle C_p \rangle$ , approximated by the average of the eight pressure transducers and evaluated independently for each time sample.

The implemented ES algorithm is shown in the block diagram of figure 3.5. Following our analysis in § 3.1.4, the implemented system had the following features not commonly used in the literature:

1. Square wave dither signal for frequency

As discussed in § 3.1.2, a sinusoidal dither signal leads to complications when the reference parameter is itself a frequency. We therefore choose to implement the method described above, varying the forcing frequency in a step-wise manner, and only updating  $\hat{r}$  at the crossing points of the square wave.

2. Exclusion of the high pass filter

As discussed in § 3.1.4, the main purpose of the high pass filter is to remove the DC component of the plant output, thereby removing a sinusoidal term generated by the demodulation. Provided that this effect can be successfully achieved using the low pass filter, the high pass filter is unnecessary. Furthermore the high pass filter introduces an additional phase lag which may impose speed restrictions.



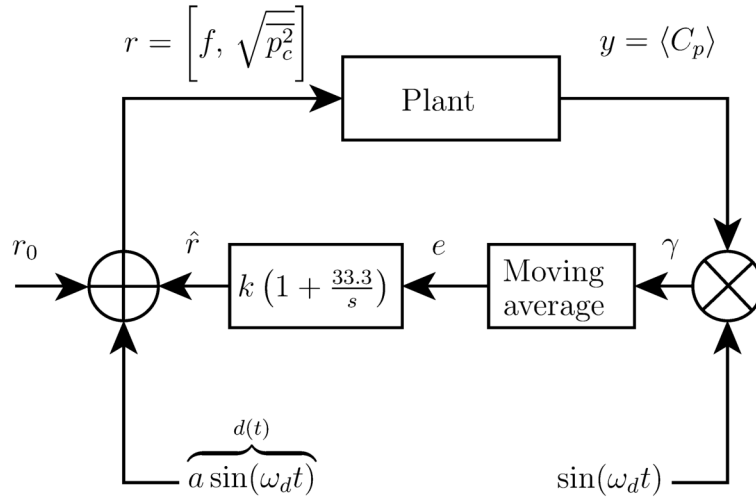


Figure 3.5: The modified ES algorithm implemented experimentally. The output  $y$  is the pressure instantaneously averaged over the base, while the reference  $r$  is either the forcing amplitude or frequency.

### 3. Use of a moving average for the low pass filter

The key components that need be removed by the low pass filter are the perturbation frequency and its harmonics. A moving average filter with period equal to the perturbation period will have zero gain at all harmonics of the inverse of this period (Smith, 1997), and is therefore the optimal filter to use for this purpose (see figure 3.3).

### 4. Use of a proportional, integral controller

To improve the speed of adaptation, a proportional term is used in addition to the usual integral term. This is in agreement with the recommendations of Krstić (2000).

## 3.2.3 Parametric investigation

Given the overall structure of the ES system described above and shown in figure 3.5, it remains only to choose the parameters of the system. If the ratio of proportional to integral gains is fixed, then only three parameters remain to be chosen: the dither amplitude  $a$ , dither frequency  $\omega_d$  and control gain  $k$ . These are defined such that

$$d(t) = a \sin(\omega_d t), \quad (3.16)$$

$$K(s) = k \left( 1 + \frac{33.3}{s} \right). \quad (3.17)$$

	$a$ , (Pa)					$\omega_d/2\pi$ , (Hz)						$k$		
	40	60	80	100	120	0.125	0.25	0.50	1.00	2.00	4.00	0.4	0.8	1.2
$T_r$ , (s)	81.1	37.0	19.5	10.0	8.2	11.8	15.4	10.0	11.3	9.8	16.1	23.1	10.0	7.6
$\sigma^2$ , (Pa)	-	46	63	78	101	99	89	77	81	-	-	73	78	108
Stable	Y	Y	Y	Y	Y	Y	Y	Y	Y	N	N	Y	Y	Y

Table 3.2: Variation of the system performance with the choice of parameters when seeking in amplitude.

The ratio of the proportional and integral gains shown here were based on the recommendations of Krstić (2000) and some initial trial and error.

The results of the parametric investigations for seeking in amplitude are shown in table 3.2. A preliminary investigation was first performed to establish approximately optimal values for these variables of  $a = 100$  Pa,  $\omega_d/2\pi = 0.5$  Hz and  $k = 0.8$ . Subsequently these initial values formed a baseline about which the parametric investigation could be performed; i.e. for investigation of  $a$ ,  $\omega_d/2\pi$  is kept at 0.5 Hz and the control gain  $k$  kept at 0.8. The table displays the half rise time, the steady-state variance and the stability of the scheme under each configuration. The half rise time is defined as the time taken for the reference to reach half of the average steady-state value, thereby giving a measure of the convergence speed. The steady-state variance is the variance of the reference value after it has reached a steady-state, including both the dither signal and the control input  $\hat{r}$ . The system is determined to be unstable if the reference parameter increases or decreases beyond the range of the actuator and well beyond the anticipated optimal condition.

In agreement with the analysis of § 3.1.1, the dither amplitude is seen to have two key influences. An increase in  $a$  is seen to increase the speed of the algorithm, – the rise time reducing by a factor of 10 with a three-fold increase – but is also naturally seen to increase the perturbations seen once a steady state is reached. Within the range tested here the system always remained stable. By contrast the dither frequency is seen to have little coherent effect on the convergence time, although at very low frequencies there seems to be more perturbation about the steady state. At high frequencies the system is found to become unstable, as anticipated: the reference increasing beyond the optimal operating point. This may be a result of the phase lag through the system becoming too large. Finally an increase in the control gain is seen to increase the convergence speed, as anticipated, but is also seen to lead to greater noise in steady state due to over-reaction of the controller.

Choice of optimal parameters require a choice of trade-off between convergence speed

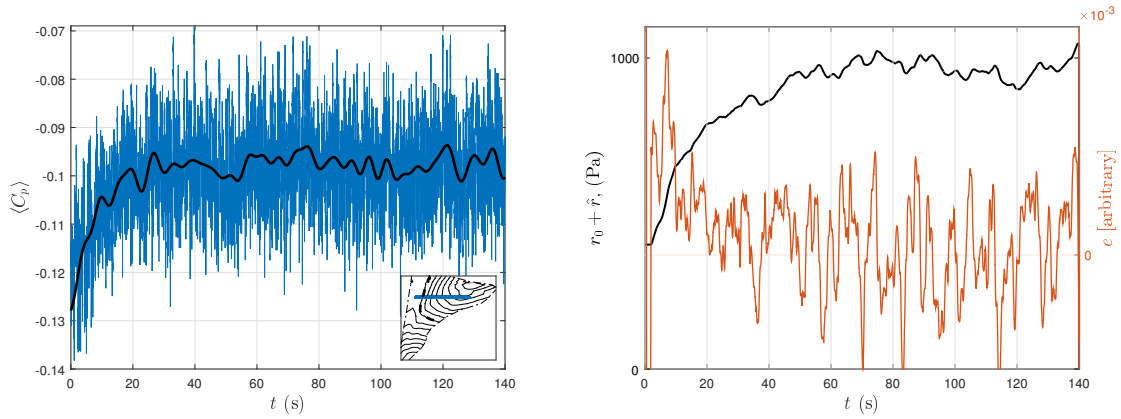


Figure 3.6: Amplitude only optimisation at a frequency of 650 Hz: (a) the spatially averaged base pressure evolution and (b) the controller variables  $r(t)$  and  $e(t)$ . Inset is the trajectory over the mapping shown in figure 3.4.

and steady-state perturbations. It was felt that the values of  $a = 100$  Pa,  $\omega_d/2\pi = 0.5$  Hz and  $k = 0.8$  provided a good compromise and were used for all subsequent tests. Similar results for frequency optimisation lead to identical choices for  $\omega_d$  and  $k$  and a dither amplitude  $a = 30$  Hz.

### 3.2.4 Single variable implementations

The extremum seeking controller was first implemented in one dimension to optimise either only the amplitude of the forcing at a fixed forcing frequency or to optimise the frequency at a fixed amplitude. Initial conditions for the amplitude optimisation were 400 Pa and 650 Hz, while those for the frequency optimisation were 250 Pa and 200 Hz, chosen in order to provide sufficient “space” in which the controller could seek. Examples of these implementations are shown in figures 3.6 and 3.7.

For the case of amplitude optimisation, the response of the output of the system under control action is shown in figure 3.6 (a). The trajectory of the system across the static mapping is shown inset. Two key observations can be made from these data. First, by looking at the filtered response (black line) the output can be seen to have adapted to an optimal condition after around 30 s, beyond which only fairly small fluctuations occur. Second, the raw data (blue) displays the level of noise resulting from the broadband turbulent fluctuations of the flow, all of which pass into the output measurement  $\langle C_p \rangle$ . These fluctuations can be seen to have been greatly attenuated within the error signal  $e$ , shown in figure 3.6 (b), although some

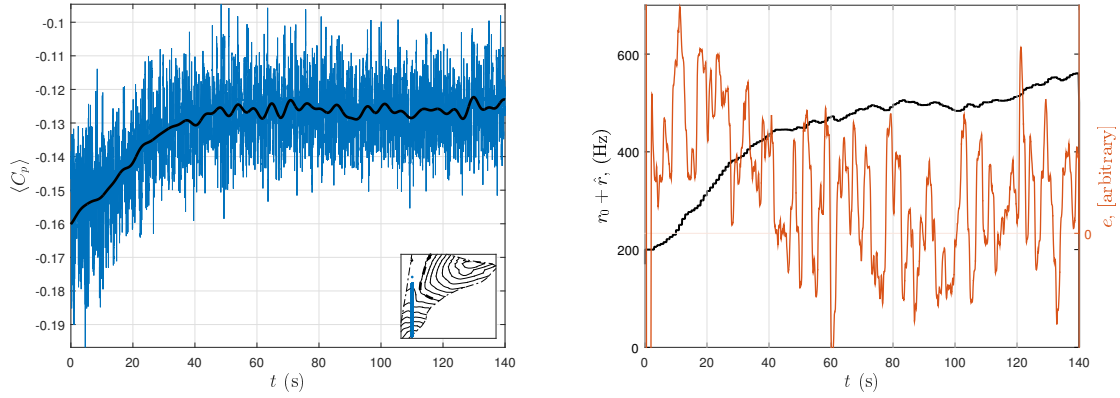


Figure 3.7: Frequency only optimisation at an amplitude of 250 Pa: (a) the spatially averaged base pressure evolution and (b) controller variables  $r(t)$  and  $e(t)$ . Inset is the trajectory over the mapping shown in figure 3.4.

fluctuations do still remain. Finally the adapted reference input can be seen as the black line in figure 3.6 (b). It is evident that the reference has been largely adapted after 30 – 40 s and that only small fluctuations remain after this time. The filters and controller are therefore effective in deciphering the effect of the dither within the noisy output signal  $y$ , and passing only minimal disturbances into the adapted reference  $\hat{r}$ .

Similar results can be seen for the case of frequency optimisation in figure 3.7. Adaptation is seen to be similarly effective in spite of the same noisy output measurement. However the key difference relative to amplitude optimisation is that the frequency is seen to continue to increase with time, because the gradient of the mapping remains slightly positive. For this particular operating point a slope (rather than extremum) seeking controller may therefore be more appropriate, however for the global optimum this is not the case. Also shown is that changes in the frequency are made in the stepwise manner described in § 3.1.2.

The adaptation time for both controllers is seen to compare well with previous flow control implementations. In particular, the adaptation time is found to be similar to, but slightly greater than, that of the system of Henning *et al.* (2008); Pastoor *et al.* (2008). In general, for a given noise level from the plant ( $w$  of figure 3.1), there exists a trade-off between the adaptation time and the level of variation once a steady state is reached, as was shown in the parametric study of § 3.2.3. For a turbulent wake we may expect the level of noise to be partly determined by the Reynolds number as with increasing  $Re$  there is an increased range of scales in the flow. If we wish

to keep the steady state perturbations below a certain level, the adaptation time would be required to increase with  $Re$ . The slight increase in adaptation time may therefore be at least partially attributed to the factor 10 higher Reynolds number in this experiment.

### 3.2.5 Dual variable implementation

While the implementation of the algorithm in each of amplitude and frequency individually allowed optimisation of the algorithm parameters, a fully working system would be operated in both dimensions. In principle the ES controller can be operated to adapt multiple references simultaneously, provided that the perturbation frequencies are not equal; a result of the orthogonality of sinusoids. However, the challenge arises in effectively filtering the variable  $\gamma$  (see figure 3.5). The moving average filter discussed in § 3.1.4 is very effective at removing one frequency and its harmonics but not optimal for other frequencies. Each moving average is therefore unable to effectively filter the dither signal applied to the other variable, since the frequency of the two dither signals must necessarily be different.

While methods do exist to avoid the filtering issue (see e.g. Gelbert *et al.*, 2012), in this study we chose to implement the algorithm in a stepwise manner, adapting each variable in turn for a fixed period of time. The results of this are shown in figure 3.8. The system converges to a steady state after about 100 s, so is clearly somewhat slower than the one-dimensional examples seen above. This may be partially a result of the stepwise nature of the control, as the controller has to effectively restart from its current position every 20 s. However, the total convergence time still compares favourably with previous studies (Pastoor *et al.*, 2008).

The trajectory of the adaptation can be seen in figure 3.8 (b), from which it is clear that the system converges to the optimal condition found in open-loop. Each stage of the route is seen to arrive at approximately optimal conditions based upon the current value of the fixed parameter (amplitude or frequency). It is possible that by reducing the time between switches from the 20 s implemented here, the net speed of the algorithm may be improved. However the best time will likely depend on the local properties of the mapping so a generally optimal value may be difficult to find.

It is worth noting that under these testing conditions the controller brings the system close to the limits of the actuator. While this is not an issue to the control scheme here, it is clear that for any practical system, care must be taken to ensure that the

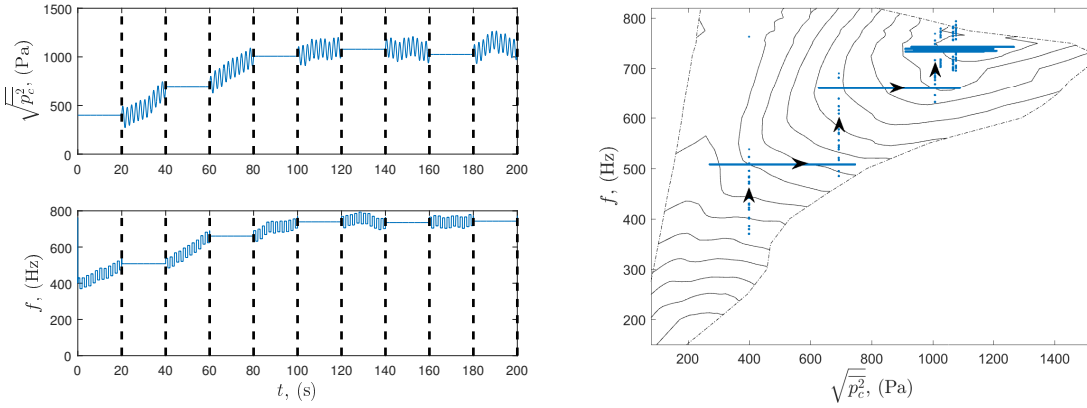


Figure 3.8: Extremum seeking in two variables: (a) time series and (b) trajectory across the mapping of figure 3.4.

controller does not try to reach an operating point that would cause damage to the actuator.

### 3.2.6 Adaptation to changing conditions

One of the key purposes of using closed-loop control over open-loop control is that the system will automatically adjust to changing operating conditions. For this ES control system, the key operating condition is the free stream velocity  $U_\infty$ , since this affects the optimal amplitude and frequency as discussed in § 3.2.1. Specifically, with increasing  $U_\infty$ , the required forcing amplitude and frequency would be expected to increase accordingly. The system was therefore tested with a slow sinusoidal variation in  $U_\infty$ , optimising in forcing amplitude only. The results of this are shown in figure 3.9.

The results indicate that the controller is able to adapt to the changing conditions well and with minimised disturbances. Over the first 50 s, the system converges to the optimal value of  $\sqrt{p_c^2} \approx 1000$  Pa, corresponding to  $U_\infty = 15$  ms<sup>-1</sup>. With varying velocity between 10 – 20 ms<sup>-1</sup>, the amplitude is seen to also vary between approximately 800 – 1600 Pa with a small lag. Adaptation is therefore larger in the positive direction than in the negative direction, possible indicative of nonlinearity in the mapping between  $\sqrt{p_c^2}$  and  $u_j$ . Regardless, the controller is here demonstrated to be able to adapt in both a positive and a negative direction.

While it is not possible to confirm that an optimal condition is maintained at all

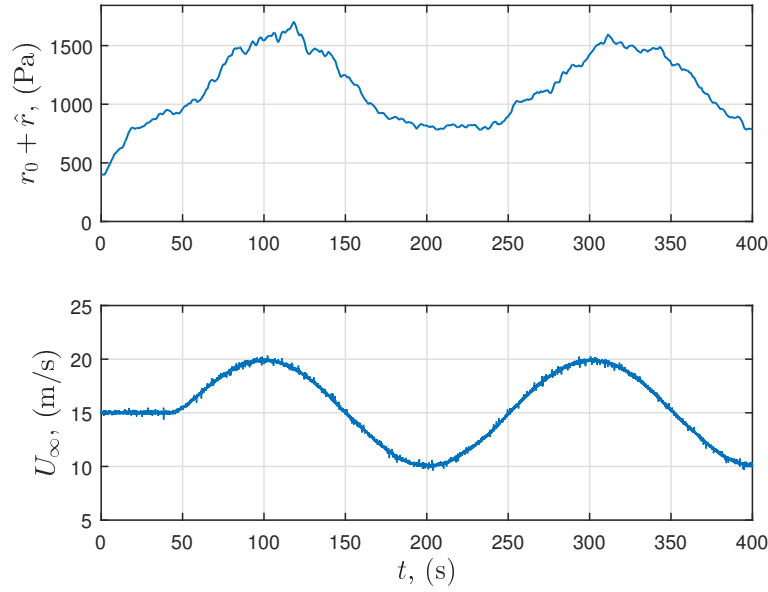


Figure 3.9: The response of the controller to a slow variation in the tunnel speed.

times, a strong adaptation is evident. While truly optimal adaptation must take place in frequency as well as amplitude, the results of shown in figure 3.8 indicate that the controller would be able to achieve this, provided that variations are sufficiently slow.

### 3.3 Concluding remarks

We have provided a heuristic analysis of the extremum seeking algorithm with a particular focus on flow control applications. Our analysis has demonstrated that the often used high-pass filter may be removed, and that the low-pass filter may be replaced with a moving average in order to optimally filter the perturbations resulting from demodulation. It has also been demonstrated that for the case where the reference parameter is the frequency of a harmonic input, implementation of a sinusoidal dither signal is problematic. In this case a step-wise dither signal can provide a suitable alternative, provided that the control adaptation  $\hat{r}$  is only updated when the step changes in the dither signal occur. This therefore provides a suitable ES method for a number of open-loop flow control applications involving a harmonic input.

Based on the analysis of the algorithm, a modified ES controller was implemented experimentally in order to demonstrate its efficacy. The controller was applied to the

open-loop control system of Oxlade *et al.* (2015), providing a closed-loop extension to the pre-existing system. Despite a noisy output signal perturbed by turbulent fluctuations, the controller is able to find optimum forcing configurations within around 30 – 40 s when operated on a single forcing variable and around 100 s when operated on two forcing variables. Furthermore the system is able to effectively filter the measured noise rather than passing it to the adaptation signal, and is therefore able to maintain a fairly steady output once convergence has taken place. The controller is also able to adapt to changing conditions, in this case free stream velocity, in real-time. While in this investigation the controller was implemented to seek maximum drag reduction, the system could just as easily be used to find an optimal condition for energy efficiency, as in Beaudoin *et al.* (2006).

In conclusion we have introduced a modified ES algorithm and demonstrated its efficacy in adjusting the open-loop forcing of a turbulent bluff body wake. We hope that the modified system proposed here will be of use for other flow control applications, particularly those involving a harmonic input signal.



# Chapter 4

## Observability of coherent structures

As summarised from chapter 1, a promising strategy for drag reduction involves the feedback control of large-scale coherent structures. However in order to achieve this from surface mounted pressure measurements it is important to understand the relationship between these structures and their pressure imprint. In control theory, the question of whether these structures (the *states* of the fluid flow system) may be deduced from the measurements is the question of *observability*. The development of an algorithm to perform this real-time deduction is the process of observer design. In this section, through the use of simultaneous PIV and pressure measurements, we aim to establish which features of the wake are observable and ultimately glean insight from this into the best approaches for their observation and control. A corollary of this effort will be an improved understanding of the link between velocity and pressure field features in three-dimensional wakes.

### 4.1 Background to the observability problem

We will begin this chapter with a brief overview of the observability problem in the context of linear state-space feedback control systems. While these linear methods are not directly applicable to the bluff body wake of this study, they still provide a useful context in which to perform the analysis.

In control theory, linear state-space methods provide a particular manner by which to describe a system for the purposes of feedback control design. The states  $x \in \mathbb{R}^n$

of a system are generally defined to be those quantities that provide information on the past of the system, and are sufficient to predict the evolution of the system into the future (see e.g. Åström & Murray, 2008, chapter 2 for an overview). In a fluid mechanics context there are essentially an infinite number of states since the unsteadily moving fluid is a continuum. Here we will therefore abuse the notation and use the term state simply to denote some of the key features of the velocity field. Given a choice of states and a linear system, the equations governing the time evolution of the system may be written as,

$$\dot{x} = Ax + Bu \quad (4.1a)$$

$$y = Cx + Du, \quad (4.1b)$$

where  $\dot{x}$  denotes the time derivative of the states,  $u \in \mathbb{R}^p$  are the inputs to the system and  $y \in \mathbb{R}^q$  are the outputs (i.e. the measurements). The matrices  $A$ ,  $B$ ,  $C$  and  $D$  define the dynamics and the relationships between input and output. For feedback purposes it is often desirable to know the states  $x$  in real-time, however these are generally different to what we can directly measure, the outputs  $y$ . The observability question is therefore can we deduce, in real-time, the states  $x$  from measurements  $y$ . For the linear state-space system described in (4.1), a general test for observability may be performed by examining the rank of the observability matrix, defined as

$$W_O = \begin{bmatrix} C \\ CA \\ CA^2 \\ \vdots \\ CA^{n-1} \end{bmatrix}. \quad (4.2)$$

If  $W_O$  is full rank (i.e. has rank  $n$ ) then the system is said to be *observable* (Åström & Murray, 2008, § 7.1) and in principle the states  $x$  may be deduced by measurement of the outputs  $y$  and inputs  $u$  over all previous times.

As displayed in (4.2) the observability matrix  $W_O$  is a function of the matrices  $A$  and  $C$ , describing respectively the dynamics of the system and the mapping between states and outputs. A special case of observability is that in which  $q \geq n$ , i.e. there are at least as many measurements as states and the measurement matrix  $C$  is of full rank. In this case the state to output mapping alone is sufficient to achieve observability, and the relationship between the outputs and states is given by

$$x = Ly - LDu, \quad (4.3)$$

where a left inverse of  $C$  exists because  $LC = I$ . For the case with no input  $u$ , (4.3) describes a method equivalent to the linear stochastic estimation (LSE) (Adrian, 1994), and is an example of a static estimation method. The alternative scenario, in which the rank of  $W_O$  is dependent upon the dynamics matrix  $A$ , requires dynamic estimation; a key method being the well-known Kalman filter (see e.g. Åström & Murray, 2008, § 7.4). In this work we will look principally at the application of static methods as a first examination of the observability problem. At the most basic level this will be an attempt to deduce the best pressure-based metrics for each velocity field feature, and to explain the various sources of the variance observed in the pressure measurements. We will not perform dynamic estimation here, as to do so we would need a good model for the dynamics of the velocity field features.

It is finally worth noting the implications to observability given by the concept of global modes (Huerre & Monkewitz, 1990; Chomaz, 2005). By definition, modes arising from an absolute instability are observable as these features contaminate the entire flow-field. The question is therefore not so much which feature may be detected, but what is the strength of this signal within the measurements. Generally speaking, locations in the flow field for which the global mode amplitude is large will be effective for measurement of the particular global mode. Examining the spatial structure of the global modes therefore provides a suitable method for choosing sensor location (Flinois & Morgans, 2016), and provides a method of heuristic observability analysis given pre-determined sensors. As we shall see below, while the global modes of the flow may determine the most energetic features of the velocity field, they will not necessarily dominate a given set of pressure measurements. Attention is therefore required beyond the global modes alone.

## 4.2 Acquisition configuration

In order to assess the link between velocity-field and surface pressure measurements we choose to take time-resolved PIV, synchronously with pressure measurements on the base. The experimental method is described fully in § 2.1.2, and provides simultaneous time-series from the 64 static pressure tappings alongside a rectangular region of the near-wake. The data are time-resolved at a frequency of 720 Hz and cover a time-period of 3.8 s.

At this point it is important to note that effective velocity-field measurement of the axisymmetric wake is complicated by the random reorientations of the SB mode.

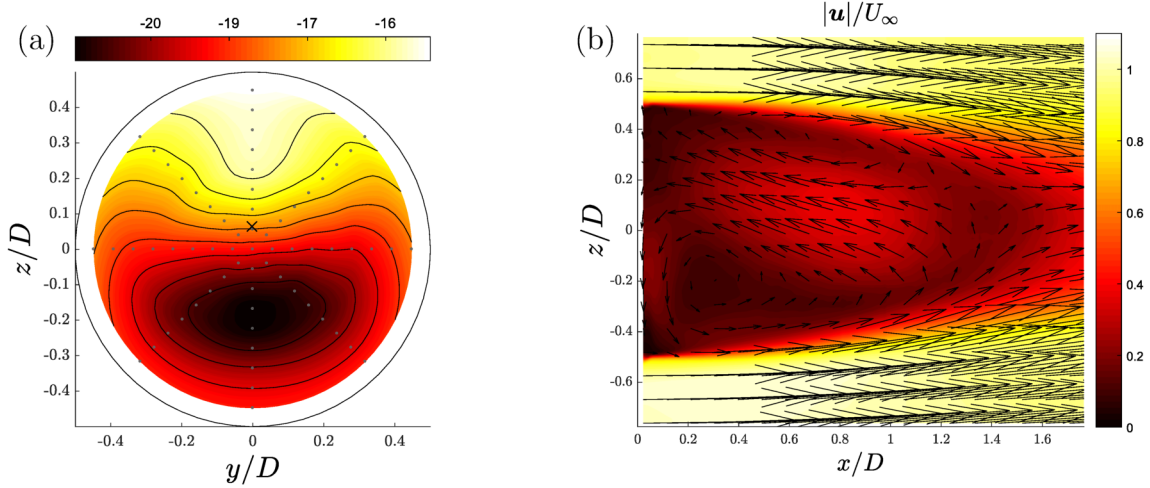


Figure 4.1: The time-averaged (a) pressure and (b) velocity fields over a given acquisition period.

Any measurements fixed at a particular azimuthal orientation with respect to the body, may therefore occupy any unknown orientation with respect to the SB wake structure. The PIV plane used here therefore gives only a slice through a non-axisymmetric structure, the relative orientation of which depends only on the particular instant in time.<sup>1</sup> The rate of reorientations of the SB structure is typically associated with a very small Strouhal number, meaning that for the body size  $D$  and chosen free-stream velocity  $U_\infty$  of our experiments, the SB mode may remain in approximately the same orientation for a few seconds at a time. The statistics of the reorientation process will be discussed further in § 6.2, but for now it is sufficient to note that we may choose to use measurements over periods of time in which the plane of the PIV intersects the SB mode in an approximately constant manner. One such example of the mean pressure and velocity fields over a 3.8 s time period is displayed in figure 4.1.

The mean fields displayed in figure 4.1 give some initial insight into the structure of the SB mode and the link between the velocity field and base pressure. The velocity field slice demonstrates a qualitatively similar structure to that observed through a horizontal slice of the Ahmed body wake by e.g. Grandemange *et al.* (2013c); Volpe *et al.* (2015), among others. This structure consists of an approximately circular vortex, seen here at  $(x, z) \approx (0.3D, -0.2D)$  and an asymmetric recirculating flow that impinges on the base away from the body centreline. The asymmetry leads to varying shear layer strength, with the greater cross-stream velocity gradient observed

<sup>1</sup>Provided that the body is well aligned with the flow and there are no other significant non-axisymmetric perturbations.

on the opposite side to the vortex. The distribution of the base pressure is seen to be consistent with the velocity field. The relatively high pressure observed at  $(y, z) \approx (0, 0.3D)$  coincides with the impinging jet from the recirculating flow, while the low pressure region at  $(y, z) \approx (0, -0.2D)$  coincides with the location of the circular vortex.

### 4.3 Choice of velocity-field features

The key question that this chapter attempts to answer is which features of the velocity field may be observed, or put another way, which features dominate the pressure measurements. It is therefore first necessary to identify and quantify some key velocity-field features for subsequent analysis. We will present here three such features which are either of interest for feedback control or will later be shown to have a strong pressure imprint.

A first obvious method for choosing velocity field features is to find those which contain the greatest fluctuating energy. This may be achieved using the proper orthogonal decomposition (POD), applied to the PIV snapshots of the wake as described in § 2.4.2. After the mean, the first two fluctuating POD modes are found to capture the asymmetric vortex shedding, which is of particular interest for control due to the anticipated link with pressure drag. The first of these POD modes is displayed in terms of velocity magnitude  $\mathbf{u}$  in figure 4.2, along with the PSD of the temporal coefficient  $a_1$ . The structure of the mode indicates the strong asymmetry in the vortex shedding, arising from the particular orientation of the SB mode which is as displayed in figure 4.1. The largest fluctuations are concentrated in the upper shear layer in which the mean shear is also larger, possibly corresponding to the one-sided vortex hoops proposed by Vilaplana *et al.* (2013) for the wake of the sphere. The PSD confirms the oscillatory nature of the shedding, showing a strong peak for  $St_D \approx 0.22$ . The second POD mode, not shown here, is essentially the complement to the first, consisting of a similar structure displaced slightly downstream. These two spatial structures together capture the convective nature of the vortex shedding, however for the purposes of estimation we need only look to estimate one, as the two modes generally change together in time with a  $\pi/2$  temporal phase difference. We therefore choose the first velocity field state  $x_1$  to be the temporal coefficient of the first POD mode alone.

After the first two POD modes capturing the vortex shedding, the remaining modes

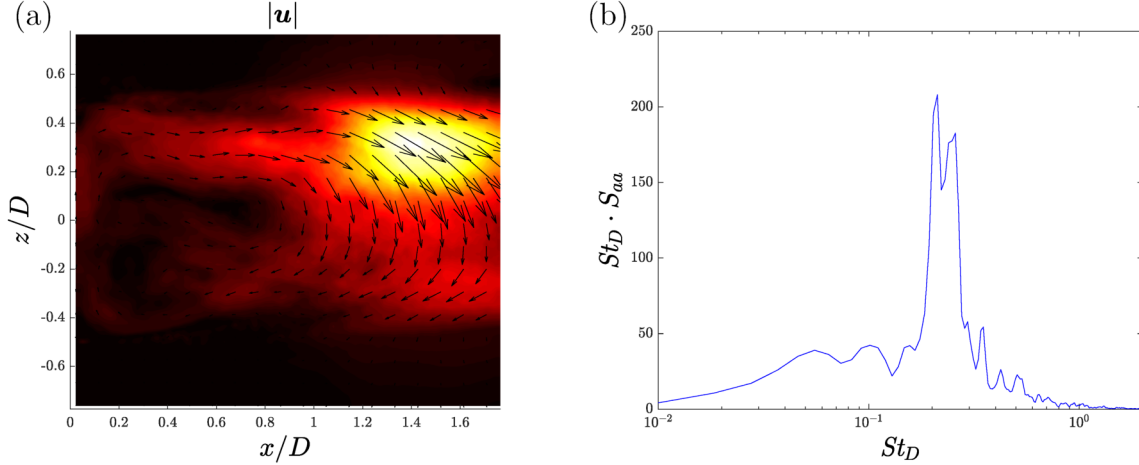


Figure 4.2: The most energetic velocity field POD mode  $\phi_{u1}$ , (a) displayed in terms of the velocity magnitude  $\mathbf{u}$  and (b) the pre-multiplied PSD of the modal coefficient. The modal coefficient  $a_1$  is chosen as the first velocity-field state  $x_1$ .

capture only smaller-scale features with higher spatial wave numbers. In particular, none of the POD modes appear to capture any variation within the recirculation bubble where the SB mode is most visible. We therefore seek another metric to quantify this feature. Based on the mean field shown in figure 4.1(b), we can see that the SB mode consists of an asymmetric recirculation within the separation bubble. We therefore choose to quantify this by a line integral evaluated as:

$$\Gamma = \oint \mathbf{u} \cdot d\mathbf{l}, \quad (4.4)$$

where the line over which the integral is evaluated is as displayed in figure 4.3. By Stokes' theorem<sup>2</sup>, this integral acts as an approximation to the circulation within this area of the flow and therefore should give a measure of the circulation asymmetry typical of the SB mode. This metric  $\Gamma$  is therefore chosen as the second velocity-field state,  $x_2$ .

An additional feature commonly reported in the literature for 3D bluff body wakes is the “bubble pumping”, observed in both axisymmetric (Berger *et al.*, 1990; Oxlade, 2013) and rectilinear (Volpe *et al.*, 2015) wakes. This consists of a quasi-random pulsation of the recirculation bubble and is known to be measurable at the body base. Here we aim to quantify the bubble pumping by estimating the instantaneous location of the rear stagnation point in the flow. Since it is difficult to define a unique

<sup>2</sup>Stokes' theorem is not technically valid here as the 2D region of interest is not a closed region of the flow, since there will be some non-zero through-plane velocity component.



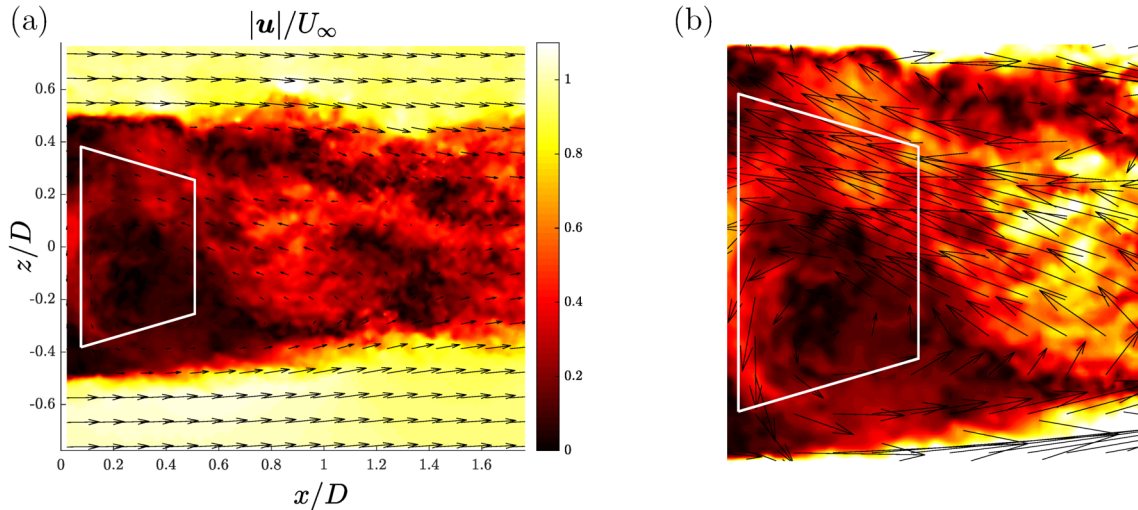


Figure 4.3: Illustration of the region defining the recirculation metric  $\Gamma$ , chosen as the velocity-field state  $x_2$ .

stagnation point in a turbulent flow we must instead find a heuristic method that approximates the length of the recirculating region. We do this by estimating the first stream-wise location at which there is no longer a coherent region of reversed flow. The precise details of this process are given in appendix D.1, and while the method naturally employs an arbitrary definition for the bubble length, we found it to qualitatively select the correct location. An illustration of a typical snapshot along with the selected bubble length is displayed in figure 4.4. This stream-wise location for the end of the separation bubble is chosen as the third state variable  $x_3$ .

## 4.4 Decompositions of base pressure data

The base pressure data consist of 64 pressure tapings distributed over the base, yet from these 64 measurements we wish to deduce only a handful of key velocity-field metrics. Given a static estimator  $x = Ly$ , the problem is overdetermined and must be solved in a best fit sense (e.g. through least squares). Methods such as the linear stochastic estimation (LSE) follow exactly this approach (see e.g. Tu *et al.*, 2013, for an overview), giving in a least-squares sense an optimal mapping between pressure measurements and velocity metrics. The downside of this method is that the mapping matrix  $L$  may not necessarily give physical insight into the links between pressure and velocity and, through the provision of an excessive number of inputs, be prone to over-fitting. An alternative is to reduce the dimension of

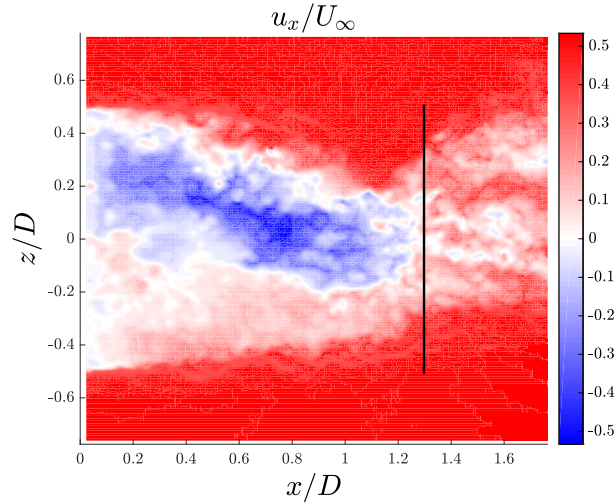


Figure 4.4: Illustration of velocity field metric  $x_s$  used for velocity-field state  $x_3$ , showing the selected location for a particular velocity field snapshot.

the measurement space first and then examine the correlations. We will follow this approach here.

Just as for the velocity field data, a first natural method for dimensional reduction is the use of the POD (see § 2.4.2). For the case of base pressure we have the advantage that we have available data from much longer time-series on which to perform the POD. A key consideration though, is that while for the simultaneous data used in this study we have only short time periods in which the SB mode orientation is approximately constant, over longer time-periods this orientation explores all possible angles  $0 \leq \phi < 2\pi$ . We therefore perform a conditional POD, following the approach of Rigas *et al.* (2014) by choosing snapshots in which the CoP orientation  $\phi$  is within a narrow range corresponding to that for the simultaneous data. The first four modes resulting from the POD are displayed in figure 4.5.

The first POD mode  $\phi_{p0}$  displayed in figure 4.5 is the ensemble mean of the snapshots and is very similar to the temporal mean over the short time window displayed in figure 4.1(a)<sup>3</sup>. This mean displays the average measurement of the SB mode given a particular azimuthal orientation. The second POD mode has the same reflectional symmetry axis as the first, and describes a modification to the magnitude of the asymmetry that is seen on average. The next POD mode is antisymmetric about the symmetry axis of the first two and is able to describe modifications to the symmetry observed on average. The fourth mode displayed here has the same symmetry axis

<sup>3</sup>This mode is actually the negative of the mean, simply implying that the modal coefficient is also negative.



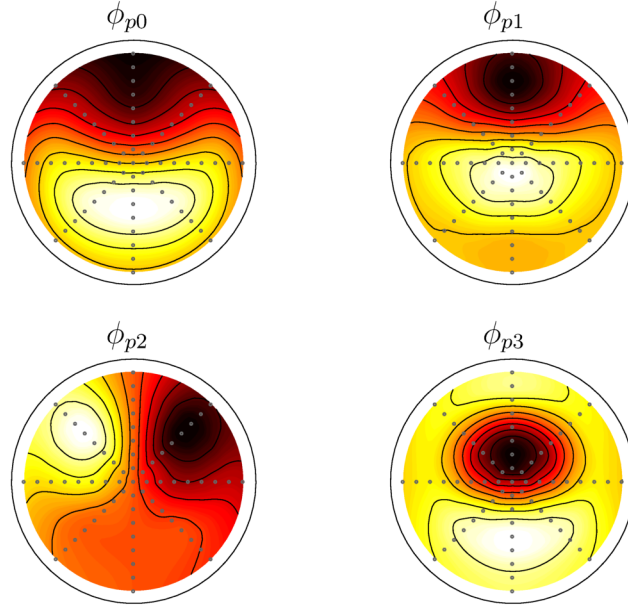


Figure 4.5: The base pressure POD modes in a rotating frame of reference.

as the first and second and describes further modifications to the spatial structure of the mode.

In addition to the POD modes we can define other pressure metrics with physical significance. The first is the spatial-mean evaluated as,

$$\langle p \rangle = \frac{1}{A} \sum_i p_i \rho_i \delta_\rho \delta_\phi, \quad (4.5)$$

where  $A$  is the area over the base,  $\rho_i$  is the radius of the  $i$ 'th pressure tapping  $\delta_\rho = 0.011$  m and  $\delta_\phi = \pi/4$ , these parameters reflecting the spatial location of the tappings on the base. The spatial mean provides a measure of the pressure force on the base of the body and its projection onto the instantaneous data describes fluctuations operating on all pressure measurements simultaneously. The second physically motivated pressure measurement we will use is the CoP radius  $\rho$ , as used in previous studies (e.g. Rigas *et al.*, 2014; Volpe *et al.*, 2015). The CoP location  $\mathbf{X} = (Y, Z)$  is defined by,

$$\mathbf{X} = \frac{1}{\langle p \rangle} \sum_i p_i \rho_i \delta_\rho \delta_\phi (y_i, z_i), \quad (4.6)$$

where  $y_i, z_i$  are the lateral and vertical coordinates of the  $i$ 'th pressure tapping. The CoP radius may then be computed as  $\rho = \sqrt{Y^2 + Z^2}$  and gives a measure of the magnitude of the asymmetry in the base pressure imprint.

## 4.5 Correlations

In order to assess the correlations between velocity and pressure-field metrics, we shall simply examine the normalised temporal cross-correlation. For two time series of the state and measurement  $x_i, y_i$  this is evaluated as,

$$R_{x_i y_i}(\tau) = \frac{\langle (x_i(t) - \bar{x}_i)(y_i(t - \tau) - \bar{y}_i) \rangle}{\sigma_{x_i} \sigma_{y_i}}, \quad (4.7)$$

where  $\bar{\cdot}$  denotes the temporal mean and  $\sigma$  the standard deviation. While a fairly simple metric, the temporal-cross-correlation will give us a good idea of the link between variables including any time delay, and yields the possibility of using time-delayed LSE as a static estimation method. We will present the cross-correlation analysis for each of the three velocity field states  $x_i$ , with the pressure metric giving the maximum values of  $R_{x_i y_i}(\tau)$ .

Examining first the state describing the vortex shedding mode, we find that the best cross-correlation is achieved using the CoP radius  $\rho$ . The results for which are displayed in figure 4.6. The time-series in the upper figure demonstrate the oscillatory nature of the first POD mode, although clearly the oscillations are somewhat irregular. By contrast the CoP radius  $\rho$  does not obviously demonstrate the same oscillatory behaviour, although it does appear to follow some of the lower frequency trends in the time-series. The cross-correlation is seen to peak to just less than 0.5 at a small lag  $\tau \approx 0.04$  s, indicating that there is a clear link between the two variables, but that one value may only account for half the variance of the other. The lag  $\tau$  is of the order  $1/f_{VS}$  so most likely corresponds to a particular phase relationship between  $\rho$  and  $a_{u1}$ .

If we look now at the velocity metric  $\Gamma$ , we find that the best cross-correlation may be found with the second pressure POD mode coefficient  $a_{p2}$ . The normalised time series and cross-correlation for these variables is shown in figure 4.7 and demonstrates greater coherence than for the case of the vortex shedding: the cross-correlation in this case peaking at around 0.75 close to  $\tau = 0$  s. Neither time-series appears to oscillate at any particular frequency, but both can be seen to move together fairly closely. The physical interpretation of this is that fluctuations in the strength of the asymmetry in the recirculation region, as approximated by  $\Gamma$ , have a strong influence on the asymmetry in the pressure measurements.

Examining the last of the velocity-field metrics  $x_s$ , we find that the strongest correlation may be found with the spatially-averaged pressure  $\langle p \rangle$ , the information for

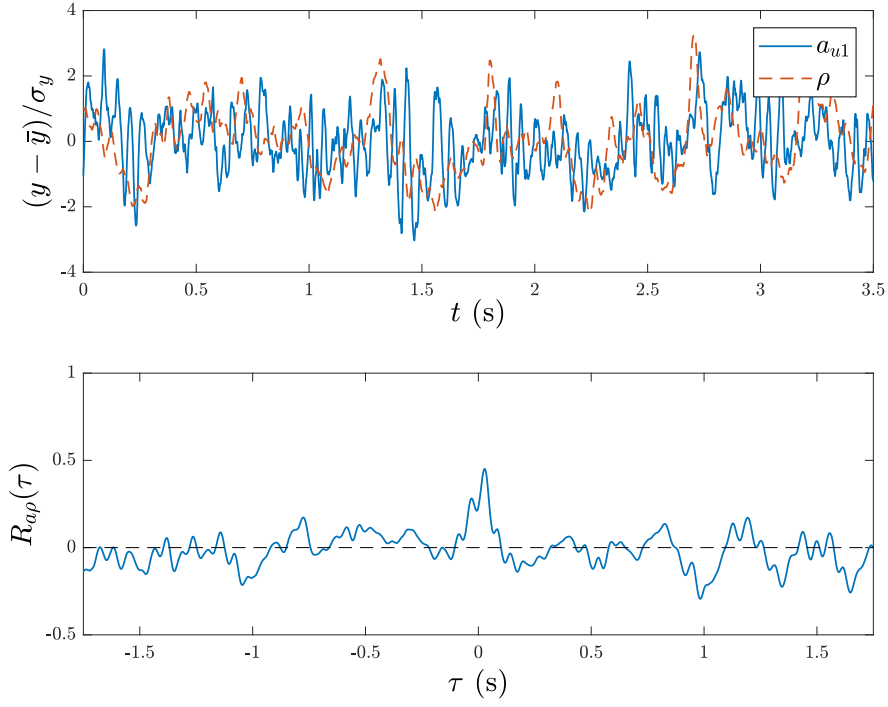


Figure 4.6: Simultaneous time-series and normalised cross-correlation between first velocity POD mode coefficient  $a_{u1}$  and CoP radius  $\rho$ .

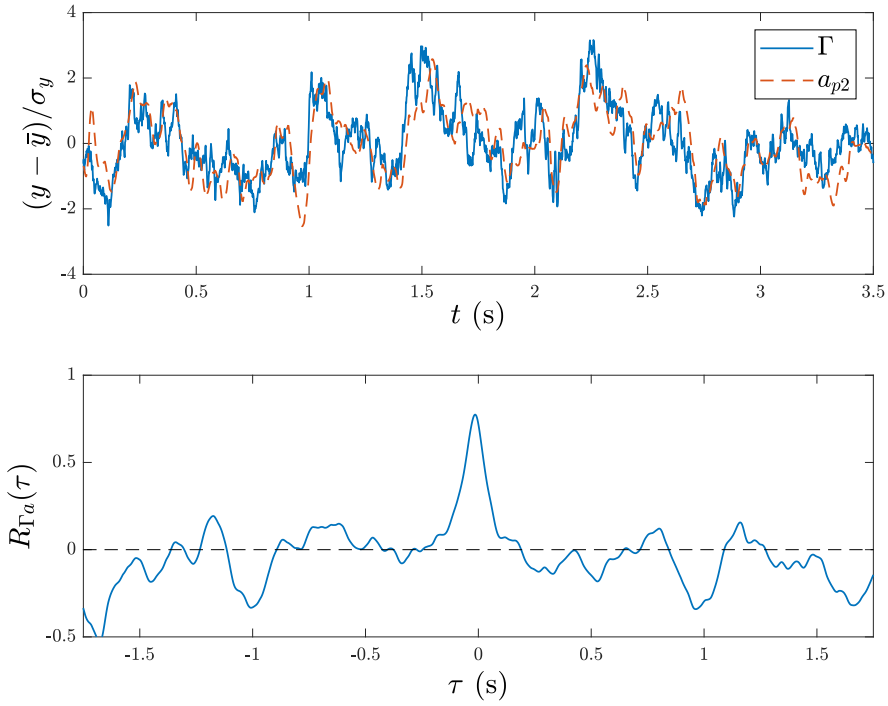


Figure 4.7: Simultaneous time-series and normalised cross-correlation between the near base circulation  $\Gamma$  and the second pressure POD mode coefficient  $a_{p2}$ .

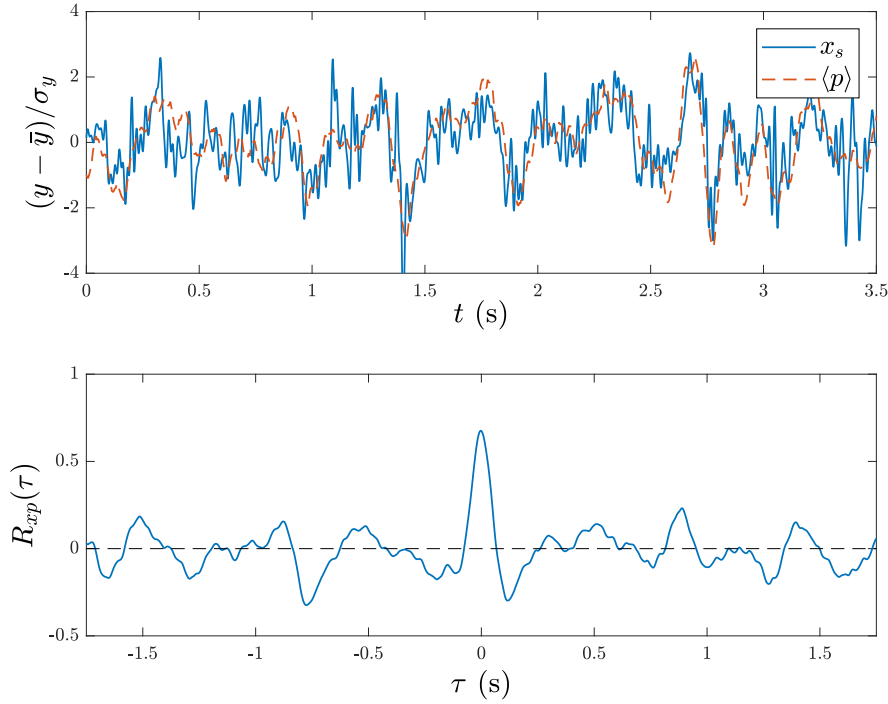


Figure 4.8: Simultaneous time-series and normalised cross-correlation between stagnation point location  $x_s$  and spatially averaged base pressure  $\langle p \rangle$ .

which is displayed in figure 4.8. As for the case of the near base circulation, the time-series exhibit no obvious pattern but are clearly strongly correlated, as confirmed by the peak cross-correlation of 0.7. The link between the time-averaged recirculation region length and pressure drag is well documented (see e.g. Roshko, 1993), and may be explained in terms of the pressure gradients associated with the streamline curvature. It is interesting to find that the same relationship holds for fluctuations and that variation in the recirculation bubble length accounts for a large fraction of the spatially uniform pressure changes.

## 4.6 Discussion and conclusions

The results presented in this section indicate that for three-dimensional wakes, the link between pressure and velocity field features may not be obvious *a priori*. For two-dimensional wakes the vortex shedding is both the dominant global mode of the wake and a dominant source of pressure fluctuations at the base. This has allowed a number of studies to use base pressure as a suitable measurement for feedback control (Pastoor *et al.*, 2008; Flinois & Morgans, 2016). For the axisymmetric wake of this

study, application of POD indicated that the vortex shedding was again a dominant source of coherent velocity fluctuations, but that it had a relatively weak pressure imprint. The pressure measurements were instead dominated by fluctuations in the spatially-averaged pressure, driven by fluctuations of the recirculation bubble length, and variation of the strength and orientation of the SB mode.

One implication of these results is that the relationship between base pressure fluctuations and velocity-field features is much more dependant on the spatial structure of those features than on their energy content. For the wake of a wide range of two-dimensional bodies, the von Kármán vortex street is both dominant in energy and is coherent very close to the body base. By contrast for three-dimensional wakes, the SB mode is the dominant structure close to the base. It makes sense that those flow structures immediately proximate to the base are able to influence the pressure to a much greater extent through direct impingement or adjacent streamline curvature. By contrast flow structures further away most likely communicate pressure changes acoustically, and therefore necessarily to a much smaller extent.

From the linear state-space perspective described at the beginning of § 4.1, the challenge associated with the application of purely static observation methods is that they rely on each state having a unique, i.e. orthogonal, imprint on the measurements. We find this not to be the case for the particular velocity states  $x$  chosen. For example the CoP measurement, while giving the best correlation with the vortex shedding, was found to be influenced by both the mean pressure (this is in fact part of the definition of the CoP) and the SB strength. This may partially be seen by examining the pre-multiplied PSD of the CoP radius  $\rho$  evaluated from a long time-series, as displayed in figure 4.9. The spatial structure of the base pressure measurement associated with the vortex shedding is therefore not unique, so the vortex shedding may not be uniquely identified by static methods alone. Having said this, it is worth noting that the frequency content of the vortex shedding is uniquely identifiable. This is demonstrated by the fairly sharp peak at  $St_D \approx 0.22$ , in an otherwise broadband frequency spectrum, consistent with the frequency seen in the PSD of figure 4.2(b). This motivates either the use of dynamic-observers that leverage knowledge of the expected frequency content as used by Tu *et al.* (2013), or the use of controllers that aim to target specific frequency ranges via a sensitivity function approach (e.g. Dahan *et al.*, 2012). Real-time control of the vortex shedding should therefore still be possible, although it is clearly more challenging than for the case of the more straightforward observation seen in some two-dimensional wakes.

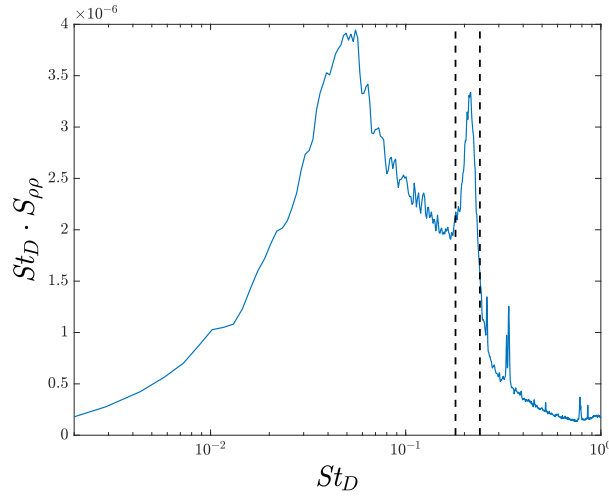


Figure 4.9: Premultiplied PSD for the CoP radius  $\rho$ . The black dashed lines approximately demarcate the frequency range of the vortex shedding.

The analysis presented in this section is by no means exhaustive, nor does it offer truly optimal links between velocity and pressure metrics, however it does provide useful insight towards feedback control methods. Firstly, it is clear that the SB mode has an extremely strong imprint on the base pressure, suggesting that through the correct choice of pressure metric the magnitude of the SB mode may be straightforwardly measured in real-time. The second key feature of interest for control, the vortex shedding, is less straightforwardly observed due to a much weaker, and spatially non-unique, measurement signal. However the characteristic frequency content, as displayed in figure 4.9, indicates that the use of frequency targeted control strategies could still be effective. Feedback controllers for each of these features in the Ahmed body wake will be the topic of chapter 7.

# Chapter 5

## Open-loop control with flaps

In this section we present the results of open-loop forcing of the Ahmed body wake with flaps located at the rear edges. The forcing presented here consists of two types, harmonic forcing whereby the flaps are oscillated sinusoidally, and static forcing with the lateral flaps where we investigate the effect of “ruddering” and “boat-tailing” when the flow is at a range of yaw angles. In both cases, forcing of the wake may allow a more detailed investigation of the flow physics, beyond that which can be achieved by observation of the natural wake alone. This may include a firmer understanding of the nature of key wake features such as the vortex shedding and the conditions for drag reduction.

All forcing of the wake presented in this chapter will consist of two flaps at a time, located either at the sides or at the upper and lower surfaces. This forcing is described by the angles of the two flaps, respectively  $\theta_1$  and  $\theta_2$ , both defined in a positive manner when the flap is moved inwards towards the base of the body. This forcing can instead be written in terms of a symmetric and anti-symmetric component, here referred to as boat-tailing and ruddering. Henceforth, the two angles defining this decomposition are as follows:

$$\theta_B = (\theta_1 + \theta_2)/2, \tag{5.1a}$$

$$\theta_R = (\theta_2 - \theta_1)/2. \tag{5.1b}$$

## 5.1 Harmonic forcing

The harmonic forcing discussed in this section is performed in an anti-symmetric manner and therefore consists of pure ruddering  $\theta_R$ . Symmetric forcing with four flaps was also performed at a preliminary stage, with the aim of direct drag reduction (see appendix A). However this was not found to be successful so we therefore instead choose to focus on anti-symmetric forcing with two flaps at a time. This form of forcing may be expected to interact directly with the anti-symmetric features of the wake. Namely, the vortex shedding and the SB mode which, depending on conditions, may arise in either a left/right (lateral) or top/down (vertical) sense (Grandemange *et al.*, 2013b). Forcing will allow additional insight into the dynamics of these features.

### 5.1.1 Frequency response

For each of the anti-symmetric forcing cases we may first look at the frequency response between the forcing  $\theta_R$  and the relevant pressure metric  $m_l$ ,  $m_v$  from the 64 ESP tappings. These pressure metrics quantify the anti-symmetric pressure imprint on the base of the body and are evaluated as described in § 2.2.2. The frequency response examines how the magnitude and phase of this measured imprint varies with frequency and is evaluated as described in § 2.4.1.

Figure 5.1 displays the lateral frequency response and drag change for a range of lateral forcing amplitudes. While there is variation between amplitudes, all responses show the same general trends. At low frequencies  $St_H \lesssim 0.05$ , the amplitude of the response is relatively flat while the phase angle decreases very gradually. We would expect that at these low frequencies the flaps may induce repeated reversals of the wake between the two asymmetric configurations arising from the SB mode. Figure 5.2 confirms this interpretation, showing that the phase-averaged response at low frequencies, here displayed for an amplitude of  $7.5^\circ$ , consists of a repeated switching between equal and opposite values of the pressure metric  $m_l$ . This interpretation is also consistent with the variation of the frequency response with forcing amplitude: for low frequencies, smaller amplitudes have a larger measured response because when repeatedly switching between the two bistable configurations, the measured response will have an approximately constant amplitude regardless of the amplitude of the forcing. Over this range of forcing frequencies the drag is seen to increase by up to a maximum of 7 %, suggesting that repeated reversals of the wake has only a



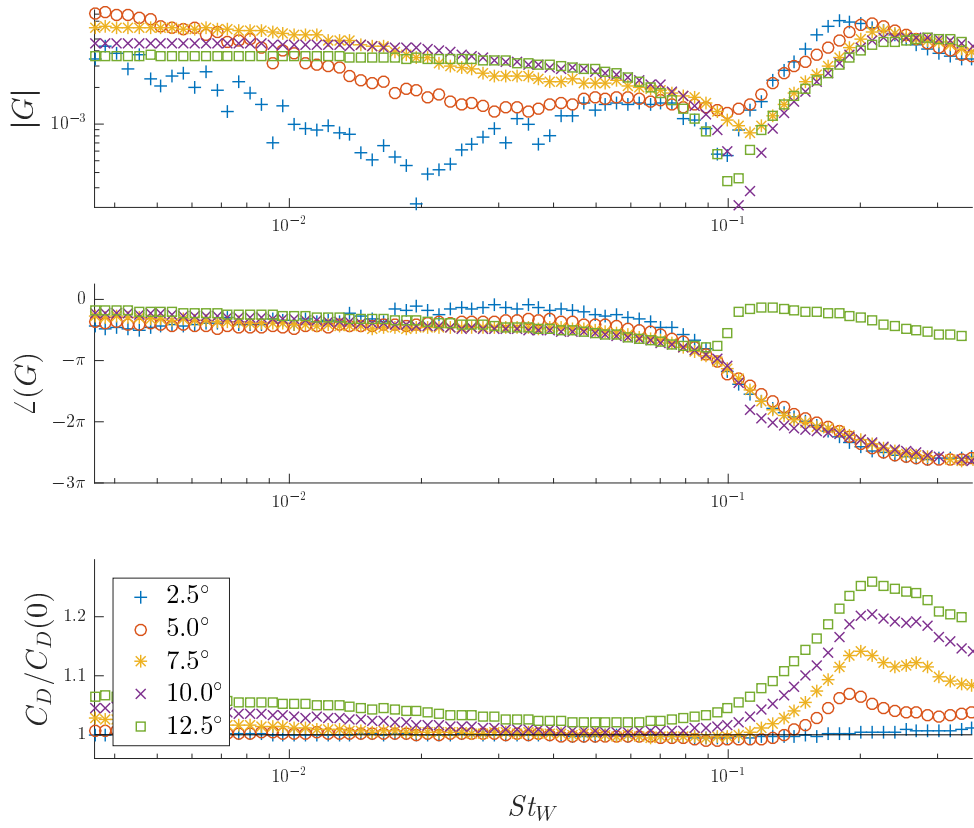


Figure 5.1: Effect of lateral anti-symmetric forcing. Plots show the frequency response (upper, middle) and average drag change (lower), as a function of forcing frequency  $St_W$  and for varying forcing amplitudes.

modest influence on the drag.

The next key feature in the frequency responses is seen at  $St_W \approx 0.1$  and is a sharp trough in the magnitude of the response, accompanied by a rapid decrease in phase angle for all but the largest amplitude forcing. For a linear system this particular combination of behaviour in magnitude and phase corresponds to the presence of right-half-plane zeros, and is often caused by a cancellation between dynamics operating at different time scales (Skogestad & Postlethwaite, 2005). It is important to note that this does not coincide with any particular response of the drag at the same frequency. It is therefore likely to be a result of cancellation between the measurement of different flow features, rather than the result of any specific flow phenomenon. This will be discussed further in chapter 7.

For  $St_W \gtrsim 0.1$  the amplitude of the responses is seen to increase rapidly, rising to

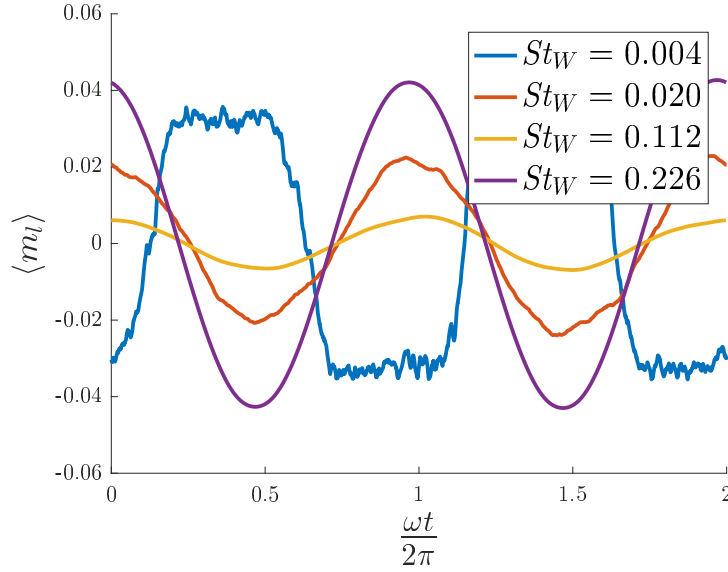


Figure 5.2: Phase-averaged response of the lateral pressure metric to lateral forcing, for a number of key forcing frequencies. Data are displayed for a speed of  $15 \text{ ms}^{-1}$  and forcing amplitude of  $7.5^\circ$ .

a peak at  $St_W \approx 0.2$ . This is seen to coincide with large increases in the drag of up to 28 % and is consistent with a strong amplification of the vortex shedding in the wake. Similar behaviour has recently been seen for three-dimensional wakes by Barros *et al.* (2016a), confirming that even if the vortex shedding has a weak pressure imprint for the case of the unforced flow, under harmonic forcing it may again become dominant and have a strong impact on the aerodynamic forces.

Figure 5.3 displays similar results for the case of vertical forcing, i.e. forcing with the top and bottom flaps. The general shape of both the frequency response and drag change is seen to be the same, but with a few key differences. At low frequencies the response is seen to be more uniform across amplitudes and generally has a smaller (negative) phase angle, as compared with the lateral forcing case. The phase-averaged response displayed in figure 5.4 suggests that the induced oscillations are more sinusoidal in nature and of smaller amplitude. This may be because the unforced wake is not bistable in the vertical dimension, therefore while vertical forcing still has a strong and measurable impact on the pressure, the effect is one of continuous deflection of the recirculation bubble, rather than the induced reversals that occurs in the lateral dimension. As for the lateral case, the total drag changes in this frequency range are again small, up to a maximum of 7 %.

At  $St_H \approx 0.09$ , the frequency responses again show a relatively sharp trough and phase angle decrease consistent with right-half-plane zeros. Above this frequency,

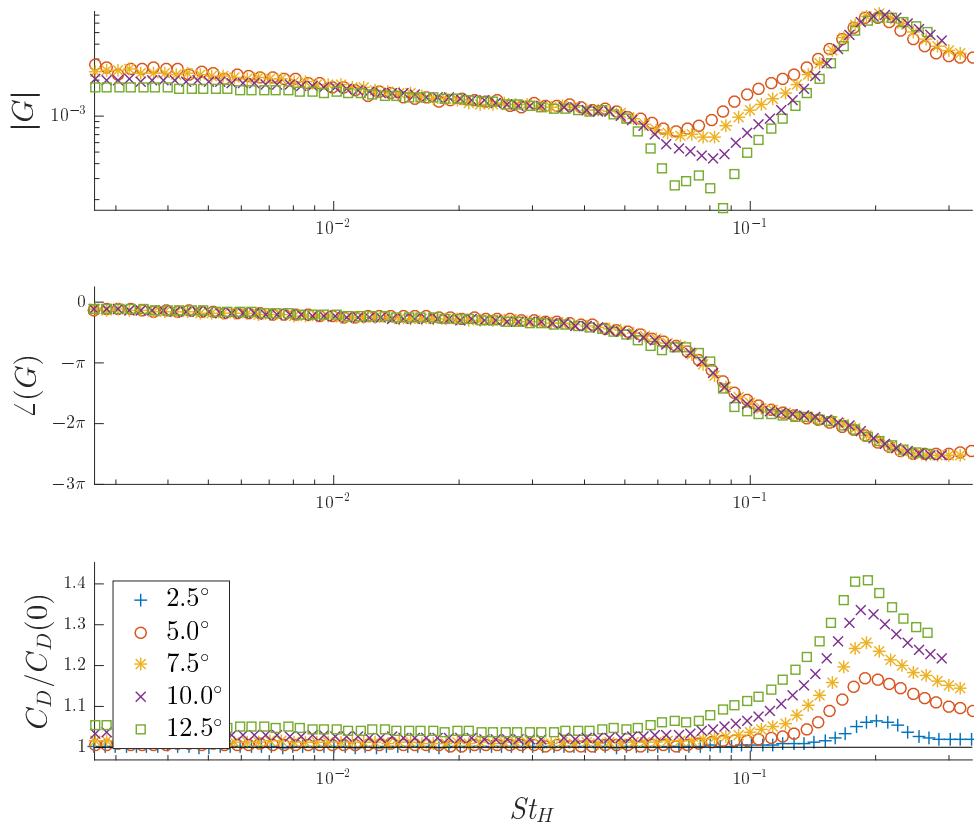


Figure 5.3: Effect of vertical anti-symmetric forcing. Plots show the frequency response (upper, middle) and average drag change (lower), as a function of forcing frequency  $St_H$  and for varying forcing amplitudes.

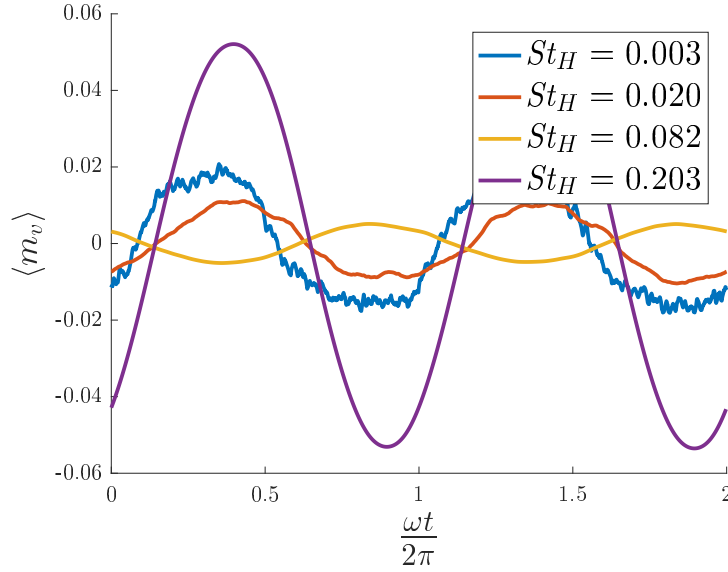


Figure 5.4: Phase-averaged response of the vertical pressure metric to vertical forcing, for a number of key forcing frequencies. Data are displayed for a speed of  $15 \text{ ms}^{-1}$  and forcing amplitude of  $7.5^\circ$ .

the response is almost identical to the lateral case, displaying a strong amplification of the vortex shedding for  $St_H \approx 0.2$ . In the vertical case both the measured response and drag change are larger, as displayed in figures 5.3, 5.4. Given that the body is wider than it is tall (see figure 2.2), this stronger interaction with the vortex shedding may be both because the flaps themselves are larger, and the shear layers are closer allowing for more intense interaction and a stronger shedding behaviour.

It is also worth noting that for the case of lateral forcing only, small open-loop drag reductions are observed. Drag reductions of up to 1% are observed for a range of intermediate frequencies  $0.03 \gtrsim St_W \lesssim 0.13$  and for small forcing amplitudes of  $5^\circ$ . This drag reduction is accompanied by a base pressure increases (not shown) of up to 1.7%. The reason for this open-loop drag reduction is unclear but it is interesting to note that it occurs only in the lateral dimension and therefore may be related to forcing of the bistability of the wake.

### 5.1.2 The forced flow

In addition to examining trends of particular variables as a function of forcing frequency, we may also look at the nature of the flow at particular forcing frequencies, as quantified by the metrics  $m_l$ ,  $m_v$  defined in § 2.2.2. While the dominant effect of either lateral or vertical forcing is on the response in the forcing dimension, there

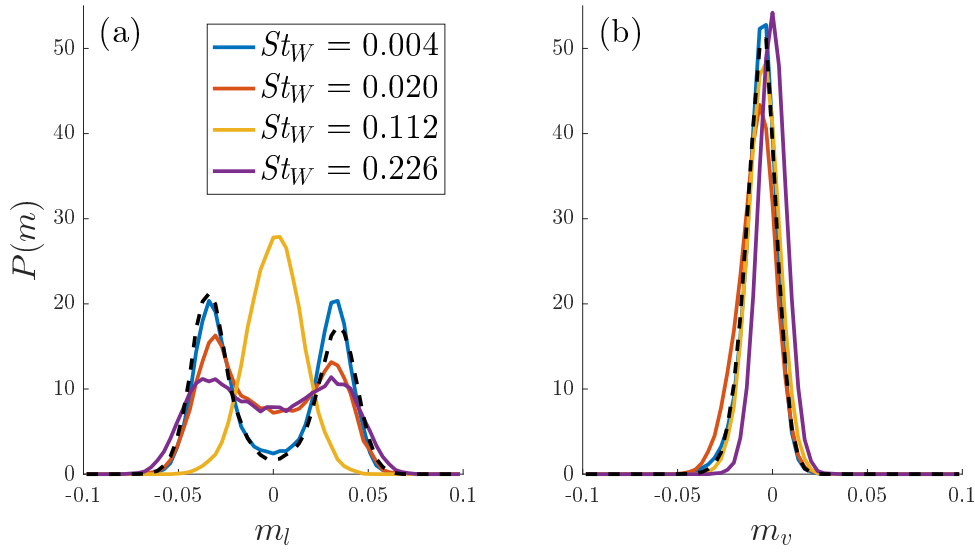


Figure 5.5: Effect of lateral anti-symmetric forcing on the distributions of vertical and lateral pressure metrics, compared with the unforced case given by the black dashed line. Data are displayed for a speed of  $15 \text{ ms}^{-1}$  and forcing amplitude of  $7.5^\circ$ .

may also be an impact on the dynamics operating in the perpendicular dimension. These could either be due to global changes to the flow or due to a coupling between perpendicular dynamics. A good way to examine this is to look at the PDF of each of the pressure metrics for a number of particular forcing frequencies. These results are displayed in figures 5.5, 5.6.

Firstly examining the effect of lateral forcing, figure 5.5 shows that for the lowest forcing frequency there is very little change to the PDF of either pressure metric. This is consistent with the idea that low-frequency lateral forcing simply induces switching between the two asymmetric flow structures that naturally occur. As the forcing frequency is increased to  $St_W = 0.02$  the PDF demonstrates that  $m_l$  is nearer to zero more of the time, consistent with an increased switching rate. A marked change is seen for forcing near to the trough of the frequency response, for  $St_W = 0.112$  the metric no longer displays bistable behaviour but has a PDF peaking at  $m_l = 0$ . This may be because the bistability of the wake is either suppressed or no longer detectable from the base pressure due to cancellation effects. Given that there is little drag change at this frequency it seems unlikely that complete suppression of the SB mode is achieved, although it is not possible to know for certain from base pressure and force data alone. For the higher forcing frequency corresponding to amplification of the vortex shedding the PDF appears bi-modal again, although for

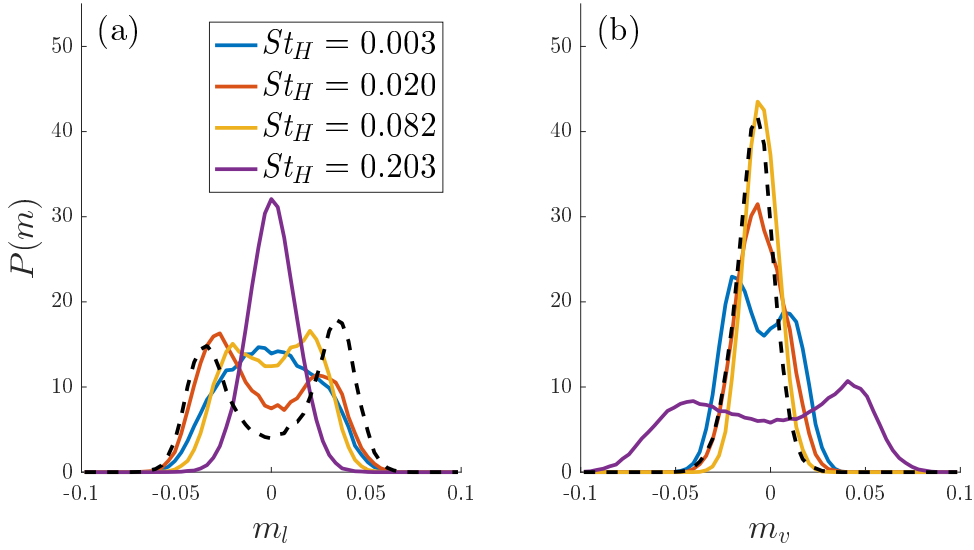


Figure 5.6: Effect of vertical anti-symmetric forcing on the distributions of lateral and vertical pressure metrics, compared with the unforced case given by the black dashed line. Data are displayed for a speed of  $15 \text{ ms}^{-1}$  and forcing amplitude of  $7.5^\circ$ .

this frequency this is most likely not indicative of a bistable wake. It is only for this final forcing case that there is significant evidence of coupling between the lateral and vertical dynamics: the PDF for  $m_v$  is seen now to become both more symmetric and with less variance, exhibiting a sharp peak at  $m_v = 0$ .

In contrast to the lateral forcing case, figure 5.6 demonstrates that the vertical forcing has a strong impact on the PDF of both pressure metrics. For the lowest frequency the lateral metric  $m_l$  appears no longer to be bimodal, but rather has a broad range of values peaking at  $m_l = 0$ . At this same frequency the vertical metric  $m_v$  does appear bimodal, although this may be a result of the sinusoidal nature of the forcing: the PDF of a sinusoid exhibits a particular bimodal behaviour. As the forcing frequency is increased, a bimodality of the lateral pressure metric is restored, though never to the extent of the unforced flow, while the PDF for  $m_v$  becomes increasingly narrow. For the resonant case of  $St_H = 0.203$ , the PDF for  $m_v$  is wide and bimodal, consistent with the large sinusoidal response displayed in figure 5.4, while that for  $m_l$  is relatively narrow and centred at  $m_l = 0$ .

### 5.1.3 Discussion and concluding remarks

The harmonically forced flaps demonstrate influence over two key features of the flow. At low frequencies lateral forcing simply induces reversals of the wake between the two bistable configurations, having negligible influence on the vertical metric and a small influence on the drag. Vertical forcing has a similar influence on the drag but appears to generate a larger change in the wake structure, possibly changing the dimension in which the SB mode dominates. At much higher frequencies around  $St \approx 0.2$  both lateral and vertical forcing generates a strong response and large drag increase, consistent with a resonance of the oscillatory vortex shedding in the wake. In these cases the variance of the pressure metric in the opposite dimension is minimised, suggesting that the SB modes of the wake are completely suppressed. Such resonant behaviour has been observed before in 3D wakes (Barros *et al.*, 2016a; Rigas *et al.*, 2017), yet it is interesting that despite the weak nature of the oscillatory modes in the unforced measurements, under forced conditions these oscillatory features can again become dominant. This may be indicative of a transition between a 3D and quasi-2D flow, much like the transition with aspect ratio seen by Norberg (1994).

The other key feature of both the lateral and vertical forcing is behaviour indicative of right-half-plane zeros at an intermediate frequency of  $St \approx 0.1$ . It is important to note that no particular changes in the drag are observed around this frequency in either case and it is therefore likely to be a limitation of the available measurements, rather than indicative of a particular fluid mechanical feature. As we shall discuss in chapter 7, such behaviour can arise from cancellation between the measurements of the low-frequency dynamics of the recirculation region and the high-frequency dynamics of the shear layers. Furthermore the presence of zeros has important implications for feedback-control design and may suggest a fundamental limitation of a system using forcing flaps.

## 5.2 Static forcing

While open-loop forcing of the wake provides interesting insight into the dynamic response, we may also hope to gain insight into the optimal fixed conditions for drag reduction. In these investigations the wake is subjected to “static forcing”, which consists of positioning the lateral flaps at a range of fixed angles. It has long been known that boat-tailing may lead to drag reduction via the higher base

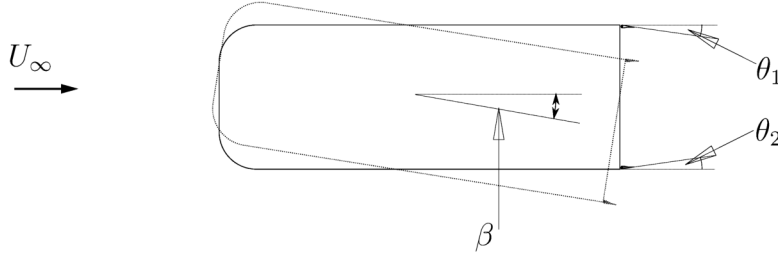


Figure 5.7: Plan view of the Ahmed body detailing the sign convention for the angles  $\beta$ ,  $\theta_1$ ,  $\theta_2$  used for static forcing. Yaw angles  $\beta$  are positive as a clockwise rotation about the  $z$  axis while flap angles  $\theta$  are positive towards the base of the body.

pressure induced by streamline curvature (Wong & Mair, 1983). However another key effect is the dependence of drag on the cross-flow forces, known in the vertical direction to have a quadratic dependence (Grandemange *et al.*, 2013a). For road vehicles a common scenario is that in which there are lateral forces induced by cross-wind (Hucho & Sovran, 1993). In this section we will therefore also investigate the influence of “ruddering” the flaps in response to cross-wind induced yaw angles in the flow, examining the conditions that achieve minimum drag.

The results discussed in this section come from parametric investigations of the flap angles  $\theta_1$ ,  $\theta_2$ , as described in § 2.3.1. These investigations were performed under eight different conditions consisting of four different yaw angles  $\beta = 0^\circ, 3^\circ, 6^\circ, 9^\circ$  and two different flap lengths  $\delta = 9\%, 13\%$  of the body width  $W$ . A schematic illustrating the sign convention for  $\theta$  and  $\beta$  is displayed in figure 5.7.

### 5.2.1 Optimal flap positioning

Figure 5.8 displays maps of the time-averaged drag coefficient  $C_D$  against the flap angles  $\theta_1$  and  $\theta_2$ , and marks the optimal flap configuration by a white  $\times$ . The maps displayed in the first column are both the result of symmetric testing conditions  $\beta = 0$ , and demonstrate that the optimal flap configuration consist here of a pure boat-tailing, i.e. a symmetric deflection of the flaps inwards. The drag is relatively insensitive to boat-tailing angles of up to  $10^\circ$  but increases markedly for non-zero ruddering, indicating that any imposed asymmetry is detrimental.

For the non-zero  $\beta$  cases, figure 5.8 demonstrates that the optimal configuration is no longer symmetric, the optimal configuration now consisting of a combination of ruddering and boat-tailing. The six maps are remarkably similar to each other, and relatively insensitive to  $\theta_1$  and  $\theta_2$  around the optimal condition. In order to further



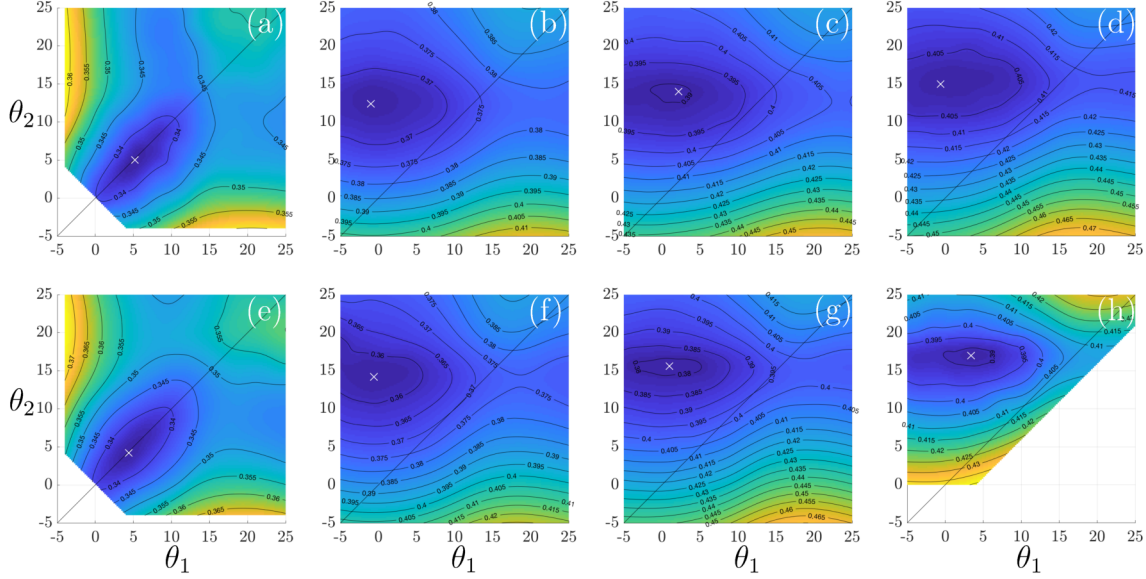


Figure 5.8: Maps of  $C_D$  against the flap angles  $\theta_1$  and  $\theta_2$ . Data is shown here for yaw angles  $\beta = 0^\circ, 3^\circ, 6^\circ, 9^\circ$  and for flap lengths  $\delta = 9\%$  (upper row), and  $\delta = 13\%$  (lower row). White crosses mark the configuration giving minimum drag.

understand the factors that control the optimal flap angles it is insightful to look at other measurements such as the base suction  $-\langle C_p \rangle$ , quantifying the pressure drag, and the lateral force coefficient  $C_y$ . Such data for one set of conditions is shown in figure 5.9. While the values shown here are particular to  $\beta = 6^\circ$  and  $\delta = 13\%$ , the trends are broadly the same for all  $\beta \neq 0$ , so this data can be considered representative.

Figures 5.9 (a), (b), (c) show parameters as a function of  $\theta_2$  for  $\theta_1 = 0^\circ, 10^\circ, 20^\circ$ . For each of these configurations, minimum lateral force is seen to be achieved at approximately the same angle as minimum base suction and total drag. This suggests that the changes seen in the drag are attributable to changes in base suction, and furthermore that this is closely related to the lateral force on the body. This is consistent with the previous experiments using base flaps of Grandemange *et al.* (2013a), who found a quadratic relationship between the drag and lift forces when using flaps at the top and bottom edges. Changes to the lateral force through  $\theta_2$  must necessarily be achieved by deflecting the flow inwards, a process that requires the boundary layer to remain largely attached to the surface of the flap. The abrupt change in the gradient of the trends seen at  $\theta_2 \approx 15^\circ$  may be due to a detachment of the flow, a theory consistent with the relative insensitivity of the optimal  $\theta_2$  with changing  $\theta_1$ .

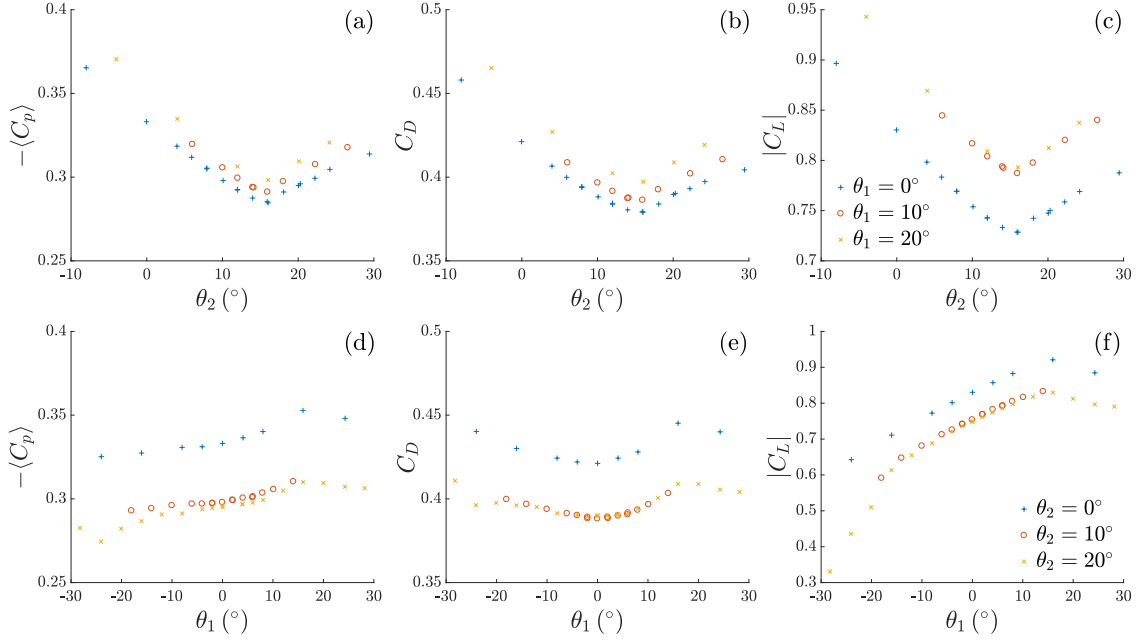


Figure 5.9: Base suction coefficient  $-\langle C_p \rangle$ , drag coefficient  $C_D$  and lateral force coefficient  $|C_y|$  as a function of each of  $\theta_1$  and  $\theta_2$  with the other held constant. For these data  $\beta = 6^\circ$  and  $\delta = 13\%$ .

Figures 5.9 (d), (e), (f) show parameters as a function of  $\theta_1$  for three fixed values of  $\theta_2$ . In this case the base suction and lateral force are again closely related, each exhibiting a maximum for the same configuration. However the drag is seen to find a minimum at values of  $\theta_1$  that do not minimise  $-\langle C_p \rangle$  or  $C_y$ . Interestingly, the drag is seen to rise for  $\theta_1 < 0$ , i.e. for configurations in which this flap extends outwards away from the body (see figure 5.7). This suggests that a trade-off must be found between minimising the base suction - by minimising  $|C_y|$  - and minimising the drag on the flap itself.

We may alternatively consider the trends with respect to the degree of ruddering and boat-tailing, as defined in (5.1). Figures 5.10 (a), (b), (c) show parameters as a function of the ruddering angle, for fixed degrees of boat-tailing. For each of these configurations, the ruddering has a strong influence on the lateral force,  $C_y$ , with the exception of the case  $\theta_B = +16^\circ$ . This is to be expected as the flaps will cause a lateral deflection of the flow. For a series of boat-tailing angles, figure 5.10 (c) demonstrates a notable collapse of the data along a single straight line with negative gradient, indicating a significant linearity in the relation between  $\theta_R$  and  $C_y$ . However, in each case there is an angle at which the data begins to deviate from this line, possibly due to a separation of the flow over one of the flaps. The

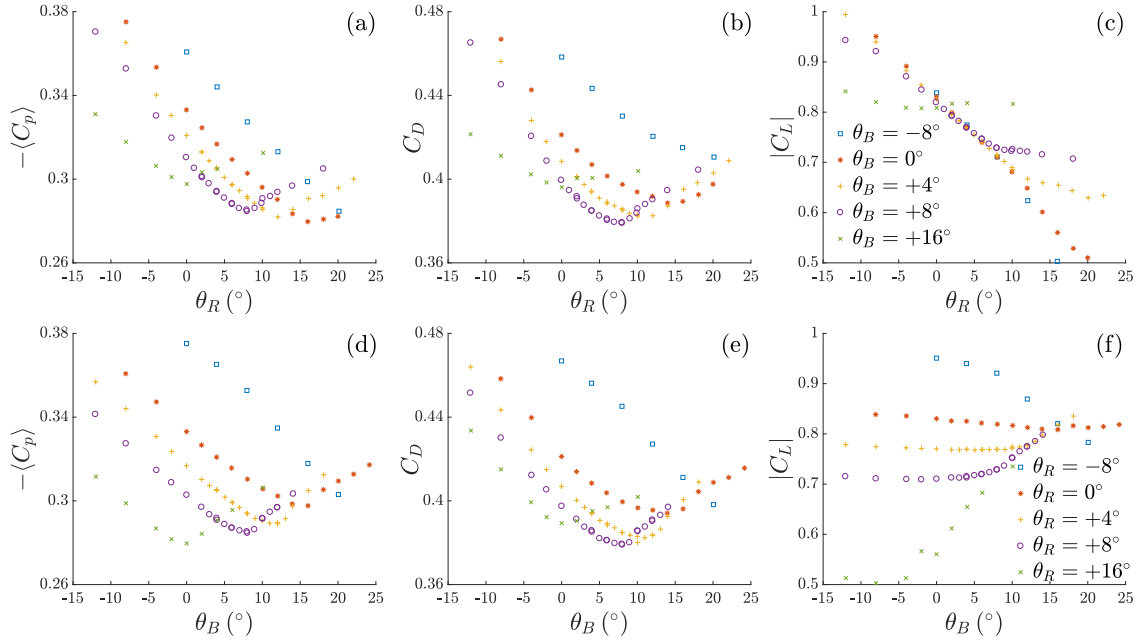


Figure 5.10: Base suction coefficient  $-\langle C_p \rangle$ , drag coefficient  $C_D$  and lateral force coefficient  $|C_y|$  as a function of each of  $\theta_R$  and  $\theta_B$  with the other held constant. For these data  $\beta = 6^\circ$  and  $\delta = 13\%$ .

point at which this deviation occurs is seen to coincide with the angle of minimum base suction, as shown in figure 5.10 (a). This indicates a strong link between the total lateral force and the pressure drag experienced by the body, consistent with previous experiments using base flaps (Grandemange *et al.*, 2013a).

Figures 5.10 (d), (e) and (f) show parameters as a function of  $\theta_B$  for three fixed values of  $\theta_R$ . In this case the lateral force is seen to be much less strongly affected, and is almost constant with changing  $\theta_B$  in some cases. This is to be expected as symmetric deflection of the flaps should provide little net lateral deflection of the flow. However for the most extreme  $\theta_R$  cases, where there is a dependence of  $C_y$ , possibly due to a separation of the flow over one of the flaps, there is again a clear relationship between  $-\langle C_p \rangle$  and  $C_y$ . For all of the data shown, the minimum  $C_D$  and  $-\langle C_p \rangle$  do now coincide. These minima are all for  $\theta_B > 0$ , i.e. for inward deflection of the flaps. This reinforces the notion that boat-tailing of the flow to achieve a narrower wake also decreases the pressure drag on the body.

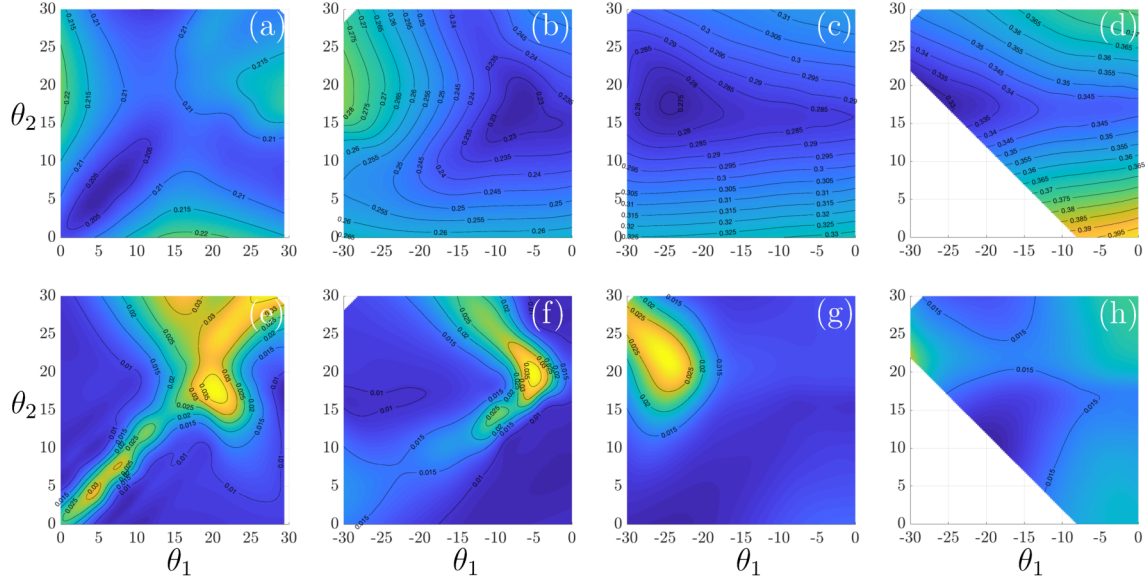


Figure 5.11: Contour maps of  $-\langle C_p \rangle$  (upper row) and the variance of the pressure metric ( $\text{var}(m_l)$ ) (lower row) as a function of  $\theta_1, \theta_2$ . Dark colours correspond to low pressure drag in the upper row which coincides with high  $\text{var}(m_l)$  (light colours) in the lower row. The flap length is  $\delta = 13\%$ .

### 5.2.2 Bistability at yaw

An additional observation may be made by examining the statistics of the pressure metric  $m_l$ . A clear indication of the presence of bistability may be found by looking at the variance of  $m_l$ , since bimodality induces a high variance. Figure 5.11 shows contour-maps of the base suction  $-\langle C_p \rangle$  along with  $\text{std}(m_l)$  for each yaw angle and the case  $\delta = 13\%$ . For  $\beta = 0^\circ$  (figures 5.11 (a), (e)), a range of symmetric deflections ( $\theta \lesssim 15^\circ$ ) gives both relatively low base suction and relatively high variance, corresponding to a bistable wake. For greater values of  $\beta$ , the configuration giving least base suction moves to increasingly asymmetric flap configurations, but is seen to again coincide with high  $\text{var}(m_l)$  indicative of a bistable wake. For the largest yaw angle of  $\beta = 9^\circ$  (figures 5.11 (d), (h)), the flaps have insufficient authority to achieve minimum pressure drag although the same relationship appears to exist towards the edge of the investigated area.

To give further clarity, figure 5.12 displays the PDF for  $m_l$  for each yaw angle, both with and without flap deflection. Without flap deflection (figure 5.12 (a)), the pressure distribution is seen to become increasingly asymmetric with increasing  $\beta$ : the initially bimodal PDF transitions to one with a single peak that moves further from zero with increasing  $\beta$ . However with the correct static flap angles,

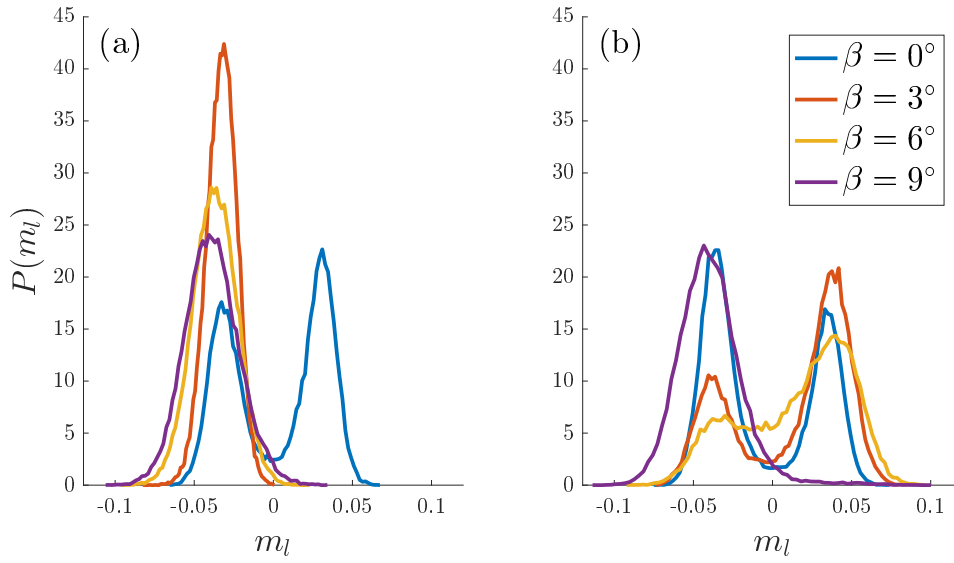


Figure 5.12: Effect of flap positioning on the distribution of the lateral pressure metric  $m_l$ . Cases for which  $\theta_1 = \theta_2 = 0$  are displayed in (a) while those giving a bistable wake are displayed in (b).

figure 5.12 (b) demonstrates that the bistable behaviour can be restored. Even for the case  $\beta = 9^\circ$ , the PDF is modified such that values  $m_l > 0.03$  occur under static forcing but not under unforced conditions. Given that the bistability is known to be highly sensitive to asymmetry in the flow, (Cadot *et al.*, 2015; Evrard *et al.*, 2015) it is certainly noteworthy that the bistability can appear even under highly asymmetric conditions. While the PDFs displayed in figure 5.12 (b) show bistable behaviour, initial results suggest that unlike under aligned conditions, the two flow conditions of  $m_l \pm 0.03$  do not correspond to equal  $C_D$  and  $C_y$ . This makes the two bistable configurations more similar to those seen under other asymmetric conditions, such as the up-down bistability observed in some real cars (Bonnavion *et al.*, 2017), for which one configuration has higher drag than the other.

Figure 5.13 illustrates schematically the behaviour of the wake under ruddered and yawed conditions. For an aligned flow small flap angles can preferentially select the orientation of the SB mode, such that the low-pressure vortex is nearest to the inwardly deflecting flap. This means that the pressure gradient on the base is consistent with that on the sides of the body, as inward/outward deflection leads to respectively low/high pressure immediately upstream of the flap. Under yaw angles, the orientation is again preferentially selected such that the base pressure is consistent with the sides: the lower pressure on the leeward side of the body is

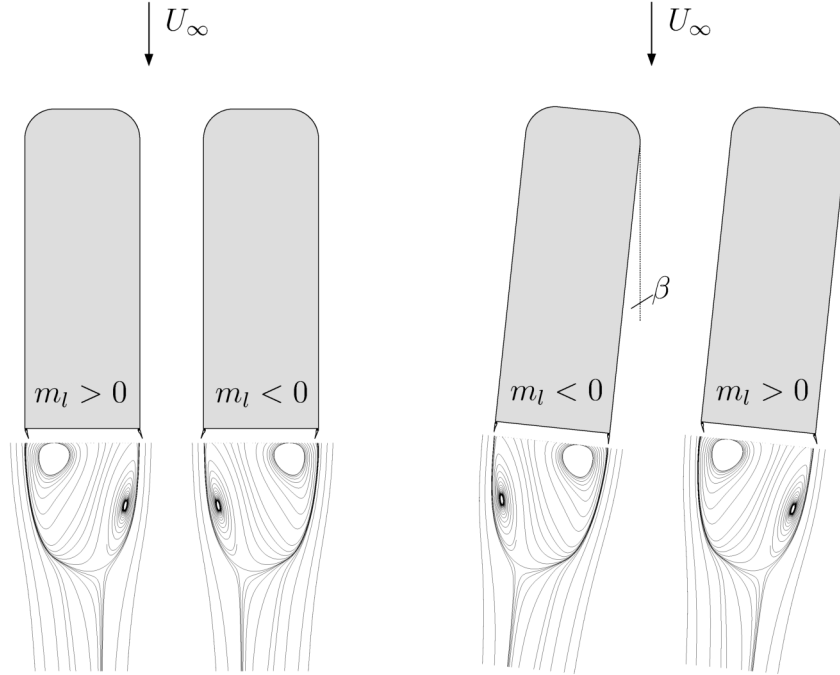


Figure 5.13: Schematic of the effect of ruddering and yaw angles in the flow. Under aligned conditions small  $\theta_R$  preferentially selects one of the two asymmetric states of the wake. Under non-zero  $\beta$  one of the states is also selected, however ruddering of the flaps is able to restore the flow to a situation in which the other state can exist.

closest to the low-pressure vortex. However by ruddering the flaps in the indicated manner, the flow may be changed to the extent that both orientations are again approximately equistable, giving the behaviour displayed in figure 5.12 (b).

It is finally interesting to examine the dynamics of the flow under asymmetric conditions consisting of non-zero  $\beta$  and  $\theta_R$ , i.e. with ruddered flaps restoring the bistable flow. This may be done by again examining the frequency response as in § 5.1.1 above. Figure 5.14 shows a comparison of the lateral frequency response under aligned and yawed conditions, where forcing in the yawed case is superposed over a mean ruddering offset. There is a clear similarity between the frequency responses, indicating that the dynamics of the bistability under yawed conditions is very similar. This implies that the dynamical modelling for the bistability that we will apply in chapter 6, and the feedback control of chapter 7, may be applicable under both aligned and yawed conditions.



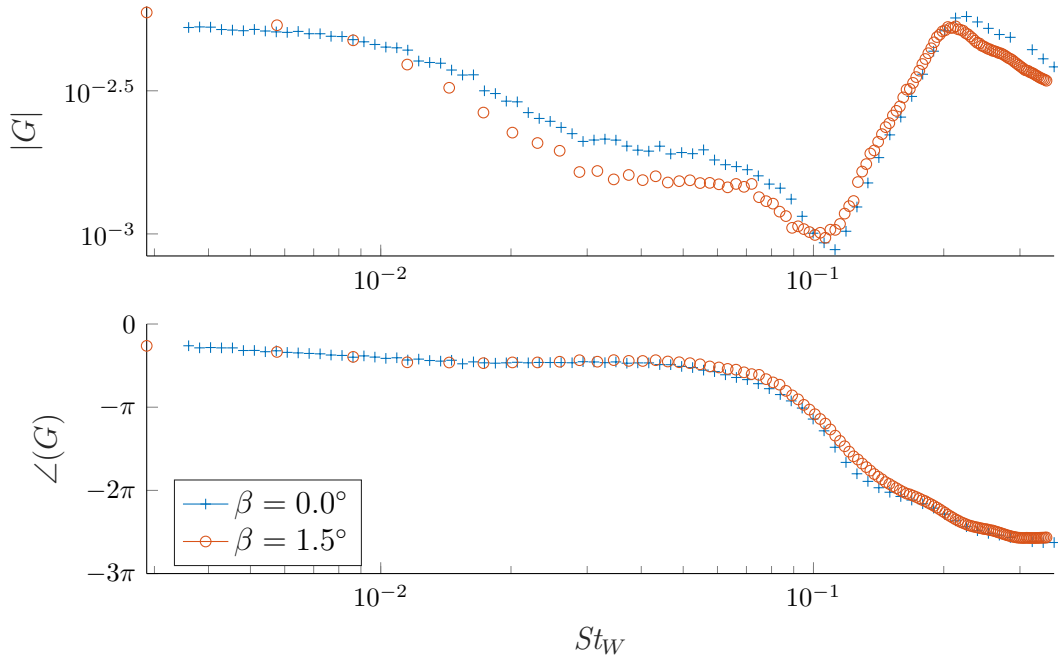


Figure 5.14: Frequency response between anti-symmetric flap forcing and pressure metric  $m_l$  under aligned and yawed conditions. For the case  $\beta = 1.5^\circ$  the mean ruddering angle of the flaps is  $\theta_R = 7.8^\circ$ .

### 5.2.3 Concluding remarks

Static deflection of the flaps may consist of either boat-tailing, ruddering or a combination of the two. Consistent with previous understanding (Wong & Mair, 1983), we have found that positive boat-tailing gives a drag reduction under aligned conditions. Under yawed conditions ruddering is also able to give drag reduction by reducing the lateral force on the body, confirming the existing understanding of the strong relationship between the stream-wise and cross-stream forces (Grandemange *et al.*, 2013a). However minimum drag generally does not coincide with minimum lateral force due to the drag induced on the flaps themselves. The globally minimised drag is achieved through the optimal combination of ruddering and boat-tailing that likely achieves a relatively narrow and symmetric wake, while minimising the drag on the flaps.

A second crucial observation is that close to the conditions giving minimum pressure drag ( $-\langle C_p \rangle$ ), the flaps restore the bistable behaviour of the wake, despite the highly asymmetric conditions. This observation confirms that the SB mode remains relevant to the flow under a wide range of scenarios, supporting the recent observations on real car geometries (Bonnavion *et al.*, 2017).

In terms of practical applications, the results from static forcing indicate that by having an adaptive system which caters for varying cross-wind, large drag reductions may be obtained. More specifically, it may be estimated that such an adaptive system would perform up to 70 % better than a static system consisting of equally sized flaps (García de la Cruz *et al.*, 2017). It is unclear how the results would differ if the aspect ratio were to change, since the SB mode may no longer be present in the lateral direction. However the strong relationship between lateral and stream-wise forces would almost certainly remain. Furthermore, it is important to note that unlike some active flow control systems, one that used adaptive flap positioning would be expected to have very low energy requirements as little flap motion would be required. An ES controller such as that described in chapter 3 would be highly suitable for this sort of application.



# Chapter 6

## Stochastic modelling of coherent structures

For the purposes of control design, it is advantageous to obtain models of low order that describe the dynamics of the coherent structures that we wish to control. Through the literature review of chapter 1 and the results of chapter 4 we have seen that the SB mode and the vortex shedding are both suitable wake features for flow control. In this section we will develop low order models for each of these coherent structures, building upon the work of Rigas (2014); Rigas *et al.* (2015). This will start with an overview and additional analysis of the SB mode for axisymmetric bluff body wakes, followed by the application of the model to the rectilinear Ahmed body wake. Finally, we will extend the model to the unsteady vortex shedding behind the Ahmed body.

### 6.1 A general model

While many different modelling strategies exist for fluid flows, what we seek here is a simple dynamical description of key features, rather than a model that accurately describes the entire flow. For example we may want to define only one or two states and find simple equations for their dynamics. This approach has been pursued before in fluid flows, for example Li & Juniper (2013*a,b*) demonstrated that the dynamics of a self-excited axisymmetric jet could be accurately modelled by a van der Pol oscillator. Other authors have looked at the modelling of vortex shedding in wakes. For example, Le Gal *et al.* (2001); Facchinetti *et al.* (2004) used respectively

complex Stuart-Landau and van der Pol models for the vortex shedding behind a cylinder.

While deterministic low-order models such as the van der Pol oscillator may accurately describe large-scale structures in low Reynolds number flows (Li & Juniper, 2013a), at higher Reynolds numbers it is necessary to model the chaotic dynamics and additional turbulent fluctuations. A first method may be to choose a deterministic model that exhibits chaotic behaviour, in much the same way that the Navier-Stokes equations do. The challenge is that to give chaotic behaviour that accurately describes the fluid-flow feature of interest, a large number of states may be required. An alternative (and simpler) method is to include a stochastic forcing term in a low-dimensional model. For example, Brown & Ahlers (2007) derived a physics-based model for the dynamics of the large-scale circulation in a convective flow, including a stochastic term to account for the random forcing from turbulent fluctuations.

The basis for the stochastic models suggested by Rigas *et al.* (2015) and developed here, is the observation that many large-scale coherent structures in turbulent wake flows result from a persistence of the laminar global modes (Rigas *et al.*, 2014). At low Reynolds numbers, these global modes arise from bifurcations in the flow and manifest as either spatial (Fabre *et al.*, 2008; Meliga *et al.*, 2009; Grandemange *et al.*, 2012a) or temporal (Jackson, 1987) symmetry breaking features. Such bifurcations may be written in terms of a normal form that describes the type of bifurcation taking place and is accurate for values of the bifurcation parameter (in this case  $Re$ ) near to that at which the bifurcation occurs (Strogatz, 1994). A stochastic model to describe the global modes at high Reynolds numbers may therefore be composed of these same normal forms, but with the addition of a stochastic term to model the noise arising due to small-scale turbulence. While this type of model does not have a firm theoretical basis, it can be shown to fairly accurately reproduce the behaviour of large-scale coherent structures in turbulent flows and provide insight into their control.

A general stochastic model of the form employed in this work may be written as

$$\dot{\mathbf{x}} = \alpha \mathbf{x} + \lambda \mathbf{x} |\mathbf{x}|^2 + \mathbf{u} + \boldsymbol{\sigma} \xi(t). \quad (6.1)$$

This equation describes a bifurcation for which  $\mathbf{x}$  is the (possibly complex or vector valued) bifurcated mode and  $\dot{\mathbf{x}}$  the time derivative. For example this could be the SB mode observed in three-dimensional wakes,  $\mathbf{x}$  quantifying the magnitude of this

asymmetry. The parameters  $\alpha$  and  $\lambda$  are real or complex, while the variable  $\mathbf{u}$  quantifies any additional forcing terms and will be required for feedback control design. The final term  $\sigma\xi(t)$  represents phenomenologically the additional forcing due to turbulence;  $\xi(t)$  is a vector of normally distributed random variables  $N(0, 1)$ , for which  $\sigma^2$  determines the variance.

There is some flexibility in the dimension of  $\mathbf{x}$  as well as the other parameters in the model, appropriate dimensions and the choice whether or not to include complex parameters depends upon the particular flow feature being modelled. For the case that  $\mathbf{x}$ ,  $\alpha$  and  $\lambda$  are real and  $\lambda < 0$ , (6.1) describes a supercritical pitchfork bifurcation, while if  $\mathbf{x}$ ,  $\alpha$  and  $\lambda$  are complex and  $\Re(\lambda) < 0$ , (6.1) describes a supercritical Hopf bifurcation (Strogatz, 1994). As we will show later, the SB mode of three-dimensional wakes may be modelled by the former of these two cases while the vortex shedding may be modelled by the latter.

## 6.2 Symmetry breaking in the axisymmetric bluff body wake

As a first application of the stochastic modelling strategy, we will recap the work of Rigas (2014); Rigas *et al.* (2015), before providing some additional data and analyses. This work provided a model for the SB mode of the axisymmetric bullet-shaped body shown in figure 2.1.

### 6.2.1 Stochastic model

The SB mode of three-dimensional wakes may be quantified by many metrics, depending upon the available data. Rigas *et al.* (2014) found the two-dimensional CoP coordinates, as evaluated on the body base, to be a suitable one. This CoP coordinate  $\mathbf{X} = (Y, Z)$ , normalised by the body diameter  $D$  may be evaluated as

$$\mathbf{X}(t) = \frac{1}{D \iint_A p(y, z, t) \, dA} \iint_A p(y, z, t)(y, z) \, dA, \quad (6.2)$$

where  $p(y, z, t)$  is the local pressure measurement,  $y, z$  are the lateral and vertical coordinates and  $A$  is the area over the base of the body. Taking these coordinates

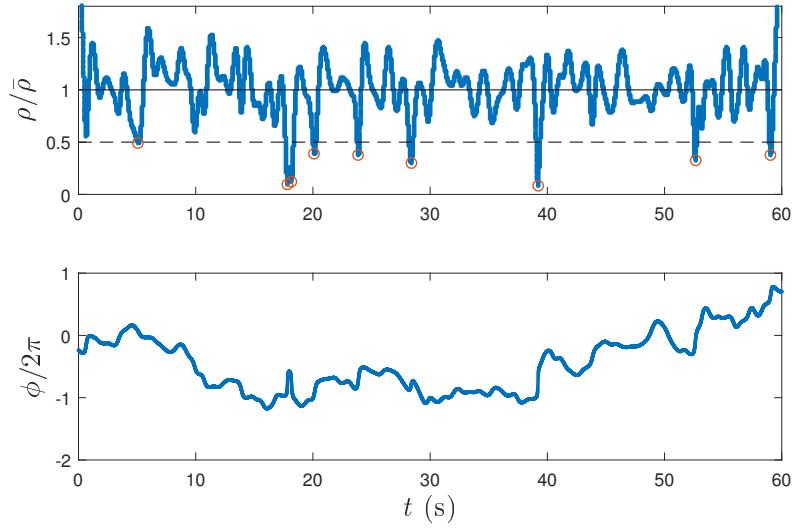


Figure 6.1: Time series of the centre of pressure coordinates  $(\rho, \phi)$ . Large changes in  $\phi$  are seen to correspond to times when  $\rho$  is small.

as a metric for the SB mode  $\mathbf{x}$  of (6.1), we obtain equations in each of  $(Y, Z)$ ,

$$\dot{Y} = \alpha Y + \lambda Y(Y^2 + Z^2) + \sigma \xi_Y(t) \quad (6.3a)$$

$$\dot{Z} = \alpha Z + \lambda Z(Y^2 + Z^2) + \sigma \xi_Z(t). \quad (6.3b)$$

If the coordinate system is now transformed from Cartesian  $(Y, Z)$  to polar  $(\rho, \phi)$ , Rigas (2014) demonstrated that (6.3) becomes,

$$\dot{\rho} = \alpha \rho + \lambda \rho^3 + \frac{\sigma^2}{2\rho} + \sigma \xi_\rho(t) \quad (6.4a)$$

$$\dot{\phi} = \frac{\sigma}{\rho} \xi_\phi(t), \quad (6.4b)$$

where each of  $\xi_\rho, \xi_\phi$  are again normally distributed random variables  $N(0, 1)$ .

## 6.2.2 Experimental data

Having detailed the model describing the SB mode in the turbulent axisymmetric body wake, we will now present some experimental data beyond that given in Rigas (2014); Rigas *et al.* (2015). These results will provide a motivation for the use of a similar model for the Ahmed body, and provide a benchmark against which the Ahmed body data may be compared.

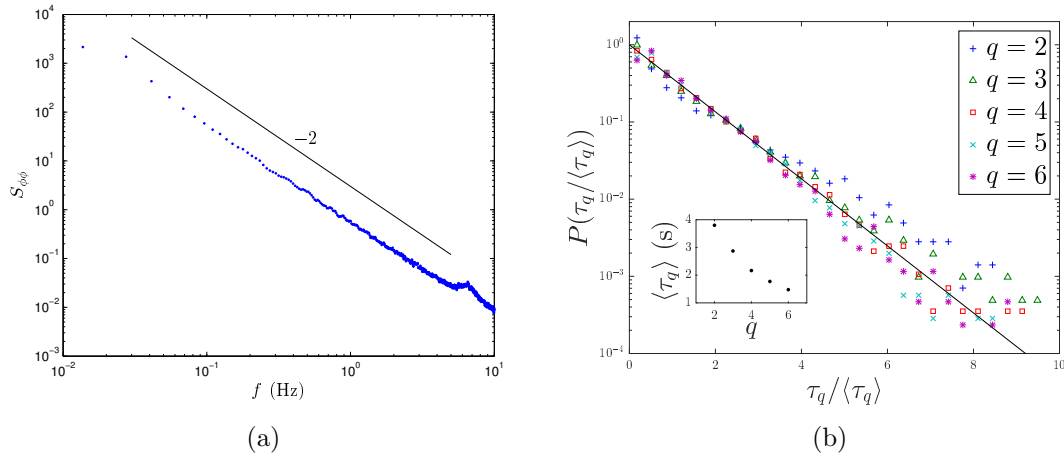


Figure 6.2: Statistics for the CoP angle  $\phi$  showing (a) the power spectral density, and (b) the escape time statistics. The solid black line shows the dimensionless exponential distribution:  $p(\tau_q) = \exp(-\tau_q/\langle\tau_q\rangle)$ . Inset is the mean escape time  $\langle\tau_q\rangle$  as a function of the number of bins  $q$ .

Figure 6.1 displays a sample time series<sup>1</sup> of the parameters  $\rho$  and  $\phi$  of (6.4). The parameter  $\rho$  can be seen to fluctuate around a mean value, intermittently reaching very small values highlighted by the red circles. Given the definition of  $\rho$  as a radius in polar coordinates it must remain positive by definition, and is also seen to remain bounded below approximately  $2\bar{\rho}$ . By contrast the angle  $\phi$  is unlimited in range as it can describe any number of rotations. Figure 6.1 shows that  $\phi$  meanders randomly with no discernible frequency or consistent direction. A key observation is in the relationship between  $\rho$  and the rate of change of  $\phi$ : small values of  $\rho$  are seen to be accompanied by large changes in  $\phi$ , consistent with the model of (6.4b) for which  $\dot{\phi} \propto 1/\rho$ .

A key feature of the model is the use of Gaussian white noise, as is standard practice for a Langevin equation (Zwanzig, 2001). Evidence for the Gaussian nature of fluctuations is given by Rigas *et al.* (2015, figure 5), however another important characteristic of a white noise process is its temporal behaviour. This can first be examined by looking at the PSD for the variable  $\phi$ , shown in figure 6.2(a). It may be shown that if the noise term in (6.4) is Gaussian with a uniform frequency spectrum, the PSD of the variable  $\phi$  should display a  $-2$  decay with frequency, and in particular should be independent of that of  $\rho$  (see appendix C.2.2). The PSD shown in figure 6.2(a) demonstrates such a  $-2$  decay with frequency over almost three decades, and is therefore consistent with the model.

<sup>1</sup>Note that the parameters displayed here are low-pass filtered. This is in order to prevent high-frequency noise from causing spurious jumps in the angle  $\phi$ .

A further key property of white noise is that it is delta correlated in time, indicating that it is memoryless (Zwanzig, 2001). For the Ahmed body, Grandemange *et al.* (2013c) demonstrated that the reversals of the bistable wake form a memoryless process, by examining the distribution of times between reversal events. A similar analysis may be performed here by dividing the range of azimuthal angles into a number of uniformly-spaced bins. Figure 6.2(b) shows the distribution of times  $\tau_q$  for which  $\phi$  remained within a specified range. For a division of the base into  $q = 2, 3, 4, 5, 6$  bins, the distribution of “escape times” can be seen to follow an exponential distribution, consistent with a memoryless process.

### 6.3 Symmetry breaking in the Ahmed body wake

The modelling strategy discussed above is now applied to the SB mode of the Ahmed body wake. For such rectilinear bodies it has been shown that the SB mode occurs in only one of the two cross-stream dimensions, the specific dimension depending upon the aspect ratio and ground effect (Grandemange *et al.*, 2013b). For the Ahmed body wake this feature occurs only in the lateral dimension (see figure 2.2). Again using the CoP as a suitable metric we may therefore take only the lateral component. Non-dimensionalised by the body width  $W$ , this is defined as,

$$r(t) = \frac{1}{W \iint_A p(y, t) \, dA} \iint_A p(y, t) y \, dA, \quad (6.5)$$

where  $p(y, t)$  is the local pressure measurement,  $y$  is the lateral coordinate and  $A$  is the area over the base of the body. Henceforth, we will use the parameter  $r$  to describe the SB mode of the Ahmed wake and, when displaying experimental results, use the metric defined by (6.5).

#### 6.3.1 Stochastic model

As for the axisymmetric bluff body wake, we start from a modified version of (6.1) but now require only a single variable  $r$  for the mode, and purely real parameters  $\alpha, \lambda, \sigma \in \mathbb{R}_{>0}$ :

$$\dot{r} = \alpha r - \lambda r^3 + b\theta_{t-\tau} + \sigma\xi(t). \quad (6.6)$$

Here, the forcing term  $\mathbf{u}$  of (6.1) is given by  $b\theta_{t-\tau}$ , modelling the effect of the forcing by the flaps. The flaps may be expected to deflect the shear layers by an amount

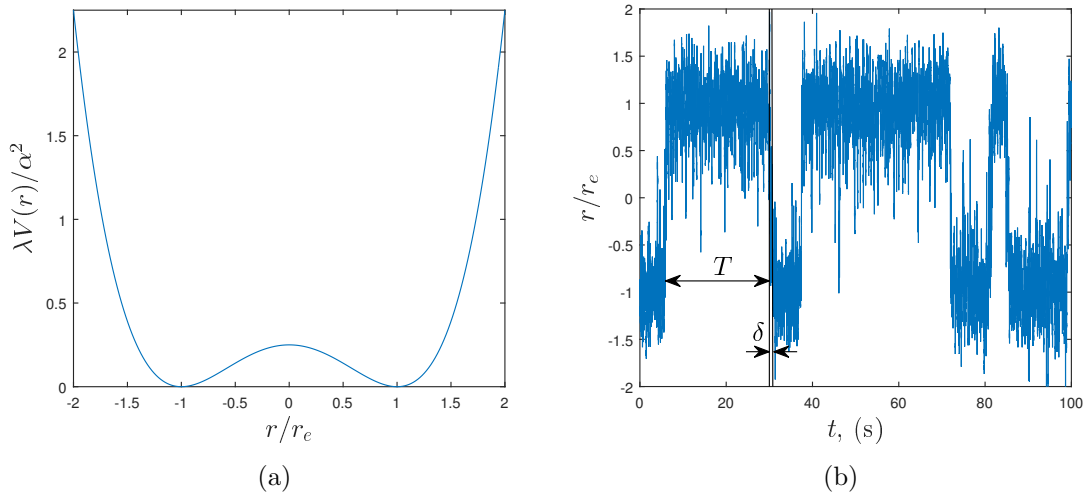


Figure 6.3: (a) The potential well  $V(r)$  for  $\theta = 0$ , and (b) an example time series demonstrating the time-scales  $T$  and  $\delta$ .

determined by their angle  $\theta$ . They thereby provide a lateral momentum flux that forces the mode  $r$ , possibly according to some linear scaling factor  $b$ . Given that any shear layer perturbation must be advected it is natural to also incorporate an advective time delay  $\tau$ . We will demonstrate later that the nature of this term fits well with the experimental observations. Furthermore, for the flaps to have good authority over the flow, we may require the term  $b\theta_{t-\tau}$  to be relatively large. We will also see that this is the case.

The system described by (6.6) may also be written in terms of the gradient of an energy potential  $V(r)$  as,

$$\dot{r} = -V'(r) + \sigma\xi(t). \quad (6.7)$$

This potential is illustrated in figure 6.3(a) and consists of a double-well with minima at  $r = \pm r_e$ . The turbulent forcing perturbs the state within this well, while the parameter  $\theta$  is able to skew the well in either direction. Such systems are commonplace and have been studied extensively in the past (see for example Gammaitoni *et al.*, 1998), therefore we will summarise only the key features here. In the absence of noise and for  $\theta = 0$ , the system has three points of equilibrium: one unstable at  $r = 0$  and two stable at  $r = \pm\sqrt{\alpha/\lambda} = \pm r_e$ . The state  $r$  will therefore tend to move in a region around one of the two stable equilibrium points until sufficiently perturbed by the noise to switch to the other. If a switching event is defined as a movement from  $r < -r_e$  to  $r > r_e$  (or vice versa), the mean time  $T$  between such switches is as illustrated in figure 6.3(b), and may be shown to be given by (see

appendix C.2.1),

$$T = \frac{\pi}{\sqrt{2}\alpha} \exp\left(\frac{\alpha r_e^2}{2\sigma^2}\right). \quad (6.8)$$

The second time-scale of the process is the instability time-scale associated with the duration of a reversal of the wake, as indicated in figure 6.3(b). This time-scale depends upon the growth rate of the instability so scales according to  $\delta \sim 1/\alpha$ . The ratio of these two time-scales therefore depends upon the ratio  $\sigma^2/\alpha$ , i.e. the argument of the exponential in (6.8), and determines the proportion of time spent around the stable equilibrium positions.

In the long-time average the distribution of values for  $r$  may be given analytically by the steady state Fokker-Planck equation (Risken, 1996), as discussed in appendix B.1. The stationary probability density function (PDF) for the system described by (6.6) with constant  $\theta$  is

$$\begin{aligned} P(r) &= C \exp\left(-\frac{2V(r)}{\sigma^2}\right) \\ &= C \exp\left(\frac{\alpha}{\sigma^2} \left(r^2 - \frac{1}{2} \frac{\lambda}{\alpha} r^4\right) + \frac{2b\theta}{\sigma^2} r\right), \end{aligned} \quad (6.9)$$

where  $C$  is a normalisation constant that ensures  $\int_{-\infty}^{\infty} P(r) dr = 1$ . This will later allow us to validate the model and determine its parameters.

The model is also consistent with expectations for the power spectral density (PSD) of the variable  $r$ . It has been shown that for a system of the form in (6.6), switching events form a Poisson process, i.e. they are independent (Gammaitoni *et al.*, 1998). This is consistent with previous observations of the bistable switching process (Grandemange *et al.*, 2013c) and, given this property of the switching events, it may also be shown that the PSD of the variable has a  $-2$  decay with frequency (Grandemange, 2013, section D.2.). For more detail see appendix C.2.2.

### 6.3.2 Parameter normalisation

It is useful at this stage to find a suitable non-dimensional form for the parameters of the model. This will aid in the interpretation of the parameters, and provide a suitable way to compare their numerical values.

The time-scales  $\alpha$  and  $\tau$  can be non-dimensionalised using the body width  $W$  and free-stream velocity  $U_\infty$ . The remaining parameters  $\lambda$ ,  $\sigma^2$  and  $b$  can all be written



	$\frac{\alpha W}{U_\infty}$	$\frac{\tau U_\infty}{W}$	$\frac{\lambda r_e^2}{\alpha}$	$\frac{\sigma^2}{\alpha r_e^2}$	$\frac{b}{\alpha r_e}$
Value	0.05	1.7	1	0.23	0.11

Table 6.1: Dimensionless parameters for the low dimensional model (6.6). The parameters are determined from the experimental data.

as ratios with respect to  $\alpha$ , thereby showing the relative importance of the terms in (6.6). However, the ratio of these parameters is dependent upon the range of values that the mode  $r$  takes. Furthermore the choice of metric for  $r$  is somewhat arbitrary; for example the CoP location could be replaced by the pressure gradient on the base or barycentre of velocity deficit in the wake. Any of these metrics quantify the same flow feature but give different numerical values for the mode  $r$ , and with different physical units. A characteristic value such as the equilibrium value  $r_e = \sqrt{\alpha/\lambda}$ , may therefore be taken into account in the normalisation<sup>2</sup>. The correct method for doing this can be seen by considering the change of variables  $q = \frac{r}{r_e}$ . Under this change (6.6) becomes

$$\begin{aligned} \dot{q} &= \frac{1}{r_e} (\alpha r_e q - \lambda r_e^3 q^3 + b \theta_{t-\tau} + \sigma \xi(t)) \\ &= \underbrace{\alpha}_{\alpha'} q - \underbrace{\lambda r_e^2}_{\lambda'} q^3 + \underbrace{\frac{b}{r_e}}_{b'} \theta_{t-\tau} + \underbrace{\frac{\sigma}{r_e}}_{\sigma'} \xi(t). \end{aligned} \quad (6.10)$$

Under the change of variables, each of the model parameters can be seen to be replaced by a normalised version, denoted by the '. As expected, the time-scale defined by  $\alpha$  remains unchanged but the other terms now depend upon  $r_e$ . This gives an appropriate method for non-dimensionalising the parameters, as shown in table 6.1<sup>3</sup>. The parameters displayed in this table are determined from the experimental data as will be detailed in § 6.3.6. The general approach is to firstly determine the time-scales  $\alpha$  and  $\tau$  from the frequency response, then determine the ratio  $\sigma^2/(\alpha r_e^2)$  from the unforced PDF. The ratio  $b/(\alpha r_e)$  may then be determined from the PDF under a number of fixed angles  $\theta$ .

A similar non-dimensional form may be given to the parameters of (6.4) for the axisymmetric wake. For comparison, these parameters are given in table 6.2 and are evaluated from those given in Rigas *et al.* (2015). Note here that the value

<sup>2</sup>Note that this is not the same as the expected value  $E[|r|]$ , for which there is not a simple analytical solution.

<sup>3</sup>Given that the model is for the temporal derivative of a spatial variable  $r$ , we could choose to non-dimensionalise in either time or space. We have chosen the spatial approach although a temporal approach would yield the same non-dimensional parameters.

	$\frac{\alpha D}{U_\infty}$	$\frac{\lambda \rho_e^2}{\alpha}$	$\frac{\sigma^2}{\alpha \rho_e^2}$
Value	0.0498	1	2.16

Table 6.2: Dimensionless parameters for the low dimensional model (6.4). Values are non-dimensionalised from those given in Rigas *et al.* (2015).

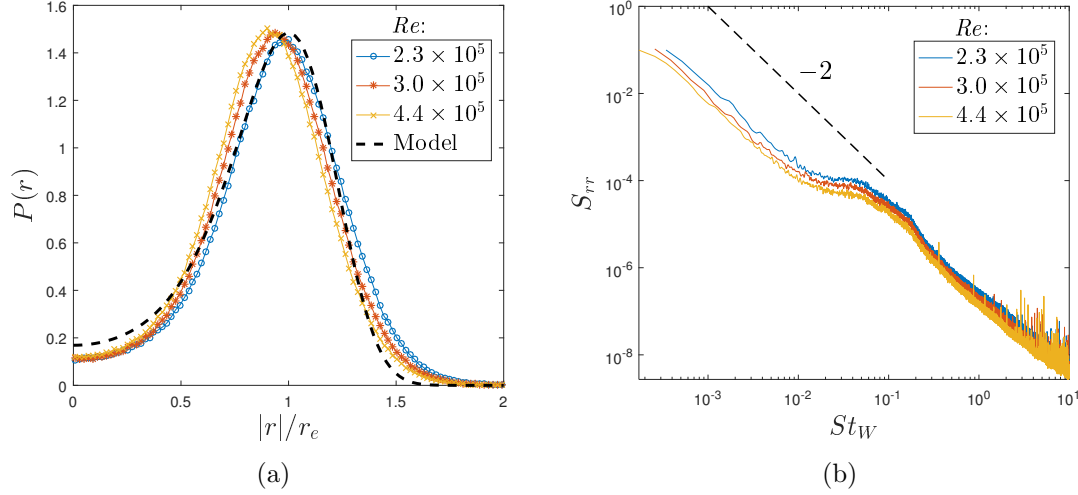


Figure 6.4: Properties of the mode  $r$  at the three tested  $Re$ : (a) probability density function and (b) power spectral density.

$\rho_e = \sqrt{\alpha/\lambda}$  is not actually the equilibrium value of  $\rho$  from (6.4a), however it is still a characteristic value and serves its purpose for non-dimensionalising.

### 6.3.3 Unforced flow

The unforced flow was examined at three different free-stream velocities corresponding to  $Re = 2.3 \times 10^5$ ,  $3.0 \times 10^5$  and  $4.4 \times 10^5$ . Figure 6.4(a) shows the PDF for  $r$ , along with the model prediction from (6.9), using the parameters values shown in table 6.1. The PDF demonstrates the asymmetry of the flow since the mode of the distribution is non-zero, i.e. the PDF peaks at  $|r| = r_e$ , the equilibrium value of (6.6). The results demonstrate both collapse of the data with  $Re$  and agreement with the model prediction.

As indicated in (6.9), the unforced ( $\theta = 0$ ) PDF can be written as a function of two ratios:  $\sigma^2/\alpha$  and  $\lambda/\alpha$ . These two ratios determine respectively the sharpness and location of the peak in the PDF and are seen to be largely  $Re$  independent. Physically, the parameter ratio  $\sigma^2/\alpha$  gives the intensity of the noise relative to the growth rate of the instability. The results therefore suggest that as  $Re$  changes,

any change in growth rate is accompanied by a roughly equal change in the noise intensity. As noted above, this parameter ratio is closely linked to the ratio of the two switching time-scales: a large  $\sigma^2/\alpha$  corresponds to a larger  $\delta/T$ . The second parameter ratio,  $\lambda/\alpha$  describes the level of asymmetry, and hence the topology of the flow, at the two stable equilibrium points. The results therefore suggest that this topology remains approximately constant.

Figure 6.4(b) shows the power spectral density of  $r$  as a function of the Strouhal number,  $St_W = fW/U_\infty$ . At lower frequencies, a region of  $\omega^{-2}$  roll off is observed for all three  $Re$ , consistent with the expectations for a randomly bistable process as described above.

### 6.3.4 Response to harmonic forcing

While the unforced results of § 6.3.3 allow assessment of the time-averaged behaviour, full quantification of the process requires knowledge of the time-scales quantified by  $\alpha$  and  $\tau$ . These time-scales can most accurately be assessed by examining the frequency response, evaluated as discussed in § 5.1.

We may begin by examining the anticipated response to harmonic forcing based upon the model (6.6), neglecting for now the time delay  $\tau$ . It is helpful at this stage to consider a normalised version of (6.6), as per the method described above. For a case with harmonic forcing this gives the following equation for  $q = r/r_e$ ,

$$\dot{q} = \alpha(q - q^3) + b'\Theta \sin(\omega t + \varphi) + \sigma'\xi(t), \quad (6.11)$$

where  $b' = \frac{b}{r_e}$  and  $\sigma' = \frac{\sigma}{r_e}$ .

As is common for SDEs, obtaining analytical solutions is extremely difficult, so we must proceed by looking at limiting cases where some terms in the model may be assumed much larger than others. One such approximation for the case in which the stochastic forcing is much stronger than the deterministic input is given by Gammaitoni *et al.* (1998). For a small harmonic input we can expect a component of the response  $q(t) = Q \sin(\omega t)$ , noting here that a phase shift is already included in the input term. Under these assumptions Gammaitoni *et al.* (1998) showed that

the parameters  $Q$  and  $\varphi$  are given as a function of frequency as,

$$Q(\omega) \propto \frac{2r_K}{\sqrt{4r_K^2 + \omega^2}}, \quad (6.12a)$$

$$\varphi(\omega) = \tan^{-1} \left( \frac{\omega}{2r_K} \right). \quad (6.12b)$$

Here the parameter  $r_K$  is the mean switching rate without forcing, equal to the inverse of (6.8). It can be shown that these equations are identical to the frequency response of a first-order low-pass filter with a corner frequency at the mean switching rate  $r_K$ .

The implication of the expressions in (6.12) is that the response of the system is critically governed by the mean switching rate which is in turn dependent upon the noise. While this will be true in the case of weak forcing, it is intuitive that for strong forcing the noise may no longer be a critical factor. This motivates an alternative approach in which the noise is neglected and we seek harmonic solutions to a deterministic version of (6.11).

Substituting an assumed solution of  $q = Q \sin(\omega t)$ , and using the identity  $\sin^3(\theta) = \frac{1}{4}(3 \sin(\theta) - \sin(3\theta))$  gives,

$$\begin{aligned} \omega Q \cos(\omega t) = \alpha Q \sin(\omega t) - \alpha \frac{1}{4} Q^3 (3 \sin(\omega t) - \sin(3\omega t)) + \\ b' \Theta (\cos(\varphi) \sin(\omega t) + \sin(\varphi) \cos(\omega t)). \end{aligned} \quad (6.13)$$

Neglecting higher harmonics and equating trigonometric terms gives the following two equations which may be solved for  $Q$  and  $\varphi$ :

$$\omega Q = b' \Theta \sin(\varphi), \quad (6.14a)$$

$$\alpha Q - \frac{3}{4} \alpha Q^3 + b' \Theta \cos(\varphi) = 0. \quad (6.14b)$$

Numerical solutions to these equations for varying dimensionless forcing amplitudes  $b' \Theta / \alpha$  are displayed in figure 6.5, along with the solution of (6.12). At low frequencies, the gain is largest for small amplitudes which is to be expected for induced switching between the two stable solutions: for the normalised system this corresponds to switching between  $q = \pm 1$ . At intermediate frequencies approaching  $\alpha$  sudden transitions are seen for the small amplitude cases, most likely caused by a transition from repeated switching, to oscillations around one of the minima. At frequencies  $\omega > \alpha$ , all responses converge towards a  $1/\omega$  decay rate and  $-\pi/2$  phase

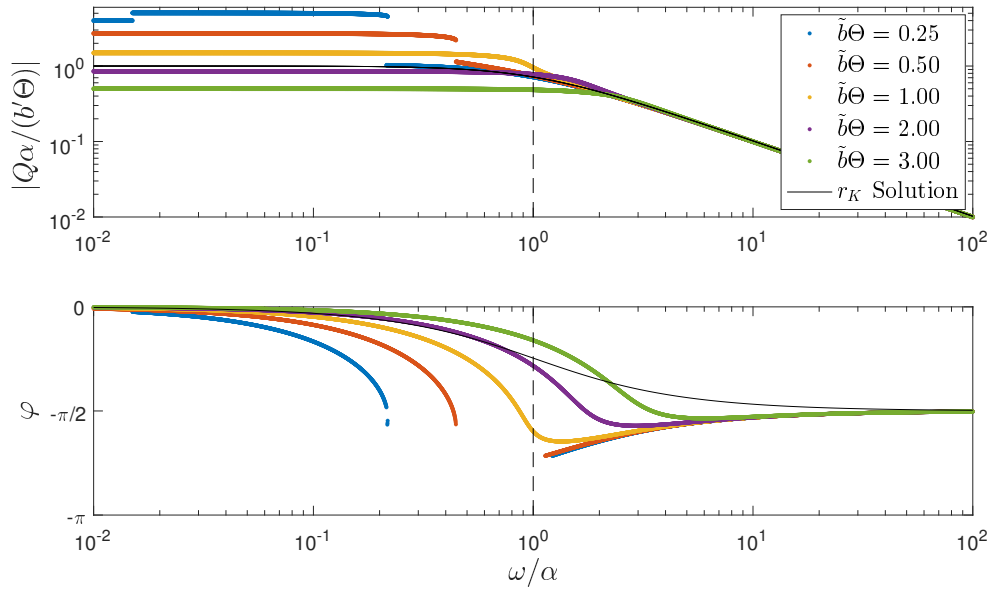


Figure 6.5: Analytical solutions to the frequency response according to (6.14) for varying forcing amplitudes and (6.12) for the case  $r_K = \alpha$ .

shift.

It is finally worth noting that the true frequency response of the system, even if accurately captured by (6.6), will not be given by either of the solutions presented here, as in practise the noise and forcing are of numerically similar size. However in both cases we may expect the system to act broadly like a first-order low-pass filter and, provided our forcing is strong enough, to have a corner frequency determined by the parameter  $\alpha$ .

Figure 6.6 shows experimental data for the antisymmetric frequency response of the flow for a particular forcing amplitude of  $10^\circ$  at the three different  $Re$ , demonstrating that the responses collapse in both magnitude and phase. This shows that the dynamics and flow topology associated with the process remain essentially identical, such that in a dimensionless form the parameters of (6.6) remain constant. As discussed in § 5.1, the bistability dynamics are evident for  $St_W \lesssim 0.1$ . Within this frequency range we observe that the magnitude of the response begins flat before beginning to decay, just as for the analytical results discussed above. From the phase response shown in the lower part of figure 6.6, we first observe that at all frequencies the output  $r$  lags the actuation. While some portion of this phase lag may be attributable to the dynamics captured by the magnitude response, some portion may be due to the advective delay. The monotonic decrease of phase angle with frequency over a region in which the magnitude response is flat ( $St_W \lesssim 2 \times 10^{-2}$ ),

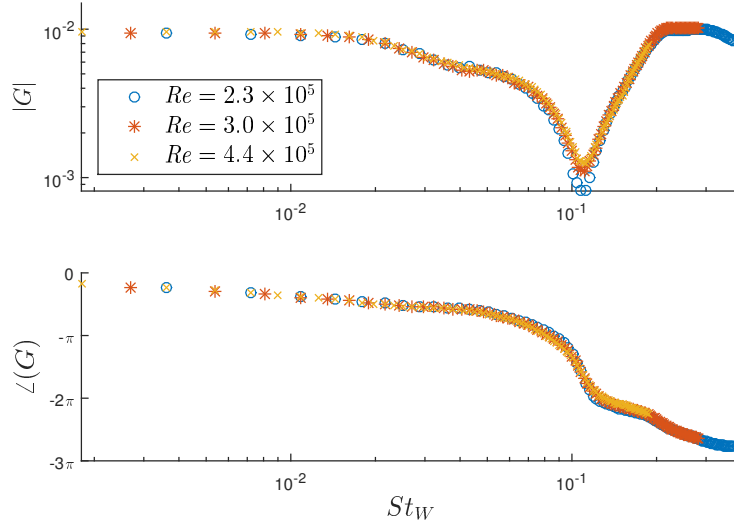


Figure 6.6: Frequency response between the antisymmetric flap oscillation and the mode  $r$  at the three  $Re$ . The flap oscillation amplitude is  $10^\circ$ .

suggests that such a delay is present<sup>4</sup>. Since the phase responses are independent of  $Re$ , this delay is observed to be constant in a dimensionless sense, i.e.  $\tau U_\infty/W$  is constant. This confirms the idea that  $\tau$  is an advection time associated with the shear layer perturbations generated by the flap.

### 6.3.5 Offset response

In addition to the frequency response discussed above, we can also consider a DC forcing where the angle  $\theta$  is held at fixed non-zero values. Experimentally the flaps may be placed at a fixed angle and their effect on the distribution  $P(r)$  is measured. Figure 6.7(a) shows the steady state PDF for a number of different flap angles at a free-stream velocity  $U_\infty = 15 \text{ ms}^{-1}$ . The data show that the flaps induce approximately equal and opposite skewness as they are moved from positive to negative offsets. At a zero offset the PDF is approximately symmetric, with any asymmetry resulting from either imperfect alignment within the experiment or insufficient averaging time.

Figure 6.7(b) shows the particular relationship between  $\theta$  and the skewness of the PDF; defined here as the natural logarithm of the ratio  $P(r_e)/P(-r_e)$ . The results demonstrate that a linear fit can be obtained for a range of angles. While more

<sup>4</sup>A delay  $\tau$  will give a phase lag  $\varphi(f) = 2\pi\tau f$  with no effect on the amplitude of the response.

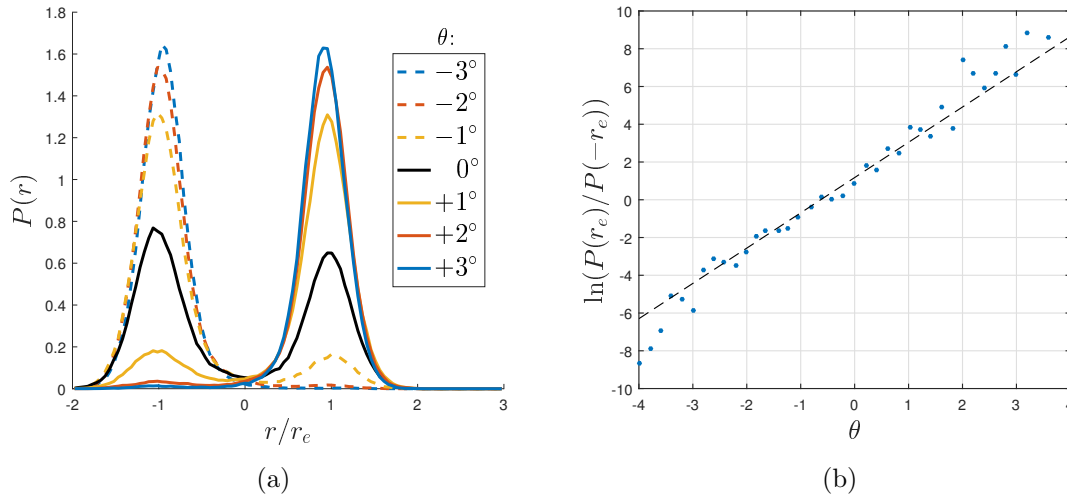


Figure 6.7: Response of the wake to static forcing: (a) Steady state PDF  $P(r)$  under a range of steady flap angles  $\theta$  and (b) skewness as a function of  $\theta$ . The dashed line in (b) shows the linear fit used to establish the parameter  $b$ , fitted for  $-2^\circ < \theta < 2^\circ$ .

details are provided below, the implication of this is that  $\theta$  has a linear influence in (6.6), justifying the choice of a linear term  $b\theta_{t-\tau}$ .

### 6.3.6 Parameter extraction

As detailed in Rigas *et al.* (2015) the parameters of (6.4) may be estimated using the steady state PDF of  $\rho$  and the mean squared displacement of  $\phi$ . These two statistics respectively provide information on the ratio of the parameters  $(\lambda/\alpha, \sigma^2/\alpha)$  and the time-scales associated with them, thereby providing sufficient information to fit the model. For the Ahmed body wake, the PDF may again provide information on the relative sizes  $(\lambda/\alpha, \sigma^2/\alpha)$ , but in this case the frequency response is required to obtain temporal information.

The first time-scale,  $\alpha$ , is estimated from the frequency response of figure 6.6. We stress here that while the frequency response is usually used as a method for the identification of linear systems, the behaviour seen here is nonlinear, as may be observed from the results of § 5.1. We therefore do not seek to fit a linear model to obtain  $\alpha$ , but are still able to use the response. Based on the frequency response analysis presented above, we may estimate the parameter  $\alpha$  as the inverse of the corner frequency, seen at  $St_W \approx 5 \times 10^{-2}$  in figure 6.6. This gives  $\delta \approx 1/\alpha \approx W/0.05U_\infty \approx 0.2$  s for a free-stream velocity of  $15 \text{ ms}^{-1}$ . Such a time-scale is sufficiently small that, when a long time series is viewed, wake reversals appear

to be instantaneous. However this is notably slower than the period of the vortex shedding: for the same  $U_\infty$ , this period is approximately 0.07 s.

Secondly, the time-scale given by the advective time delay is estimated via the slope of the phase response; the precise method for doing this is described in appendix D.2. The value of this parameter,  $1.7W/U_\infty$ , is consistent with the interpretation that  $\tau$  is associated with the stream-wise advection of perturbations generated by the flaps. The parameters  $\lambda$  and  $\sigma$ , quantifying respectively the saturation and noise intensity, are estimated from the shape of the PDF shown in figure 6.4(a). As stated above,  $\lambda/\alpha$  determines the location of the peak while  $\sigma^2/\alpha$  determines the width of the distribution. Based upon this understanding of how the parameter ratios change the PDF, a combination may be found that provides a close fit between the model and experimental data.

Estimation of the parameter  $b$  can be found by examining the Fokker-Planck prediction, (6.9). As can be seen, only the term involving  $\theta$  gives an effect that is asymmetric about  $r = 0$ . Taking the natural logarithm of the ratio of  $P(\pm r_e)$  we obtain

$$\ln \left( \frac{P(r_e)}{P(-r_e)} \right) = \frac{4b\theta r_e}{\sigma^2}. \quad (6.15)$$

As shown in figure 6.7(b), the left-hand side of this equation is seen to be linear with respect to  $\theta$ , within a certain range. Provided that  $\sigma$  is already estimated, the dimensionless form for  $b$  is estimated by the slope of the fit and given in table 6.1.

The dimensionless form for  $\lambda$  is by definition equal to unity since  $r_e = \sqrt{\alpha/\lambda}$ , while those for  $\sigma$  and  $b$  are seen to be of  $O(0.1)$  (see table 6.1). The relative size of  $\lambda$  and  $\sigma^2$  is therefore consistent with the fairly sharp peaks in the PDFs of figures 6.4(a), 6.7(a). Given flap angles  $\theta$  of  $O(10^\circ)$ , the  $b\theta$  term is therefore large relative to the noise and instability terms, suggesting that the flaps have good control authority.

It is finally interesting to note by comparing tables 6.1 and 6.2 that the dimensionless values of  $\alpha$  are almost identical for the two models of (6.4) and (6.6). This parameter quantifies in some sense the strength of the instability associated with the SB mode. Since this mode is believed to be essentially the same, but with different spatial symmetries in each case, it may not be surprising that the values are numerically very similar. In contrast, the dimensionless values for  $\sigma$  are an order of magnitude different. This may indicate a deficiency in the modelling and estimation approach, or suggest that the SB mode of the axisymmetric wake is more susceptible to turbulent fluctuations.



## 6.4 A model for the vortex shedding

Having successfully applied the stochastic modelling approach to the SB mode of three-dimensional turbulent wakes, we now look to apply a similar approach to the vortex shedding in the Ahmed body wake. The vortex shedding is believed to appear in both the top-down (vertical) and left-right (lateral) dimensions (Volpe *et al.*, 2015) and is visible as broadband fluctuations in the base pressure spectrum. This is confirmed by the results shown in chapter 5, that the wake exhibits resonant behaviour under the influence of antisymmetric forcing in both the lateral and vertical dimensions. A model is therefore required that can display both broadband self-excited oscillations when unforced, as well as resonant behaviour under the influence of forcing. We will not seek to find a model that accurately reproduces the behaviour seen experimentally in a quantitative sense, but rather demonstrate that the general form of model proposed here may qualitatively capture the key characteristics.

### 6.4.1 The stochastic model

As for the SB mode, we again start from a modified version of (6.1), but in this case use complex parameters:  $\alpha = \alpha_r + i\alpha_i$ ,  $\lambda = \lambda_r + i\lambda_i$ ,  $\mathbf{u} = u_r + iu_i$ ,  $\sigma = \sigma(1 + i)$ . This is then analogous to a Hopf bifurcation with the addition of noise. Writing  $\mathbf{x} = ae^{i\psi}$ , (6.1) becomes,

$$\dot{a}e^{i\psi} + ia\dot{\psi}e^{i\psi} = (\alpha_r + i\alpha_i)ae^{i\psi} - (\lambda_r + i\lambda_i)a^3e^{i\psi} + u_r + iu_i + \sigma(1 + i)\xi(t). \quad (6.16)$$

Splitting (6.16) into real and imaginary parts gives equations in each of the magnitude and phase of  $\mathbf{x}$ ,

$$\dot{a} = \alpha_r a - \lambda_r a^3 + u_r \cos(\psi) + u_i \sin(\psi) + \sigma (\cos(\psi) + \sin(\psi)) \xi(t), \quad (6.17a)$$

$$\dot{\psi} = \alpha_i - \lambda_i a^2 + \frac{1}{a} (u_i \cos(\psi) - u_r \sin(\psi)) + \frac{\sigma}{a} (\cos(\psi) - \sin(\psi)) \xi(t). \quad (6.17b)$$

The equation for the amplitude in (6.17a) is very similar to that for  $r$  in (6.6). In the absence of forcing the dynamics of  $a$  would be the same as those for  $r$ , consisting of bistable switching and fluctuations around a non-zero equilibrium value of  $a_e = \pm\sqrt{\alpha_r/\lambda_r}$ . For the case again of no input  $\mathbf{u}$ , the equation for the phase (6.17b) describes a process with a mean drift,  $E[\dot{\psi}] = \alpha_i - \lambda_i E[a^2]$ , and a stochastic forcing. Together these terms impose a mean frequency to the variable  $\mathbf{x}$ , and

	$\frac{\alpha_r}{\alpha_i}$	$\frac{\lambda_r a_e^2}{\alpha_r}$	$\frac{\alpha_i W}{U_\infty}$	$\frac{\lambda_i a_e^2}{\alpha_r}$	$\frac{\sigma^2}{\alpha_r a_e^2}$	$\frac{U}{\alpha_r a_e}$
Value	0.25	1	4	0	0.4	0.8

Table 6.3: Dimensionless parameters for the low dimensional model (6.17). The growth rate is determined by  $\alpha_r$  while the natural frequency ( $\omega_0$ ) is determined by  $\alpha_i$ . By definition  $\lambda_r a_e^2 / \alpha_r = 1$ , and by choice  $\lambda_i = 0$ .

random fluctuations which give a broadening of the frequency content, as observed in turbulent flows.

While this equation is complex, it is important to be able to provide a single input and to evaluate from it a single output. In this way the model may be made consistent with the experiment, from which a single input (flap angle) and single output (base pressure metric) are defined. If applying a purely real input  $\mathbf{u} = u_r + 0i$ , we may define our single input as  $u = u_r$ , and for the case of a harmonic input we have  $u = U \sin(\omega t)$ . We take a single output as  $y = a \sin(\psi)$ .

Initially, it is insightful to understand how the nature of the system described by (6.17) varies with each of the model parameters. As described in § 6.3.2 it is important to normalise the parameters in a suitable way. These normalised parameters are displayed in table 6.3, along with representative values from a comparison to experimental data. Note that unlike for the models presented in § 6.3, these values have not been found via rigorous fitting procedures, but are simply chosen to illustrate the desired behaviour.

The parameter  $\alpha_r$  gives the growth rate of the instability in a very similar manner to the parameter  $\alpha$  of (6.4) and (6.6). This describes in some sense the strength of the instability and the speed at which the magnitude  $a$  can change. Similarly  $\alpha_i$  also describes a time-scale but in this case one quantifying the oscillatory frequency. In the dimensionless form,  $\alpha_i W / U_\infty$  is the Strouhal number of the process. The real saturation parameter  $\lambda_r$  specifies the equilibrium values for  $a$  and as for the previous models, has a value of unity in a dimensionless sense. The imaginary parameter  $\lambda_i$  provides a coupling between the amplitude and frequency and is neglected for simplicity. Finally the parameters  $\sigma$  and  $U$  provide the amplitude of the stochastic and deterministic forcing terms. Larger values of  $\sigma^2 / (\alpha_r a_e^2)$  tend to give more broadband dynamics for the output  $y$ , while smaller values give more narrow-band frequency content and a narrower resonant region under forcing. Finally, while the unforced behaviour is unaffected by  $U$ , larger values change the range of frequencies over which resonance can occur, demonstrating a non-linearity in the frequency response. Further examples of how the behaviour varies with these parameters is

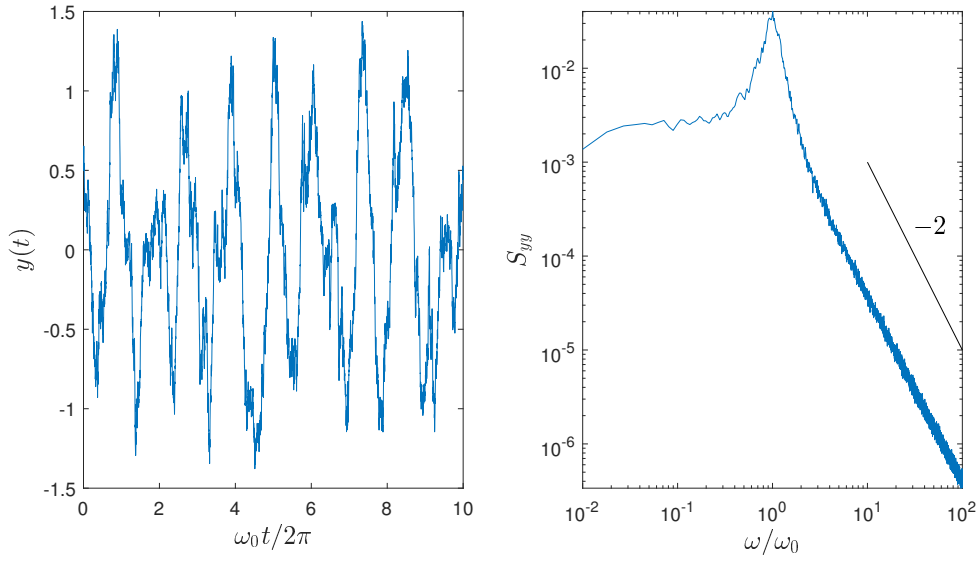


Figure 6.8: Unforced time series (left) and power spectral density (right) for the variable  $y = a \sin(\psi)$  of (6.17).

given in appendix E.

### 6.4.2 Simulations

To demonstrate the properties of the model we may examine time series and spectra for the output variable  $y$ . We cannot expect a very close fit to experimental data, as the CoP measurement is dominated by other features of the wake, however we may still assess the qualitative behaviour. Figure 6.8 displays these data, evaluated from a realisation of (6.17). The time series demonstrates oscillatory behaviour but also significant broadband fluctuations. This is corroborated by the PSD which displays a broad peak, centred at the frequency  $\omega_0$ . At higher frequencies the spectrum decays with a  $-2$  slope. The model therefore qualitatively displays the noisy, self-excited oscillations typical of vortex shedding in turbulent flows.

Figure 6.9 displays the frequency response of (6.17), subject to a purely real input  $u_r = U \sin(\omega t)$ . The behaviour is almost identical to that of a lightly-damped 2nd-order oscillator with natural frequency equal to  $\omega_0$ . Such a fit is shown by the solid black line and is seen to match the response almost perfectly in both magnitude and phase.

To summarise, it is clear that the stochastic model of (6.16) is able to provide broadly the correct behaviour for the vortex shedding. Namely, broadband frequency content

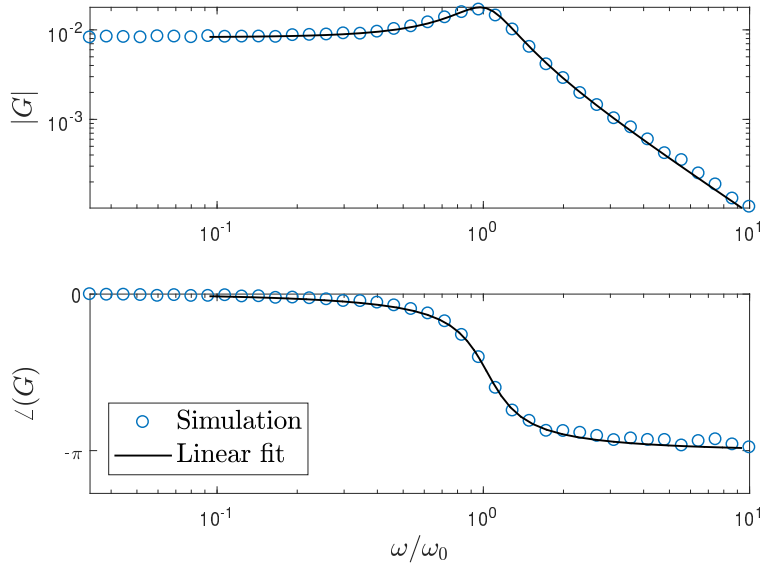


Figure 6.9: Frequency response of the model (6.17) between real input  $u_r = U \sin(\omega t)$  and output  $y = a \sin(\psi)$ . Also shown is a linear 2nd-order fit to the data.

for self-excited oscillations and resonant behaviour under the influence of forcing. It is also interesting to note that the frequency response is very similar to that for a 2nd-order linear oscillator. This suggests that a linear 2nd-order transfer function may provide a useful step in the design of feedback controllers. We shall examine the application of this in chapter 7.

## 6.5 Summary

The modelling approach presented in this chapter has consisted of the simple equations governing pitchfork or Hopf bifurcations with the addition of a stochastic forcing term. While this type of approach was first suggested by Rigas *et al.* (2015), here we have additionally applied the approach to the SB mode of the Ahmed body wake and to the oscillatory vortex shedding. For the case of the SB mode, we have demonstrated that the model may provide a good fit to the experimental data under both unforced and forced conditions. For the vortex shedding we have demonstrated that the model may provide qualitatively the correct behaviour.

Part of the value of these models is in the qualitative description that they give. For the case of the bistability this is of a wake flipping between two stable equilibrium positions, perturbed by the noise arising due to turbulence. Further to this, the bistability model provides parameters that quantify the physical processes: e.g. the

time scales  $\delta$  and  $T$  that are respectively the instability time scale and the flipping period. We have demonstrated here through the frequency response that the former is finite and notably larger than the vortex shedding period. Our model suggests that the ratio of these time scales may be related to the ratio  $\sigma^2/\alpha$  which the experimental results demonstrate to be roughly constant with Reynolds number. This indicates that any increase in the growth rate  $\alpha$  is accompanied by a proportionate change in the noise intensity  $\sigma^2$ . Our model and observations are consistent with those of Grandemange *et al.* (2013c) who found a linear increase in the flipping rate with increased free-stream velocity, corresponding to a reduction in the time scale  $T$  and therefore an increase in  $\sigma^2$ . Since we find that  $\alpha \propto U_\infty$ , this increased flipping rate is accompanied by an increased growth rate and therefore the ratio  $\sigma^2/\alpha$  may remain constant with changing  $Re$ .

For the vortex shedding the model describes an oscillatory limit cycle, wherein the phase follows a random walk with a drift term equal to the mean frequency. This describes well the broadband frequency content typical of vortex shedding in turbulent flows.

An interpretation of these models is that despite the high-dimensionality of the fluid flow system under investigation, the large-scale features follow relatively simple, low-dimensional behaviour. Furthermore, this reinforces the idea that the instabilities observed at laminar and transitional Reynolds numbers are persistent and important to the nature of the flow even under fully turbulent conditions. Perhaps the greatest utility for these models is the insight that they bring in the work towards control of fluid flows. In particular, we have found that the input-output behaviour of the wake may be described by fairly simple models that, as will be discussed in the following chapter, allow effective feedback-control design.



# Chapter 7

## Closed-loop control with flaps

Having examined the effect of open-loop forcing and also developed models for both the SB mode and the vortex shedding in three-dimensional wakes, we now look at the application of feedback control to these features of the wake. As will be explained below, control of each will require subtly different approaches but will involve some of the same challenges associated with the particular nature of the frequency response of the wake. We will therefore start this chapter with a discussion of the frequency responses displayed in chapter 5 and the implications for feedback control. We will then move onto the detailed control design and results for each of the SB mode and the vortex shedding.

### 7.1 System interpretation

The frequency responses displayed in § 5.1 displayed some particular characteristics that have implications for feedback control. The responses evaluated from both the lateral flaps (figure 5.1) and the vertical flaps (figure 5.3), demonstrated a fairly strong response at low frequencies  $St < 0.05$  and a resonance of the vortex shedding at  $St \approx 0.2$ . However crucially for feedback control both responses also demonstrated a sharp trough in the response at  $St \approx 0.1$ , indicative of what are known as right-half-plane (RHP) zeros. In this section we will provide a possible explanation for these RHP zeros and discuss the implications for control.

As seen in the frequency responses in § 5.1, RHP zeros may be exemplified by a sharp trough in the frequency response accompanied by a rapid decrease in phase angle. A common cause for such behaviour is the cancellation between dynamics occurring at

different frequencies (see e.g. Skogestad & Postlethwaite, 2005, § 5.7), if the output is composed as the sum of the response to these different dynamics. For the system consisting of the three-dimensional wake and forcing flaps, it is plausible that there are indeed two separate sets of dynamics in evidence. At low frequencies the flaps deflect the separation bubble, either leading to induced flipping of the bistability or deflection in a continuous sense. In either case we may expect the response to be largest at low-frequencies and to gradually decay as the forcing frequency increases, similar to a first-order low-pass filter (see e.g. figure 6.5). At higher frequencies the flaps excite the oscillatory vortex shedding, which may be expected to act as a second-order resonant system, as described by the model of § 6.4. Approximate transfer functions for the forced response of each of these dynamics may therefore be,

$$G_1(s) = g_1 \frac{1}{1 + sT_1} = \frac{n_1}{d_1}, \quad (7.1)$$

$$G_2(s) = g_2 \frac{1}{1 + 2\zeta sT_2 + s^2T_2^2} = \frac{n_2}{d_2}. \quad (7.2)$$

Here  $T_1/T_2$  give the time constants of the first/second-order systems respectively, and  $\zeta$  gives the damping ratio of the second-order system.

In order for a cancellation to occur, the two transfer functions must be added together,  $G = G_1 + G_2$ . This is based on the idea that the two features are essentially independent, therefore the total response of the wake may be considered as the sum of the two responses. The poles of the resulting transfer function  $G$  will be the poles of the two constituent transfer functions, however the zeros will not be the same but are instead given by the roots of

$$\begin{aligned} n(s) &= n_1(s)d_2(s) + n_2(s)d_1(s) \\ &= g_1 (1 + 2\zeta sT_2 + s^2T_2^2) + g_2 (1 + sT_1) \\ &= g_1 + g_2 + (2g_1\zeta T_2 + g_2T_1) s + g_1T_2^2 s^2 \\ &= g (1 + 2\zeta_z T_z s + T_z^2 s^2), \end{aligned} \quad (7.3)$$

where  $g = g_1 + g_2$ ,  $\zeta_z = (2g_1\zeta T_2 + g_2T_1)/(2T_2\sqrt{g_1^2 + g_1g_2})$  and  $T_z = T_2\sqrt{g_1/(g_1 + g_2)}$ . By Routh-Hurwitz, the criteria for the pair of RHP zeros observed experimentally are therefore,

$$g_1 + g_2 = g > 0, \quad (7.4a)$$

$$2g_1\zeta T_2 + g_2T_1 = 2g\zeta_z T_z < 0, \quad (7.4b)$$

$$g_1T_2^2 = gT_z^2 > 0. \quad (7.4c)$$



These criteria may be satisfied by appropriate choice of the parameters, and furthermore the properties of the response may be chosen to fit with observations. For example, if we specify the DC gain  $g$ , the properties of the zeros (specified by  $T_z$  and  $\zeta_z$ ) and the properties of the poles (specified by  $\zeta$  and  $T_2$ ), we have enough information to determine all remaining parameters. We will discuss a full application of this fitting approach in § 7.3, but for now the key point is that modelling the wake response as the sum of high and low-frequency dynamics provides a possible explanation for the observed behaviour. Furthermore, a suitable form for these dynamics is one consistent with the modelling of chapter 6.

### 7.1.1 Implications for feedback control

Having found that the observed frequency response may be explained by the models of chapter 6 and that the behaviour is indicative of RHP zeros, it is important to consider the implications of these observations for feedback control design. Intuitively, it is clear that for the range of frequencies in which the measured response is very small, it will be difficult to provide effective control. Further to this, the large decrease in phase angle associated with the presence of RHP zeros may be considered similar to a delay in the response. It may also be intuitive that if the response of the system is consistently delayed relative to the input, it will be difficult to provide the correct input in response to unpredictable disturbances. For a more rigorous understanding of the effect of RHP zeros we can look at what is known as the sensitivity function  $S(i\omega)$ .

The sensitivity function defines the expected ratio of measured fluctuations, with and without control. Considering the system displayed in the block diagram of figure 7.1, we can first define a “loop” transfer function as  $L = (G_1 + G_2)AK$ . If no control is present then the measurement  $m$  will consist purely of the disturbances  $d$ . With the negative feedback loop in place it may be shown that,

$$\begin{aligned} m &= \frac{1}{1 + L}d, \\ &= Sd, \end{aligned} \tag{7.5}$$

where we define the sensitivity function as  $S = 1/(1 + L)$ . This transfer function describes, as a function of frequency, how the exogenous disturbances  $d$  are amplified or attenuated by the action of the feedback control. For a system with no RHP poles but a complex conjugate pair of RHP zeros at  $z = x \pm iy$  it may be shown that the

following integral must be satisfied (Freudenberg & Looze, 1985)

$$\int_0^\infty \ln |S(i\omega)| w(z, \omega) d\omega = 0, \quad (7.6)$$

where<sup>1</sup>

$$w(z, \omega) = \frac{x}{x^2 + (y - \omega)^2} + \frac{x}{x^2 + (y + \omega)^2}. \quad (7.7)$$

This is similar to the classical waterbed formula from Bode (1945), the difference being the frequency dependent weighting function  $w(z, \omega)$ . The weighting function is large near to the frequency of the zeros and decays away from this frequency. The result of this is that any attenuation ( $S < 1$ ) in a frequency range near to that of the zeros must be compensated by an amplification ( $S > 1$ ) within a similar range. As we shall see below, such amplification is often detrimental with regard to drag reduction, therefore the limitation of (7.6) is of key importance and will impose limitations to the control efficacy.

## 7.1.2 Control approaches

The block-diagram schematic for the feedback systems that we will develop is displayed in figure 7.1. As discussed above, the response of the wake is shown as the sum of transfer functions  $G_1$  and  $G_2$ , quantifying respectively the response of the low and high frequency dynamics to flap angles  $\theta$ . The measurement  $r$  is also seen to be influenced by disturbances  $d$ , that capture both measurement noise and all remaining unmodelled dynamics of the wake. In the case without any control or open-loop forcing the measurement consists entirely of the disturbance signal  $d$ . The input to the combined wake model is the antisymmetric flap angle  $\theta$  which is in turn determined by the voltage  $v$  and actuator transfer function  $A$ . As discussed in § 2.2.1, the actuator dynamics behave as a 2nd-order oscillator, for which the resonant frequency is determined by choice of the mechanical components. Control design consists of deciding the dynamics of the controller  $K$  that determines  $v$  based upon real-time measurement of the wake.

Control design may now proceed along one of two approaches, either targeting the *static* asymmetry of the wake influenced by the bistability, or the *unsteadiness* which is strongly influenced by the vortex shedding. The former of these approaches is the

---

<sup>1</sup>Note that the actual values of this function are unimportant, what matters is the variation with frequency.

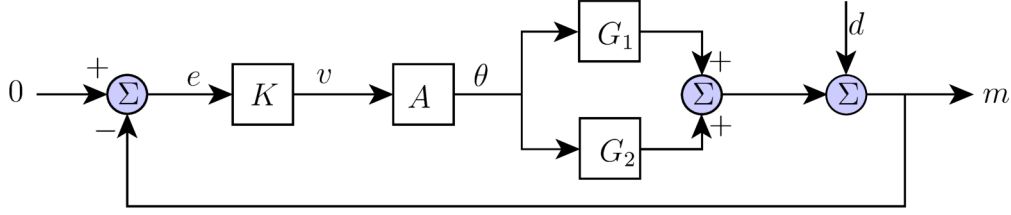


Figure 7.1: A schematic of the feedback control loop comprising the wake  $G_{1,2}$ , actuator  $A$  and feedback controller  $K$ .  $G_1$  captures the low-frequency dynamics of the bistability (lateral) or near-wake deflection (vertical), while  $G_2$  captures the vortex shedding and shear layer dynamics at higher frequencies.

topic of § 7.2 and is applied in the lateral dimension. The latter approach is applied in the vertical dimension and is the topic of § 7.3.

## 7.2 Control of bistability

The model (6.6) for the SB mode describes a pitchfork bifurcation. In agreement with the suggestion of Cadot *et al.* (2015), there is therefore an unstable equilibrium corresponding to a symmetric flow. Furthermore the model is seen to be valid over a range of  $Re$ , justifying its use in the design of linear controllers that try to recover this unstable equilibrium. In the context of the block diagram schematic shown in figure 7.1, we are seeking to design a controller that aims to keep the measurement  $m$  close to a value of zero. This real-time measurement will be an approximation of  $r$  that, due to the inherent instability leading to an asymmetric flow, typically has a non-zero value. In the following discussion, the measurement  $m$  will be referred to as  $r$  for consistency with the notation of § 6.3.

### 7.2.1 System formation

Here, we form the transfer functions that appear in figure 7.1 for the plant,  $G_{1,2}$ . As discussed above, in the lateral dimension the wake is considered to comprise the sum of the bistability dynamics ( $G_1$ ), and those of the vortex shedding occurring at higher frequencies ( $G_2$ ).

Using the model and results shown in § 6.3 we can form the linear model  $G_1$  of figure 7.1. The model described by (6.6) is a nonlinear time-delayed differential equation. In order to design a linear controller we first linearise about the desired equilibrium point of  $r = 0$ , which essentially eliminates the  $\lambda r^3$  term. This is

unproblematic since this term provides a saturation so is likely to help the control action. Moreover, the controller will be aiming to make  $r$  small, and thereby achieve a flow state in which this term is negligible. Secondly, having transformed the system to the Laplace domain, we use a first-order Padé approximation for the time delay (Skogestad & Postlethwaite, 2005, § 4.1.6). This gives the following transfer function between  $\theta$  and  $r$ :

$$G_1(s) = \frac{\bar{r}(s)}{\bar{\theta}(s)} = \frac{b(2/\tau - s)}{(s - \alpha)(2/\tau + s)}, \quad (7.8)$$

where  $s$  is the complex Laplace transform variable. This transfer function has one unstable pole at  $s = \alpha$  corresponding to the flow instability, as well as a pole and zero at  $s = \pm 2/\tau$ , resulting from the time delay. The presence of the unstable pole and right half-plane zero both imply that control of the system will have limitations (Freudenberg & Looze, 1985); in particular this implies that we cannot hope to have control authority over a wide frequency range.

It is worth noting here that the transfer function given by (7.8) is of course different to that given by (7.1), however this is not really a contradiction, just a result of different assumptions. For the full nonlinear system, (7.1) provides a stable transfer function that approximates the phase-averaged response, as seen in § 6.3.4. However in this section we are hoping to suppress the instability underlying this behaviour and therefore choose to use the linearised version of the unstable system, as captured by (7.8).

In addition to the transfer function specifying the dynamics of the bistability, it is insightful to capture the dynamics present at higher frequencies. These dynamics are evident for  $St_W > 0.1$ , as shown in figure 6.6. In order to best cater for these dynamics in the control design, we seek to fit a linear model that captures the necessary amplitude and phase information. Our fit to the higher frequency dynamics is shown in figure 7.2. As shown, we only fit the response for  $St_W > 0.11$ . Below this frequency the bistability dynamics are dominant, and we therefore do not require a linear fit to the (nonlinear) dynamics. For  $St_W > 0.11$  the response of the flow to open-loop forcing is much more sinusoidal than at lower frequencies (figure 5.2) and a linear fit such as that applied in (Dahan *et al.*, 2012) may be appropriate. We emphasize that the purpose of this is simply to understand any interactions between the controller and these higher frequency dynamics, it is (7.8) that captures the key information about the dynamics of the SB mode.

Finally it is necessary to identify  $A$ , the dynamics of the actuator consisting of the lateral motors and flaps. This is important since the finite bandwidth of the

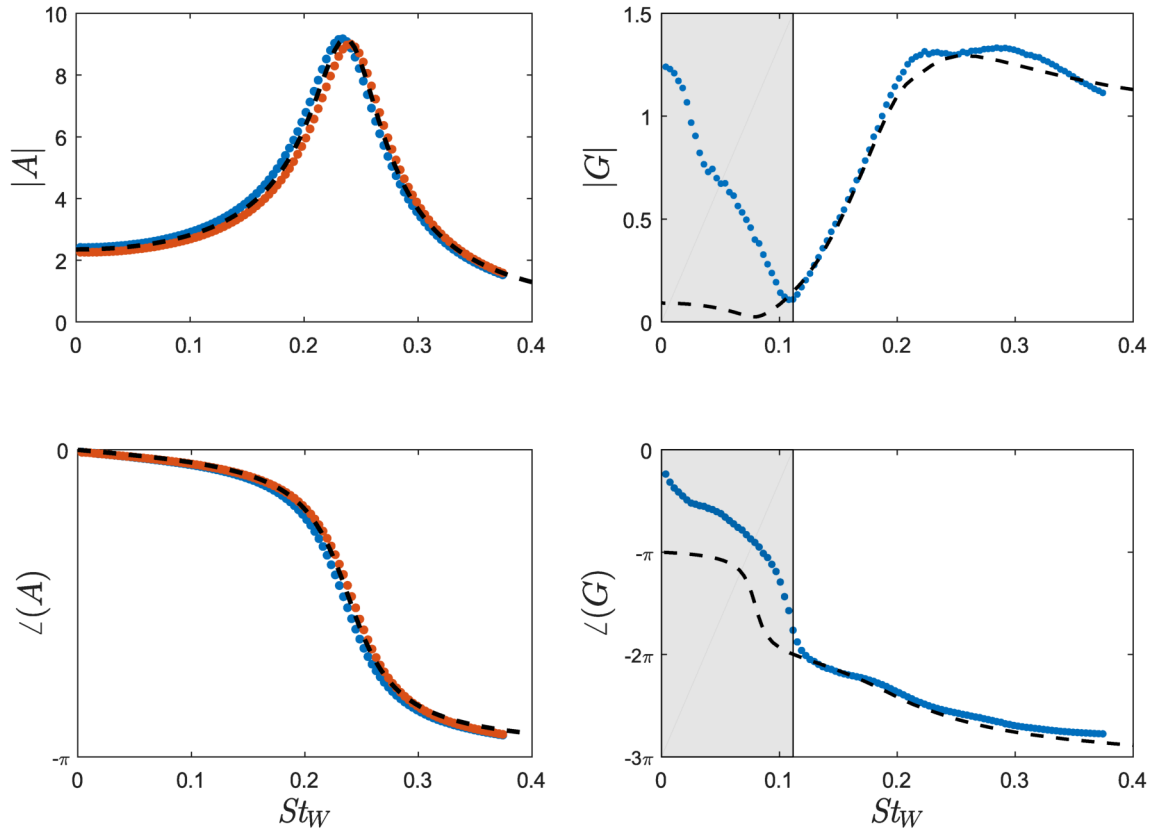


Figure 7.2: Linear fits to the actuator dynamics (left) and higher frequency wake dynamics (right). A second-order fit is found for the actuator, between an input in volts and output in degrees. The red and blue dots are for each of the two lateral actuators. A fifth-order linear fit to the wake dynamics is found using the MATLAB command `fitfrd`, applied only to the part of the frequency response to the right of the shaded region.

actuator, and the limitations this imposes, must be included in the control design. As was discussed in § 2.2.1, the actuator acts as a second-order linear oscillator to which we may readily fit a linear transfer function. We choose the actuator to have a natural frequency corresponding to  $St_W \approx 0.24$  at  $15 \text{ ms}^{-1}$ , giving sufficient bandwidth to control the bistability which manifests for  $St_W \lesssim 0.1$ . The frequency response and transfer function fit are displayed again here in figure 7.2.

## 7.2.2 Preliminary control design

Based purely upon the transfer function  $G_1$  derived from our model, the system shown in figure 7.1 has a closed loop transfer function given by

$$\begin{aligned} T(s) &= \frac{A(s)K(s)G_1(s)}{1 + A(s)K(s)G_1(s)} \\ &= \frac{n_A n_K n_G}{d_A d_K d_G + n_A n_K n_G}, \end{aligned} \quad (7.9)$$

where  $n$  and  $d$  respectively denote the numerator and denominator of the individual transfer functions. The stability, among other closed-loop properties, is determined by the roots of the denominator of  $T(s)$  (denoted  $d_T(s)$ ). For an initial analysis we can consider the case without actuator dynamics, i.e.  $A = a_0$ , a static gain. For  $K = k_p$ , a simple proportional gain we have

$$d_T(s) = s^2 + \left( \frac{2}{\tau} - k_p b a_0 - \alpha \right) s + \frac{2}{\tau} (k_p b a_0 - \alpha). \quad (7.10)$$

All variables here have the same meaning as in (7.8). For stability, the Routh-Hurwitz criterion requires that each of the bracketed terms are positive (Åström & Murray, 2008). This requires that

$$\frac{\alpha}{b a_0} < k_p < \frac{2 - \tau \alpha}{\tau b a_0}. \quad (7.11)$$

There is therefore expected to be a gain window, just as there is for the control of vortex shedding over cylinders (Illingworth *et al.*, 2014). A necessary condition for the existence of a  $k_p$  satisfying (7.11) is therefore

$$\alpha \tau < 1. \quad (7.12)$$

This makes intuitive sense because if the time delay is equal to, or greater than the time scale of the SB instability, the feedback system will be unable to respond

Controller	$k_i$	$\Delta C_D$ (%)	$\langle \Delta C_p \rangle$ (%)	$P_{\text{act}}$ (%)	$St_{\text{max}}$
Open loop	-	-1.0	1.7	-	-
$K_1$	0.07	-0.9	1.7	11	0.22
$K_2$	0.13	-1.6	3.7	15	0.19
$K_3$	0.20	-2.0	3.9	24	0.13

Table 7.1: The controllers and their performance including the controller gain, drag reduction, base pressure change, actuation power as a percentage of the power saving and the most amplified frequency. For comparison, the results for the open-loop forcing giving approximately maximal drag reduction are also shown, taken from the results displayed in figure 5.1.

quickly enough. Inspection of the values in table 6.1 confirms that this condition is satisfied<sup>2</sup> and therefore that, in the absence of other wake and actuator dynamics, the bistable wake mode can be stabilised using proportional feedback.

### 7.2.3 Detailed control design and performance

Given the models for  $G(s)$  and  $A(s)$  we can now design controllers,  $K(s)$ . We present the results here from the application of three controllers of increasing complexity. In each case the form of the controller is chosen before the gain is manually tuned to identify the condition for maximum drag reduction. Each controller also features a low pass filter ( $K_{LP}$ ) with a 3 dB frequency corresponding to  $St_W \approx 10$ , intended to filter out noise in order to reduce power consumption. The properties and results from the three controllers are summarised in table 7.1.

#### Proportional controller, $K_1$

Based upon the above analysis, a first controller was chosen to be of the form

$$K_1(s) = k_1 \underbrace{\frac{1}{1 + sT_L}}_{K_{LP}}, \quad (7.13)$$

where  $T_L$  is the time constant of the low-pass filter  $K_{LP}$ . The optimal gain  $k_1$  with respect to drag reduction was found by manual tuning. It can be seen from table 7.1 that such a controller achieves a drag reduction of 0.9% and requires only 11% of the saved power in order to drive the actuators. By comparing the curves for  $K_1$

<sup>2</sup>This product is given by the product of the dimensionless parameters:  $\frac{\alpha W}{U_\infty} \frac{\tau U_\infty}{W} = \alpha \tau = 0.05 \times 1.7 = 0.085$ .

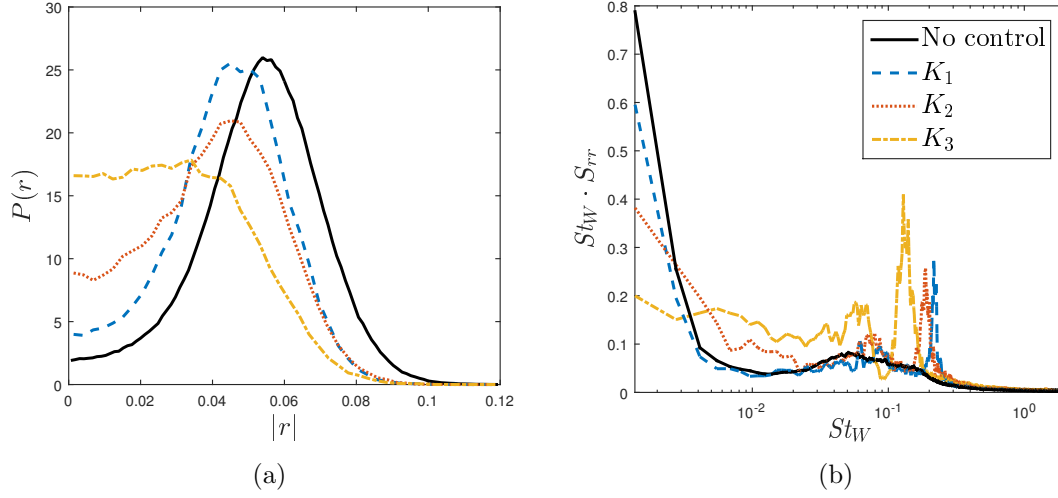


Figure 7.3: PDF for  $r$  (a) and premultiplied PSD (b) under the three controllers. The solid black line shows the uncontrolled case for comparison.

and the uncontrolled case in figure 7.3(a), it can also be seen that the controller makes the wake more symmetric on average, i.e. the peak of the PDF has moved to a smaller value of  $r$ .

The limitations of the proportional controller can be seen by looking at the sensitivity function  $S(s) = 1/(1 + A(s)K(s)G(s))$ . This is shown in figure 7.4. For a stable system, the sensitivity function gives the expected ratio of fluctuations with and without control, therefore values of greater than unity indicate that the controller amplifies fluctuations. It can be seen that for  $K_1$  there is a large peak at  $St_W \approx 0.23$ . The prediction of the sensitivity function is borne out in the closed loop PSD, shown in figure 7.3(b), where there is evidently a large peak in the fluctuations at  $St_W \approx 0.22$ . The open-loop results displayed in figure 5.1 demonstrate that fluctuations at this frequency lead to a large drag increase, and most likely correspond to an interaction with the vortex shedding. Since any further increase in gain increases the magnitude of these fluctuations, the optimal gain is found as the trade-off between providing increasing suppression of the bistability and avoiding the undesired higher-frequency interaction.

### Filtered controller, $K_2$

The limitation of the proportional controller arises in part due to the actuator dynamics: the peak sensitivity coincides with the resonant frequency of the actuator at  $St_W \approx 0.23$ , as seen in figure 7.2. These dynamics may be catered for by the



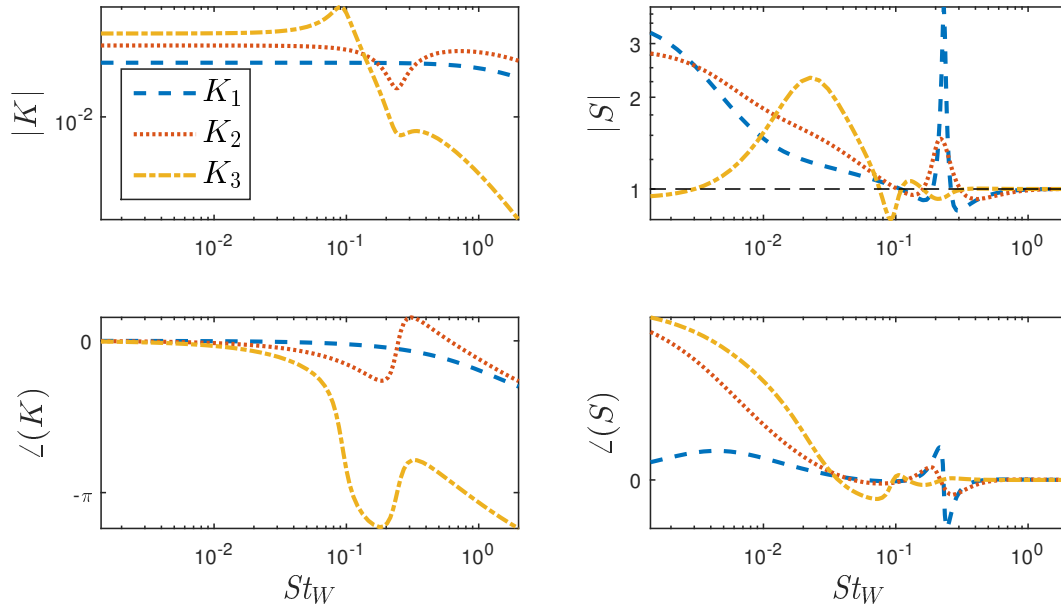


Figure 7.4: Bode plot for the controllers (left) and the expected sensitivity function  $S$  (right).

inclusion of a notch filter ( $K_N$ ) that counteracts the resonant behaviour, giving a controller of the form

$$K_2(s) = k_2 \underbrace{\frac{1 + 2\zeta_n s T_A + s^2 T_A^2}{1 + 2\zeta_d s T_A + s^2 T_A^2}}_{K_N} \underbrace{\frac{1}{1 + s T_L}}_{K_{LP}}, \quad (7.14)$$

where  $\zeta_n < \zeta_d$  and  $T_A$  is the time constant of the actuator. The controller may again be tuned by minimising the drag with respect to the DC gain  $k_2$ . The optimal drag reduction and base pressure increase, shown in table 7.1, are significantly increased to 1.6% and 3.7% respectively, while the control is only marginally less efficient than for  $K_1$ . Figure 7.3(a) demonstrates that bistability is suppressed further relative to the  $K_1$  case since the peak in the PDF is reduced.

As in the previous control case, the limitation to the gain comes from fluctuations occurring at higher frequencies. This is consistent with the sensitivity function shown in figure 7.4 which predicts amplification at  $St_W \approx 0.22$  and also confirmed by the PSD in figure 7.3(b) which shows a distinct peak for  $St_W \approx 0.19$ . The controller again represents a trade-off between achieving sufficient gain to suppress the SB mode and avoiding amplification of high-frequency fluctuations that are detrimental to drag reduction.

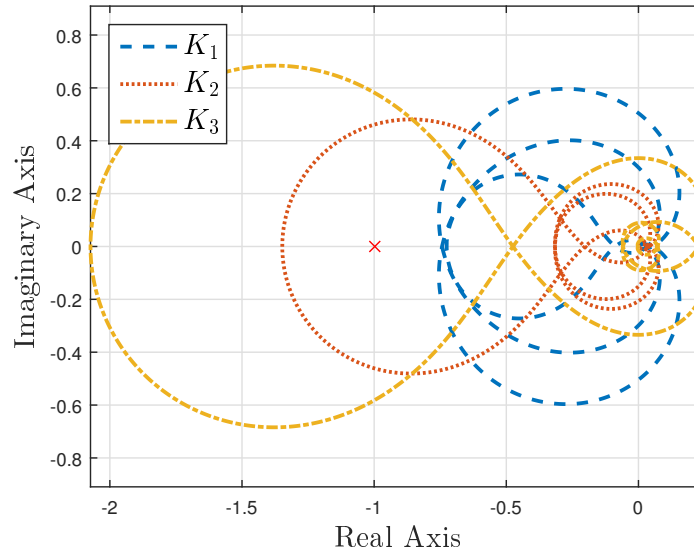


Figure 7.5: The Nyquist diagram for the three controllers. For stabilisation of the SB mode we require one encirclement of the  $-1$  location, as marked by the red cross.

### Loop shaped controller, $K_3$

The previous two controllers are both limited by the presence of fluctuations at higher frequencies that tend to increase the drag. These fluctuations limit the gain that can be achieved at lower frequencies, thus imposing a limitation on the extent to which the bistability can be suppressed. In order to improve this, it is insightful to look at the Nyquist diagram for each controller, as shown in figure 7.5.

The Nyquist diagram plots the real and imaginary parts of the loop transfer function  $L(i\omega) = G(i\omega)A(i\omega)K(i\omega)$ , and can be used to determine the expected stability and robustness. In order to stabilise the instability that leads to the SB mode, one anti-clockwise encirclement of the  $-1$  point on the Nyquist diagram is required (Åström & Murray, 2008). Practically, this means that the DC gain must be sufficiently large, as discussed in § 7.2.2. It can be seen from figure 7.5 that  $K_1$  does not achieve an encirclement while  $K_2$  does. The nonlinear saturation means that an encirclement is not strictly necessary in order for a positive effect to be achieved, but the Nyquist curves still help explain why greater suppression of the asymmetry is achieved with  $K_2$ .

The Nyquist diagram also gives insight into the sensitivity function: since  $S(s) = 1/(1 + L(s))$ , the sensitivity at any given frequency is determined by the distance between the Nyquist curve at that frequency and the  $-1$  point (shown by the cross).

Minimising the sensitivity function therefore necessitates keeping the Nyquist curve as far from the  $-1$  location as possible. However, it is also important to understand that there are fundamental limitations to the extent to which this can be achieved, as discussed above in § 7.1. In particular, while the sensitivity function may be designed to be small at some frequencies, over some other frequency range fluctuations must be amplified by the controller. In terms of drag reduction, it is important to try and place these fluctuations in a frequency range that has the least negative effect on the drag. This frequency range may be estimated from the open-loop forcing shown in figure 5.1, which displays that the generated drag increases approximately linearly for  $0.15 \lesssim St_W \lesssim 0.25$ .

The final loop-shaped controller can be seen in figure 7.4, and the “loop” seen on the Nyquist diagram of figure 7.5. The controller consists of the same notch filter as  $K_2$  but with the addition of a second-order resonant filter ( $K_R$ ), specified by the parameters  $\zeta_3$  and  $T_3$ . The objective of this filter is to reduce the loop gain over the frequency range in which vortex shedding is amplified, while minimising the phase lag at lower frequencies. This shaped controller is given by

$$K_3(s) = k_3 \underbrace{\frac{1}{1 + 2\zeta_3 s T_3 + s^2 T_3^2}}_{K_R} \underbrace{\frac{1 + 2\zeta_n s T_A + s^2 T_A^2}{1 + 2\zeta_d s T_A + s^2 T_A^2}}_{K_N} \underbrace{\frac{1}{1 + s T_L}}_{K_{LP}}. \quad (7.15)$$

The loop shape can be seen to be improved by the wider encirclement of the  $-1$  location, indicating that the low frequency gain and phase are appropriate. This is consistent with the sensitivity function of figure 7.4, which is seen to demonstrate a much smaller peak and at a lower frequency compared to the previous two controllers. The frequency of this peak is therefore now at frequencies leading to a smaller drag increase under open-loop forcing.

As shown in table 7.1 the loop-shaped controller  $K_3$  gives the highest drag reduction and base pressure increase as 2.0% and 3.9%, while also maintaining good energy efficiency. From figure 7.3(a), it is clear that the bistability has now been almost entirely suppressed as there is no longer a peak present in the PDF. This can be attributed to the higher DC gain of the controller, made possible by the loop-shaping design. Conversely, it can be seen from figure 7.3(b) that  $K_3$  led to the largest energy fluctuations of all the controllers, but was still able to achieve the highest drag reduction. This was done by placing these fluctuations at lower frequencies at which their effect on the drag is smaller, as demonstrated from the results in figure 5.1.

## 7.2.4 The controlled flow

Having observed that the controller may achieve up to a 2% drag reduction, it is worth assessing the changes that the controller makes to the flow. This may first be done by examining the time series of the mode  $r$ , as shown in figure 7.6. The complete time series shows data before and after the controller is turned on at  $t = 0$ . For  $t < 0$ ,  $r$  is seen to flip randomly, as is typical for the natural flow. With the application of the control there is an abrupt change in the behaviour, the random flipping ends and smaller values of  $r$  become much more probable, as also indicated in the PDF shown in figure 7.3(a).

Figure 7.6 also displays the drag coefficient  $C_D$  and lateral force coefficient  $C_y$ . It is evident that with the application of control there is an almost immediate reduction in  $C_D$ . This reduction is seen to be accompanied by a significant change in the lateral force. For  $t < 0$ ,  $C_y$  is seen to switch between two equal and opposite values as a result of the bistable wake. The average size of this lateral force is shown by the dashed lines. For  $t > 0$  the bimodal behaviour is suppressed and the average magnitude of the lateral force is significantly reduced, although the fluctuations are still significant. While the magnitude of the lateral force is shown here, it is important to note that the drag is likely related to the square of the lateral force  $\langle C_y^2 \rangle$ , due to induced drag effects (Grandemange *et al.*, 2013a, 2014b). However a quantitative evaluation of  $\langle C_y^2 \rangle$  may not be made from this experiment, as the inertial forces associated with the flap motion provide a significant fluctuating contribution to  $C_y$ .

We may also assess the motion of the flaps, in order to deduce the mechanism by which the controller is able to reduce the drag and lateral forces. Figure 7.7(a) shows a snapshot of the time series of  $r$  and  $\theta$ . It is clear from the time series that the two signals are closely linked, resulting from the DC gain of the controller. It can be seen that as the mode moves towards one extreme (e.g. at  $t \approx 29, 32$  s), the flaps also move in order to compensate, thereby causing the mode to move back towards a value of zero. The reactive motion of the flaps leads to a broadband spectrum for their motion, as displayed in figure 7.7(b). This indicates that the flaps do not achieve suppression of the bistability via a quasi-open-loop effect. Rather, they rely on the nature of a true feedback control system.

Although the time series of  $r$  and  $\theta$  look superficially similar, the spectra demonstrates some key differences, principle among which is the peak in  $S_{rr}$  at  $St_W \approx 0.13$ , as displayed in figure 7.3(b). As noted above, this peak is predicted by the sensitivity

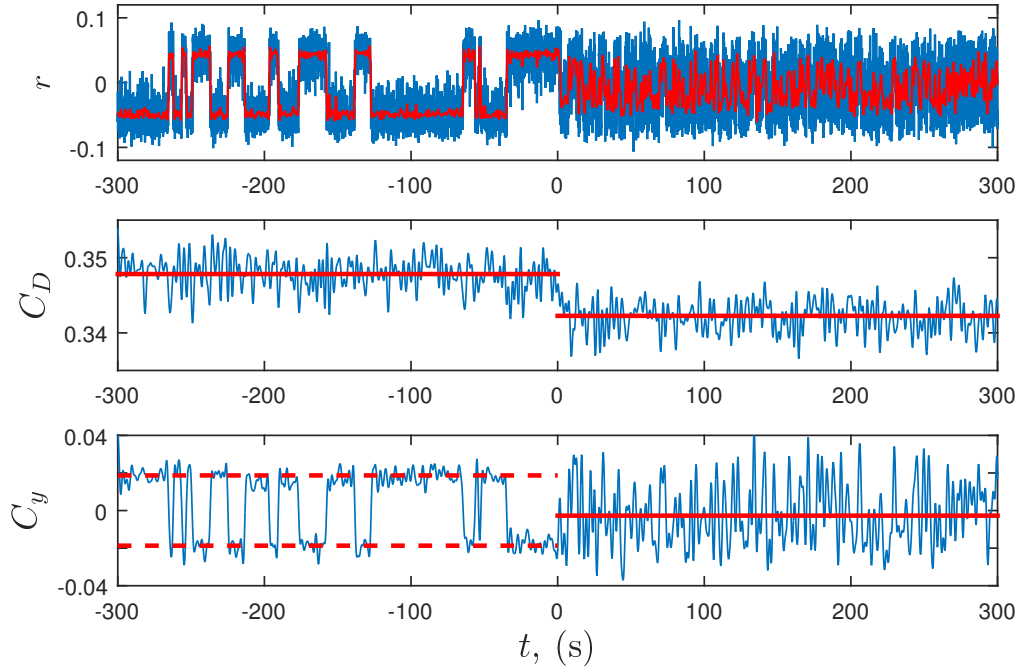


Figure 7.6: Time series of the pressure metric ( $r$ ), drag coefficient ( $C_D$ ) and lateral force coefficient ( $C_y$ ). The controller is turned on at  $t = 0$ . Red lines show the low pass filtered  $r$  and mean forces over the uncontrolled and controlled periods.

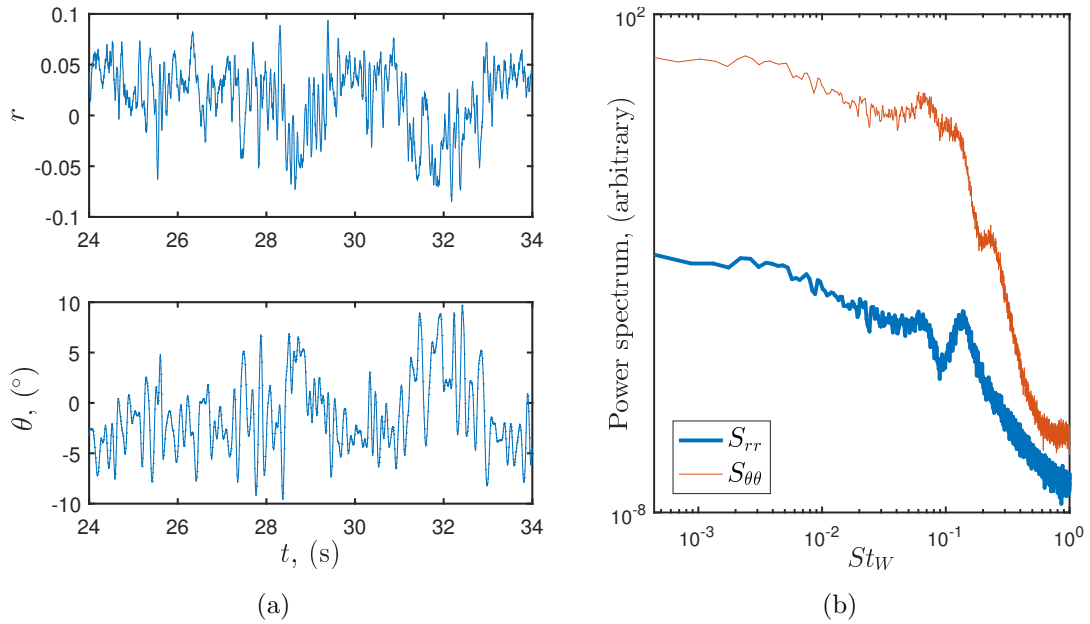


Figure 7.7: The dynamics of the actuator showing (a) a short time series of the mode  $r$  and flap angles  $\theta$ , and (b) their power spectrum.

function displayed in figure 7.4, and is therefore a result of the interaction between the flaps and the wake, arising due to the feedback. While we do not have velocity measurements to confirm the exact nature of these oscillations, it is likely that they result from an interaction with the vortex shedding of the wake since both the forcing and measurement are antisymmetric, just as for a von Kármán vortex street. Furthermore, the open-loop results shown in figure 5.1 demonstrate that open-loop forcing at  $St_W = 0.13$  leads to a small drag increase irrespective of the amplitude. It is therefore reasonable to expect that these oscillations in the closed-loop system act to increase the drag on the body and that if they could be avoided the drag reduction may be improved.

Finally, it is important to note that the measurements here cannot distinguish drag reduction from any thrust produced by the flaps. Such thrust could manifest as a force directly on the flaps or as a pressure force on the body. However, any thrust producing mechanism would have negative efficiency: the power required would be greater than the power saving. The efficiency of the system detailed in table 7.1 therefore suggests that the primary drag reduction mechanism is not thrust generation.

### 7.3 Control of vortex shedding

The principle behind the control design presented in this section is to suppress measured fluctuations over prescribed frequency ranges; the aim being to suppress vortex shedding and thereby reduce the drag. Attenuation of unsteadiness for drag reduction is an approach that has been previously applied to a number of flows in numerical simulations, including: the flow over a backward facing step (Dahan *et al.*, 2012), a D-shaped bluff body (Dalla Longa *et al.*, 2017) and the Ahmed body (Evstafyeva *et al.*, 2017). While in these examples the approach has proven effective at achieving drag reduction, there is in general no *a priori* guarantee that measured fluctuations are directly linked to the drag. In this work, we may be fairly confident that the vortex shedding is related to the drag and, from the results of chapter 4, that the fluctuations at  $St \approx 0.2$  are linked to the vortex shedding. Nevertheless, the optimal choice of controller for drag reduction is non-obvious given the necessary amplification of disturbances discussed in § 7.1.1. We therefore test a large number of controllers in order to determine the best characteristics. This will be described in detail below.

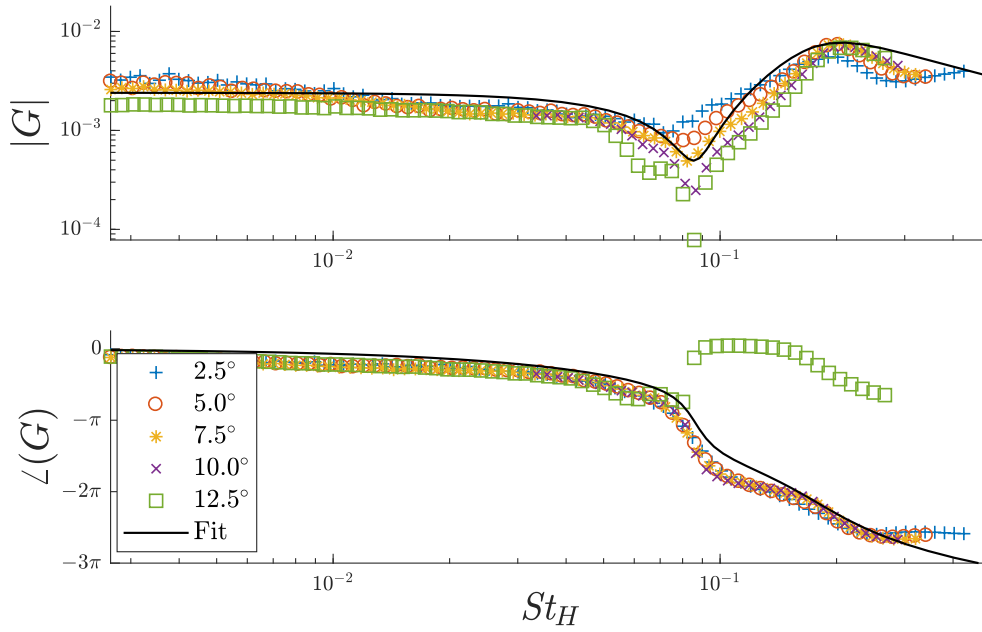


Figure 7.8: Comparison of the experimental frequency response and the composite model evaluated as the sum  $G_1(s) + G_2(s)$ .

### 7.3.1 System formation

As for the bistability control described above, we must now find the transfer function  $G(s)$  describing the response of the wake to flap forcing. As we are now considering the vertical dimension for which the flow is not bistable, the transfer function of (7.8) is no longer applicable. Instead we choose to model the wake as the sum of first and second order transfer functions, as described above in § 7.1. The resulting fit, combined with a small time delay, is displayed in figure 7.8. While this fit is imperfect, it broadly captures all the key features of the response in both magnitude and phase and will be suitable for control design. As above we will also need to include the transfer function for the actuators  $A$ , which again consists of a 2nd-order linear oscillator.

### 7.3.2 Control design

A starting point for the design of fluctuation-suppressing controllers is to examine the unforced spectrum in order to identify the frequency range of interest, as well as the drag change that open-loop forcing generates. Figure 7.9 displays the PSD

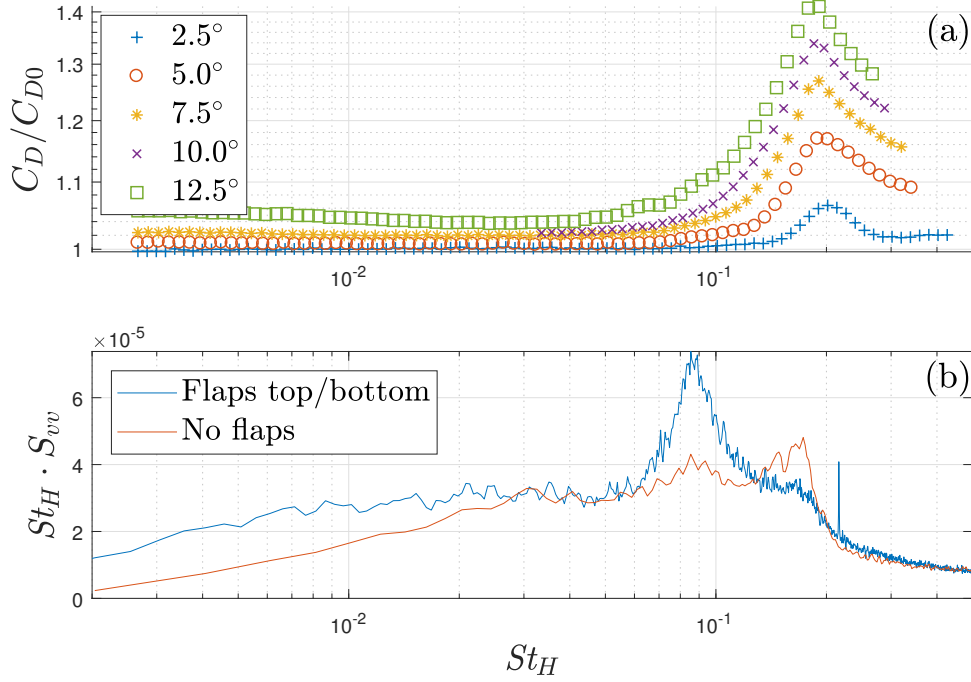


Figure 7.9: Drag change with open-loop forcing frequency (a) and PSD of the vertical pressure metric  $m_v$  for the unforced flow (b).

of the pressure metric  $m_l$  for the case both with and without vertical flaps in place and repeats the drag change data of figure 5.3 for comparison. As discussed in § 5.1, the flaps are seen to interact very strongly with the vortex shedding for  $St_H \approx 0.2$ . This frequency range is seen to approximately coincide with a “hump” in the premultiplied spectra of figure 7.9(b). This hump is actually much clearer for the case without flaps in place, but is still present for the case with flaps. The reasons for differences between these two spectra are unclear, but may consist of a combination of changes to flow features and changes to the observability of these features. Regardless of this, the control must necessarily be applied with the flaps in place. The frequency of the shedding is also consistent with previous results for the Ahmed body from Grandemange *et al.* (2013c) and Volpe *et al.* (2015).

Motivated by the spectra and observed drag changes displayed in figure 7.9 we may design controllers aiming to provide suppression in a frequency range around  $St_H \approx 0.2$ . Given the relative complexity of the system we are trying to control, it is desirable to use one of the many automated control-design algorithms available. We choose to use what is known as  $\mathcal{H}_\infty$  synthesis, using the MATLAB function `hinfscn`. As explained below, this allows automated shaping of the sensitivity function  $S$ ,



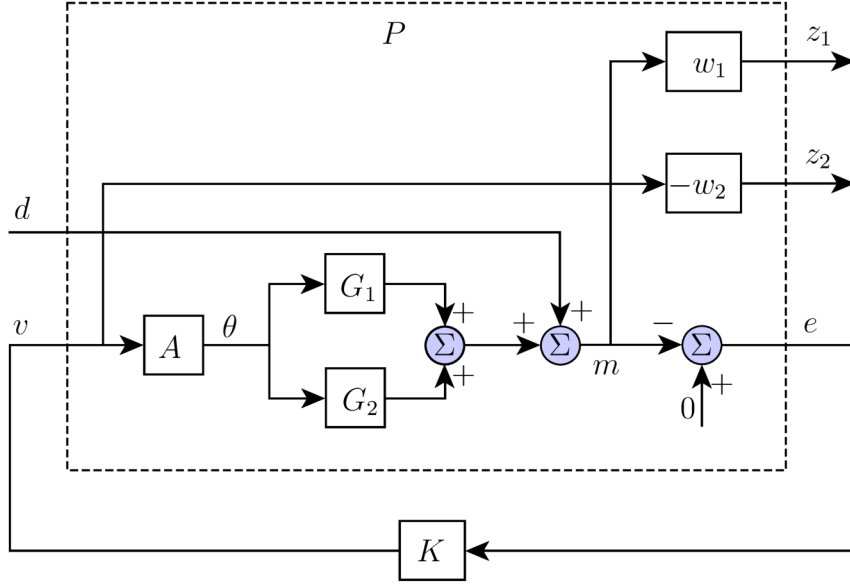


Figure 7.10: A schematic of the feedback control loop of figure 7.1, reformatted for the  $\mathcal{H}_\infty$  synthesis problem. The additional blocks  $w_1$  and  $w_2$  are weighting functions that are chosen in order to specify the desired properties of the closed-loop system.

while attempting to maintain predicted stability of the closed-loop system.

Application of  $\mathcal{H}_\infty$  synthesis requires us to rewrite our model for the system, in order to conform with the general  $\mathcal{H}_\infty$  synthesis problem. Figure 7.10 displays a schematic of the feedback control set-up, reformulated appropriately. The system is shown as a generalised plant  $P$  and controller  $K$  connected in mutual feedback. The generalised plant  $P$  has two inputs: the voltage  $v$  applied to the motors and the exogenous disturbance  $d$  discussed in § 7.1. We also choose for  $P$  to have three outputs: the error signal  $e$  and two additional errors  $z_1$  and  $z_2$ . These additional error signals are chosen such that for the closed-loop system they are related to the inputs via the following transfer functions:

$$z_1 = w_1 \left( \frac{1}{1 + GAK} \right) d = w_1 Sd, \quad (7.16)$$

$$z_2 = w_2 \left( \frac{K}{1 + GAK} \right) d = w_2 KSd. \quad (7.17)$$

The  $\mathcal{H}_\infty$  synthesis algorithm then finds a  $K$  that minimises the cost  $\gamma$ , such that for all frequencies  $\omega$ ,

$$w_1(i\omega)S(i\omega) \leq \gamma, \quad (7.18)$$

$$w_2(i\omega)K(i\omega)S(i\omega) \leq \gamma. \quad (7.19)$$

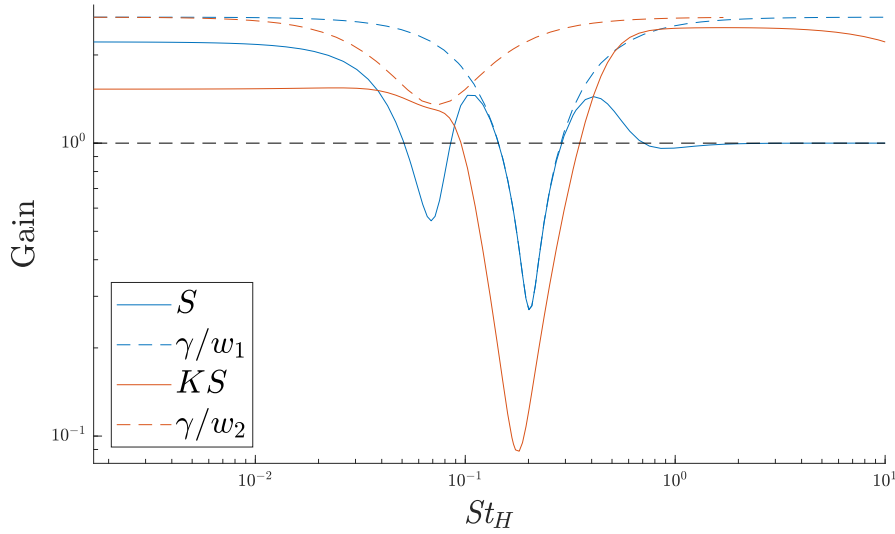


Figure 7.11: Illustration of a particular control design showing the weighting functions  $w_1$ ,  $w_2$  and the corresponding closed-loop transfer functions  $S$ ,  $KS$ .

The power of the  $\mathcal{H}_\infty$  control-design process described above is that by choosing the frequency response of the weighting functions  $w_1$  and  $w_2$  we can shape directly the *closed-loop* properties of the system; something that is otherwise challenging to do in an ad-hoc manner. More specifically, we choose  $w_1$  to be large over the frequency range in which we require fluctuation suppression. If we perform the design process specifying only  $w_1$ , overly aggressive control action may result, characterised by a controller with very high gain at some frequency. We can therefore employ the weighting function  $w_2$  to prevent such behaviour by first finding the frequency at which  $K$  is large, then choosing  $w_2$  to be large at this same frequency. Our control-design procedure is therefore a two-stage process where we first specify only  $w_1$ , then specify both  $w_1$  and  $w_2$ .

To further clarify how the control-design process works, figure 7.11 displays the transfer functions from a particular controller design. Displayed are the scaled weighting functions  $\gamma/w_1$  and  $\gamma/w_2$  and the corresponding closed-loop transfer functions  $S$  and  $KS$ . As displayed,  $1/w_1$  is chosen to be a “notch” function, dipping in a particular frequency range of  $St_H \approx 0.2$ . The  $\mathcal{H}_\infty$  control-design generates a  $K$  such that  $S$  is also small in this same frequency range, but is necessarily large elsewhere. The particular frequency and the width of the notch specified by  $1/w_1$  can be varied and a large number of variants were designed. The two-stage process of control design is detailed further in algorithm 1.

---

**Algorithm 1** The  $\mathcal{H}_\infty$  control design process.

---

- 1: Specify range of parameters for array of weighting functions  $W_1$
  - 2: **for**  $w_1^i$  in  $W_1$  **do**
  - 3:    $P^i \leftarrow P(GA, w_1^i, 1)$
  - 4:    $K_0 \leftarrow \text{hinfsyn}(P^i)$
  - 5:   find  $St_H^i$  for which  $K_0$  is maximum
  - 6:   generate  $w_2^i$  to be minimum at  $St_H^i$
  - 7:    $P^i \leftarrow P(GA, w_1^i, w_2^i)$
  - 8:    $K^i \leftarrow \text{hinfsyn}(P^i)$
  - 9:   check stability of  $K^i$
  - 10: **end for**
  - 11: Test all stable  $K^i$  experimentally
- 

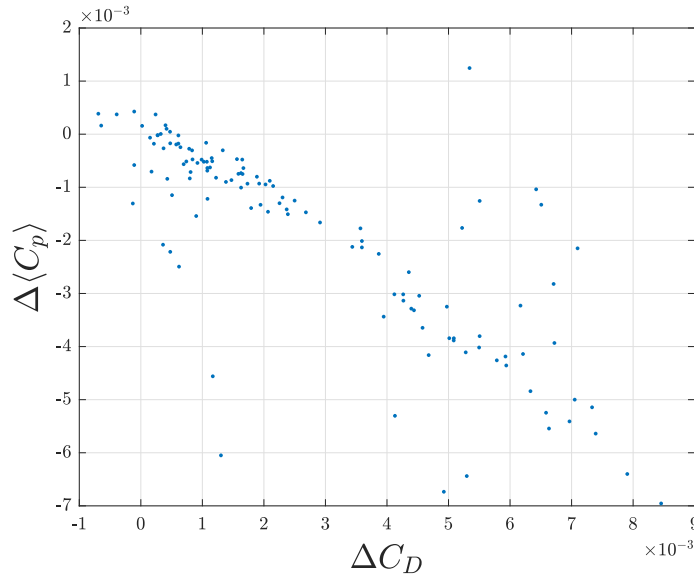


Figure 7.12: Scatter plot of the drag and base pressure changes achieved by all of the tested controllers. Positive  $\Delta C_D$  corresponds to a drag increase.

### 7.3.3 Controller performance

Following the application of the procedure outlined above, a total of  $N = 123$  controllers were tested, all achieving attenuation and amplification of fluctuations over different frequency ranges. The performance of these controllers quantified by the achieved changes in  $C_D$  and  $\langle C_p \rangle$ , is displayed in figure 7.12. Only five of the controllers give a measured drag reduction, and for all of these the drag change is within the experimental uncertainty.

The PSD for the pressure metric  $m_v$  under the action of a particular controller is displayed in figure 7.13. It is clear that for this particular controller suppression of

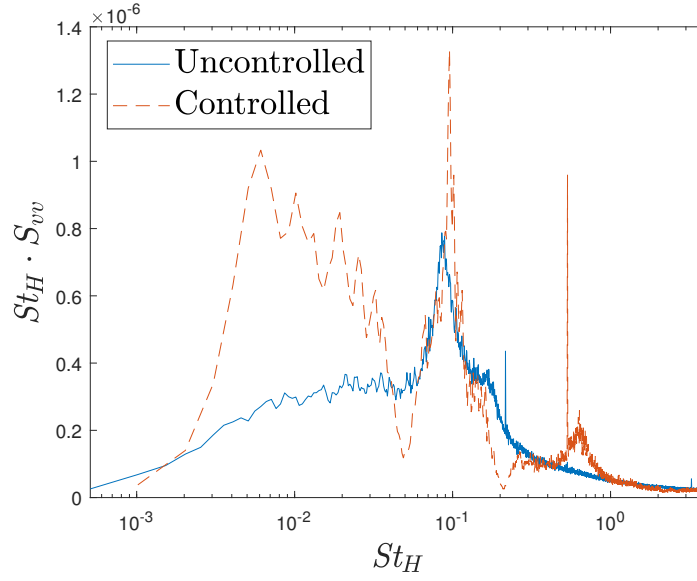


Figure 7.13: PSD of the vertical pressure metric  $m_v$  for a particular controller. Suppression is achieved around  $St_H \approx 0.2$ , however the drag is not reduced.

the measured fluctuations is achieved around the shedding frequency of  $St_H \approx 0.2$ . Also clear is the large amplification that is imposed at other frequencies, just as for the bistability control displayed in figure 7.3(b). From the changes to  $C_D$  and  $\langle C_p \rangle$ , we know that the net effect of these changes is to increase the drag, although from this example alone it not possible to decouple the beneficial and detrimental effects of the control.

### 7.3.4 Analysis of the controlled flow

The results presented above demonstrate that for the particular controllers that were tested, it was not possible to find one that could achieve measurable drag reduction. Given these results we wish to know if there is something inherently wrong with the strategy of measurement attenuation and amplification, or if drag reduction would be possible given the correct choice of controller. While for any particular controller it is only possible to observe the net impact of the changes in measured fluctuations, leveraging the information from many controllers we may hope to learn the average effect of attenuation or amplification as a function of frequency.

From the experimental implementations we have  $N$  controllers, each with a predicted sensitivity function  $S_i$  and drag change  $D_i$ . Since the predictions of the  $S_i$  will not be exactly borne out in the results, we define the experimentally determined spectral

changes as,

$$M_i(\omega) = \ln \left( \frac{\tilde{m}_v^i(\omega)}{\tilde{m}_v^0(\omega)} \right). \quad (7.20)$$

Here  $\tilde{m}_v^i$  and  $\tilde{m}_v^0$  are the magnitude of the Fourier transform of  $m_v$  for the  $i$ 'th controller and baseline case respectively. Due to the use of the logarithm in (7.20), the parameter  $M_i$  has the property that for the case of no control, it will be expected to have a value of zero for all frequencies.

As a first try, we may look to fit a linear relationship between  $M_i(\omega)$  and  $D_i$ . Such a relationship can be defined by the linear integral relation,

$$D(M) = \int_0^\infty F(\omega) M(\omega) d\omega, \quad (7.21)$$

where  $F(\omega)$  is the frequency dependent mapping function. We may hypothesize that  $F$  be large and positive around  $St_H \approx 0.2$ , as this would be consistent with our expectation that amplification/attenuation of the vortex shedding would lead to drag increases/decreases respectively. At this point it is worth noting the similarity between (7.21) and the waterbed constraint of (7.6). For the case that the sensitivity function is entirely accurate,  $M(\omega) = \ln |S(\omega)|$ , so we may therefore gain some insight from the differences between  $F(\omega)$  and the waterbed weighting function  $w(z, \omega)$ , as defined in (7.7). For example, if  $F(\omega) = w(z, \omega)$  and the relation of (7.21) were true, it would be impossible to cause drag changes through the action of feedback control. An alternative for a “frequency independent” flow might be a constant  $F(\omega) = c$ . In this case drag reduction could be achieved by placing amplification in the region where  $w(z, \omega)$  is large, thereby achieving large suppression over other frequencies. In practice neither of these seem likely to be the case, but as examples give some of the possible implications arising from the particular form of the function  $F(\omega)$ .

The linear fitting may be estimated via a least-squares minimisation, seeking to approximate  $F(\omega)$  in a piecewise manner. This procedure is detailed in appendix D.3, and consists of finding a vector  $\hat{F}$  that minimises the error between the observed drag and that predicted by (7.21). The frequency bins of this discretised weighting function are chosen to be logarithmically spaced, as this gives the fairest way to capture possible changes at all frequencies within the range of interest. The weighting function is displayed in figure 7.14(a), plotted alongside the open-loop spectrum for reference. Figure 7.14(b) shows the relationship between the true drag change induced by each controller, and that given by our approximation (7.21). These results demonstrate a good agreement, suggesting that we may have some faith in the

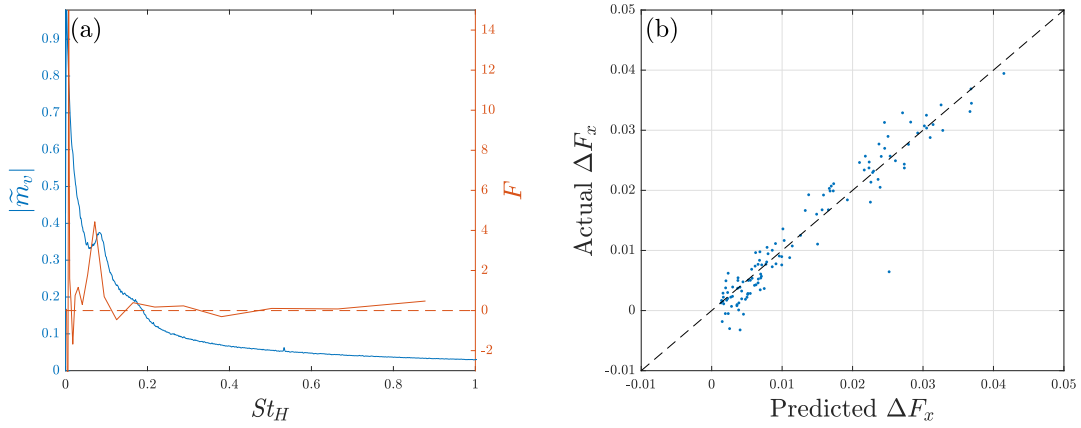


Figure 7.14: (a) A comparison of the best-fit weighting function  $\hat{F}$  with the uncontrolled spectrum, and (b) a comparison of the actual and predicted drag changes from the least-squares fit.

best-fit vector  $\hat{F}$  and the relationship described by (7.21).

At very low frequencies,  $\hat{F}$  is seen to vary between large positive and negative values. This is likely a result of over-fitting and the limited frequency resolution at this end of the spectrum, so may not necessarily have any physical significance. A possibly more significant positive value is seen for  $St_H \approx 0.09$ . Conversely for  $St_H \approx 0.2$ , the value of  $\hat{F}$  is fairly small, although still positive. This would imply that, in fact, attenuation/amplification around the frequency of the shedding has relatively little effect, compared with at frequencies approximately half that of the shedding. Regardless of this, the form of the weighting function may give some clue as to why the control was generally unsuccessful, and is displayed in figure 7.15. The peak close to  $St_H \approx 0.09$  coincides approximately with that of  $w(z, \omega)$  which is in turn the location of the RHP zeros in the frequency response. This means that it is practically very difficult to design a stable controller that provides suppression around this frequency. Moreover, most of the controllers tested in this study aimed at providing suppression at frequencies higher than  $St_H = 0.1$  so generally generated amplification over this frequency range, therefore if the form of  $\hat{F}$  is to be trusted, it is not surprising that these controllers failed to achieve drag reduction. Further work targeting lower frequency ranges may therefore prove more successful.

It is finally important to note the (significant) limitations to the above analysis approach. The founding assumption of a linear relation between  $D$  and  $M$  is of course unlikely to hold in practice, although is a natural first approximation. This is especially the case given that we are considering both amplification and attenuation

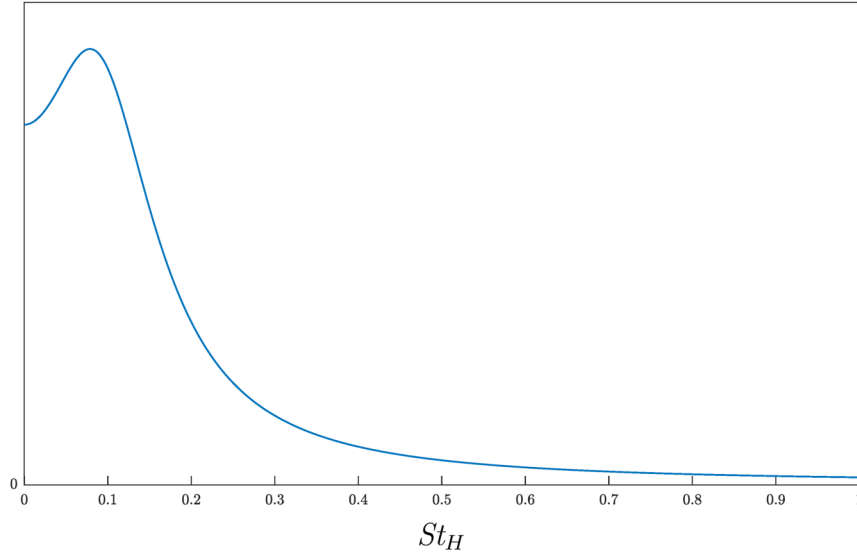


Figure 7.15: The frequency weighting function  $w(z, \omega)$ , displayed as a function of  $St_H$ .

under the same relationship. The main issue is that since none of the controllers achieved any real drag reduction, drawing insight towards more effective controllers effectively involves extrapolation of the observed trends into unknown operating conditions. The linear basis for the relationship may then be insufficient. It is also possible that the range of controllers tested had insufficiently varying characteristics for the full frequency-dependent form of  $\hat{F}$  to be determined. This problem makes the preceding arguments for the poor performance somewhat circular: all controllers increased the drag and many gave amplification near  $St_H \approx 0.1$ , possibly therefore leading to the form of  $\hat{F}$ , rather than the drag increases being the result of it. More thorough analysis ought really to include an estimate of the uncertainty in  $\hat{F}$ , based upon the range of spectral changes observed within each frequency bin. Despite these limitations, it seems likely that if due care is taken to explore more fully the frequency range of interest and to evaluate the statistical uncertainty, the above suggested method should provide a more rigorous basis on which to design controllers via the sensitivity approach.

## 7.4 Summary

Following on from the modelling of chapter 6, we have applied two different control strategies to target two different features of the Ahmed body wake. The first targeted the static mode of the wake, aiming to suppress the asymmetry associated with the

bistable behaviour. Our analysis and experimental results demonstrate that effective control requires an adequate DC gain, but that care also needs to be taken to shape the frequency response at higher frequencies, avoiding the addition of detrimental fluctuations. This strategy proved effective and achieved an efficient drag reduction of 2%. The second control approach aimed to target a fluctuating feature of the wake, namely the vortex shedding. In this case controllers were designed that targeted the fluctuations directly via a quasi-automated shaping of the sensitivity function. While this method proved able to suppress fluctuations over various frequency ranges, it did not achieve measurable drag reduction.

It is especially encouraging for the case of the bistability control that the strategy proved energetically efficient. This not only demonstrates the efficiency of the forcing flaps as actuators, but also indicates that the direct suppression of coherent structures such as the bistability is a fundamentally correct strategy. To our knowledge this strategy is one of the first to prove energy efficiency for active control of a turbulent three-dimensional wake. For the control of the vortex shedding we implemented an analysis that sought to understand the trade-offs inherent in the sensitivity function approach to control design. While the method gave some insight into the poor control performance, it is ultimately unclear whether the strategy is fundamentally flawed or if feedback control following this approach could be successful.

With regard to the actuators, it is important to note that because the flaps used here consist of a mass-spring system, minimising their power consumption requires a trade-off against control efficacy. Much of the power consumption arises due to inertial loads and the work done in deforming the springs: low power consumption therefore requires a low mass and soft springs. This is in contrast to the requirements of the control for which a stiff spring is required to maximise the actuator bandwidth.

It appeared that both controllers were limited by the presence of the RHP zeros in the frequency response, and the necessary amplification of disturbances discussed in § 7.1.1. As discussed, the zeros may be a result of the combined ability of the flaps to influence both low-frequency quasi-static features, and the oscillatory vortex shedding. This may therefore represent a limitation of forcing flaps as an actuator for this flow. The related limitation imposed by the waterbed constraint of (7.6), is one that applies in the context of the linear feedback-control methods employed in this work. It is perceivable that through the use of more complex nonlinear methods such as sum-of-squares optimisation (Chernyshenko *et al.*, 2014; Lasagna *et al.*, 2016), this limitation could to some extent be circumvented. Such approaches



---

would require an accurate (nonlinear) model for the system, of which the models of chapter 6 may be a suitable example, although the inclusion of stochasticity may prove problematic.



# Chapter 8

## Conclusions

In this thesis we have examined the application of active feedback-control techniques for the drag reduction of three-dimensional bluff bodies. We have demonstrated that efficient drag reduction is achievable, although ultimately some strategies prove to be more effective than others.

We firstly examined in chapter 3 the application of extremum-seeking control, as an improvement to the open-loop control system of Oxlade *et al.* (2015). The controller proved effective at finding the optimum operating conditions, but is naturally unable to perform better than the underlying open-loop system. Such adaptive control algorithms are certainly useful, but for efficient drag reduction an open-loop efficient system must first be developed.

The bulk of the work in this thesis has then focussed on the development of feedback control targeting particular coherent structures within the flow. Through the observability analysis of chapter 4, we demonstrated that for the axisymmetric bluff body wake the large scale asymmetry associated with the SB mode generated an extremely strong pressure imprint; readily facilitating real-time measurement. We also demonstrated that the vortex shedding had a much weaker pressure imprint, but that due to a unique frequency signature, it may still be targeted with the correct observation and control methods. As detailed in chapter 7, we were then able to develop feedback controllers that targeted each of these wake features in the Ahmed body wake. For the SB mode which manifests as a bistability in the wake, suppression through feedback control resulted in efficient drag reductions of up to 2%. For the vortex shedding control no drag reduction was achieved, despite the suppression of measured fluctuations over the frequency range in which the shedding

operates.

A key aspect of the work underlying the feedback control was the development of the low-order stochastic models for each of the SB mode and the vortex shedding, as detailed in chapter 6. These models consist of the normal form of the underlying low Reynolds number bifurcation, with the addition of a random forcing term to cater for the influence of high Reynolds number turbulence. In addition to the qualitative description that these models provide, they also capture the expected response to forcing. Therefore providing both insight for feedback control design, and giving an explanation for some of the behaviour seen under open-loop forcing.

Both the open and closed-loop forcing were performed using dynamic flaps as an active flow control actuator. These flaps provide forcing on the wake through shear layer deflection, rather than by the direct generation of momentum flux typical of other flow control actuators. Through this mechanism the flaps were able to provide forcing in both a static and dynamic sense. However, while this meant that the flaps could be used to control both the bistability and vortex shedding, this dual ability of the flaps may also have been the cause of the RHP zeros that provided an additional challenge for feedback control.

A final utility for both the open- and closed-loop forcing is the improved understanding of the conditions under which aerodynamic drag may be reduced. The static forcing results displayed in chapter 5 and the bistability control discussed in chapter 7, both confirm the link between the lateral and stream-wise forces on bluff bodies. Suppression of lateral forces with movable flaps therefore proves to be an effective drag reduction strategy. The confirmed relationship between forces clarifies some of the conditions under which bluff body drag may be minimised. In contrast, it remains unclear if suppression of measured fluctuations in general - and the vortex shedding more specifically - is a suitable control approach for drag reduction. We have also presented a method to attempt to quantify the effect of fluctuations, which may prove suitable as the basis of further investigations.

## 8.1 Possible future work

Motivation for the effective drag reduction of bluff bodies remains strong, with economic and environmental influences not likely to fade in the near future. The application of closed-loop active methods for drag reduction therefore remains a

promising and worthwhile approach, but must continue to be based on improved physical understanding. Specific items to address following on from this work could be as follows:

1. The application of extremum-seeking algorithms to a system using quasi-statically positioned flaps.

For bodies positioned at yaw angles with respect to the flow, e.g. due to cross-wind, the asymmetric static positioning of lateral flaps offers significant drag reductions. Given that the yaw angles of the flow vary only gradually, this would be an ideal application for an ES control algorithm that minimised the drag as a function of the two flap positions. In principle, an additional control algorithm such as the bistability suppressing control could be implemented in parallel.

2. The development of more advanced observation algorithms for real-time flow measurement in three-dimensional wakes.

These algorithms could involve finding optimal spatial structures on which to project the pressure measurements, and the use of known dynamics through, for example, a Kalman filtering approach. Pressure measurements in three-dimensional wake flows often reveal spectral peaks, and may be decomposed into orthogonal spatial structures, however deducing the particular flow-field features associated with these structures remains a challenge.

3. A full understanding of the differences between two- and three-dimensional wakes.

There is a general understanding that the vortex shedding in three-dimensional wakes is weaker and less coherent than for two-dimensional cases. Further to this it is clear that the SB mode is only present in three-dimensional wakes, along with additional features such as a vortex shedding “sub-harmonic” (Rigas *et al.*, 2014). However, a full understanding of these features and a quantitative assessment of their relative drag contributions is still lacking.

4. Improved understanding of the physical mechanism underlying the instability leading to the SB mode.

While the SB mode can be predicted by stability analysis, accurately simulated by numerical methods and observed experimentally over a wide range of Reynolds numbers, a physical mechanism underlying the instability is not yet known. What is likely required are numerical or practical experiments that

can isolate particular flow features to fully develop mechanistic understanding. For the SB mode this may involve investigations that can separate the effects of the shear layers and internal flow within the recirculation region.

5. Investigation into the effect of Reynolds number on the controllability of coherent flow structures.

Over low Reynolds numbers it is understood that for flows such as the circular cylinder wake, feedback control efficacy decreases with  $Re$  (Illingworth, 2016). Ranging over higher Reynolds numbers the trend is not so clear, as a very limited number of studies have attempted control in such cases. Through the modelling approach employed in this work, we have considered the turbulence simply as a noise/disturbance term and have found that over a limited range of  $Re$  dimensionless parameters remain approximately constant. From this viewpoint, global flow instabilities should be stabilisable even up to a very large Reynolds number, albeit with increased disturbance levels. It remains to be seen if this is in fact possible. Analysis of many flows demonstrates a very large number of “global modes” for the linearised system (Barbagallo *et al.*, 2011), several of which are unstable. With increasing Reynolds number it seems likely that the number of unstable modes will increase.

6. Further investigation of fluctuation suppressing controllers in three-dimensional wakes.

Several previous studies have demonstrated effective use of fluctuation suppressing controllers for 2D or low  $Re$  flows. However, in this work we were unable to find an effective strategy for a high  $Re$  3D wake. While fluctuations may be suppressed over various frequency ranges, effective drag reduction could not be achieved. It would be interesting to pursue the approach tried here further, taking care to cover a wider range of controllers and estimate the uncertainty in any empirical relationship between drag changes and fluctuation frequency. Ultimately, one would hope to establish if a sensitivity-function-based linear control strategy could ever be effective, or whether there is a fundamental limitation.

7. The application of nonlinear control methods, designed to overcome some of the limitations inherent in the system.

Standard linear control methods may be unable to overcome the limitations imposed by features such as RHP zeros. It is possible that more sophisticated nonlinear methods may be able to do so, given a suitably informative model of

---

the system. This would be something worth exploring initially in simulations, perhaps based on the stochastic models given in this work.





# Bibliography

- ADRIAN, R. J. 1994 Stochastic estimation of conditional structure: a review. *Applied Scientific Research* **53** (3), 291–303.
- AHMED, S., RAMM, G. & FALTIN, G. 1984 Some salient features of the time-averaged ground vehicle wake. *SAE Tech. Rep.* **840300**, Society of Automotive Engineers.
- ALEKSIĆ-ROESSNER, K., KING, R., LEHMANN, O., TADMOR, G. & MORZYŃSKI, M. 2014 On the need of nonlinear control for efficient model-based wake stabilization. *Theor. Comput. Fluid Dyn.* **28** (1), 23–49.
- ARIYUR, K. B. & KRSTIĆ, M. 2003 *Real-Time Optimization by Extremum-Seeking Control*. John Wiley & Sons Inc.
- ÅSTRÖM, K. J. & MURRAY, R. M. 2008 *Feedback Systems An Introduction for Scientists and Engineers*. Princeton University Press.
- BALACHANDAR, S., MITTAL, R. & NAJJAR, F. M. 1997 Properties of the mean recirculation region in the wakes of two-dimensional bluff bodies. *J. Fluid Mech.* **351**, 167–199.
- BARBAGALLO, A., DERGHAM, G., SIPP, D., SCHMID, P. J. & ROBINET, J.-C. 2012 Closed-loop control of unsteadiness over a rounded backward-facing step. *J. Fluid Mech.* **703**, 326–362.
- BARBAGALLO, A., SIPP, D. & SCHMID, P. J. 2009 Closed-loop control of an open cavity flow using reduced-order models. *J. Fluid Mech.* **641**, 1–50.
- BARBAGALLO, A., SIPP, D. & SCHMID, P. J. 2011 Input–output measures for model reduction and closed-loop control: application to global modes. *J. Fluid Mech.* **685**, 23–53.

- BARROS, D., BORÉE, J., NOACK, B. R. & SPOHN, A. 2016a Resonances in the forced turbulent wake past a 3D blunt body. *Phys. Fluids* **28**, 065104.
- BARROS, D., BORÉE, J., NOACK, B. R., SPOHN, A. & RUIZ, T. 2016b Bluff body drag manipulation using pulsed jets and Coanda effect. *J. Fluid Mech.* **805**, 429–455.
- BEAUDOIN, J. F., CADOT, O., AIDER, J.-L. & WESFREID, J. E. 2006 Bluff-body drag reduction by extremum-seeking control. *J. Fluids Struct.* **22**, 973–978.
- BECKER, R., KING, R., PETZ, R. & NITSCHKE, W. 2007 Adaptive Closed-Loop Separation Control on a High-Lift Configuration Using Extremum Seeking. *AIAA J.* **45** (6), 1382–1392.
- BENARD, N., MOREAU, E., GRIFFIN, J. & CATTAFESTA III, L. N. 2009 Slope seeking for autonomous lift improvement by plasma surface discharge. *Exp. Fluids* **48** (5), 791–808.
- BERGER, E., SCHOLZ, D. & SCHUMM, M. 1990 Coherent Vortex Structures in the Wake of a Sphere and a Circular Disk at Rest and under Forced Vibrations. *J. Fluid Struct.* **4**, 231–257.
- BIGGER, R. P., HIGUCHI, F. & HALL, J. W. 2009 Open-Loop Control of Disk Wakes. *AIAA J.* **47** (5), 1186–1194.
- BODE, H. W. 1945 *Network Analysis and Feedback Amplifier Design*. Van Nostrand, New York.
- BOHORQUEZ, P., SANMIGUEL-ROJAS, E., SEVILLA, A., JIMÉNEZ-GONZÁLEZ, J. I. & MARTÍNEZ-BAZÁN, C. 2011 Stability and dynamics of the laminar wake past a slender blunt-based axisymmetric body. *J. Fluid Mech.* **676**, 110–144.
- BONNAVION, G., CADOT, O., ÉVRARD, A., HERBERT, V., PARPAIS, S., VIGNERON, R. & DÉLERY, J. 2017 On multistabilities of real car's wake. *J. Wind Eng. Ind. Aerodyn.* **164**, 22–33.
- BORÉE, J. 2003 Extended proper orthogonal decomposition: a tool to analyse correlated events in turbulent flows. *Exp. Fluids* **35** (2), 188–192.
- BRACKSTON, R. D., GARCÍA DE LA CRUZ, J. M., WYNN, A., RIGAS, G. & MORRISON, J. F. 2016a Stochastic modelling and feedback control of bistability in a turbulent bluff body wake. *J. Fluid Mech.* **802**, 726–749.

- BRACKSTON, R. D., WYNN, A. & MORRISON, J. F. 2016*b* Extremum seeking to control the amplitude and frequency of a pulsed jet for bluff body drag reduction. *Exp. Fluids* **57** (10), 159.
- BROWN, E. & AHLERS, G. 2007 Large-Scale Circulation Model for Turbulent Rayleigh-Bénard Convection. *Phys. Rev. Lett.* **98**, 134501.
- BRUNTON, S. L. & NOACK, B. R. 2015 Closed-loop turbulence control: Progress and challenges. *ASME. Appl. Mech. Rev.* **67**, 050801.
- BURY, Y. & JARDIN, T. 2012 Transitions to chaos in the wake of an axisymmetric bluff body. *Phys. Lett. A* **376** (45), 3219–3222.
- CABITZA, S. 2014 *Active Control of the Wake from a Rectangular-Sectioned Body*. PhD thesis, Imperial College London.
- CADOT, O., EVRARD, A. & PASTUR, L. 2015 Imperfect supercritical bifurcation in a three-dimensional turbulent wake. *Phys. Rev. E* **91**, 063005.
- CALLI, B., CAARLS, W., JONKER, P. & WISSE, M. 2012 Comparison of extremum seeking control algorithms for robotic applications. In *IEEE Int. Conf. Intell. Robot. Syst.*, pp. 3195–3202. Vilamoura: IEEE.
- CHABERT, T., DANDOIS, J. & GARNIER, É. 2014 Experimental closed-loop control of flow separation over a plain flap using slope seeking. *Exp. Fluids* **55** (1797).
- CHABERT, T., DANDOIS, J. & GARNIER, É. 2016 Experimental closed-loop control of separated-flow over a plain flap using extremum seeking. *Exp. Fluids* **57** (37).
- CHEN, K. K. & ROWLEY, C. W. 2011  $H_2$  optimal actuator and sensor placement in the linearised complex Ginzburg–Landau system. *J. Fluid Mech.* **681**, 241–260.
- CHERNYSHENKO, S. I., GOULART, P., HUANG, D. & PAPACHRISTODOULOU, A. 2014 Polynomial sum of squares in fluid dynamics: a review with a look ahead. *Phil. Trans. R. Soc. A* **372**.
- CHOI, H., JEON, W.-P. & KIM, J. 2008 Control of flow over a bluff body. *Annu. Rev. Fluid Mech.* **40**.
- CHOMAZ, J. 2005 Global Instabilities in Spatially Developing Flows: Non-Normality and Nonlinearity. *Annu. Rev. Fluid Mech.* **37**, 357–392.

- DAHAN, J. A., MORGANS, A. S. & LARDEAU, S. 2012 Feedback control for form-drag reduction on a bluff body with a blunt trailing edge. *J. Fluid Mech.* **704**, 360–387.
- DALLA LONGA, L., MORGANS, A. S. & DAHAN, J. A. 2017 Reducing the pressure drag of a D-shaped bluff body using linear feedback control. *Theor. Computat. Fluid Dyn.* pp. 1–11.
- DURGESH, V. & NAUGHTON, J. W. 2010 Multi-time-delay LSE-POD complementary approach applied to unsteady high-reynolds-number near wake flow. *Exp. Fluids* **49** (3), 571–583.
- ECKHARDT, B., SCHNEIDER, T. M., HOF, B. & WESTERWEEL, J. 2007 Turbulence transition in pipe flow. *Annu. Rev. Fluid Mech.* . 39: **39**, 447–468.
- EVARD, A., CADOT, O., HERBERT, V., RICOT, D., VIGNERON, R. & DÉLERY, J. 2015 Fluid force and symmetry breaking modes of a 3D bluff body with a base cavity. *J. Fluid Struct.* **61**, 99–114.
- EVSTAFYEVA, O., MORGANS, A. S. & DALLA LONGA, L. 2017 Simulation and feedback control of the Ahmed body flow exhibiting symmetry breaking behaviour. *J. Fluid Mech.* **817**, R2.
- FABRE, D., AUGUSTE, F. & MAGNAUDET, J. 2008 Bifurcations and symmetry breaking in the wake of axisymmetric bodies. *Phys. Fluids* **20**, 051702.
- FACCHINETTI, M. L., DE LANGRE, E. & BIELLEY, F. 2004 Coupling of structure and wake oscillators in vortex-induced vibrations. *J. Fluids Struct.* **19**, 123–140.
- FFOWCS WILLIAMS, J. E. & ZHAO, B. C. 1989 The active control of vortex shedding. *J. Fluid Struct.* **3** (2), 115–122.
- FLINOIS, T. L. B. & MORGANS, A. S. 2016 Feedback control of unstable flows: a direct modelling approach using the eigensystem realisation algorithm. *J. Fluid Mech.* **793**, 41–78.
- FREUDENBERG, J. S. & LOOZE, D. P. 1985 Right Half Plane Poles and Zeros and Design Tradeoffs in Feedback Systems. *IEEE Transactions on Automatic Control* **AC-30** (6), 555–565.
- GAMMAITONI, L., HÄNGGI, P., JUNG, P. & MARCHESONI, F. 1998 Stochastic resonance. *Rev. Mod. Phys.* **70** (1), 223–287.

- GARCÍA DE LA CRUZ, J. M., BRACKSTON, R. D. & MORRISON, J. F. 2017 Adaptive base-flap under variable cross-wind. In *52nd 3AF International Conference on Applied Aerodynamics Progress in Flow Control*. Lyon: 3AF.
- GARCÍA DE LA CRUZ, J. M., OXLADE, A.R. & MORRISON, J. F. 2014 Drag reduction of an axisymmetric bluff body using splitter plates. Personal communication.
- GAUTIER, N. & AIDER, J.-L. 2014 Feed-forward control of a perturbed backward-facing step flow. *J. Fluid Mech.* **759**, 181–196.
- GAUTIER, N., AIDER, J.-L., DURIEZ, T., NOACK, B. R., SEGOND, M. & ABEL, M. 2015 Closed-loop separation control using machine learning. *J. Fluid Mech.* **770**, 442–457.
- GELBERT, GREGOR, MOECK, JONAS. P., PASCHEREIT, CHRISTIAN O. & KING, RUDIBERT 2012 Advanced algorithms for gradient estimation in one- and two-parameter extremum seeking controllers. *J. Process Control* **22**, 700–709.
- GENTILE, V., SCHRIJER, F. F. J., VAN OUDHEUSDEN, B. W. & SCARANO, F. 2016 Low-frequency behavior of the turbulent axisymmetric near-wake. *Phys. Fluids* **28**, 06510.
- GENTILE, V., VAN OUDHEUSDEN, B. W., SCHRIJER, F. F. J. & SCARANO, F. 2017 The effect of angular misalignment on the low-frequency axisymmetric wake instability. *J. Fluid Mech.* **813**, R3.
- GRANDEMANGE, M. 2013 *Analysis and Control of Three-dimensional Turbulent Wakes: from Axisymmetric Bodies to Road Vehicles*. PhD thesis, École Polytechnique — ENSTA ParisTech.
- GRANDEMANGE, M., A., MARY, GOHLKE, M. & CADOT, O. 2013a Effect on drag of the flow orientation at the base separation of a simplified blunt road vehicle. *Exp. Fluids* **54**, 1529.
- GRANDEMANGE, M., CADOT, O., COURBOIS, A., HERBERT, V., RICOT, D., RUIZ, T. & VIGNERON, R. 2015 A study of wake effects on the drag of Ahmed's squareback model at the industrial scale. *J. Wind Eng. Ind. Aerodyn.* **145**, 282–291.
- GRANDEMANGE, M., CADOT, O. & GOHLKE, M. 2012a Reflectional symmetry breaking of the separated flow over three-dimensional bluff bodies. *Phys. Rev. E* **86**, 035302.

- GRANDEMANGE, M., GOHLKE, M. & CADOT, O. 2013*b* Bi-stability in the turbulent wake past parallelepiped bodies with various aspect ratios and wall effects. *Phys. Fluids* **25**, 095103.
- GRANDEMANGE, M., GOHLKE, M. & CADOT, O. 2013*c* Turbulent wake past a three-dimensional blunt body. Part 1. Global modes and bi-stability. *J. Fluid Mech.* **722**, 51–84.
- GRANDEMANGE, M., GOHLKE, M. & CADOT, O. 2014*a* Statistical axisymmetry of the turbulent sphere wake. *Exp. Fluids* **55**, 1838.
- GRANDEMANGE, M., GOHLKE, M. & CADOT, O. 2014*b* Turbulent wake past a three-dimensional blunt body. Part 2. Experimental sensitivity analysis. *J. Fluid Mech.* **752**, 439–461.
- GRANDEMANGE, M., GOHLKE, M., PAREZANOVIĆ, V. & CADOT, O. 2012*b* On experimental sensitivity analysis of the turbulent wake from an axisymmetric blunt trailing edge. *Phys. Fluids* **24**, 035106.
- GREENBLATT, D. & WYGNANSKI, I. J. 2000 The control of flow separation by periodic excitation. *Prog. Aerosp. Sci.* **36** (7), 487–545.
- HENNING, L., BECKER, R., FEUERBACH, G., MUMINOVIC, R., KING, R., BRUNN, A. & NITSCHKE, W. 2008 Extensions of adaptive slope-seeking for active flow control. *Proc. Inst. Mech. Eng. Part I J. Syst. Control Eng.* **222**, 309–322.
- HERRY, B., KEIRSBULCK, L., LABRAGA, L. & PAQUET, J-B. 2011 Flow bistability downstream of three-dimensional double backward facing steps at zero-degree sideslip. *J. Fluids Eng.* **133**, 054501.
- HERVÉ, A., SIPP, D., SCHMID, P. J. & SAMUELIDES, M. 2012 A physics-based approach to flow control using system identification. *J. Fluid Mech.* **702**, 26–58.
- HO, Y. C. & PEPYNE, D. L. 2002 Simple explanation of the no-free-lunch theorem and its implications. *J. Optim. Theory Appl.* **115**, 549–570.
- HOLMES, P., LUMLEY, J. L. & BERKOOZ, G. 1998 *Turbulence, Coherent Structures, Dynamical Systems and Symmetry*. Cambridge University Press.
- HOSSEINI, Z., MARTINUZZI, R. J. & NOACK, B. R. 2015 Sensor-based estimation of the velocity in the wake of a low-aspect-ratio pyramid. *Exp. Fluids* **56** (1), 13.

- HUCHO, W. & SOVRAN, G. 1993 Aerodynamics of road vehicles. *Annu. Rev. Fluid Mech.* **25**, 485–537.
- HUDY, L. M., NAGUIB, A. & HUMPHREYS, W. M. 2007 Stochastic estimation of a separated-flow field using wall-pressure-array measurements. *Phys. Fluids* **19** (2), 024103.
- HUERRE, P. & MONKEWITZ, P. A. 1990 Local and global instabilities in spatially developing flows. *Annu. Rev. Fluid Mech.* **22**, 473–537.
- ILLINGWORTH, S. J. 2016 Model-based control of vortex shedding at low reynolds numbers. *Theor. Comput. Fluid Dyn.* **30** (5), 429–448.
- ILLINGWORTH, S. J., MORGANS, A. S. & ROWLEY, C. W. 2012 Feedback control of cavity flow oscillations using simple linear models. *J. Fluid Mech.* **709**, 223–248.
- ILLINGWORTH, S. J., NAITO, H. & FUKAGATA, K. 2014 Active control of vortex shedding: An explanation of the gain window. *Phys. Rev. E* **90**, 043014.
- JACKSON, C. P. 1987 A finite-element study of the onset of vortex shedding in flow past variously shaped bodies. *J. Fluid Mech.* **182**, 23–45.
- JONES, B. L., HEINS, P. H., KERRIGAN, E. C., MORRISON, J. F. & SHARMA, A. S. 2015 Modelling for robust feedback control of fluid flows. *J. Fluid Mech.* **769**, 687–722.
- JUANG, J. N. & PAPPAS, R. S. 1985 An eigensystem realization algorithm for modal parameter identification and model reduction. *J. Guid. Control Dyn.* **8** (5), 620–627.
- KIM, J. & BEWLEY, T. R. 2007 A linear systems approach to flow control. *Annu. Rev. Fluid Mech.* **39**, 383–417.
- KIM, K., KASNAKOĞLU, C., SERRANI, A. & SAMIMY, M. 2009 Extremum-Seeking Control of Subsonic Cavity Flow. *AIAA J.* **47** (1), 195–205.
- KIRCHHOFF, G. 1869 Zur theorie freier flüssigkeitsstrahlen. *J. für die reine und Angew. Math.* **70**, 289–298.
- KOTAPATI, R. B., MITTAL, R., MARXEN, O., HAM, F., YOU, D. & CATTAFESTA III, L. N. 2010 Nonlinear dynamics and synthetic-jet-based control of a canonical separated flow. *J. Fluid Mech.* **654**, 65–97.



- KOURTA, A. & LECLERC, C. 2013 Characterization of synthetic jet actuation with application to Ahmed body wake. *Sensors Actuators A: Physical* **192**, 13–26.
- KRSTIĆ, M. 2000 Performance improvement and limitations in extremum seeking control. *Syst. Control Lett.* **39**, 313–326.
- KRSTIĆ, M. & WANG, H. 2000 Stability of extremum seeking feedback for general nonlinear dynamic systems. *Automatica* **36**, 595–601.
- LASAGNA, D., HUANG, D., TUTTY, O. R. & CHERNYSHENKO, S. 2016 Sum-of-squares approach to feedback control of laminar wake flows. *J. Fluid Mech.* **809**, 628–663.
- LASAGNA, D., ORAZI, M. & IUSO, G. 2013 Multi-time delay, multi-point linear stochastic estimation of a cavity shear layer velocity from wall-pressure measurements. *Phys. Fluids* **25** (1), 017101.
- LAUGA, E. & BEWLEY, T. R. 2003 The decay of stabilizability with reynolds number in a linear model of spatially developing flows. *Proc. R. Soc. London A* **459** (2036), 2077–2095.
- LAUGA, E. & BEWLEY, T. R. 2004 Performance of a linear robust control strategy on a nonlinear model of spatially developing flows. *J. Fluid Mech.* **512**, 343–374.
- LE GAL, P., NADIM, A. & THOMPSON, M. 2001 Hysteresis in the forced stuart–landau equation: Application to vortex shedding from an oscillating cylinder. *J. Fluids Struct.* **15** (3), 445–457.
- LEE, S. J. & BEARMAN, P. W. 1992 An experimental investigation of the wake structure behind a disk. 6, . *J. Fluids Struct.* **6**, 437–450.
- LI, L. K. B. & JUNIPER, M. P. 2013a Lock-in and quasiperiodicity in a forced hydrodynamically self-excited jet. *J. Fluid Mech.* **726**, 624–655.
- LI, L. K. B. & JUNIPER, M. P. 2013b Phase trapping and slipping in a forced hydrodynamically self-excited jet. *J. Fluid Mech.* **735**, R5.
- LI, R., BARROS, D., BORÉE, J., CADOT, O., NOACK, B. R. & CORDIER, L. 2016 Feedback control of bimodal wake dynamics. *Exp. Fluids* **57**, 158.
- MA, Z., AHUJA, S. & ROWLEY, C. W. 2010 Reduced-order models for control of fluids using the eigensystem realization algorithm. *Theor. Computat. Fluid Dyn.* **25** (1), 233–247.



- MARIOTTI, A. & BURESTI, G. 2013 Experimental investigation on the influence of boundary layer thickness on the base pressure and near-wake flow features of an axisymmetric blunt-based body. *Exp. Fluids* **54**, 1612.
- MEILE, W., LADINEK, T., BRENN, G., REPPENHAGEN, A. & FUCHS, A. 2016 Non-symmetric bi-stable flow around the ahmed body. *Int. J. Heat Fluid Flow* **57**, 34–47.
- MELIGA, P., CHOMAZ, J-M. & SIPP, D. 2009 Global mode interaction and pattern selection in the wake of a disk: a weakly nonlinear expansion. *J. Fluid Mech.* **633**, 159–189.
- MONKEWITZ, P. A. 1988 A note on vortex shedding from axisymmetric bluff bodies. *J. Fluid Mech.* **192**, 561–575.
- MONKEWITZ, P. A. 1996 Modeling of self-excited wake oscillations by amplitude equations. *Exp. Therm. Fluid Science* **12** (2), 175–183.
- MORGANS, A. S. & DOWLING, A. P. 2007 Model-based control of combustion instabilities. *J. Sound Vib.* **299**, 261–282.
- NEŠIĆ, D. 2009 Extremum Seeking Control: Convergence Analysis. *Eur. J. Control* **15**, 331–347.
- NOACK, B. R., AFANASIEV, K., MORZYŃSKI, M., TADMOR, G. & THIELE, F. 2003 A hierarchy of low-dimensional models for the transient and post-transient cylinder wake. *J. Fluid Mech.* **497**, 335–363.
- NORBERG, C. 1994 An experimental investigation of the flow around a circular cylinder: influence of aspect ratio. *J. Fluid Mech.* **258**, 287–316.
- OXLADE, A. R. 2013 *High-frequency Pulsed Jet Forcing of an Axisymmetric Bluff Body Wake*. PhD thesis, Imperial College London.
- OXLADE, A. R., MORRISON, J. F., QUBAIN, A. & RIGAS, G. 2015 High-frequency forcing of a turbulent axisymmetric wake. *J. Fluid Mech.* **770**, 305–318.
- PARKIN, D. J., SHERIDAN, J. & THOMPSON, M. C. 2015 Numerical analysis of periodic open-loop flow control on bluff bodies in ground proximity. *J. Wind Eng. Ind. Aerodyn.* **145**, 339–350.
- PARKIN, D. J., THOMPSON, M. C. & SHERIDAN, J. 2014 Numerical analysis of bluff body wakes under periodic open-loop control. *J. Fluid Mech.* **739**, 94–123.

- PASTOOR, M., HENNING, L., NOACK, B. R., KING, R. & TADMOR, G. 2008 Feedback shear layer control for bluff body drag reduction. *J. Fluid Mech.* **608**, 161–196.
- PEARSON, D. S. 2012 *Characterisation and estimation of the flow over a forward-facing step*. PhD thesis, Imperial College London.
- PIER, B. 2008 Local and global instabilities in the wake of a sphere. *J. Fluid Mech.* **603**, 39–61.
- QUBAIN, A. 2009 *Active Control of a Turbulent Bluff Body Wake*. PhD thesis, Imperial College London.
- RAVELET, F., MARIE, L., CHIFFAUDEL, A. & DAVIAUD, F. 2004 Multistability and memory effect in a highly turbulent flow: Experimental evidence for a global bifurcation. *Phys. Rev. Lett.* **93**, 164501.
- RIGAS, G. 2014 *Modelling of turbulent wakes*. PhD thesis, Imperial College London.
- RIGAS, G., MORGANS, A. S., BRACKSTON, R. D. & MORRISON, J. F. 2015 Diffusive dynamics and stochastic models of turbulent axisymmetric wakes. *J. Fluid Mech.* **778**, R2.
- RIGAS, G., MORGANS, A. S. & MORRISON, J. F. 2017 Weakly nonlinear modelling of a forced turbulent axisymmetric wake. *J. Fluid Mech.* **814**, 570–591.
- RIGAS, G., OXLADE, A. R., MORGANS, A. S. & MORRISON, J. F. 2014 Low-dimensional dynamics of a turbulent axisymmetric wake. *J. Fluid Mech.* **755**, R5.
- RISKEN, H. 1996 *The Fokker-Planck Equation. Methods of Solutions and Applications*, 2nd edn. Springer-Verlag.
- ROSHKO, A. 1993 Perspectives on Bluff Body Aerodynamics. *J. Wind Eng. Ind. Aerodyn.* **49**, 79–100.
- ROUSSOPOULOS, K. & MONKEWITZ, P. A. 1996 Nonlinear modelling of vortex shedding control in cylinder wakes. *Physica D: Nonlinear Phenomena* **97** (1), 264–273.
- RUELLE, D. & TAKENS, F. 1971 On the nature of turbulence. *Commun. Math. Phys.* **20**, 167–192.

- SCHMID, P. J. & SIPP, D. 2016 Linear control of oscillator and amplifier flows. *Phys. Rev. Fluids* **1**, 040501.
- SEIFERT, A., STALNOV, O., SPERBER, D., ARWATZ, G., PALEI, V., DAVID, S., DAYAN, I. & FONO, I. 2008 Large Trucks Drag Reduction Using Active Flow Control. In *46th AIAA Aerosp. Sci. Meet. Exhib.*. Reston, Virginia.
- DA SILVA, C. B., HUNT, J. C. R., EAMES, I. & WESTERWEEL, J. . 2014 Interfacial layers between regions of different turbulence intensity. *Annu. Rev. Fluid Mech.* **46**, 567–590.
- SIROVICH, L. 1987 Turbulence and the dynamics of coherent structures part i: Coherent structures. *Quart. J. Appl. Math.* **45** (3), 561–590.
- SKOGESTAD, S. & POSTLETHWAITE, I. 2005 *Multivariable Feedback Control. Analysis and Design*, 2nd edn. John Wiley & Sons Inc.
- SMITH, S. W. 1997 *The Scientist and Engineer's Guide to Digital Signal Processing*, 1st edn. California Technical Publishing.
- SON, D., JEON, S. & CHOI, H. 2011 A proportional-integral-differential control of flow over a circular cylinder. *Philos. Trans. A. Math. Phys. Eng. Sci.* **369** (1940), 1540–55.
- SREENIVASAN, K. R., BERSHADSKII, A. & NIEMELA, J. J. 2002 Mean wind and its reversal in thermal convection. *Phys. Rev. E* **65**, 056306.
- SREENIVASAN, K. R., STRYKOWSKI, P. J. & OLINGER, D. J. 1987 Hopf bifurcation, landau equation, and vortex shedding behind circular cylinders. In *Forum on Unsteady Flow Separation* (ed. K. N. Ghia), pp. 1–13.
- STROGATZ, S. 1994 *Nonlinear Dynamics and Chaos*, 1st edn. Westview Press.
- TADMOR, G., LEHMANN, O., NOACK, B. R., CORDIER, L., DELVILLE, J., BONNET, J.-P. & MORZYŃSKI, M. 2011 Reduced-order models for closed-loop wake control. *Phil. Trans. R. Soc. A* **369** (1940), 1513–1524.
- TAN, Y., MOASE, W. H., MANZIE, C., NEŠIĆ, D. & MAREELS, I. M. Y. 2010 Extremum seeking from 1922 to 2010. In *29th Chinese Control Conf.*, pp. 14–26. Beijing.
- TAN, Y., NEŠIĆ, D. & MAREELS, I. 2008 On the choice of dither in extremum seeking systems: A case study. *Automatica* **44**, 1446–1450.

- TAYLOR, J. A. & GLAUSER, M. N. 2004 Towards practical flow sensing and control via pod and lse based low-dimensional tools. *ASME. J. Fluids Eng.* **126**, 337–345.
- TOMBOULIDES, A. G. & ORSZAG, S. A. 2000 Numerical investigation of transitional and weak turbulent flow past a sphere. *J. Fluid Mech.* **416**, 45–73.
- TU, J. H., GRIFFIN, J., HART, A., ROWLEY, C. W., CATTAFESTA III, L. N. & UKEILEY, L. S. 2013 Integration of non-time-resolved PIV and time-resolved velocity point sensors for dynamic estimation of velocity fields. *Exp. Fluids* **54**, 1429.
- UKEILEY, L. S., MURRAY, N., SONG, Q. & CATTAFESTA III, L. N. 2008 Dynamic surface pressure based estimation for flow control. In *IUTAM Symposium on Flow Control and MEMS: Proceedings of the IUTAM Symposium held at the Royal Geographical Society, 19–22 September 2006, hosted by Imperial College, London, England* (ed. J. F. Morrison, D. M. Birch & P. Lavoie), pp. 183–189. Springer Netherlands.
- VARON, E., EULALIE, Y., EDWIGE, S., GILOTTE, P. & AIDER, J.-L. 2017 Chaotic dynamics of large-scale structures in a turbulent wake. *Phys. Rev. Fluids* **2**, 034604.
- VILAPLANA, G., GRANDEMANGE, M., GOHLKE, M. & CADOT, O. 2013 Global mode of a sphere turbulent wake controlled by a small sphere. *J. Fluids Struct.* **41**, 119–126.
- VOLPE, R., DEVINANT, P. & KOURTA, A. 2015 Experimental characterization of the unsteady natural wake of the full-scale square back Ahmed body: flow bi-stability and spectral analysis. *Exp. Fluids* **56**, 99.
- WEN, C., POOLE, R. J., WILLIS, A. P. & DENNIS, D. J. C. 2017 Experimental evidence of symmetry-breaking supercritical transition in pipe flow of shear-thinning fluids. *Phys. Rev. Fluids* **2**, 031901.
- WILLIAMSON, C. H. K. 1996 Vortex dynamics in the cylinder wake. *Annu. Rev. Fluid Mech.* **28**, 477–539.
- WONG, D. T.-M. & MAIR, W. A. 1983 Boat-tailed afterbodies of square section as drag-reduction devices. *J. Wind Eng. Ind. Aerodyn.* **12**, 229–235.
- WU, Z., WONG, C. W., WANG, L., LU, Z., ZHU, Y. & ZHOU, Y. 2015 A rapidly settled closed-loop control for airfoil aerodynamics based on plasma actuation. *Exp. Fluids* **56**, 158.

- WYNN, A., PEARSON, D. S., GANAPATHISUBRAMANI, B. & GOULART, P. J.  
2013 Optimal mode decomposition for unsteady flows. *J. Fluid Mech.* **733**, 473–503.
- ZWANZIG, R. 2001 *Nonequilibrium Statistical Mechanics*. Oxford University Press.



# Appendix A

## Open-loop forcing with four flaps

This appendix contains preliminary results of open-loop forcing with all four flaps. Results presented in this chapter are preliminary in nature, and do not have the benefit of fully zeroed instrumentation (as described in § 2.3.1), or PID controlled flaps. However the data may still give an indication of some of the challenges and general features of open-loop forcing.

A first key aim in the use of harmonic forcing is direct drag reduction. Motivated by the work of Pastoor *et al.* (2008) and Parkin *et al.* (2014), it may be anticipated that symmetric forcing of the wake would achieve drag reduction. These previous works had demonstrated that for a 2D bluff body, symmetric forcing with ZNMF jets at  $St \approx 0.1$  could achieve drag reduction by symmetrisation of the shear layer dynamics. We therefore performed open-loop forcing in a similarly symmetric manner, i.e. consisting of oscillatory boat-tailing, and with the flaps located at all four rear edges.

Restricted to symmetric forcing, there are still two manners in which the flaps may be operated: the four flaps may either all move inwards and outwards together (synchronous), or the top/bottom flaps may move inwards while the lateral flaps move outwards (asynchronous). Differences between these strategies should give insight into the specific dynamics of the 3D wake, and in particular the interaction of the vertical and lateral vortex shedding. Figure A.1 displays the drag and base suction as a function of forcing frequency for each of these types of forcing. Within the experimental uncertainty, the data always demonstrate a drag increase and a trend of increasing drag with forcing frequency. There is a notable difference between the two forcing methods, namely that the synchronous case gives consistently lower

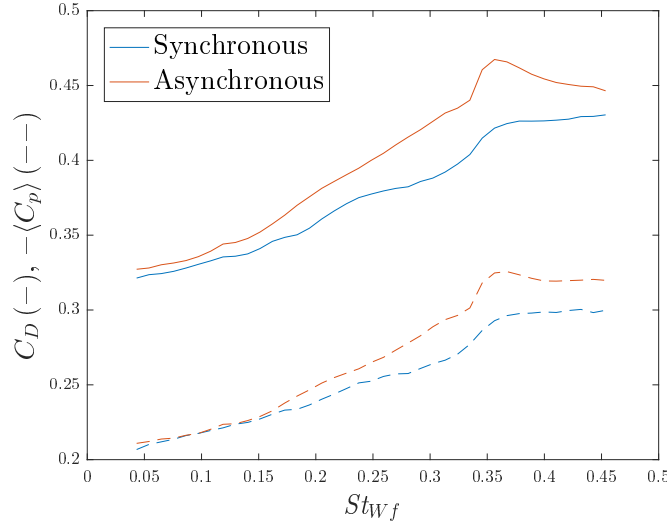


Figure A.1: Effect of symmetric harmonic forcing with all four flaps operating either synchronously or asynchronously. Drag coefficient  $C_D$  and base suction coefficient  $-\langle C_p \rangle$  are shown by the solid and dashed lines respectively.

drag than the asynchronous case. While both forcing methods display a larger drag increase for  $St_{Wf} \approx 0.35$ , this may be due to inconsistency in the flap oscillation amplitude.

In order to understand better the effect of the open-loop forcing, we may examine how the frequency spectrum of the base pressure modes  $m_l$  and  $m_v$  change with forcing frequency. This may best be viewed as waterfall plots, as displayed in figure A.2. it is important to note here that while the forcing is *symmetric*, these displayed results are for *antisymmetric* pressure measurements. Therefore from symmetry arguments we would not expect any particular response at the forcing frequency, shown in each plot by the black dashed lines. An important observation is therefore that for the case of the pressure mode  $m_v$ , significant energy is seen at the forcing frequency itself. A possible reason for the generation of antisymmetric fluctuations is the asymmetry imposed by the ground. Unequal strength of the upper and lower shear layers would cause symmetric flap motion to generate an antisymmetric forcing component. This generation of antisymmetric fluctuations could amplify the vortex shedding in the wake, just as for the antisymmetric forcing displayed in § 5.1, and may be partially responsible for the consistent drag increases displayed in figure A.1.

It is worth also noting that the work of Parkin *et al.* (2015) also found that open-loop forcing may be ineffective when in ground proximity. Their results (for a 2D body)



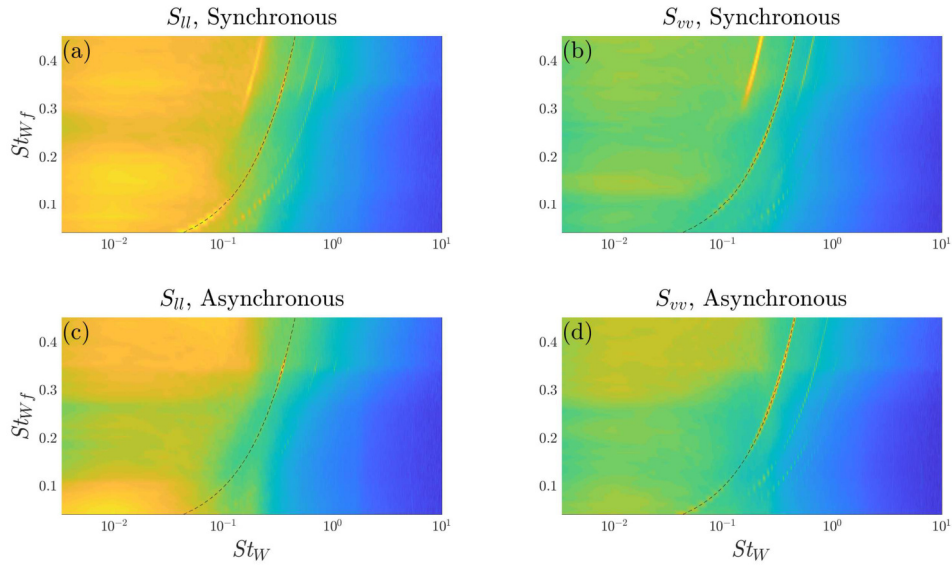


Figure A.2: Waterfall plots illustrating the effect of harmonic forcing on the spectra of the pressure modes  $m_l$ ,  $m_v$ , under synchronous forcing (a), (b) and asynchronous forcing (c), (d).

found that the presence of the ground disrupted vortex shedding in the wake, thereby rendering the forcing inapplicable. This is somewhat in contrast to our results which suggest that the shedding is still present and, moreover, may be amplified to the detriment of the drag reduction.

While all the plots display some energy at the harmonics of the forcing frequency, a key difference between the synchronous and asynchronous cases is seen at the subharmonic of the forcing. For the synchronous cases only, forcing above  $St_W \approx 0.35$  results in an increase in energy in both the lateral and vertical pressure modes at half the forcing frequency. This is indicative of a subharmonic resonance, just as observed by Barros *et al.* (2016a) for a similar rectilinear body, and Berger *et al.* (1990); Rigas *et al.* (2017) for axisymmetric bodies. It is interesting to note that this does not occur at all for the case of asynchronous forcing, reinforcing the understanding that “axisymmetric” forcing is essential in order to generate this effect. It is finally interesting to note that this subharmonic resonance effect does not lead to significantly higher drag, as compared with asynchronous forcing from which it is not generated. This is possibly in contrast to the above cited works for which notable drag increases were observed under conditions of subharmonic resonance.

### A.0.1 Summary

In summary, the open-loop forcing strategy attempted here has proved ineffective for drag reduction. This may firstly be due to the obvious differences between this experiment and that of Pastoor *et al.* (2008); Parkin *et al.* (2014), namely the replacement of ZNMF jets with oscillating flaps and the change from a 2D to 3D geometry. From this work it is not possible to quantify the differences between ZNMF jets and oscillating flaps, however there are many clear differences between the structure of 2D and 3D wakes that may be important here. In particular, the relative importance of the vortex shedding will have strong implications for the applicability of symmetric open-loop forcing. Given that the vortex shedding is likely less coherent in a 3D wake, the ability to readily control it in open-loop is not guaranteed. Finally, the asymmetry imposed by the ground effect, and to a lesser extent the SB mode, means that symmetric flap motion will lead to a degree of antisymmetric forcing. The results of § 5.1 show that this consistently increases the drag, thereby working against any other drag reduction mechanisms.

# Appendix B

## Stochastic differential equations

Much of the modelling discussed in chapter 6 is based on stochastic differential equations (SDE). Here we provide a brief summary of SDEs and some common methods for their analysis.

A SDE consists of a differential equation or set of equations, including one or more stochastic terms. A SDE may most accurately be written as an integral equation as

$$X_{t+s} - X_t = \int_t^{t+s} \mu(X_h, h) dh + \int_t^{t+s} \sigma(X_h, h) dW_h. \quad (\text{B.1})$$

This may then be written in a differential form as

$$dX_t = \mu(X_t, t) dt + \sigma(X_t, t) dW. \quad (\text{B.2})$$

Here it is important to note that the term  $dW$  refers to the integral of a Wiener process and is not integrable in the usual sense, instead requiring the use of Stochastic calculus and a particular interpretation. Heuristically, it is easiest to interpret by understanding that increments of a Wiener process are independent and normally distributed. Bearing the special properties of the stochastic term in mind and without time dependence, the SDE may be written least formally as

$$\dot{x} = f(x) + g(x)\xi(t) \quad (\text{B.3})$$

$$= -V'(x) + g(x)\xi(t). \quad (\text{B.4})$$

Here the term  $f(x, t)$  represents a standard deterministic function, while  $g(x, t)$  multiplies a normally distributed random variable  $\xi(t)$ . As shown, the deterministic term may also be written in terms of the gradient of a potential  $V(x)$ , the ' here

denoting the derivative with respect to  $x$ .

## B.1 Fokker-Planck equation

The Fokker-Planck equation (FPE) is a partial differential equation describing the time evolution of the probability density function for a random variable governed by an SDE. In this work we will make use of the steady state FPE, as the nature of the SDEs examined permit a steady-state solution. For a SDE of the form in (B.4), the FPE is given by

$$\frac{\partial}{\partial t} [P(x, t)] = \frac{\partial}{\partial x} [V'(x)P(x, t)] + \frac{\partial^2}{\partial x^2} \left[ \frac{1}{2} g^2(x) P(x, t) \right]. \quad (\text{B.5})$$

The steady state distribution  $P_s(x)$ , is therefore given as the solution to the equation

$$0 = \frac{\partial}{\partial x} \left[ V'(x) P_s(x, t) + \frac{\partial}{\partial x} \left[ \frac{1}{2} g^2(x) P_s(x, t) \right] \right] \quad (\text{B.6})$$

$$= \frac{\partial}{\partial x} [J(x)]. \quad (\text{B.7})$$

Here the term  $J(x)$  is known as a “flux” and must be constant over  $x$ . The distribution  $P_s(x)$  must tend to zero as  $x \rightarrow \infty$ , implying that  $J(\infty) = 0$  and hence that  $J(x) = 0$ . This reduces (B.6) to a first order ODE in  $P(x)$ , which can be solved to give

$$P_s(x) \propto \frac{1}{g^2(x)} \exp \left( -2 \int^x \frac{V'(x')}{g^2(x')} dx' \right). \quad (\text{B.8})$$

For the case of constant  $g(x) = \sigma$  (B.8) simplifies to

$$P_s(x) \propto \exp \left( -\frac{2V(x)}{\sigma^2} \right). \quad (\text{B.9})$$

# Appendix C

## Miscellaneous proofs

### C.1 Extremum seeking with a square dither signal

In § 3.1.2, it was proposed that a square wave dither signal could be used to overcome the issue of varying the frequency of an input signal. To check that a square wave perturbation and associated square wave demodulation will work, we can write the signal in terms of its Fourier series. For a square wave  $s(t)$  of period  $T = 2\pi/\omega_d$ ,

$$s(t) = \frac{4}{\pi} \sum_{m=1}^{\infty} \frac{\sin((2m-1)\omega_d t)}{2m-1}. \quad (\text{C.1})$$

If we have a reference to the plant  $r(t) = f(t) = f_0 + \hat{f} + as(t)$  then we may take a Taylor expansion about the slowly varying part  $(f_0 + \hat{f})$ . The output from the plant may then be written to include a modified version of the original square wave:

$$y \approx \bar{y} + aN' \left( f_0 + \hat{f} \right) \cdot \sum_{m=1}^{\infty} \frac{|G(i(2m-1)\omega_d)| \sin((2m-1)\omega_d t - \phi_{G(i\omega_d)})}{2m-1} + w_G. \quad (\text{C.2})$$

Following application of the HP filter, demodulation with the square wave  $s(t)$  results in the multiplication of two summations to give

$$\gamma = aN' (f_0 + \hat{f}) \cdot \left( \sum_{m=1}^{\infty} \frac{|G(i(2m-1)\omega_d)| \sin((2m-1)\omega_d t - \phi_{G(i\omega_d)})}{2m-1} \right) \cdot \left( \sum_{n=1}^{\infty} \frac{\sin((2n-1)\omega_d t)}{2n-1} \right) + \tilde{w}_G s(t), \quad (\text{C.3})$$

which may be rewritten as,

$$\gamma = aN' (r) \cdot \sum_{m,n=1}^{\infty} \left[ \frac{|G(i(2m-1)\omega_d)|}{(2m-1)(2n-1)} \sin((2m-1)\omega_d t - \phi_{G(i\omega_d)}) \sin((2n-1)\omega_d t) \right] + \tilde{w}_G s(t). \quad (\text{C.4})$$

The items within this summation can be split into two cases after applying the trigonometric identity

$$\sin(A) \sin(B) = \frac{1}{2} (\cos(A-B) - \cos(A+B)). \quad (\text{C.5})$$

For  $m = n$  we have a sum over terms of the form given in (3.4) which include a DC component, while for  $m \neq n$  we have purely sinusoidal terms. Given a sufficiently effective low pass filter, only the DC terms will pass into  $e$ :

$$e \approx \frac{1}{2} aN' (f_0 + \hat{f}) \sum_{m=1}^{\infty} \left[ \frac{|G(i(2m-1)\omega_d)|}{(2m-1)^2} \cos(\phi_{G(i(2m-1)\omega_d)}) \right] + w_e. \quad (\text{C.6})$$

This square wave extremum seeking system can therefore be expected to work in a very similar manner to the original system with a sinusoidal dither, and is suitable for use in optimising the frequency of a harmonic signal.

## C.2 Statistics of bistable processes

### C.2.1 Switching statistics

A bistable stochastic process may be written as

$$\begin{aligned}\dot{x} &= \alpha x - \lambda x^3 + \sigma \xi(t) \\ &= -V'(x) + \sigma \xi(t),\end{aligned}\tag{C.7}$$

where the potential well is

$$V(x) = \frac{1}{4}\lambda x^4 - \frac{1}{2}\alpha x^2 + \frac{\alpha^2}{4\lambda}.\tag{C.8}$$

This gives  $V(0) = \alpha^2/4\lambda$ , and  $V(\pm\sqrt{\alpha/\lambda}) = 0$ . The potential well therefore has a potential barrier,  $E_b = \alpha^2/4\lambda$ , meaning that at least this much energy input (from noise) is required to flip from one equilibrium point to another. A key parameter is the ratio of the noise intensity to the barrier size. In the weak noise limit ( $\sigma^2/2E_b \ll 1$ ), the expected mean first passage time is given by (Zwanzig, 2001),

$$T = \frac{\pi}{\omega_0\omega_e} \exp\left(\frac{2E_b}{\sigma^2}\right),\tag{C.9}$$

where the two frequencies are defined as  $\omega_0^2 = |V''(0)|$  and  $\omega_e^2 = V''(\pm\sqrt{\alpha/\lambda})$ . It can be shown that

$$V''(x) = 3\lambda x^2 - \alpha,\tag{C.10}$$

hence,  $\omega_0\omega_e = \sqrt{2\alpha}$ . Substituting this and the expression for  $E_b$  into (C.9) gives

$$\begin{aligned}T &= \frac{\pi}{\sqrt{2\alpha}} \exp\left(\frac{2\alpha^2}{4\lambda\sigma^2}\right) \\ &= \frac{\pi}{\sqrt{2\alpha}} \exp\left(\frac{\alpha r_e^2}{2\sigma^2}\right).\end{aligned}\tag{C.11}$$

It is also worth noting that in the weak noise limit where the potential barrier is high and symmetric, each crossing of the barrier is statistically independent (Gammaitoni *et al.*, 1998). This means that crossings of the barrier form a Poisson process, for which the distribution of times between crossings is exponential with mean  $T$ :

$$P(x) = \frac{1}{T} e^{-\frac{x}{T}}.\tag{C.12}$$

This distribution for the flipping times has been demonstrated before by Grange *et al.* (2013c).

### C.2.2 Power spectral density

It has been regularly observed that measurements in the wakes of three-dimensional bluff bodies exhibit a -2 exponent in the PSD at low frequencies. For the axisymmetric bluff body this is a result of the random walk in azimuthal angle, and we will show below that this is consistent with the model of (6.4). For the bistable dynamics of rectilinear wakes this region is attributed to the random flipping. A key difference between these two observations is that while the -2 slope continues to the lowest frequency bins for axisymmetric wakes, in rectilinear wakes this slope becomes zero below a minimum frequency. Here we will provide an explanation for this behaviour.

#### Axisymmetric body

The modelled stochastic differential equation for  $\phi$  consists of the following:

$$d\phi = \frac{1}{\rho} \xi_\phi(t) \quad (\text{C.13})$$

Here the variable  $\xi_\phi(t)$  is a Gaussian random variable, delta correlated in time. We therefore have a modified Wiener process where our variable of interest,  $\phi$  is equal to the integral of Gaussian white noise divided by the instantaneous radius. Hence:

$$\frac{d\phi}{dt} = \frac{1}{\rho(t)} \eta(t) \quad (\text{C.14})$$

Defining the variable  $q = 1/\rho$  and taking Fourier transforms:

$$\begin{aligned} i\omega\Phi(\omega) &= \frac{1}{2\pi} Q(\omega) \star H(\omega) \\ &= \frac{1}{2\pi} \int_{-\infty}^{\infty} Q(\Omega) H(\omega - \Omega) d\Omega \\ &= \frac{H_0}{2\pi} \int_{-\infty}^{\infty} Q(\Omega) d\Omega \\ &= \frac{H_0}{2\pi} I_q \end{aligned} \quad (\text{C.15})$$



Where  $H_0$  is the uniform Fourier transform of  $\eta$  and  $I_q$  is the integral under the Fourier transform of  $q$ .

The power spectral density of  $\phi$  can now be found as:

$$\begin{aligned} S_{\phi\phi} &= |\Phi(\omega)|^2 \\ &= \left| \frac{H_0 I_q}{i2\pi\omega} \right|^2 \\ &= \frac{H_0^2 I_q^2}{4\pi^2 \omega^2} \end{aligned} \tag{C.16}$$

The spectrum of the angle  $\phi$  should therefore have  $\omega^{-2}$  roll off provided that the variable  $q = 1/\rho$  has finite mean squared value. Notably, the spectra of  $\phi$  is independent of the spectra of  $\rho$ .

## Ahmed body

A proof for the -2 exponent seen in the pressure spectrum is given in Grandemange (2013, section D.2.2). Here we provide a more heuristic explanation that also explains the saturation of the -2 exponent at very low frequencies.

A random flipping process may be considered to be a square wave signal, for which the period is random according to a certain probability distribution. A square wave signal  $s(t)$  of period  $T = 2\pi/\omega_d$ , may be written as the series,

$$s(t) = \frac{4}{\pi} \sum_{m=1}^{\infty} \frac{\sin((2m-1)\omega_d t)}{2m-1}. \tag{C.17}$$

The Fourier transform therefore consists of a series of delta functions having  $1/\omega$  decay in their amplitude, giving a single sided PSD of,

$$|S(\omega)|^2 = 16 \sum_{m=1}^{\infty} \frac{\delta(\omega - (2m-1)\omega_d)}{(2m-1)^2}. \tag{C.18}$$

This power spectrum consists of delta functions with  $1/\omega^2$  decay, and a lowest frequency content of  $\omega_d$ . If the period of the square wave is random with time it is reasonable to expect that on average the spectrum is “filled out”, such that there is a frequency range over which there is a continuous -2 decay. However, for frequencies below  $\omega_d$  this is not the case. At very low frequencies  $\omega \ll 1/T$ , there will be very few fundamentals as there will be very few time periods over which there are not

flipping events. These low frequencies correspond to long time-scales of the cross-correlation function  $R_{xx}(\tau)$ . Since all flipping periods are likely much smaller than these time-scales, the cross correlation would be expected to be zero. This implies a uniform power spectrum at low frequencies, as observed in the data.

# Appendix D

## Analyses

### D.1 Bubble length estimation

As described in § 4.3, we wish to estimate the length of the recirculation region from time-resolved PIV data of the near wake. For a laminar wake or the temporal mean of a turbulent one, we could simply select the stream-wise location at which the stream-wise velocity becomes entirely positive. For the fully turbulent wake of our study, this approach will not work since even well after the location at which the separation bubble has ended, turbulent fluctuations may lead to small patches of reversed flow. We therefore instead require a method to detect where the coherent region of reversed flow ends, on a time-resolved basis. This is performed via a two-stage process: for all stream-wise ( $x$ ) locations we find the range of cross-stream ( $y$ ) coordinates at which the stream-wise velocity ( $u_x$ ) is negative; we then find the average  $u_x$  in the full range of  $y$  coordinates between the minimum and maximum locations of negative  $u_x$ . In this way we find the average  $u_x$  within an approximately identified recirculating region. The end of the recirculation bubble is identified as the location at which this “wake averaged” velocity changes from negative to positive. This process is detailed below in algorithm 2.

---

**Algorithm 2** The method for estimating recirculation bubble length.

---

- 1: **for**  $x_i$  in  $\mathbf{x}$  **do**
  - 2:   Find vector  $\hat{\mathbf{y}}$  for which  $u_x(x_i, \hat{y}_j) < 0$
  - 3:   Fill in the range  $\hat{\mathbf{y}}$  to include all  $\hat{y}$  for which  $\min(\hat{\mathbf{y}}) \geq \hat{y} \leq \max(\hat{\mathbf{y}})$
  - 4:   Evaluate wake average as  $\bar{u}_w \leftarrow \text{mean}(u_x(x_i, \hat{\mathbf{y}}))$
  - 5: **end for**
  - 6: Choose  $x_s$  as first  $x_i$  for which  $\bar{u}_w > 0$
-

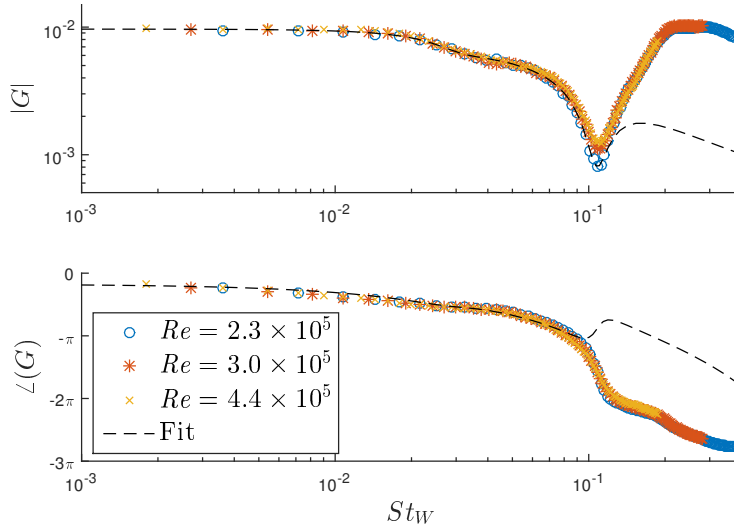


Figure D.1: The response of the wake shown in figure 6.6 along with the linear fit used to estimate the time delay  $\tau$ .

## D.2 Time delay estimation

The model discussed in § 6.3 incorporated a time delay  $\tau$ . Estimation of this convective time scale can be achieved from the frequency response shown in figure D.1. The magnitude response allows the definition of a linear, minimum-phase system using the `fitmagfrd` MATLAB function. This fitted system has a phase corresponding to the minimum-phase part of the system. Any remaining phase response can be attributed to the dead zone (evaluated for the lowest frequency case) and the delay, both of which are non minimum-phase features. A delay term simply gives a linear decrease in phase angle with frequency while the dead zone gives a constant (negative) phase angle. This delay can simply be adjusted until the phase response of the modelled system matches that of the experiment.

## D.3 Least squares fitting

For the  $N$  tested controllers, we wish to find the optimal frequency weighting  $F(\omega)$  that minimises the error between the observed drag changes  $D_i$  and that predicted by the relation:

$$D(M) = \int_0^\infty F(\omega) M(\omega) d\omega, \quad (\text{D.1})$$

where  $M(\omega)$  is the spectral change as defined in § 7.3.4. We firstly discretise  $F$  into a piecewise representation according to,

$$F(\omega) = \sum_{j=1}^P \hat{f}_j \chi_{[\omega_j, \omega_{j+1}]}, \quad (\text{D.2})$$

where the frequencies  $\omega_j$  are fixed frequencies ranging from  $\omega_1$  to  $\omega_{P+1}$ . These frequencies need not be uniformly distributed and need only cover the bandwidth of the controller. The characteristic functions are defined by,

$$\chi_{[a,b]}(x) = \begin{cases} 1, & a \leq x \leq b, \\ 0, & \text{otherwise.} \end{cases} \quad (\text{D.3})$$

For each controller (D.1) therefore gives the expected relation,

$$D_i = \sum_{j=1}^P \hat{f}_j \int_{\omega_j}^{\omega_{j+1}} M_i(\omega) d\omega. \quad (\text{D.4})$$

Given the experimental data we can form a matrix  $A = (a_{ij})$  where  $a_{ij} := \int_{\omega_j}^{\omega_{j+1}} M_i(\omega) d\omega$ . The relation of (D.4) may then be rewritten as  $A\hat{F} = \mathbf{D}$  where  $\hat{F} = (\hat{f}_j)_{j=1}^P$  and  $\mathbf{D} = (D_i)_{i=1}^N$ . Given that this relation is likely approximate, we hope to find an optimal  $\hat{F}$  in a least squares sense as,

$$\min_{\hat{F}} \|A\hat{F} - \mathbf{D}\|_2^2. \quad (\text{D.5})$$

This has the standard least-squares solution  $\hat{F} = (A^\top A)^{-1} A^\top \mathbf{D}$  provided that  $N \geq P$ .



# Appendix E

## Parameter influence in the stochastic models

In this chapter we present results of simulations and analysis for the stochastic model for the vortex shedding discussed in § [6.4](#). The results aim to illustrate the influence of parameter variation upon the behaviour of the models.

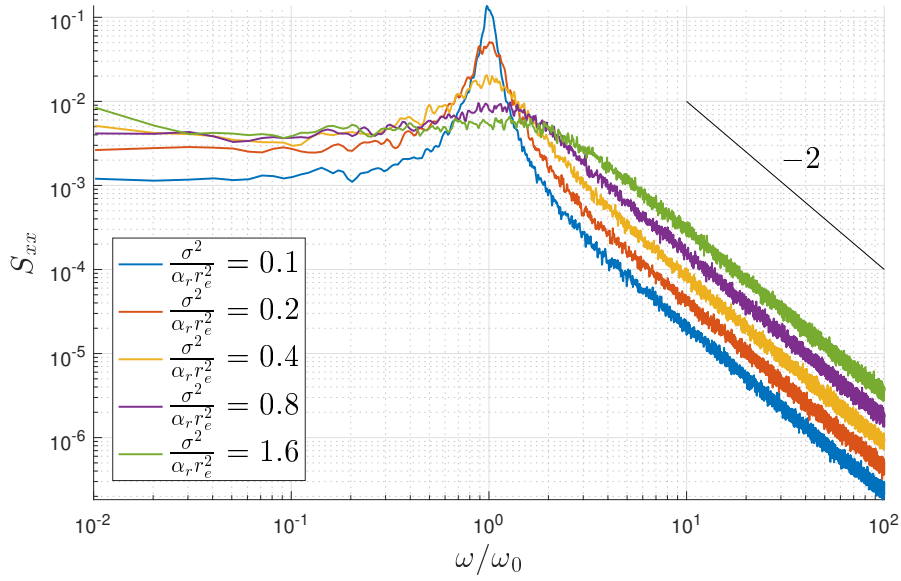


Figure E.1: Unforced power spectral density for the parameter  $y = a \sin(\psi)$  for varying noise intensity.

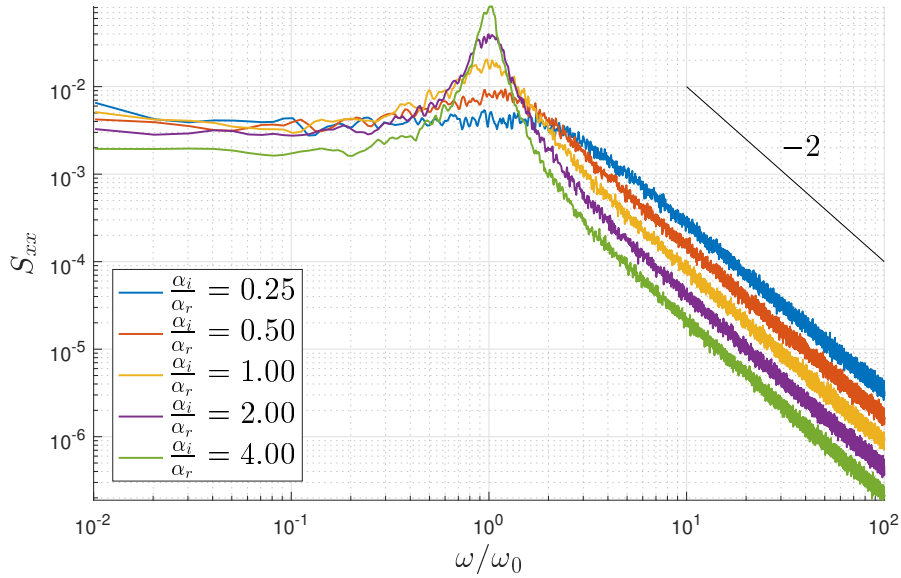


Figure E.2: Unforced power spectral density for the parameter  $y = a \sin(\psi)$  for varying ratios  $\alpha_i/\alpha_r$ .



**CAMBRIDGE UNIVERSITY PRESS LICENSE  
TERMS AND CONDITIONS**

Jun 19, 2017

This Agreement between Rowan Brackston ("You") and Cambridge University Press ("Cambridge University Press") consists of your license details and the terms and conditions provided by Cambridge University Press and Copyright Clearance Center.

License Number	4132390329888
License date	Jun 19, 2017
Licensed Content Publisher	Cambridge University Press
Licensed Content Publication	The Journal of Fluid Mechanics
Licensed Content Title	Properties of the mean recirculation region in the wakes of two-dimensional bluff bodies
Licensed Content Author	S. BALACHANDAR, R. MITTAL, F. M. NAJJAR
Licensed Content Date	Nov 25, 1997
Licensed Content Volume	351
Licensed Content Issue	undefined
Start page	167
End page	199
Type of Use	Dissertation/Thesis
Requestor type	Author
Portion	Text extract
Number of pages requested	1
Author of this Cambridge University Press article	No
Author / editor of the new work	Yes
Order reference number	
Territory for reuse	World
Title of your thesis / dissertation	Feedback Control of Three-Dimensional Bluff Body Wakes for Efficient Drag Reduction
Expected completion date	Jun 2017
Estimated size(pages)	174
Requestor Location	Rowan Brackston Department of Aeronautics Imperial College London Exhibition Road London, Greater london SW7 2AZ United Kingdom Attn: Rowan Brackston
Publisher Tax ID	GB823847609
Customer VAT ID	GB649926678
Billing Type	Invoice
Billing Address	Rowan Brackston

This Agreement between Rowan Brackston ("You") and Elsevier ("Elsevier") consists of your license details and the terms and conditions provided by Elsevier and Copyright Clearance Center.

License Number	4133760528053
License date	Jun 21, 2017
Licensed Content Publisher	Elsevier
Licensed Content Publication	Physics Letters A
Licensed Content Title	Transitions to chaos in the wake of an axisymmetric bluff body
Licensed Content Author	Yannick Bury,Thierry Jardin
Licensed Content Date	Oct 1, 2012
Licensed Content Volume	376
Licensed Content Issue	45
Licensed Content Pages	4
Start Page	3219
End Page	3222
Type of Use	reuse in a thesis/dissertation
Portion	figures/tables/illustrations
Number of figures/tables/illustrations	1
Format	electronic
Are you the author of this Elsevier article?	No
Will you be translating?	No
Order reference number	
Original figure numbers	3(b)
Title of your thesis/dissertation	Feedback Control of Three-Dimensional Bluff Body Wakes for Efficient Drag Reduction
Expected completion date	Jun 2017
Estimated size (number of pages)	174
Elsevier VAT number	GB 494 6272 12
Requestor Location	Rowan Brackston Department of Aeronautics Imperial College London Exhibition Road London, Greater london SW7 2AZ United Kingdom Attn: Rowan Brackston
Publisher Tax ID	GB 494 6272 12
Customer VAT ID	GB649926678

**AMERICAN PHYSICAL SOCIETY LICENSE  
TERMS AND CONDITIONS**

Jun 21, 2017

---

This Agreement between Rowan Brackston ("You") and American Physical Society ("American Physical Society") consists of your license details and the terms and conditions provided by American Physical Society and Copyright Clearance Center.

License Number	4133760746206
License date	Jun 21, 2017
Licensed Content Publisher	American Physical Society
Licensed Content Publication	Physical Review E
Licensed Content Title	Reflectional symmetry breaking of the separated flow over three-dimensional bluff bodies
Licensed Content Author	Mathieu Grandemange, Olivier Cadot, and Marc Gohlke
Licensed Content Date	Sep 27, 2012
Licensed Content Volume	86
Type of Use	Thesis/Dissertation
Requestor type	Student
Format	Electronic
Portion	chart/graph/table/figure
Number of charts/graphs/tables/figures	1
Portion description	Figure 2(c)
Rights for	Main product
Duration of use	Life of Current Edition
Creation of copies for the disabled	no
With minor editing privileges	no
For distribution to	Worldwide
In the following language(s)	Original language of publication
With incidental promotional use	no
The lifetime unit quantity of new product	0 to 499
The requesting person/organization is:	Rowan Brackston
Order reference number	
Title of your thesis / dissertation	Feedback Control of Three-Dimensional Bluff Body Wakes for Efficient Drag Reduction
Expected completion date	Jun 2017
Expected size (number of pages)	174
Requestor Location	Rowan Brackston

**CAMBRIDGE UNIVERSITY PRESS LICENSE  
TERMS AND CONDITIONS**

Jun 21, 2017

This Agreement between Rowan Brackston ("You") and Cambridge University Press ("Cambridge University Press") consists of your license details and the terms and conditions provided by Cambridge University Press and Copyright Clearance Center.

License Number	4133760874363
License date	Jun 21, 2017
Licensed Content Publisher	Cambridge University Press
Licensed Content Publication	The Journal of Fluid Mechanics
Licensed Content Title	Local and global instabilities in the wake of a sphere
Licensed Content Author	BENOÎT PIER
Licensed Content Date	May 25, 2008
Licensed Content Volume	603
Licensed Content Issue	undefined
Start page	39
End page	61
Type of Use	Dissertation/Thesis
Requestor type	Author
Portion	Text extract
Number of pages requested	1
Author of this Cambridge University Press article	No
Author / editor of the new work	Yes
Order reference number	
Territory for reuse	World
Title of your thesis / dissertation	Feedback Control of Three-Dimensional Bluff Body Wakes for Efficient Drag Reduction
Expected completion date	Jun 2017
Estimated size(pages)	174
Requestor Location	Rowan Brackston Department of Aeronautics Imperial College London Exhibition Road London, Greater london SW7 2AZ United Kingdom Attn: Rowan Brackston
Publisher Tax ID	GB823847609
Customer VAT ID	GB649926678
Billing Type	Invoice
Billing Address	Rowan Brackston Imperial College London



**Title:** Perspectives on bluff body aerodynamics

**Author:** A. Roshko

**Publication:** Journal of Wind Engineering and Industrial Aerodynamics

**Publisher:** Elsevier

**Date:** December 1993

Copyright © 1993 Published by Elsevier B.V.

Logged in as:  
Rowan Brackston  
Account #:  
3001048928

[LOGOUT](#)

## Order Completed

Thank you for your order.

This Agreement between Rowan Brackston ("You") and Elsevier ("Elsevier") consists of your license details and the terms and conditions provided by Elsevier and Copyright Clearance Center.

Your confirmation email will contain your order number for future reference.

[Printable details.](#)

License Number	4133761303628
License date	Jun 21, 2017
Licensed Content Publisher	Elsevier
Licensed Content Publication	Journal of Wind Engineering and Industrial Aerodynamics
Licensed Content Title	Perspectives on bluff body aerodynamics
Licensed Content Author	A. Roshko
Licensed Content Date	Dec 1, 1993
Licensed Content Volume	49
Licensed Content Issue	1-3
Licensed Content Pages	22
Type of Use	reuse in a thesis/dissertation
Portion	figures/tables/illustrations
Number of figures/tables/illustrations	1
Format	electronic
Are you the author of this Elsevier article?	No
Will you be translating?	No
Order reference number	
Original figure numbers	2
Title of your thesis/dissertation	Feedback Control of Three-Dimensional Bluff Body Wakes for Efficient Drag Reduction
Expected completion date	Jun 2017
Estimated size (number of pages)	174
Elsevier VAT number	GB 494 6272 12
Requestor Location	Rowan Brackston Department of Aeronautics Imperial College London Exhibition Road London, Greater london SW7 2AZ United Kingdom Attn: Rowan Brackston
Publisher Tax ID	GB 494 6272 12
Customer VAT ID	GB649926678
Total	0.00 GBP



**Title:** Extremum seeking to control the amplitude and frequency of a pulsed jet for bluff body drag reduction

**Author:** Rowan D. Brackston

**Publication:** Experiments in Fluids

**Publisher:** Springer

**Date:** Jan 1, 2016

Copyright © 2016, The Author(s)

Logged in as:  
Rowan Brackston  
Account #:  
3001048928

LOGOUT

## Permissions Request

This is an open access article distributed under the terms of the Creative Commons Attribution License, which permits unrestricted use, distribution, and reproduction in any medium, provided the original work is properly cited.

Springer and BioMed Central offer a reprint service for those who require professionally produced copies of articles published under Creative Commons Attribution (CC BY) licenses. To obtain a quotation, please email [reprints@springeropen.com](mailto:reprints@springeropen.com) with the article details, quantity(ies) and delivery destination. Minimum order 25 copies.

CLOSE WINDOW

Copyright © 2017 [Copyright Clearance Center, Inc.](#) All Rights Reserved. [Privacy statement.](#) [Terms and Conditions.](#)  
Comments? We would like to hear from you. E-mail us at [customer care@copyright.com](mailto:customer care@copyright.com)



**Title:** Stochastic modelling and feedback control of bistability in a turbulent bluff body wake

**Author:** R. D. Brackston, J. M. García de la Cruz, A. Wynn, G. Rigas, J. F. Morrison

**Publication:** The Journal of Fluid Mechanics

**Publisher:** Cambridge University Press

**Date:** Aug 10, 2016

Copyright © © 2016 Cambridge University Press

Logged in as:  
Rowan Brackston  
Account #:  
3001048928

[LOGOUT](#)

## Order Completed

Thank you for your order.

This Agreement between Rowan Brackston ("You") and Cambridge University Press ("Cambridge University Press") consists of your license details and the terms and conditions provided by Cambridge University Press and Copyright Clearance Center.

Your confirmation email will contain your order number for future reference.

[Printable details.](#)

License Number	4133760978229
License date	Jun 21, 2017
Licensed Content Publisher	Cambridge University Press
Licensed Content Publication	The Journal of Fluid Mechanics
Licensed Content Title	Stochastic modelling and feedback control of bistability in a turbulent bluff body wake
Licensed Content Author	R. D. Brackston, J. M. García de la Cruz, A. Wynn, G. Rigas, J. F. Morrison
Licensed Content Date	Aug 10, 2016
Licensed Content Volume	802
Licensed Content Issue	undefined
Start page	726
End page	749
Type of Use	Dissertation/Thesis
Requestor type	Author
Portion	Full article
Author of this Cambridge University Press article	Yes
Author / editor of the new work	Yes
Order reference number	
Territory for reuse	World
Title of your thesis / dissertation	Feedback Control of Three-Dimensional Bluff Body Wakes for Efficient Drag Reduction
Expected completion date	Jun 2017
Estimated size(pages)	174
Requestor Location	Rowan Brackston Department of Aeronautics Imperial College London Exhibition Road London, Greater london SW7 2AZ United Kingdom Attn: Rowan Brackston
Publisher Tax ID	GB823847609